Rasika Dhavse
Vinay Kumar
Salvatore Monteleone   *Editors*

Emerging Technology Trends in Electronics, Communication and Networking

Select Proceedings of the Fourth International Conference, ET2ECN 2021

Springer

Lecture Notes in Electrical Engineering

Volume 952

The book series *Lecture Notes in Electrical Engineering* (LNEE) publishes the latest developments in Electrical Engineering—quickly, informally and in high quality. While original research reported in proceedings and monographs has traditionally formed the core of LNEE, we also encourage authors to submit books devoted to supporting student education and professional training in the various fields and applications areas of electrical engineering. The series cover classical and emerging topics concerning:

- Communication Engineering, Information Theory and Networks
- Electronics Engineering and Microelectronics
- Signal, Image and Speech Processing
- Wireless and Mobile Communication
- Circuits and Systems
- Energy Systems, Power Electronics and Electrical Machines
- Electro-optical Engineering
- Instrumentation Engineering
- Avionics Engineering
- Control Systems
- Internet-of-Things and Cybersecurity
- Biomedical Devices, MEMS and NEMS

For general information about this book series, comments or suggestions, please contact leontina.dicecco@springer.com.

To submit a proposal or request further information, please contact the Publishing Editor in your country:

China

Jasmine Dou, Editor (jasmine.dou@springer.com)

India, Japan, Rest of Asia

Swati Meherishi, Editorial Director (Swati.Meherishi@springer.com)

Southeast Asia, Australia, New Zealand

Ramesh Nath Premnath, Editor (ramesh.premnath@springernature.com)

USA, Canada

Michael Luby, Senior Editor (michael.luby@springer.com)

All other Countries

Leontina Di Cecco, Senior Editor (leontina.dicecco@springer.com)

** This series is indexed by EI Compendex and Scopus databases. **

Rasika Dhavse · Vinay Kumar ·
Salvatore Monteleone
Editors

Emerging Technology Trends in Electronics, Communication and Networking

Select Proceedings of the Fourth International Conference, ET2ECN 2021

Springer

Editors
Rasika Dhavse
Department of Electronics Engineering
Sardar Vallabhbhai National Institute
of Technology
Surat, India

Vinay Kumar
Department of Electronics
and Communication Engineering
MNNIT Allahabad
Prayagraj, India

Salvatore Monteleone
Department of Computer Engineering
Kore University of Enna
Enna, Italy

Organization

Chief Patron

Ravipudi Venkata Rao, Director, Sardar Vallabhbhai National Institute of Technology, India

Patrons

P. L. Patel, Dy. Director, Sardar Vallabhbhai National Institute of Technology, India
U. D. Dalal, Sardar Vallabhbhai National Institute of Technology, India

General Chairs

Abhilash Mandloi, Sardar Vallabhbhai National Institute of Technology, India
Kishor Upla, Sardar Vallabhbhai National Institute of Technology, India
Kirti Inamdar, Sardar Vallabhbhai National Institute of Technology, India

Organizing Secretary

Shilpi Gupta, Sardar Vallabhbhai National Institute of Technology, India

Program Chair

J. N. Sarvaiya, Sardar Vallabhbhai National Institute of Technology, India

Convenor

P. N. Patel, Sardar Vallabhbhai National Institute of Technology, India

Co-convenor

P. K. Shah, Sardar Vallabhbhai National Institute of Technology, India
A. H. Lalluwadia, Sardar Vallabhbhai National Institute of Technology, India

Local Chairs

J. N. Patel, Sardar Vallabhbhai National Institute of Technology, India
Suman Deb, Sardar Vallabhbhai National Institute of Technology, India

Publicity Chairs

Abhishek Acharya, Sardar Vallabhbhai National Institute of Technology, India
Kamal Captain, Sardar Vallabhbhai National Institute of Technology, India

Sponsorship Chairs

A. D. Darji, Sardar Vallabhbhai National Institute of Technology, India
Z. M. Patel, Sardar Vallabhbhai National Institute of Technology, India

Registration Chairs

Shweta Shah, Sardar Vallabhbhai National Institute of Technology, India
Deepak Joshi, Sardar Vallabhbhai National Institute of Technology, India

Exhibition Chairs

N. B. Kanirkar, Sardar Vallabhbhai National Institute of Technology, India
Golak Santra, Sardar Vallabhbhai National Institute of Technology, India

Publication Chairs

Rasika Dhavse, Sardar Vallabhbhai National Institute of Technology, India
Salvatore Monteleone, Kore University of Enna, Italy
Vinay Kumar, Motilal Nehru National Institute of Technology, India

Web Chairs

P. J. Engineer, Sardar Vallabhbhai National Institute of Technology, India
M. C. Patel, Sardar Vallabhbhai National Institute of Technology, India

Technical Program Committee

Dr. Shrivishal Tripathi, IIIT, Naya Raipur, India
Dr. Joydeep Sengupta, VNIT Nagpur, India
Dr. Maulin Joshi, SCET Gujarat, India
Dr. Taimoor Khan, NIT, Silchar, India
Dr. Vrinda Gupta, NIT, Kurukshetra, India
Dr. Vishnu Awasthi, Saffrony Institute of Technology, Ahmedabad, India
Dr. Amit Joshi, MNIT Jaipur, India
Dr. Raghvendra Chaudhary, ISM, Dhanbad, India
Dr. Tarun Kr. Gupta, MANIT Bhopal, India
Dr. Arvind Sharma, NIT, Kurukshetra, India
Dr. Prabhat Sharma, VNIT Nagpur, India
Dr. Ravi Maddila, MNIT Jaipur, India
Dr. Prakash Pareek, VIT, Andhra Pradesh, India
Dr. Vandana Rohokale, Singhad Institute of Technology, Pune, India
Dr. Yogendra Kumar Prajapati, MNNIT Allahabad, India
Vamsi Krishna Allam, Raghu Engineering College, Vishakhapatnam, India
Prof. Gaurav Gambhir, PIET, Panipat, India
Dr. Amit Patel, Charusat, Anand, India
Dr. Neeraj Rao, VNIT Nagpur, India

Prof. Ravi Kumar Palla, GMR Institute of Engineering, Rajam, Andhra Pradesh, India
Prof. Harminder Kaur, PIET, Panipat, India
Dr. Ashish Bhandari, NIT, Patna, India
Dr. Gaurav Verma, NIT, Kurukshetra, India
Dr. R. Murugan, NIT, Silchar, India
Dr. Niket Shastri, SCET, Surat, India
Dr. Satyasai Jagannath Nanda, MNIT, Jaipur, India
Dr. Atanu Chowdhury, NIT, Agartala, India
Dr. Apangshu Das, NIT, Agartala, India
Dr. Prasanth G. R., NIT Goa, India
Dr. C. M. Negi, Banasthali Vidhyapith University, Rajasthan, India
Dr. Sargi Abadal, University of Catalunya, Spain
Dr. Kiran Raja, NTNU, Norway
Dr. Aakash Shanbhag, University of Southern California, USA
Dr. Zahid Akhtar, State University of New York Polytechnic Institute
Dr. Vijayshree Chaurasiya, MANIT Bhopal, India
Dr. Deepak Gupta, KIET, Ghaziabad, India
Dr. Amit Garg, IIIT, Kota, India
Dr. E. S. Gopi, NIT Trichy, India
Dr. Subhashish Tiwari, CMR University, Bangalore, India
Dr. Rakesh Ranjan, NIT, Patna, India
Dr. Meena Panchore, NIT, Patna, India
Dr. Ghanshyam Singh, MNIT Jaipur, India
Dr. Dharmendra Kumar, MMMUT, Gorakhpur, India
Dr. Anamika Singh, VNIT Nagpur, India
Dr. Shishir Jagtap, PEC Mumbai, India
Dr. Jeychitra, NIT Trichy, India
Dr. Pradnya Ghare, VNIT Nagpur, India
Dr. P. Maheswaran, NIT Trichy, India
Dr. Ara Ali Khan, IIT Jodhpur, India
Dr. Pooja Lohia, MMMUT, Gorakhpur, India
Prof. Stuti Mehla, PIET, Panipat, India
Dr. Sudhanshu Verma, MMMUT, Gorakhpur, India
Dr. Kavicharan Mummaneni, NIT, Silchar, India
Mangal Singh, Nirma University, Ahmedabad, India
Dr. Subodh Srivastava, NIT, Patna, India
Dr. Sudhanshu Choudhary, NIT, Kurukshetra, India
Dr. Nehal Shah, SCET, Surat, India
Dr. Rajesh Saha, MNIT Jaipur, India
Dr. Robin Khosla, NIT, Silchar, India
Dr. Priyanka Choudhury, NIT, Agartala, India
Dr. Yash Agarwal, DAIICT, Gandhinagar, India
Dr. S. Tolani, SVNIT, Surat, India
Gangireddy Sushnigdha, SVNIT, Surat, India

Dr. Mudasir Ahmad Wani, NTNU, Norway
Dr. Filip Lemic, University of Antwerp, Belgium
Dr. Ankur Shukla, NTNU, Norway
Dr. Hirenkumar Gami, Miami University, USA
Dr. Akshay Jain, Senior Telecommunications Engineer, Neutroon, Spain

Advisory Committee

International Advisory Committee

Dr. Santosh Kumar, Liaocheng University, China
Dr. Kiran Raja, NTNU, Norway
Dr. Hiren Gami, Miami University, USA
Dr. Angela Amphawan, Sunway University, Malaysia
Dr. Arokiaswami Alphones, Nanyang Technological University, Singapore
Dr. Naser Damer, IGD, Fraunhofer, Germany
Dr. Zahid Akhtar, State University of New York Polytechnic Institute, USA
Dr. Ana Filipa Sequeira, Centre for Telecommunications and Multimedia, Porto, Portugal

National Advisory Committee

Dr. Vipul Rastogi, IIT Roorkee, India
Dr. V. S. Tripathi, MNNIT Allahabad, India
Dr. Vijay Janyani, MNIT Jaipur, India
Dr. Manjunath Joshi, DAIICT, Gandhinagar, India
Dr. Dhaval Pujara, Nirma University, Ahmedabad, India
Dr. Mehul Raval, Ahmedabad University, Ahmedabad, India
Dr. Y. P. Kosta, Vice Chancellor, Rajkot, India
Dr. K. P. Ray, Defence Institute of Advanced Technology (DIAT), Pune, India

Preface

It is a matter of great privilege to write a preface for the proceedings of the Fourth International Conference on Emerging Technology Trends in Electronics, Communication and Networking (ET2ECN 2021), organized by Department of Electronics Engineering, Sardar Vallabhbhai National Institute of Technology, Surat, India, during November 17–18, 2021. This conference was followed by a great success of the previous three international conferences organized in 2012, 2014 and 2020. The year 2021 is being celebrated as the Diamond Jubilee Year of our institute, S. V. National Institute of Technology (SVNIT), Surat. This conference was part of this Diamond Jubilee Celebration.

The Fourth International Conference on Emerging Technology Trends in Electronics, Communication and Networking (ET2ECN 2021) is soliciting original and previously unpublished papers addressing research challenges and advances in the areas of electronics, communication and networking systems. The objective of the conference is to provide an opportunity for researchers, academicians and students to discuss and exchange ideas on issues, trends and developments in electronics, communication and networking. The ET2ECN 2021 conference takes a broader view and seeks papers describing innovative research contributions to the broad field of electronics, communication and latest as well as upcoming technologies. The conference addresses a broad range of research and real-life application topics, including theory, methods, applications and tools. The contributions will enrich knowledge and motivate the young researchers and experienced electronics and communication engineers who wish to explore new areas in electronics, communication and networking. These will also be beneficial for the professionals/researchers working in research and development laboratories and in areas like machine learning, artificial intelligence, soft computing, etc.

The program committee of ET2ECN 2021 is extremely grateful to the authors who showed an overwhelming response to the call for papers. Totally, 71 papers were submitted by authors in three tracks. The entire review team expanded tremendous efforts to ensure selection of quality papers. Best quality papers were selected based on the review from three reviewers for each paper. Similarity checking and

overlapping were based on international norms and standards. Based on the recommendations of reviewers, this present book contains 26 papers accepted for publications. The proceedings of the conference are published as one volume in the Lecture Notes in Electrical engineering (LNEE) series by Springer. We place our gratitude as the chairs to the organizing committee members and students, whose constant involvement and dedication supported us at every stage of this task.

We, in our capacity as the volume editors, convey our sincere gratitude to springer for providing the opportunity to publish the proceedings of ET2ECN 2021 in their LNEE series.

The conference program had beautiful array of keynote and invited speakers from all over the world. The program consists of keynote sessions and paper presentations, covering a wide range of topics in electronics, communication and networking. Keynote speakers included Prof. Y. P. Kosta, Dr. Santosh Kumar, Dr. Sergi Abadal, Ms. Neha Raj, Dr. Ashwin Kothari, Dr. Raghavendra Ramachandra and Prof. D. C. Jinwala. We are grateful to them for sharing their insights on their latest research with us.

Finally, we would like to express our sincere thanks to the SVNIT administration and advisory committee members for their support and guidance in organizing this conference. We are also thankful to other sponsoring agencies for joining their hands with us to make this conference a great success.

It is expected that the delegates and the participants have been enriched by the experience of this conference and the legacy of knowledge dissemination will continue.

Surat, India   Rasika Dhavse
Prayagraj, India   Vinay Kumar
Enna, Italy   Salvatore Monteleone
November 2021

Plenary Talk

Microstrip Antennas

Y. P. Kosta
CHARUSAT University
Gujarat, India

This presentation session will include introductory aspects of microstrip antennas such as radiation mechanism, antenna parameters, feeding techniques and measurement aspects. This will be followed by a quick way to estimate the resonant frequency of a microstrip antenna and arrive at its physical size. The know-how of the physical dimensions will function as plug-in to an antenna software and quick start design and design optimization. Finally, toward the end, a new concept of liquid antennas will also be introduced to the participants. The liquid antenna concept was first reported and introduced by the author(s) in 1989 in a regional conference at IIT Roorkee. Liquid antennas were extensively introduced to the antenna community in an IEEE Antenna Conference as a publication in 2004. The title of the research paper was "Liquid Antenna Systems". This conference paper can easily be extracted by Google.

Keynote Speeches

Optical Fiber-Based Plasmonic Biosensor for Cancer Detection

Dr. Santosh Kumar
Senior Member SPIE
Associate Professor
School of Physics Science and Information Technology
Liaocheng University
Liaocheng, China

Plasmonic fiber-optic biosensors utilize the flexibility and compactness of optical fibers in conjunction with the high sensitivity of nanomaterials to their surrounding medium to detect biological species such as cancer cells. Due to their small size, accuracy, low cost and ability to perform remote and distributed sensing, plasmonic fiber-optic biosensors are promising alternatives to conventional cell detection methods. They have the potential to benefit clinical diagnostics, drug discovery, food process control, disease detection and environmental monitoring. Recent advances in cancer cell detection have resulted in the development of multicore optical fiber-based biosensors. Six distinct normal and cancer cells were cultured and detected using a newly developed sensor. I would like to discuss the fabrication of optical fiber plasmonic sensors and the establishment of a cell culture laboratory for the purpose of developing biosensors for the detection of cancer cells and other microorganisms. The discussion will benefit researchers working in optical fiber technology and biosensing.

Toward the Internet of Everything with Reconfigurable Intelligent Surfaces and Graphene Antennas

Dr. Sergi Abadal
Distinguished Researcher
Coordinator of the FET-OPEN Project WiPLASH
Ambassador of the European Innovation Council
Universitat Politècnica de Catalunya (UPC)
Barcelona, Spain

Abstract: Advances in RF design enable the implementation of wireless communications at the mmWave to THz bands, potentially leading to very high speeds while using tiny antennas and transceivers. This is expected to be translated into wireless networks with unprecedented levels of performance and efficiency, as well as the capacity to enter into uncharted territories such as inside the body or inside the chips, opening a plethora of disruptive applications in the context of the Internet of Everything. In this keynote, we will describe two groundbreaking technologies and their implications in wireless networks in 6G and beyond. On the one hand, we will review the concept of Reconfigurable Intelligent Surfaces (RIS), whose powerful control over electromagnetic waves allows them to modify the characteristics of the wireless channel in unprecedented and software-defined ways. This will be particularly critical in the THz band, since multiple phenomena impair propagation and limit the transmission distance in this part of the wireless spectrum. We will briefly revisit the fundamentals of RIS in the mmWave-THz bands, to then summarize the main applications in the contexts of 6G networks. On the other hand, we will introduce recent works on graphene antennas, whose plasmonic properties at THz frequencies lead to extreme levels of miniaturization and unprecedented tunability. We will finally describe Wireless Network-on-Chip (WNoC), a novel area-constrained application uniquely suited to the characteristics of the highly integrated, ultra-high-speed wireless communications enabled by graphene and that shows potential for a paradigm shift in the field of computer architecture.

Recent Trends in Communication Engineering and Issues and Challenges Thereof

Dr. Ashwin Kothari
Associate Professor
Visvesvaraya National Institute of Technology
Nagpur, India

Consistent demand of high performance and reliability, spectrum efficacy, high data speed and environment-friendly technology with sustainability has made communication engineering to undergo a paradigm shift or evolution. Tremendous research

efforts pursued all over the world have come up with new and recent methodologies or techniques to achieve desired goals. This has resulted in many interesting problem statements or research fields open for the researchers to be pursued worldwide. Such efforts demand amalgamation of approaches based on interdisciplinary fields which further results in issues to be addressed related to compliance at various levels. A serious attention must be given to the needs of design of newer standards, protocols and algorithms not only for implementation of these newer technologies but also for their testing and validation. My talk would be covering an overview of such trends and issues and challenges related to them.

Electronic Trends of Upcoming Integrated Technology

Ms. Neha Raj
Member of Technical Staff
Global Foundries
Singapore

Semiconductor industry makes modern life possible. Without semiconductor chips, smartphones, computers, healthcare equipment, military devices, transportation and thousands of other devices could not function. Thus far, the industry has managed to consistently provide more powerful integrated chips in response to demand, allowing electronic innovations to develop at a staggering rate. That said, the increasing demands for smaller, faster semiconductor chips raise an important question: Is the system scaling made possible by Moore's Law reaching its limits? And if so, how can semiconductor manufacturers surmount this technological roadblock? At some point, the industry will reach the physical limitations of existing semiconductor materials, making it impossible to continue doubling transistors indefinitely. This limit is expected to be reached soon and could have grave implications for the future of AI and high-performance computing.

Two interconnected solutions to overcome these obstacles to Moore's Law are as follows: More Moore and More than Moore. More Moore recommends reducing chip size and increasing logic and memory capabilities through improvements in logic, dynamic random-access memory and nonvolatile memory systems, pushing chip performance beyond existing complementary metal-oxide semiconductor limits. And More than Moore recommends the growth of silicon technologies that do not scale with Moore's Law, such as radio frequency, solid-state lighting, system in package and organic technology. The future technology challenges are the innovations and effective integrations of above solutions focusing mainly on digital, non-digital function and heterogeneous integration.

Adversarial Machine Learning: An Introduction and Case Studies

Prof. D. C. Jinwala
Professor and Dean R&C
SVNIT
Surat, India

In this talk, we shall focus on understanding how the machine learning (ML) techniques can be and are being exploited to orchestrate security attacks on the machine learning-based solutions. Recently, Google, Microsoft and IBM have signaled and focused initiatives to secure their ML systems. Prior to that there have been several published reports from the leading industry market research firms, too that have cautioned the designers and the developers to safeguard against the risks of data corruption, model theft and adversarial samples. In this talk after an introduction to how the taxonomy of the role of machine learning in the information security in general, several examples of the adversarial attacks on the machine learning solutions shall be presented. In addition, an attempt would also be made to understand the extent to which organizations across different industries are protecting their ML systems from attacks, detecting adversarial manipulation and to responding to attacks on their ML systems.

Face Morphing Attacks: Vulnerability and Detection

Dr. Raghavendra Ramachandra
Institute of Information Security and Communication Technology (IIK)
Norwegian University of Science and Technology
Gjovik, Norway

Morphing is the process of seamlessly combining the face images from different data subjects to generate the composite (or morphing) image that can share the facial characteristics from the contributing data subjects. Face morphing attacks have shown high vulnerability on the commercial face recognition system. In this keynote, deep learning-based morphed attack generation will be presented. Further, 3D face morphing generation will also be discussed. Lastly, part of the talk will focus on the detection of face morphing attacks.

Contents

Networking

About the Editors

Rasika Dhavse is an Associate Professor in the Department of Electronics Engineering of Sardar Vallabhbhai National Institute of Technology, Surat. She pursued her doctoral degree in the field of nanocrystal-based flash memory devices. She has over 22 years of academic experience. She is currently supervising five doctoral theses. She has completed a DST-funded project and two DeiTY-funded projects (under the INUP program) related to flash memory devices in the capacity of a Co-principal Investigator. She has published several papers in national and international conferences and journals.

Vinay Kumar is an Assistant Professor (Grade-I) in the Department of Electronics and Communication Engineering, Motilal Nehru National Institute of Technology (MNNIT), Allahabad. He received his bachelor's degree in Electronics and Communications from Dr. A. P. J. Abdul Kalam Technical University, in 2006, and his M.Tech. and Ph.D. degrees from the Electronics and Communication Engineering Department, MNNIT, in 2010 and 2015, respectively. He is currently dealing with three projects sponsored by Government of India based on underwater and underground communication. His broad research interests include underwater, underground, and terrestrial wireless sensor networks. He has authored/co-authored over 65 research papers in international/national journals/conference proceedings.

Salvatore Monteleone received a Ph.D. in Computer and Communication Engineering from the Department of Electrical, Electronic, and Computer Engineering at the University of Catania, Italy, in 2014. There he worked as a research assistant and Adjunct Computer architecture Professor for the Electronic Engineering course until October 2019. From November 2019 to October 2020, Dr. Monteleone was a research fellow within the Fellows-in-Residence program at the CY Advanced Studies, CY Cergy Paris University (formerly known as the University of Cergy-Pontoise), and at the ETIS Lab, a joint research laboratory of CNRS (UMR 8051), ENSEA, and CY Cergy Paris University, in France. Since November 2020, Dr. Monteleone is a research fellow at the STMLab, Department of Computer Engineering, Faculty of Engineering and Architecture, Kore University of Enna, Italy. The

research activity of Dr. Monteleone mainly focuses on cyber-physical systems and network-on-chip-based architectures with particular reference to low-power design and applications.

Electronics

Comparative Analysis of Static Bias Methods for Basic Differential Amplifier

Dipesh Panchal and **Amisha Naik**

Abstract The power budget is a very stringent requirement for portable instruments. In this paper, static dynamic methods for ultra-low power and voltage are identified like gate driven, bulk driven (non-conventional method), and dynamic threshold methods which are applied on basic differential amplifier cell, and comparative analysis is performed for various parameters like power dissipation, gain bandwidth product, etc. The ultra-low voltage is selected for low power dissipation and simulations performed under TSMC 180 nm Technology node. The results show that the dynamic threshold method (gate driven, bulk driven) method is superior as compared to other methods in the aspect of all performance parameters. For selected technology nodes, total power dissipation is 4nW and maximum gain 40 dB with the acceptable value of the gain bandwidth product.

Keywords Ultra-low power · Gate driven · Bulk-driven MOS · Dynamic threshold · Differential amplifier

1 Introduction

The use of CMOS analog circuits in advanced mixed-signal VLSI integrated circuits (ICs) is very commonly used for portable and biomedical applications like a digital hearing aid and analog frontend. The technology is scaling of semiconductor devices in CMOS technology with reduction of supply voltage and the threshold voltage of MOS transistor, which is not equally scaled (Fig. 1) [1].

Hence, difficulties are created for analog design engineers to handle the reduction in voltage headroom. Also, at the same time, other constraints are with the degradation of the transistor's intrinsic gain and cut-off frequency [2].

The different types of methods for ultra-low voltage and ultra-low power are classified in basically two categories as follows: [3] The basic classifications are either static bias or dynamic bias methods. The static bias methods are further classified as

D. Panchal (✉) · A. Naik
Nirma University, Ahmedabad, Gujarat, India
e-mail: dipesh_panchal@nirmauni.ac.in
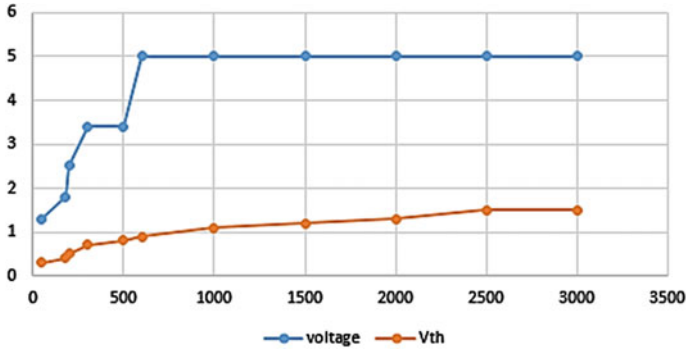
Fig. 1 Channel length versus supply voltage

gate driven, bulk driven, gate–bulk driven, and inverter-based methods. The analog circuits are designed based on these methods for ultra-low-voltage and low-power applications. However, gate-driven method is suitable for large Vdd but having large power dissipation, bulk driven having low power dissipation with low gain and low input-referred noise. Also, static bias methods require large area and power, and their performance will not contribute to analog circuits (Fig. 2).

The various methodologies for gate drive, bulk driven, and dynamic threshold techniques are discussed in the literature [4–7]. Also, operational transconductance amplifiers (OTAs) as fundamental building blocks as the analog frontend for sensor interfaces, the ultra-low-voltage operation has been performed by using, bulk-driven differential pairs [8], and inverter-based approach [9]. In this paper, these methods are compared for a differential amplifier in terms of various parameters. Section 1 gives an introduction, Sect. 2 gives circuit description followed by results and discussion and conclusion.
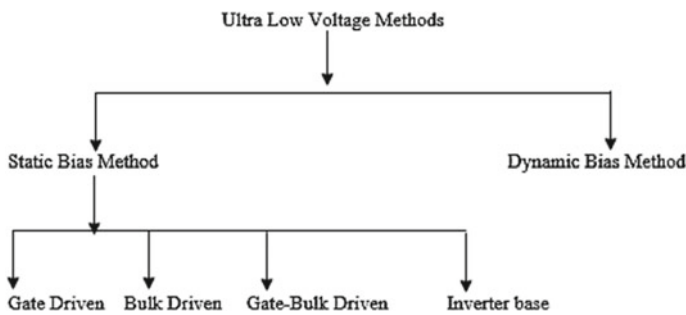
Fig. 2 Classifications for ultra-low-voltage methods

2   Circuit Description

The basic differential amplifier cell is selected for comparative analysis of gate-driven and bulk-driven configuration. All three configurations are common in terms of PMOS input stage, NMOS current mirrors, and bias by a constant tail current with source supply Vdd. Figure 3 shows the basic differential amplifier [10] with gate-driven input. The PMOS Q1 and Q2 act as input transistors, while Q3 and Q4 act as an NMOS current mirror load. The drain terminal output of Q1 acts as a single-ended output terminal. The supply voltage is selected near threshold voltage about Vdd = 400 mV, and DC bias current is about 10nA for subthreshold operation. The DC analysis is performed for drain currents of Q1 and Q2 which is half of I1 as bias current.

$$IQ1 = IQ2 = I1/2 \tag{1}$$

The DC analysis of the given differential amplifier is performed as Fig. 4 where a 4.4nA current is carried by each pair of NMOS and PMOS (Q1–Q4). The change in DC input voltage from −400 to 400 mV is where saturation level is achieved at required voltage range. Each MOS transistor is expected to operate in a subthreshold region with the following aspect ratio: (Table 1).

The small signal analysis of basic differential amplifier was performed to evaluate DC gain as:

Fig. 3 Gate-driven differential amplifier
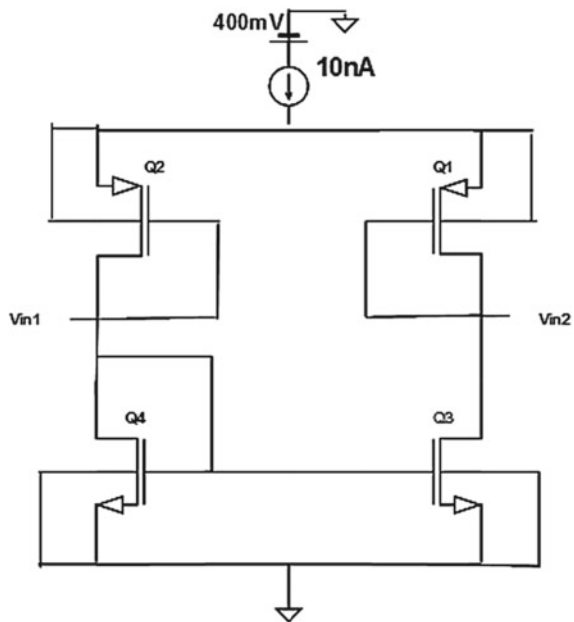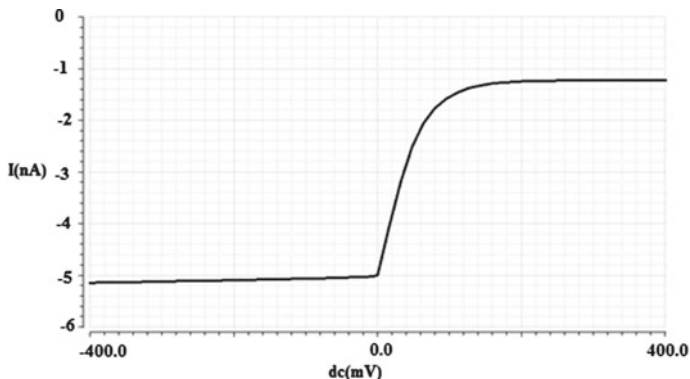
Fig. 4 DC analysis gate-driven differential amplifier

Table 1 Aspect ratio

MOS transistor	Aspect ratio
Q1,Q2	16μ//1μ
Q3,Q4	20μ/1μ

$$\text{Avdc} = \frac{\text{gm1, 2}}{\text{gds1} + \text{gds3}} \tag{2}$$

By performing high-frequency analysis, the transition frequency of gate-driven method is given by:

$$\text{ft} = \frac{\text{gm}}{2\Pi\text{Cgs}} \tag{3}$$

The fundamental limitation of the conventional gate-driven technique is that threshold voltage is not reducing as low as possible because of the transconduction contribution of the input transistor for output drain current. Hence, the solution is a bulk-driven method where threshold voltage limitations are overcome by applying input signals at the bulk terminal [11]. The gate terminal for PMOS body-driven MOS is grounded; hence, transconductance gmb of input transistor contributes for output current. The bulk transconductance gmb is due to the second-order effect of a MOS transistor, which is controlled by bulk to source voltage V_{BS} and given by

$$\text{gmb} = \frac{\gamma\,\text{gm}}{2\sqrt{-2\emptyset f - \text{VBS}}} \tag{4}$$

where gm is the transconductance of the conventional gate-driven MOS transistor in S, Y is the body effect constant in V^{-1}, and φf is the bulk Fermi potential in V. The bulk transconductance gmb is also expressed as the ratio of gmb/gm as follows:

$$n = \frac{gmb}{gm} = n - 1 = \frac{Cdep}{Cox} \tag{5}$$

where Cdep is the capacitance of the depletion layer in F and Cox is the oxide capacitance in F. However, gmb is lower than gm (2 to 4 times) and hence decreases the overall device transconductance and increases the input capacitance, which lowers the gain bandwidth (GBW) and lower transition frequency ft of bulk driven in comparison to the transit frequency ft of gate driven.

The bulk-driven transition frequency is given by:

$$ft = \frac{gmb}{2\Pi(Csb + Cdb + Cbsub)} \tag{6}$$

However, the bulk-driven technique gives low transconductance, low transition frequency, higher noise (due to small gmb), and large chip area (addition $6\lambda \times 6\lambda$). To take advantage of both gate-driven and bulk-driven methods, a new method is proposed in [12] where the input signal is applied simultaneously at bulk and gate terminals. So both transconductance gm and gmb are useful for generating current conduction. This method is also identified as the dynamic threshold method since threshold voltage is variable due to gate and body bias. Figure 5a and 5b show these two methods where PMOS transistors (Q1–Q2) act as input and current mirror as a load formed by NMOS transistor (Q3–Q4).

The threshold voltage of the bulk–gate (BG)-driven method is given by Eq. (7) which is the same as gate-driven method if the input signal is not present and decreases by amount Vgs when the input signal is present.
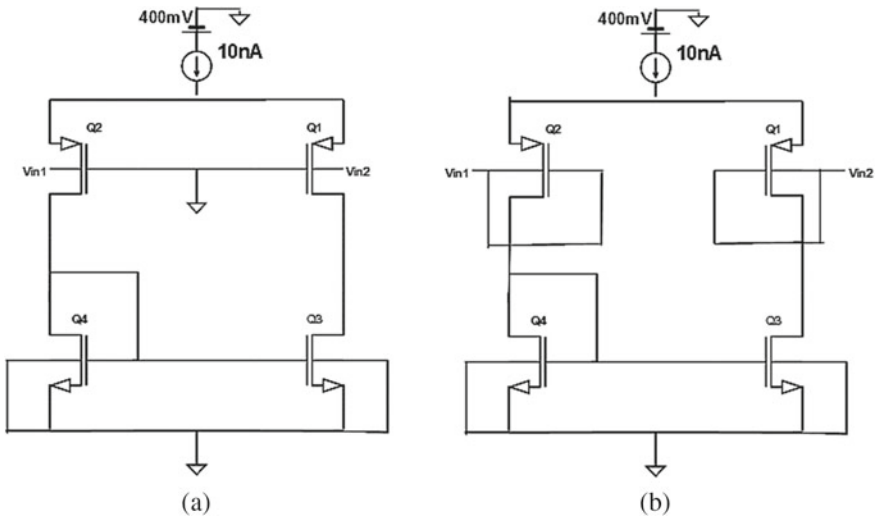
Fig. 5 Bulk driven and dynamic threshold differential amplifier

$$Vth = vto + \Upsilon \sqrt{\psi s - Vgs} - \sqrt{\psi s} \tag{7}$$

The total transconductance is given by (gm + gmb), and hence, effective gain of BG-driven differential amplifier is

$$Avdc = \frac{gm + gmb}{gds1 + gds3} \tag{8}$$

The transition frequency ft of BG differential amplifier is given by

$$ft = \frac{gm + gmb}{2\Pi(Cgs + Cbody)} \tag{9}$$

Also, the input-referred noise referred noise of BG-driven differential amplifier is greatly reduced by a factor of (gm + gmb). The simulation of all their methods is performed for power dissipation, gain bandwidth product, and DC gain.

3   Results and Discussion

All the three approaches gate driven, bulk driven, and dynamic threshold methods are simulated for DC analysis, small signal analysis, and high-frequency analysis. The simulation is performed in 180 nm Technology node using Cadence Virtuoso. Figure 6 shows the AC analysis for all three methods where low-frequency gain found a maximum of 40 dB in the dynamic (gate–bulk driven) method.

The power dissipation and −3 dB bandwidth with the gain bandwidth product are compared in Table 2 and Fig. 7.

The Monte Carlo analysis was performed for bulk–gate-driven method for 100 sample points with the process and mismatch variation at 27° temperature. The corner analysis was performed with results as shown in Table 3. The mean value is 43 dB with a standard deviation of 2.6u (Fig. 8).

The noise analysis for all three methods is performed where large input-referred noise is in bulk driven, moderate in gate driven, and small in gate–bulk-driven differential amplifier (Fig. 9a, b, c).

The post-layout simulation was performed for gate–bulk-driven method with DRC, LVS, and parasitic extraction. The results are similar to the pre-layout simulation (Fig. 10).
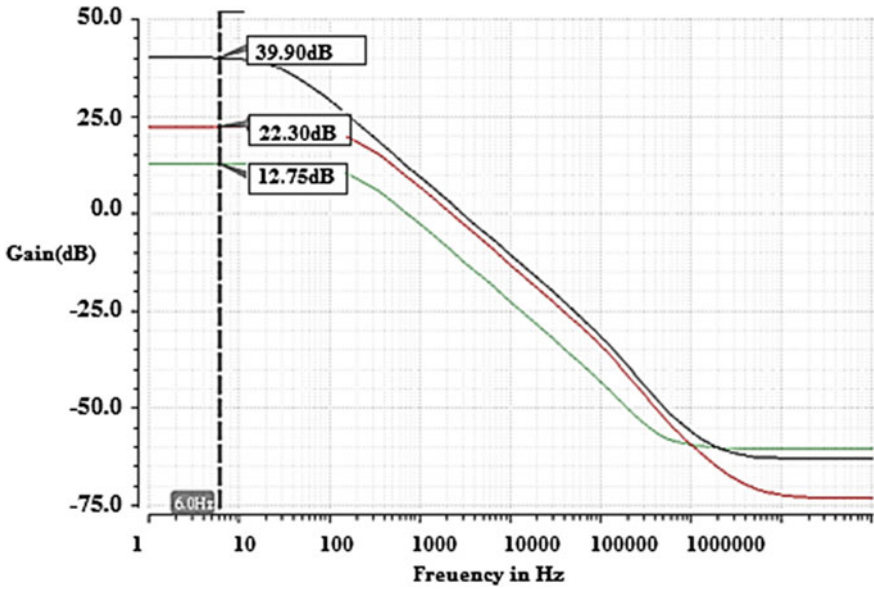
Fig. 6 Frequency response of differential amplifier

Table 2 Result comparison

Methods	Power dissipation (nW)	Gain bandwidth product	Gain (dB)
Gate driven	4	2.24 kHz	22.30
Bulk driven	4	700 Hz	12.75
Gate–bulk driven	4	2.18 kHz	40.12
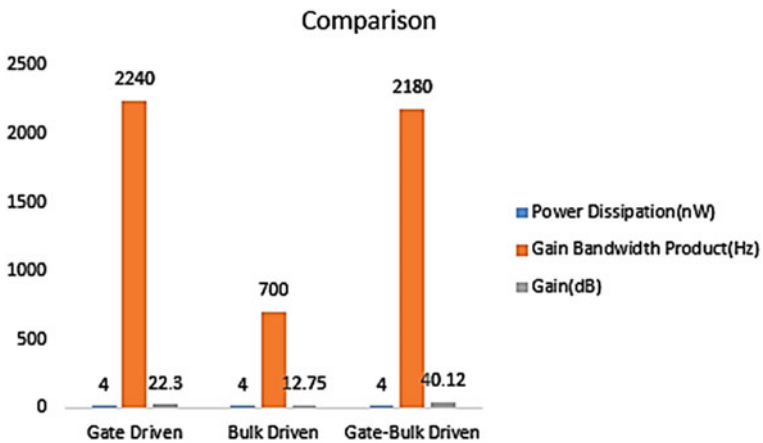
Fig. 7 Result comparison

Table 3 Monte Carlo analysis

Parameters	FF	FS	NN	SF	SS
DC Gain(dB)	25.06	24.48	40.47	43.47	41.41
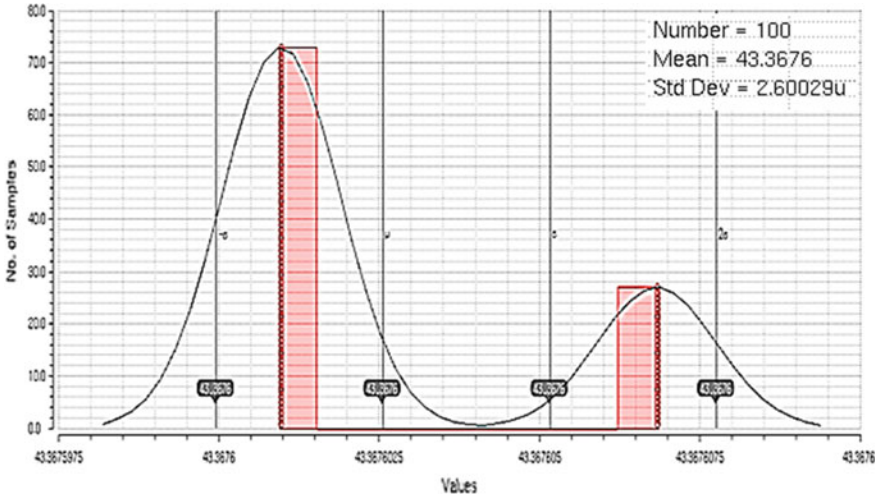
Fig. 8 Monte Carlo simulation

4 Conclusion

In this paper, ultra-low-voltage methods in the category of static bias methods are identified like gate driven, bulk driven, and dynamic threshold methods which are applied on the basic differential amplifier, and different analysis is performed for various parameters like power dissipation and gain. The simulation results are performed for ultra-low voltage using TSMC 180 nm Technology node. The results show that the gate–bulk-driven method is superior as compared to other methods in the aspect of different parameters. The result can be further improved by digital dynamic methods.
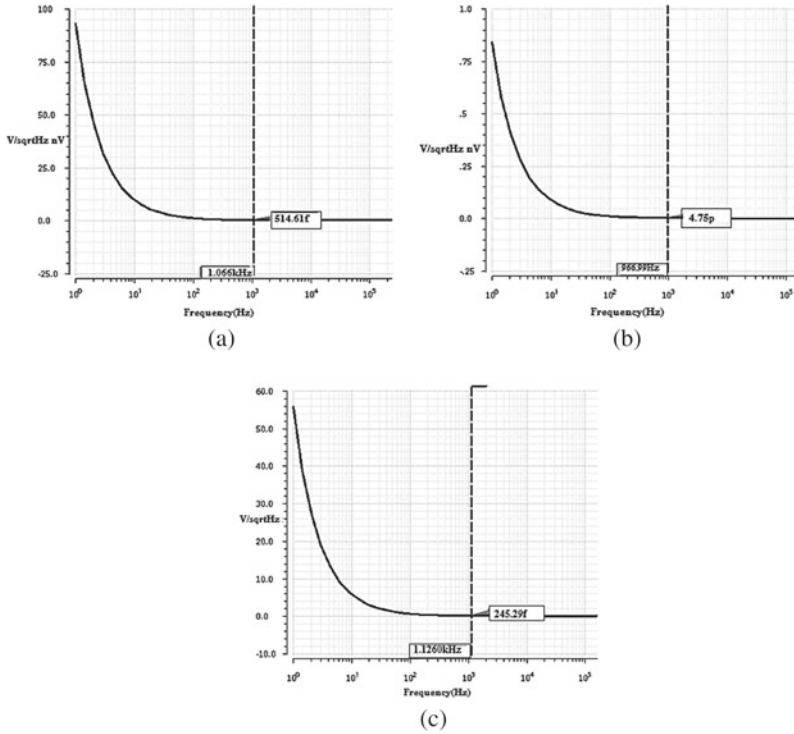
Fig. 9 Noise analysis

Fig. 10 Layout of bulk–gate method
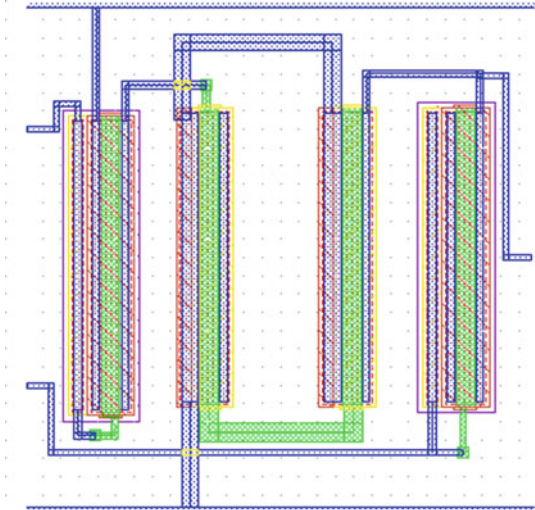
References

1. Bult K (2000) Analog design in deep sub-micron CMOS. In: European solid-state circuits conference. Stockholm: IEEE, pp 126–132
2. Yan S, Sanchez S (2000) Low voltage analog circuit design techniques: a tutorial. IEICE Trans Analog Integr Circ Syst E00–A(2), pp 1–17
3. Toledo P et al (2021) 300mV-supply, sub-nW-power digital-based operational transconductance amplifier. IEEE Trans Circ Syst II: Express Briefs
4. Haga Y, Kale I (2009) Bulk-driven flipped voltage follower. In: Proceedings of the IEEE International Symposium on Circuits and Systems, Taipei, pp.2717–2720
5. Hesari SH et al (2019) Ultra low-power OTA for biomedical applications. In: 2019 United States National Committee of URSI National Radio Science Meeting (USNC-URSI NRSM). IEEE, pp 1–2
6. Ferreira LHC, Sameer RS (2014) A 60-dB gain OTA operating at 0.25-V power supply in 130-nm digital CMOS process. IEEE Trans Circ Syst I: Regular Papers 61(6):1609–1617
7. Kulej T, Khateb F (2019) A compact 0.3-V class AB bulk-driven OTA. IEEE Trans Very Large Scale Integr (VLSI) Syst 28(1):224–232
8. Lv L, Zhou X, Qiao Z, Li Q (2019) Inverter-based subthreshold amplifier techniques and their application in 0.3V $\Delta\Sigma$-modulators. IEEE J Solid-State Circ 54(5):1436–1445
9. Michel F, Steyaert MSJ (2012) A 250 mV 7.5μW 61 dB SNDR SC $\Delta\Sigma$ modulator using near-threshold-voltage-biased inverter amplifiers in 130 nm CMOS. IEEE J. of Solid-State Circ 47(3):709–721
10. Johns DA, Martin K (2008) Analog integrated circuit design. John Wiley & Sons
11. Rakus M, Stopjakova V, Arbet D (2018) Analysis of bdmos and dtmos current mirrors in 130 nm cmos technology. Adv Electr Electron Eng 16(2):226–232
12. Assaderaghi F, Sinitsky D, Parke SA, Bokor J, Ko PK, Hu C (1997) Dynamic threshold voltage MOSFET (DTMOS) for ultra low voltage VLSI. IEEE Trans Electron Devices 44(3):414–422

Millimeter Wave Overmoded Circular Waveguide Tapers for ECRH Applications

Pujita Bhatt, Amit Patel, Keyur Mahant, K. Sathyanarayana, and S. V. Kulkarni

Abstract The design methodology of the overmoded circular waveguide tapers to connect the gyrotron (ø85mm) output power at 42 ± 0.2 GHz/200 kW/3secs with different diameters (ø63.5 and ø31.75 mm) of transmission line components has been carried out. Design parameter of taper is optimized using coupling theory in such a manner that it provides an appropriate match between input and output of transition with lower spurious modes conversion. There are linear and nonlinear applicable methods for designing internal taper profile. These methods are implemented, and the results of linear tapers are compared with the analogous expressions for raised cosine (nonlinear) tapers. The overall loss in circular linear tapers is less than 1% for the length of approximately 107λ. However, raised cosine tapers may provide lower insertion loss, but linear tapers with moderate values of diameter ratio may be attractive because of its simplicity in fabrication. Both the tapers are designed and simulated using computer simulation technology (CST) Microwave Studio software.

Keywords Circular waveguide · Gyrotron · Insertion loss · Mode conversion · Taper

1 Introduction

The multi-institutional program for the development of a 42 ± 0.2 GHz/200 kW/3 s operating in TE_{03} mode gyrotron has been undertaken [1, 2]. Aperture of the precisely

P. Bhatt (✉)
Department of Mechatronics Engineering, Parul Institute of Technology, Parul University, Vadodara, India
e-mail: pujitabhatt@gmail.com

A. Patel · K. Mahant
CHARUSAT Space Research and Technology Center, Chandubhai S Patel Institute of Technology, Charotar University of Science & Technology, District—Anand, Nadiad, Gujarat State 388421, India

K. Sathyanarayana · S. V. Kulkarni
Institute of Plasma Research, Bhat, Gandhinagar, Gujarat State, India

developed gyrotron is Ø85mm with TE$_{03}$ operating mode. In electron cyclotron resonance heating (ECRH) applications, operating mode should be a polarized mode which is HE$_{11}$ mode generally known as Gaussian mode [1]. The transmission line components convert unpolarized TE$_{03}$ mode into a polarized mode. With gyrotron output aperture Ø85mm, the length of transmission line components will immensely increase (because the length is directly proportional to the radius) [3]. Thus to reduce the length of the transmission line components and to connect with gyrotron is bridged by introducing down taper. A tapered waveguide section is often used in gyrotron or in microwave system for connecting two waveguides of different apertures. The requirement of a waveguide taper is to provide a good impedance match between input and output of taper with spurious mode suppression at its waveguide ports and to acquire less transmission loss. The optimum goal of the designing the taper is to reduce the spurious mode conversion at the operating frequency, and the length of the taper should be minimum as possible. The design of taper is to be linear with smoothly varying the diameter of the waveguide with respect to its length. This gradual change in radius reduces impedance mismatching.

The connecting output diameter of gyrotron is Ø85mm, and the diameter of mode converter [4] is Ø31.75 mm (where the converter length is acceptable); thus for connecting these two diameters, down taper is required. The connection of these diameters in one face is not feasible as mode conversion loss increases, so two down taper is designed with Ø85 to Ø63.5 mm and Ø63.5 to Ø31.75 mm. At the optimized diameter of taper, different transmission line component has been designed as mode converters [4–6], miter bends [7, 8] at 42 ± 0.2 GHz. The main objective to design waveguide tapers is to have optimum diameter at which other mode converters can be designed. Thus, Ø31.75 mm diameter is the optimum diameter at which unpolarized mode will be converted into polarized mode developing different mode converter in the system.

The organization of this paper is likewise, Sect. 1 introduces the prerequisite of designing this millimeter wave component. The theoretical concept is meticulously explained in Sect. 2. Section 3 involves with the indispensable designing of the taper and as an outcome, and the simulation results are evaluated in Sect. 4. Comparing design methodologies and related results are tabulated in Sect. 5. Concluding remarks are delineated in Sect. 6.

2 Theoretical Approach

In millimeter wave system, to connect waveguide with different diameters, linear or nonlinear tapered waveguide is designed. In the past few decades, significant work has been done on circular waveguide tapers. The approaches suggest that, if one gradually increase/decrease the radius of the taper, then impedance mismatching problem can be avoided. The millimeter wave propagation in the tapered section can easily be understood by an infinite set of first-order differential equations. If the tapers vary smoothly corresponding to its length than power in the TE$_{0m}$ term

gradually vary (increase or decrease) compared to the power of TE$_{03}$ [3]. Thus, we then consider only coupling between TE$_{03}$ and one of the TE$_{0m}$ terms at one time. The power couples from forwarding wave to backward are given by coupling Eqs. (1) and (2) as follows [3],

$$\frac{dA_1}{dz} = -j\beta_1 A_1 + k_{21} A_2 \tag{1}$$

$$\frac{dA_2}{dz} = -j\beta_2 A_2 + k_{12} A_1 \tag{2}$$

where A_1, A_2 are the complex amplitudes of the two power modes, TE$_{03}$ and TE$_{0m}$. β_1 and β_2 are the phase constant of the waveguide, and k_{21} and k_{12} are the coupling coefficients. Coupling coefficient and phase constant are the functions along the length of the taper.

On basis of this concept, the normalized amplitude coupling coefficient C for the linear taper at the output junction is given by [3, 9],

$$C = 0.142 \frac{d_2(d_2 - d_1)}{\lambda L} \tag{3}$$

Here, d_1 and d_2 are the diameters of input and output section of taper, respectively, L is the length of taper, and λ is a wavelength corresponding to operating frequency, i.e., 42 GHz. Here, the length of taper is optimized with the coupling coefficient at 42 ± 0.2 GHz frequency. Ideally, the value of coupling coefficient should be zero, but for this value, taper length becomes infinite which is not possible to fabricate practically. Thus, one can tolerate maximum 1% power loss in spurious modes [9, 10]. As per the requirement, input diameter (d_1) and output diameter (d_2) of taper are Ø85mm and Ø31.75 mm, respectively. While calculating the length of taper by means of Eq. (3), it becomes 126λ which is practically not feasible. However, due to manufacturing limitation, we cannot fabricate taper in single part, thus down tapers were designed in two sections: first section down taper with diameter converting from Ø85 to Ø63.5 mm and second with Ø63.5 to Ø31.75 mm. Table 1 shows the design parameters of both the down tapers. This taper is to be used for Q-band applications, and it is one part of transmission line components at 42 ± 0.2 GHz frequency. The optimum length of taper is shown in Table 1.

Table 1 Taper dimensions

Parameters	Down taper (Ø85–Ø63.5)	Down taper (Ø63.5–Ø31.75)
d$_1$ (mm)	Ø85	Ø63.5
d$_2$ (mm)	Ø63.5	Ø31.75
C	0.1	0.1
L (mm)	≈ 363	≈ 401

3 Design Approaches

To connect waveguide with different diameters, the number of the inner profile has been incorporated by researchers [11–17]. This waveguide section has various profiles for tapers like exponential, raised cosine [11], parabola [12], linear. While designing with these different profiles, the length of the taper may vary. Out of these four inner profiles, linear and raised cosine give the best transmission efficiency as compared to other two. The comparative study is as shown in Table 2 [11] and that will be discussed in detail here. In the raised cosine profile, transmission efficiency is high with the same length, but the fabrication of the raised cosine taper is a bit difficult with the required tolerances. Raised cosine profile is obtained as shown in Eq. (4). Thus, the linear-profiled taper is preferred, whose length can be optimized [16].

$$a(z) = 0.5(a_2 - a_1) + 0.5(a_2 - a_1) \cos\left((\frac{z}{L} - 1)\pi\right) \qquad (4)$$

where a_1: taper input diameter, a_2: taper output dimension and taper length L. Length of taper can similarly as linear taper given in Eq. (3).

The approach we stipulated was to design the down taper with linear and raised cosine inner pattern. Figure 1 shows the design of linear down taper converting from diameter 85 to 63.5 mm. The flexibility of mechanical design we incorporated is unique and that will be discussed later.

Another taper converting diameter from Ø(63.5 to 31.75 mm) is designed with two profile techniques. This taper is designed with linear and nonlinear techniques (raised cosine taper). Figure 2a and b shows the down taper with both the profiles.

Table 2 Transmission efficiency of basic taper-shaped profiles

Profile	Transmission (%)
Linear	89.9
Exponential	32.5
Parabola	71.5
Raised cosine	93.9
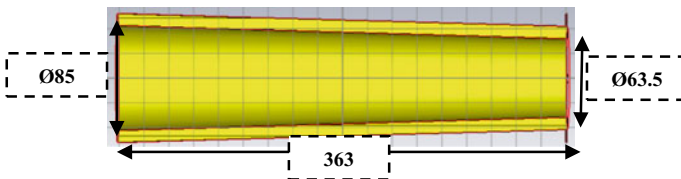
Fig. 1 Linear down taper (Ø85–63.5 mm)

Fig. 2 a Linear down taper
(Ø63.5–31.75 mm), **b**
Nonlinear down taper
(Ø63.5–31.75 mm)

(a)

(b)
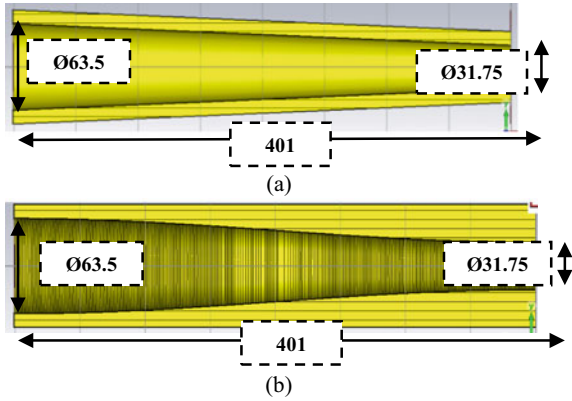
4 Simulation Outcome

In this section, the simulation results of the down taper are bulleted using CST Microwave Studio software. As we discussed the design of two down taper, they are essential to carry the same TE_{03} mode in the transmission line system. Here, the simulations of two down taper with frequency 42 ± 0.2 GHz are highlighted in brief.

4.1 Down Taper Ø (85 to 63.5) mm

The down taper carries power from gyrotron with aperture Ø85mm and mode TE_{03}. Linear down taper has been simulated in CST Microwave Studio. For this down taper, the input and output modes should remain same, without converting it into spurious modes. Input mode, i.e., TE_{03} pattern is depicted in Fig. 3a, and it should be propagating in the tapered waveguide section shown in Fig. 3b.

The S-parameters of the taper are as shown in Fig. 4, which depicts that the insertion loss is 0.14 dB at operating frequency range. This simulated result specifies that the importance of taper designing is resolved with minimal loss. This insertion loss gives the transmission efficiency of the components that are shown in Fig. 5. The efficiency of this linear tapered section is 96.68%.

4.2 Down Taper Ø (63.5 to 31.75) mm

In continuation of the output aperture of the first down taper, another taper is simulated with diameter Ø (63.5–31.75) mm. Here, two internal profiled tapers are simulated, and its corresponding results are depicted. A raised cosine taper varies stepwise, with respect to the length of the taper. The mode pattern of TE_{03} at the input of the

Fig. 3 a Input mode pattern
at Ø85mm, **b** electric field
pattern inside the taper

(a)

(b)
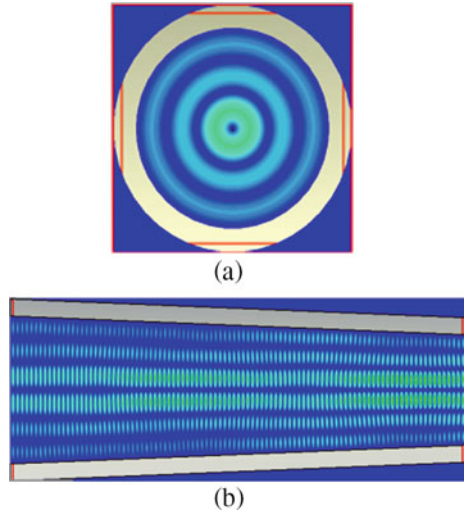
Fig. 4 Scattering parameter
of linear down taper
(Ø85–Ø63.5 mm)
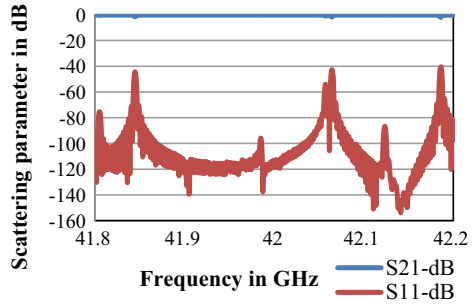
Fig. 5 Transmission
efficiency (Ø85–Ø63.5 mm)
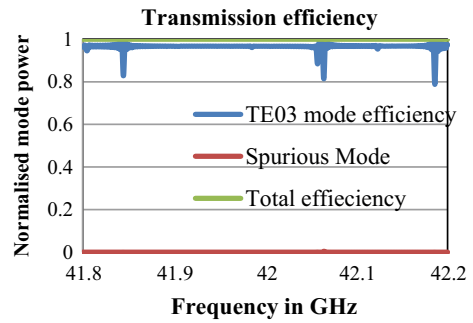
waveguide section is as shown in Fig. 6. The electric field pattern of the taper with both profiles, linear and nonlinear, is as shown in Fig. 7a and b, respectively.

The output mode pattern which has to maintain the same, as input mode pattern, is shown in Fig. 8. The scattering parameter for both linear and nonlinear profiles is depicted in Fig. 9 and Fig. 10, respectively.

The required amount of power transmitted through microwave component is justified by the transmission efficiency of the system. Figures 11 and 12 depict that power

Fig. 6 Input mode pattern at Ø63.5 mm
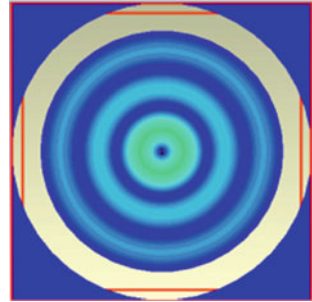
Fig. 7 Electric field pattern inside **a** linear down taper, **b** nonlinear down taper

(a)

(b)
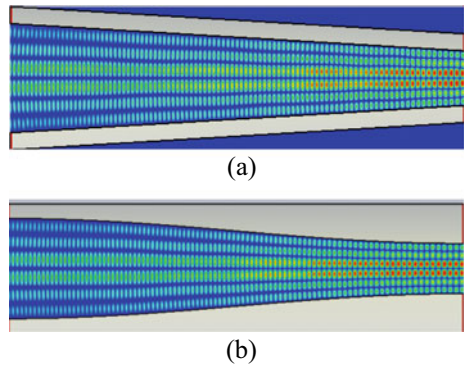
Fig. 8 Output mode pattern at Ø31.75 mm
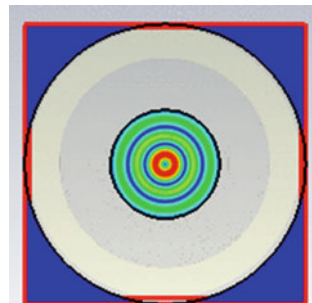
Fig. 9 Scattering
parameters of linear down
taper (Ø63.5–Ø31.75) mm
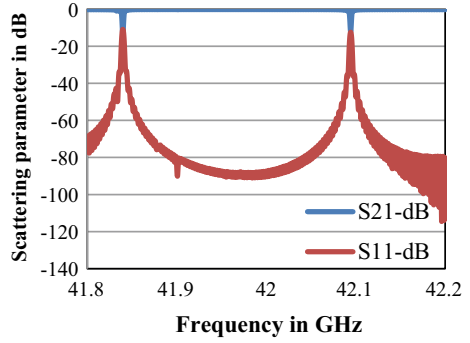
Fig. 10 Scattering
parameters of nonlinear
down taper (Ø63.5–Ø31.75)
mm
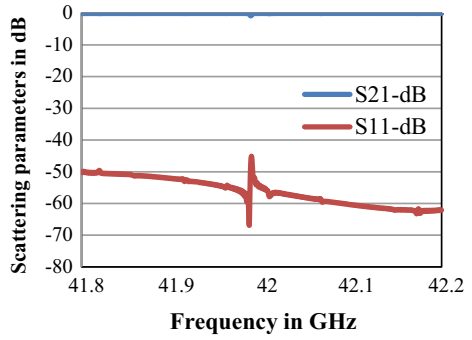
transferred into the linear taper and nonlinear taper is ∼ 97.60% and ∼ 98.91%, respectively, without converting it into spurious modes.

Fig. 11 Transmission
efficiency of linear
(Ø63.5–Ø31.75 mm)
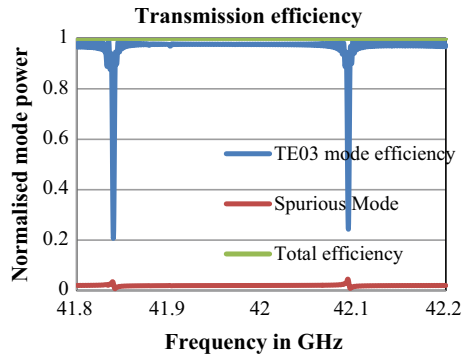
Fig. 12 Transmission efficiency of nonlinear (Ø63.5–Ø31.75 mm)
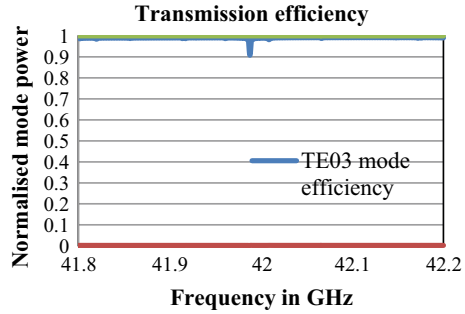
Table 3 Comparison of linear and nonlinear taper

Parameters	Linear taper	Nonlinear taper
Diameter (mm)	Ø63.5 to Ø31.75	Ø63.5 to Ø31.75
Insertion loss (dB)	−0.105	−0.047
Transmission efficiency(η) (%)	97.60	98.91%

5   Comparison and Discussion

The design approaches and simulation results that were discussed will be compared in this section. Out of the four profile techniques, we choose the best two technologies for the final designing and simulation. Table 3 compares these two design and its corresponding results. It signifies that nonlinear tapers give the best outcome in terms of insertion loss and transmission efficiency as compared to linear. But at the contrary from the manufacturing point of view, nonlinear taper is a bit difficult to fabricate. Nonlinear tapers have to maintain its accuracy while manufacturing process, whereas linear tapers can be easily manufactured with the required tolerances and with efficient cost.

6   Conclusion

This paper takes into account the analytical designing of millimeter wave tapers and simultaneously simulating them. Linear and nonlinear designing of tapers was described in details, where the power transformation of the TE_{03} mode without converting into other spurious modes. For fabrication simplicity, the linear taper is acquainted. However, the transmission efficiency of nonlinear taper is more compared to linear one. Both the tapers give more than 97% transmission efficiency.

References

1. Singh U, Kumar N, Khatun H, Kumar N, Yadav V, Kumar A, Sharma M, Alaria M, Bera A, Jain PK, Sinha AK (2013) Design of 42GHz gyrotron for Indian fusion tokamak system. Fusion Eng Des, pp. 2898–2906
2. Chandra ABR, Jain PK (2012) Multimode behavior of a 42 GHz, 200kW gyrotron. Prog Electromagnet Res B 42, 75{91
3. Unger H (1958) Circular waveguide taper of improved design. Bell Syst Tech J, pp 899–912
4. Patel A, Goswami R, Mahant K et al (2019) High power millimeter wave TE03 to TM11 mode converters. Int J Electron 106:1141–1163
5. Patel A, Goswami R, Mahant K, Bhatt P, Mewada H, Vala A, Sathyanarayan K, Kulkarni S (2018) Millimeter-wave TE01–TE11-HE11 mode converter using overmoded circular waveguide. J Electromagnet Wave Appl 32(14)
6. Patel A, Goswami R, Bhatt P (2019) TM11 to HE11 mode converter in overmoded circular corrugated waveguide. IET Antenna Microwave Propag, pp 1–6
7. Patel A, Bhatt P, Mahant K, Vala AD, Chaudhari J, Mewada H, Sathyanarayan K (2021) Quasi-optic based HE11 Miter bend at 42 GHz for ECRH application. Progress Electromagnet Res 108:37–48
8. Pujita Bhatt et al TE01 mode miter bend for high power millimeter wave gyrotron transmission line system. Int J Adv Sci Technol 29(3):11730–11749
9. Quine JP Oversize Tubular Metallic Waveguides, pp 180–197
10. Donda KD, Kumar R, Pandya HB (2015) Design, development and testing of circular waveguide taper for millimeter wave transmission line. Int J Microwaves Appl 4(4):22–25
11. Nagarkoti DS, Sharma R, Dua RL, Jain PK (2012) Analysis of nonlinear cylindrical waveguide taper using modal matching technique. Int J Microwaves Appl 1(1):5–12
12. Doane JL (1984) Parabolic tapers for overmoded waveguides. Int J Infrared Millimeter Waves 5:737–751
13. Flugel H, Kuhn E (1988) Computer-aided analysis and design of circular waveguide tapers. IEEE Trans Microwave Theory Tech 36(2):332–336
14. Lawson WG (1990) Theoretical evaluation of nonlinear tapers for a high-power gyrotron. IEEE Trans Microw Theory Tech 38(11):1617–1622
15. Lawson W (1994) Theoretical mode conversion in overmoded nonlinear coaxial waveguide tapers. IEEE Trans Microw Theory Tech 42(1):127–131
16. Tang CCH (1961) Optimization of waveguide tapers capable of multimode propagation. IRE Trans Microw Theory Tech 442–452
17. Schaub SC (2016) Simple expressions for the design of linear tapers in overmoded corrugated waveguides. J Infrared Millim Terahertz Waves

Analysis of Logical Effort-Based Optimization in the Deep Submicron Technologies

Shivam Singh, Prakash Kumar Ojha, and Abhijit R. Asati

Abstract A convenient way to estimate and optimize the delay of VLSI digital circuits is the popular logical effort-based optimization. In this paper, we analyzed the effect of various circuit parameters such as logical effort (G), branching effort (B), electrical effort (H), and parasitic effort (P) on the delay of a given circuit for two different technology nodes, namely 180 and 16 nm. The analysis results show the variation of delay with a particular logical effort parameter. The variation between simulation delay and logical effort delay is indicated by a parameter τ', which is compared with the τ which is the delay of an inverter driving an identical inverter with no parasitic for a chosen technology. The effectiveness of the logical effort-based optimization is explored. Further, the logical effort-based delay reduction, a super buffer-based delay reduction, and delay of an un-optimized circuit are also compared. The effect of technology on logical effort method for each parameter in the deep submicron sizes has also been investigated in this research work.

Keywords Logical effort · Electrical effort · Branching · Parasitic · PDP · LTspice · Super buffer

1 Introduction

The high-speed design consuming minimum power is essential for many data processing digital VLSI applications. The logical effort-based method can be used to decide the number of logic stages on a path and also to determine the sizes of the CMOS transistors in a digital logic circuit. This method offers an easy way to estimate the delay in a CMOS digital circuit by technology independent manner by isolating technology-dependent part and including it at the end.

S. Singh (✉) · P. K. Ojha · A. R. Asati
Department of Electrical & Electronics Engineering, Birla Institute of Technology & Science, Pilani (Pilani Campus), Rajasthan, India
e-mail: Shivamsinghvns33@gmail.com

A. R. Asati
e-mail: abhijit_asati@pilani.bits-pilani.ac.in

The conventional logical effort-based analysis does not optimize the ratio of PMOS and NMOS width. In this paper, in order to apply logical effort parameters calculation we determined the ratio of PMOS and NMOS width in a given technology to not just to balance the trans-conductance effect but also to provide minimum power–delay product (PDP).

In digital electronics, fanout of 4 (FO-4) load, i.e., an inverter is driving similar 4 inverters in parallel, is typically used as load to optimize PMOS to NMOS width ratio in the digital CMOS circuits. FO-4 is generally used as a load since in case of chained buffers driving large loads, for such buffers the optimum fanout generally varies from 2.7 to 5.3 [1]. The logical effort model provides the dimensionless logic circuit delay as D = GH + P [2]. Regular CMOS inverter has pull-up and pull-down transistors which do not have equal charging, discharging times when dealing with output capacitor due to inherent carrier mobility. Thus, having an inverter to drive any off-chip large capacitors or some other critical circuit is not a reliable solution (asymmetric rise, fall delays) [3, 4].

The high-performance circuits utilize computational blocks such as adders, multipliers, or divider circuits to achieve better speed by compromising the power consumption, noise margins, and/or design effort. The method of logical effort is applicable to this network of logic gates, where each of these gates has one or more inputs [5]. In the near-threshold region, the characteristics of MOS transistors are very different from those in the strong-inversion region. In [6], the logical effort and parasitic delay values for logic gates using multiple supply voltage for both the subthreshold and super-threshold regimes have been discussed.

However, a systematic study of logical effort-based analysis to monitor the effect of individual parameter variation along with the effect of technology scaling particularly in deep submicron technologies is missing in the literature. In this research, we utilized 180 and 16 nm technologies for logical effort-based analysis.

In Sect. 2, we first determined the optimum PMOS-to-NMOS ratio for minimum PDP in both the submicron technologies, which are utilized for the entire logical effort-based analysis. Section 3 describes the logical effort-based method, and Sect. 4 describes the logical effort parameters for 180 nm and 16 nm technologies. Section 5 concludes the research outcomes.

2 Determining the Optimum PMOS-To-NMOS Ratio

As discussed earlier a FO-4 inverter circuit is used to determine the PMOS-to-NMOS width ratio for both 180 and 16 nm technologies using LTspice simulator (Fig. 1).

The FO-4 inverter circuit is simulated for particular NMOS width (W_n) and varying PMOS width (W_p). The simulation is then repeated for other NMOS width to obtain the minimum overall PDP as shown in indicated in Tables 1 and 2. The T_{PLH} is low to high propagation delay, T_{PHL} is a high to low propagation delay, and Pavg is the average power dissipated for the inverter under consideration, i.e., inverter on left. Note the lengths of both NMOS and PMOS transistors are kept minimum (i.e.,
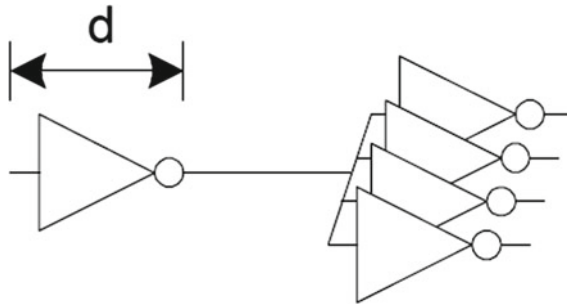
Fig. 1 FO-4 inverter circuit used to calculate minimum PDP

Table 1 PDP calculation for NMOS W/L $= 1$ in 180 nm technology

W_n(nm)	W_p(nm)	T_{PLH} (ps)	T_{PHL} (ps)	Avg. delay (ps)	P_{avg} (pw)	PDP
180	180	66.40	26.40	46.40	177.96	8257.33
	220	68	30.50	49.25	198.17	9760.62
	270	79	33	56	219.86	12,312.16
	360	69	33.33	51.16	219.86	11,249.13
	450	65	43.90	54.50	288.87	15,743.40
360	180	105.20	25.80	65.50	275.84	18,067.52
	220	108.30	28.80	68.55	295.44	20,252.41
	270	104.70	31.83	68.26	317.92	21,702.81
	360	95.90	35.81	65.85	353.2	23,260.01
	440	90.30	38.76	64.53	387.55	25,479.03

L_{min} is 180 for the 180 nm technology and L_{min} is 16 for the 16 nm technology, respectively, for the entire further analysis of logical effort-based method).

It can be concluded from Table 1 that PDP is minimum when NMOS width and PMOS width both are at 180 nm. Further Table 2 also concludes that PDP is minimum when NMOS width and PMOS width both are at 16 nm. Thus, optimum PMOS-to-NMOS ratio was found to be 1 in both the submicron technologies.

3 Logical Effort Method

3.1 *Logical Effort Parameters [2]*

The logical effort model defines the dimensionless delay of a logic gate as:

$$D = \text{GH} + P \tag{1}$$

Table 2 PDP calculation for NMOS W/L = 1 in 16 nm technology

W_n (nm)	W_p (nm)	T_{PLH} (ps)	T_{PHL} (ps)	Avg. delay (ps)	P_{avg} (pw)	PDP
16	16	9.50	5	7.25	793.04	5749.54
	20	12	6.30	9.15	902.47	8257.60
	24	14.20	7.50	10.85	1247.30	13,533.20
	32	13	9.40	11.20	1248.20	13,979.84
	40	13.20	13.50	13.35	2771.90	37,004.86
32	16	19.60	6.80	13.20	1296.40	17,112.48
	20	21.30	7.40	14.35	1369.10	19,646.58
	24	21.60	8.04	15	2216.10	33,241.50
	32	19.19	9.91	14.55	2129.60	30,985.68
	40	16.07	11.6	13.84	2982.20	41,273.64

where 'G': logical effort, 'H': electrical effort, and 'P': parasitic delay

The logical effort linear delay model has been derived using RC model approximation, where D is the normalized logical effort delay, C_P is the parasitic capacitance, and C_{out} is output load capacitance.

$$D \alpha R (C_P + C_{out}) \tag{2}$$

The normalized delay is multiplied by delay τ (delay of standard inverter driving another inverter without parasitic) to obtain the total delay.

$$D\tau \alpha R (C_P + C_{out})$$

$$D \alpha [R (C_P + C_{out})]/t \tag{3}$$

(where $\tau = R_{inv} * C_{inv}$)

$$D \alpha \{R(C_{out} + C_P)]/ R_{inv} * C_{inv}\}$$

$$D \alpha (RC_{in}/R_{inv} * C_{inv}) (C_{out}/ C_{in}) + (R * C_P)/(R_{inv} * C_{inv}) \tag{4}$$

where C_{in} is input capacitance of a gate and C_{inv} is input capacitance of a reference inverter.

$$G \alpha (RC_{in}/R_{inv} * C_{inv}) \tag{5}$$

$$H \alpha (C_{out}/C_{in}) \tag{6}$$

$$P \alpha \ (R * C_P)/(R_{\text{inv}} * C_{\text{inv}}) \tag{7}$$

The derivation of G, H, and P of a digital circuit is explained in Eq. (1)–(7). The gate-specific logical effort and parasitic delay are constant for a particular gate and indicated by same symbol in small case, assuming $R = R_{\text{inv}}$, i.e., gate and inverter with the equal driving strength. For example, a reference inverter has logical effort $g = 1$ and parasitic delay $p = 1$. Even after scaling the reference inverter in size by increasing its transistor widths, these values do not change. An inverter that is having double size as that of the reference inverter also has similar logical effort ($g = 1$) and parasitic delay ($p = 1$).

However, the electrical effort 'h' of a logic gate depends on its size. If a gate with input capacitance C_{in} drives a capacitive load C_{out}, then the gate electrical effort is (i.e., $h = C_{\text{out}}/C_{\text{in}}$). The logical effort '$g$' of a gate is defined as the ratio of the input capacitance of the gate under consideration to the input capacitance of reference inverter (i.e., $g = C_{\text{in}}/C_{\text{inv}}$). For both the 180 and 16 nm technologies, C_{inv} is equal to 2, as the PMOS-to-PMOS width ratio are same for minimum PDP case as determined earlier.

The parasitic delay 'p' due to its own internal capacitance, expressed as the intrinsic delay of the gate. The diffusion capacitance is the principal contributor to parasitic delay of the source or drain regions of the transistors that drive the gate's output. The parasitic delay 'p' is the ratio of the parasitic capacitance of gate to the parasitic capacitance of the inverter (i.e., $p = C_p/C_{\text{inv}}$), where C_p is diffusion capacitance of gate.

3.2 Delay Optimization Using Logical Effort [2]

We study the delay of the generic path as shown in Fig. 2 with two gates in series, gate-1 and gate-2, where capacitive load C_L is driven by the gate-2. Gate-1 has logical effort 'g_1', parasitic delay 'p_1' and is scaled such that its input capacitance is C_1. Also, gate-2 has logical effort 'g_2', parasitic delay 'p_2', and input capacitance C_2.

The delay of the path is given by the sum of the individual gate delays. The input capacitance of gate-2 is the load capacitance of gate-1. Thus, gate-1 has electrical effort $h_1 = C_2/C_1$ and delay is $d_1 = f_1 + p_1 = g_1 h_1 + p_1 = g_1 * (C_2/C_1) + p_1$.

Gate-2 has electrical effort $h_2 = C_L/C_2$, and delay is $d_2 = f_2 + p_2 = g_2 h_2 + p_2 = g_2*(C_L/C_2) + p_2$.

The path delay is given by the sum of the gate delays:

Fig. 2 Two gates in series and capacitive load C_L (A 2-stage path)
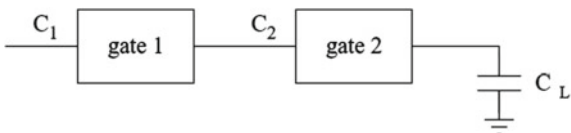
$$D = d_1 + d_2 = g_1 * (C_2/C_1) + p_1 + g_2 * (C_L/C_2) + p_2 \tag{8}$$

Writing path delay D in terms of stage efforts f1 and f2 yields

$$D = (f_1 + f_2) + (p_1 + p_2) = F + P \tag{9}$$

The product of the stage efforts is:

$$f_1 \cdot f_2 = g_1 * (C_2/C_1) g_2 * (C_L/C_2) = g_1 * g_2 (C_L/C_1) \tag{10}$$

Since it is independent of C_2, hence, the geometric mean of the stage efforts $f_1 \cdots f_2$ remains constant under changes of C_2. As the logical efforts and capacitances of a circuit are positive numbers, therefore by applying the theorem of arithmetic and geometric means, which minimizes the path effort as explained next $[(\mathbf{f_1 + f_2})/\mathbf{2} \geq \sqrt{\mathbf{f_2 * f_1}}]$. This equality holds only if the stage efforts are equal, i.e., $\mathbf{f_1 = f_2}$. If the geometric mean is constant, then the arithmetic mean assumes its minimum for equal stage efforts. Hence, if the stage efforts are equal, then the path effort is minimal:

$$f_1 = f_2 \Rightarrow \min F = f_1 + f_2 = 2\sqrt{\mathbf{f_2 * f_1}} \tag{11}$$

This is the crucial insight that enables us to minimize the path delay by sizing gate- 2. Gate-2 must have an input capacitance C_2 that yields equal stage efforts: $f_1 = f_2$.

Therefore, the minimum path effort for multiple stages is

$$\min F = f_1 + f_2 + \cdots + f_n = n * \sqrt[n]{f_1 f_2 \cdots f_n} \tag{12}$$

Since path parasitic delay 'P' is constant for a given path, we conclude that the path delay of an n-stage path assumes its minimum

$$D = n * \sqrt[n]{\mathbf{GH}} + P = nF^{1/n} + P \tag{13}$$

Also, the optimum number of stages (i.e., N) for a n-stage path is approximated as:

$$N = \log_4 F \tag{14}$$

In general, after including the B and H the path effort becomes,

$$F = GBH \text{ (Path effort of given circuit)}$$

The delay expression using logical effort-based method is indicated using the set of equations from Eq. (8)–(14).
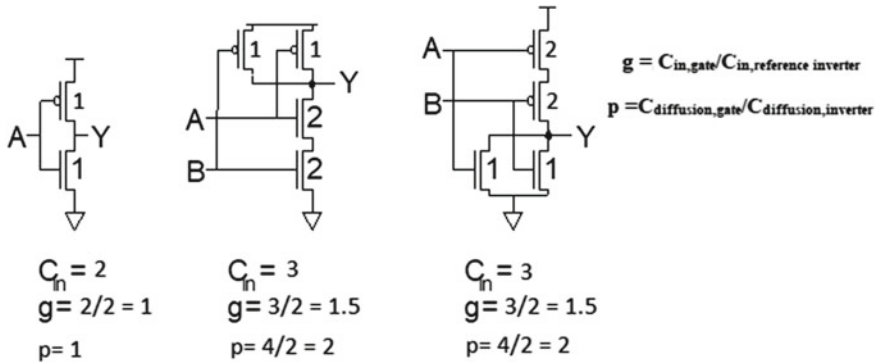
Fig. 3 Logical and parasitic effort of different gates both 180 and 16 nm technologies

4 Logical Effort Parameters for 180 and 16 nm Technologies

4.1 Logical and Parasitic Effort of Different Gates

Since minimum PDP for 180 nm as well as 16 nm occurs when PMOS-to-NMOS width ratio is one. Hence, we get same values of logical effort parameters for both technologies. Figure 3 shows the logical and parasitic effort of different gates.

Logical effort of a gate expresses how much input capacitance a gate presents to deliver the same output current as a reference inverter, i.e., maintaining the similar driving strength as that of reference inverter [5].

4.2 Defining T

The τ is the delay of an inverter driving an identical inverter with no parasitic (Fig. 4).

Delay of reference inverter circuit (τ) = 15.75 ps (180 nm).

Delay of reference inverter circuit (τ) = 3.75 ps (16 nm).

For each technology analysis, this τ is used for all further analyses.

A new parameter τ' is also defined which is the ratio simulation delay to dimensionless logical effort-based delay (D). For the various logical effort parameter analysis, the τ' is calculated to measure its closeness with delay of reference inverter (τ). The input rise and fall time both are kept 50 fs for all simulations.
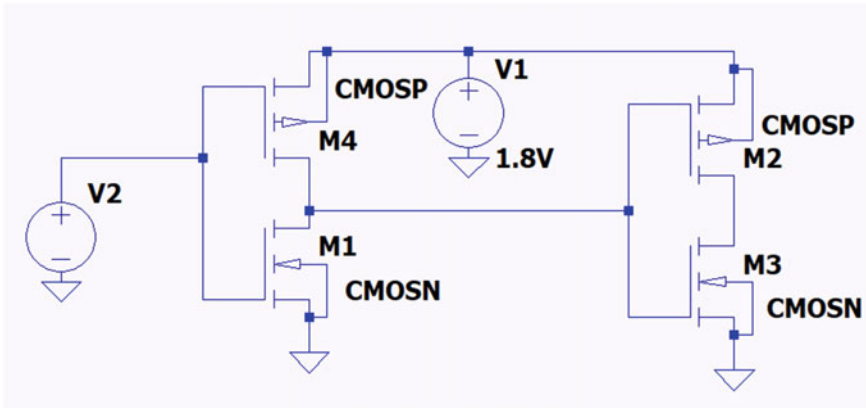
Fig. 4 Inverter circuit driving another identical inverter

4.3 Delay Variation Due to Branching Effort (B)

For estimating the delay variation due to branching effort, we used variable fanout inverter circuits ranging from FO-2 to FO-16. We also optimized the number of stages using logical effort for each circuit.

As evident from Tables 3 and 4 that the delay increases as the value of B increases due to increased fanout; e.g., it reaches to 213 ps in FO-16 from 93.5 ps in FO-2 (almost 115% increase) in 16 nm technology.

Also, in case of 180 nm technology the delay almost saturates from FO-10 onwards. However, in 16 nm technology it saturates from FO-12 onwards. So, we can say that after a certain stage, the effect of branching effort on delay becomes almost insignificant for driving similar inverters.

τ' is varying from 14.72 to 16.60 for 180 nm technology which is closer to τ while it's between 5.95 and 8.86 for 16 nm technology which is not closer to τ. Thus, 180 nm

Table 3 Effect of branching effort in different fanout inverters in 180 nm technology

Circuit type	D	Simulation delay (ps)	Logical effort delay = D* τ	τ'	% Change in delay
FO-2	17.16	246 (reference)	270.27	14.72	0
FO-4	19.04	295	299.88	15.49	19.91
FO-6	20.64	336	325.08	16.28	36.58
FO-8	21.88	345	344.61	15.76	40.24
FO-10	22.91	379.5	360.83	16.56	54.26
FO-12	22.97	381.5	361.80	16.60	55.08
FO-14	23.53	383.5	370.66	16.30	55.89
FO-16	24.03	391	378.56	16.26	58.94

Table 4 Effect of branching effort in different fanout inverters in16 nm technology

Circuit type	D	Simulation Delay (ps)	Logical effort delay = D* τ	τ'	% Change in delay
FO-2	17.160	93.5(reference)	64.35	5.95	0
FO-4	19.040	116.25	71.40	6.10	16.83
FO-6	20.640	127	77.40	6.15	27.63
FO-8	21.880	137	82.05	6.26	37.68
FO-10	22.910	144	85.91	6.28	44.72
FO-12	22.972	189.40	86.14	8.24	90.35
FO-14	23.534	196	88.25	8.32	96.98
FO-16	24.036	213	90.135	8.86	114.07

technology shows less variation between simulation and logical effort delay while variation is more in 16 nm technology may be due to some other technology-related effects.

4.4 Delay Variation Due to Parasitic Effort (P)

For estimating the delay variation due to parasitic effort, we used 4-stage logical effort optimized FO-4 and FO-14 inverter circuits. Using simulation, we calculated respective delay for each circuit.

From Tables 5 and 6 results for FO-4 case, the delay increases from 4.07% to almost 20% in 180 nm technology while it goes from 1.67% to 10.10% in 16 nm technology. Hence, delay increases with increase in parasitic capacitance.

From Tables 7 and 8 results for the higher fanout FO-14, we see that % change in delay is within 0–3% which is quite negligible even if we increase the parasitic

Table 5 Effect of parasitic effort in FO-4 inverter circuit in 180 nm technology

Capacitance added (fF)	Simulation delay (ps)	% Change in delay (with respect to FO-4 inverter without intermediate external capacitance)
0	295	0
10	307	4.07
20	314.5	6.61
30	324	9.83
40	332.5	12.71
50	335.5	13.72
60	355.5	20.50

Table 6 Effect of parasitic effort in FO-4 inverter circuit in 16 nm technology

Capacitance added (fF)	Simulation delay (ps)	% Change in delay (with respect to FO-4 inverter without intermediate external capacitance)
0	116.2	0
10	118.2	1.67
20	121.5	4.51
30	122.7	5.54
40	124	6.66
50	127	9.24
60	128	10.10

capacitance by changing intermediate node capacitance in both technologies. Hence, we can say that the effect of parasitic is negligible when the branching is quite high.

Table 7 Effect of parasitic effort in FO-14 inverter circuit in 180 nm technology

Capacitance added (fF)	Simulation delay (ps)	% Change in delay (with respect to FO-14 inverter without intermediate external capacitance)
0	383.5	0
10	383.6	0.026
20	383.8	0.078
30	384	0.130
40	387.5	1.040
50	387.9	1.140
60	393	2.470

Table 8 Effect of parasitic effort in FO-14 inverter circuit in 16 nm technology

Capacitance added (fF)	Simulation delay (ps)	% Change in delay (with respect to FO-14 inverter without intermediate external capacitance)
0	196	0
10	197.50	0.765
20	199	1.530
30	199.20	1.630
40	199.35	1.710
50	199.38	1.720
60	199.50	1.785

4.5 Delay Variation Due to Electrical Effort (H)

For estimating the delay variation due to electrical effort, we used 4-stage logical effort optimized FO-4 inverter circuit.

The results in Tables 9 and 10 show that the % change in delay is almost 20% as we increase H from 50 to 100 in both technologies. Hence, we can see that the delay increases as H is increased. Also, τ' varies from 15.49 to 16.08 for 180 nm technology which is closer to τ while it varies between 6.10 and 6.44 for 16 nm technology which is not closer to τ.

Thus, 180 nm technology shows less variation between simulation and logical effort delay while variation is more in 16 nm technology may be due to some other technology-related effects.

Table 9 Effect of electrical effort in FO-4 inverter circuit in 180 nm technology [$H = C_{out}/C_{in}$ (where $C_{in} = 1$ fF)]

H	D	Simulation Delay (ps)	Logical effort delay = D* τ	τ'	% Change in delay
50	19.040	295(reference)	299.880	15.49	0
60	19.744	314.5	310.968	15.92	6.61
70	20.360	325.5	320.670	15.98	10.33
80	20.917	335.5	329.442	16.03	13.72
90	21.423	344.5	337.412	16.08	16.78
100	21.888	351.5	344.736	16.05	19.15

Table 10 Effect of electrical effort in FO-4 inverter circuit in 16 nm technology [$H = C_{out}/C_{in}$ (Where $C_{in} = 1$ fF)]

H	D	Simulation delay (ps)	Logical effort delay = D* τ	τ'	% Change in delay
50	19.040	116.25(reference)	71.40	6.10	0
60	19.744	122.75	74.04	6.21	5.59
70	20.360	127.80	76.35	6.27	9.93
80	20.917	133.60	78.43	6.38	14.92
90	21.423	136.70	80.33	6.38	17.59
100	21.888	141	82.08	6.44	21.29

4.6   Comparison Between Electrical Effort (H) and Parasitic Effort (P)

Here we used FO-4 circuit with two different values of H-60 and 100. For each value of H, we varied the capacitance value of one of the intermediate nodes which will contribute to change in parasitic of that node. Thus, we got a comparative analysis between H and P variation and how the delay gets affected by varying P for a constant H.

As observed from Table 11, for $H = 60$, the % change in delay is about 10% on increasing intermediate node capacitance from 10 to 50 fF in 180 nm technology. While for $H = 100$, the change is about 7%. Hence, the effect of P on delay reduces at higher H.

As observed from Table 12 for 16 nm at $H = 60$ as well as $H = 100$, the percentage change in delay is about 4% only. So, the effect of P on delay is smaller due to H, due to lower driving currents.

Table 11 H versus P comparative analysis in FO-4 inverter circuit in 180 nm technology

H	C at intermediate node (fF)	Delay (ps)	% Change in delay
60	10	319.75	1.67
	30	326.50	3.81
	50	346	10.01
100	10	356.40	1.39
	30	366.95	4.39
	50	376.50	7.11

[$H = C_{out}/C_{in}$ (where $C_{in} = 1$ fF), delay of FO-4 circuit with $H = 60$: 314.5 ps from Table 9, delay of circuit with H = 100 is 351.5 ps from Table 9].

Table 12 H versus P comparative analysis in FO-4 inverter circuit in 16 nm technology

H	C at intermediate node (fF)	Delay (ps)	% Change in delay
60	10	124.4	1.340
	30	126.6	3.130
	50	119.7	4.032
100	10	142.6	1.134
	30	145.3	3.050
	50	147.2	4.397

[$H = C_{out}/C_{in}$ (where $C_{in} = 1$ fF), delay of circuit with $H = 60$: 122.75 ps from Table 10, delay of circuit with $H = 100$ is 141 ps from Table 10].

4.7 Delay Variation Due to Logical Effort (G)

For studying the effect of G on delay of a circuit, we used 4-stage circuit as shown in Fig. 5. The logical effort is changed by additionally inserting an input shorted NAND or NOR gate. This also inserts additional parasitic which is also considered. The change in parasitic is assumed to be negligible. Using simulation delay of τ' for each circuit is determined as shown in Table 12.

As seen from Tables 13 and 14 as we increase G by 125%, the delay increases by 23.83% in 180 nm technology. However, for same increase in G for 16 nm technology the % change in delay is quite large (76%) may be due to the reduced effect of parasitic.
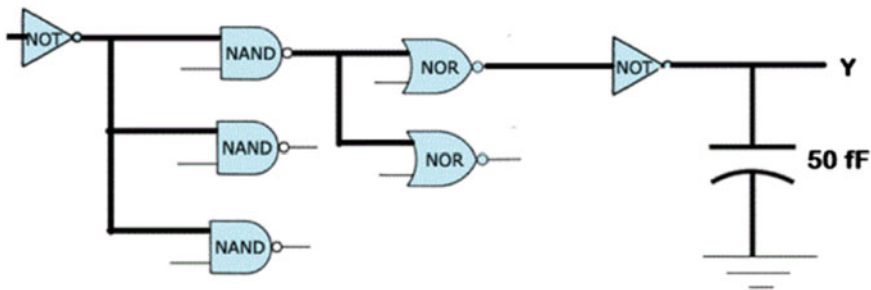
Fig. 5 4-stage circuit for calculation of delay variation due to G with $C_{in} = 1fF$

Table 13 Delay due to variation of G in 180 nm technology

G	P	$D = (NF^{1/N} + P)$	Simulation Delay (ps)	Logical effort delay $= D^* \tau$	τ'	% Change in delay
5.062	9	30.64	437	482.58	14.26	23.83
3.375	8	27.95	391	440.21	13.99	10.76
2.250	7	25.40	353	400.05	13.89	0 (reference)
1.500	6	23.40	333	368.55	14.23	−5.66

Table 14 Delay due to variation of G in 16 nm technology

G	P	$D = (NF^{1/N} + P)$	Simulation Delay (ps)	Logical effort delay $= D^* \tau$	τ'	% Change in delay
5.062	9	30.640	288.8	114.90	9.42	76
3.375	8	27.950	202.4	104.81	7.24	23.41
2.250	7	25.400	164.0	95.25	6.45	0 (reference)
1.500	6	22.965	146.0	87.75	6.35	-10.97

Also, τ' varies from 13.89 to 14.26 for 180 nm technology while it varies between 6.35 and 9.42 for 16 nm technology.

Thus, 180 nm technology shows less variation between simulation and logical effort delay while variation is more in 16 nm technology may be due to some other technology-related effects.

4.8 Delay Reduction Using Logic Effort-Based Optimization or Super Buffer Circuit [6]

To mitigate this problem, we insert N-inverter stages in cascade between any given input circuit and the load capacitance. This N-inverter stage has good drive strength and provides symmetric driving behavior (equal rise and fall times) leading to significant reduction in overall delay. This N-inverter cascade circuit is called super buffer.

The super buffer used for our calculation has $N = 4$, and it is of non-inverting type. We have used 4-stage circuit as the given circuit (used previously in calculating delay variation due to G) and kept its size as $W = 220$ nm: $L = 180$ nm for both PMOS and NMOS (un-optimized PMOS-to-NMOS width ratio). The results are calculated for 16 nm and 180 nm technology as given below: (Fig. 6).

We can see a significant decrease in delay by using the super buffer circuit at the output stage of our reference 4-stage circuit. From our previous calculation the delay of 4-stage circuit (without sizing, i.e., minimum size device and assuming normal PMOS-to-NMOS width ratio of 1.2 for given circuit) is 560 ps in 180 nm technology. However, after using the super buffer to drive the load, we observe that the delay decreased to 375 ps (about 33% assuming un-optimized PMOS-to-NMOS width ratio of 1.2 for given circuit while optimized PMOS-to-NMOS ratio of 1 for super buffer). Further, after sizing the circuit without using super buffer delay is 353 ps (using optimized PMOS-to-NMOS width ratio of 1).

This decrement is becoming more prominent in 16 nm technology as the delay reduces from 4610 to 407.5 ps (83.8%). Also, after sizing the circuit without using super buffer delay is 164 ps.
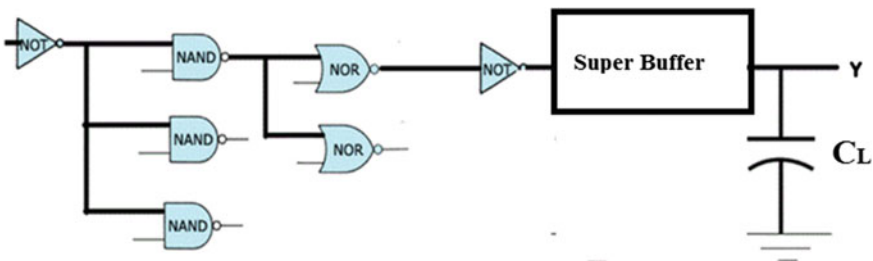
Fig. 6 Super buffer added to 4-stage minimum size circuit

5   Conclusion

The logical effort-based methods are more suitable if the load capacitor is present and designer needs to resize the transistors so as to achieve minimum power–delay product.

The effect of each logical effort parameters on delay has been studied for 16 and 180 nm technology. Although effect of B increases delay, it saturates after a certain fanout. The effect of P on delay can be seen for FO-4 but at higher fanout (FO-14) the increase in delay is negligible. The comparative analysis between effect of H and P on delay shows that at higher value of H the increase in delay due to P is almost insignificant. The variation in parameter G shows that the delay increases as G increases, the increase in the delay is more in case of 16 nm technology.

Also, we have defined a new parameter τ' which is the ratio of simulation delay and logical effort delay to observe the variation between simulation and logical effort delay. The super buffer circuit offers a significant decrease in delay by using connecting it at the output stage of a circuit as evident from our results in both technologies. The reduction in delay by about 33% in 180 nm technology while 83.8% in 16 nm technology utilizing the limited knowledge of logical effort at the expense of slight increase in the number of gates.

References

1. Harris D, Ho R, Wei GY, Horowitz M (1998) The Fanout-of-4 Inverter Delay Metric. Stanford University, Stanford, CA 94305
2. Sutherland I, Sproull B, Harris D (1999) In: Logical effort: design fast CMOS circuit. Morgan Kaufmann publishers
3. Raghav HS, Maheshwari S, Gupta A (2014) A comparative analysis of power & delay optimize digital logic families for high performance system design. Int J Signal Imaging Syst Eng 7(1):12–20
4. Rabaey JM, Chandrakasan A, Nikolic B (2004) Digital integrated circuits, 2nd edn. Pren-tice Hall of India Private Limited
5. Anacan RM, Bagay JL (2015) Logical effort analysis of various VLSI design algorithms. In: IEEE international conference on control system, computing and engineering, 27–29 November 2015, Penang, Malaysia
6. Lin X, Wang Y, Nazarian S, Pedram M (2014) An improved logical effort model and framework applied to optimal sizing of circuits operating in multiple supply voltage regimes. University of Southern California, CA USA, Department of Electrical Engineering

A Single Electron Transistor-Based Floating Point Multiplier Realization at Room Temperature Operation

Sanghamitra Banik, Rachesh Trivedi, Abhishek Kalavadiya, Yash Agrawal, and Rutu Parekh

Abstract Floating point numbers provide more range as compared to the fixed point values. The multiplier is one of the main blocks of a processor. For improved performance, there is a need for fast and efficient floating point multipliers. The single electron transistor (SET) is a prominent advanced device structure for achieving high-end computing system. This paper describes the implementation of single precision floating point multiplier using SET (single electron transistor) for better performance. Design and simulation of floating point multiplier have been performed using Cadence Virtuoso. In this paper, we are comparing SET-based floating point multiplier with 16 nm CMOS and then power and delay had been compared. The main objective of this paper is to reduce power consumption and increase the speed or reduce the delay of execution. IEEE 754 standard has been used to represent floating point numbers. Here, floating point multiplier is implemented and verified using the Cadence Virtuoso tool. Thus, SET-based floating point multiplier provides better execution in lowering the power and increasing the speed.

Keywords IEEE 754 standard · Floating point number · CMOS · Single electron transistor · Coulomb blockade

1 Introduction

As the CMOS process technology scales into the nanoregime, the performance and reliability of the chip degrade. With advancements in semiconductor technology, the future roadmap by ITRS for research and development is on nanoelectronics. For the emerging nanodevices, the performance can be measured in many different ways: least delay, higher density, low power and more functionality. Among such devices, single electron transistor (SET) is one of the most promising device that has low power usage, high speed functionalities or capabilities and highly scalable [1, 2].

S. Banik · R. Trivedi · A. Kalavadiya (✉) · Y. Agrawal · R. Parekh
Dhirubhai Ambani Institute of Information and Communication Technology Gandhinagar, Gandhinagar 382007, India
e-mail: amkalavadia74@gmail.com

Building low power high speed electronics is a never-ending demand. Using SET technology basic gates [3, 4], periodic symmetric functions generation [5], ultra-high frequency operation [6], half adder [7], 4 × 1 multiplexer [8], D-type flip flop [9], 3-bit multiplier [10], frequency doubler [11], random number generator [12], 4-bit ADC [13] and 8 × 8 memory [14] have been designed. To our best of the knowledge, there is no logic implemented for floating point arithmetic.

Arithmetic operations are classified as fixed point and floating point. Floating point multiplier (FPM) is one of the significant block in digital applications such as digital signal processor, filtering and microprocessors. Floating point operations require large resources as compared to fixed point operations. Floating point numbers support much wider range of values than fixed point, with the ability to represent very small and very large numbers. In this paper, FPM is implemented, using a SET. IEEE 754 standard single precision binary floating representation has been used for the same [15]. It uses 32 bits with one bit reserved for sign, 8 bits for exponent and 23 bits for mantissa. Size of mantissa indicates precision, and size of exponent indicates range.

This paper implements single precision FPM using a metallic SET operating at a room temperature. The parameters implemented are of a realistic SET fabricated using nanodamascene process [1, 16]. The metallic SET can be fabricated using back-end-of-line fabrication process (BEOL), which facilitates less interconnect parasitics and a low thermal budget process. The SET operates on quantum mechanical principle of coulomb blockade and single electron tunneling. It is observed that during the coulomb blockade region current is almost zero. SET can be regarded as simple switch controlled by a gate voltage. Switch is 'OFF' when coulomb blockade exists, otherwise in 'ON' state. SET and MOSFeT have complementary properties. Performance analysis of SET and CMOS has been done based FPM is performed and achieved. Figure 1a shows SET symbol and the drain current characteristics at a constant drain to source voltage (V_{ds}). The electrical parameters to conduct simulations are junction resistance $R_T = 1M\Omega$, gate capacitance $C_{g1} = 0.045aF$, tuning gate capacitance $C_b = 0.050aF$, temperature T = 300 k, power supply (high logic) is 800 mV, and low logic is taken as 0 V [1]. This high voltage of 800 mV is applied to ensure high speed and low power and that it can be interfaced with CMOS circuit. V_b is the biasing voltage of the tuning gate or back gate. SET can be used as a PSET and NSET if the back gate is biased. Unbiased back gate acts as a PSET, and biased back gate (logic one) acts as an NSET. There is phase difference of 90° between current of PSET and NSET as shown in Fig. 1b.

2   Architecture of Floating Point Multiplier

FPM consists of a mantissa block for multiplying the mantissa field, exponent block to calculate the exponent field of the result, normalizing unit to normalize the result, overflow/underflow block and sign block to calculate the sign field of result. The block diagram of FPM is shown in Fig. 2a. Algorithm of floating point multiplication is

Fig. 1 Single electron transistor **a** SET symbol, **b** oscillation characteristics of PSET and NSET

(a)

(b)
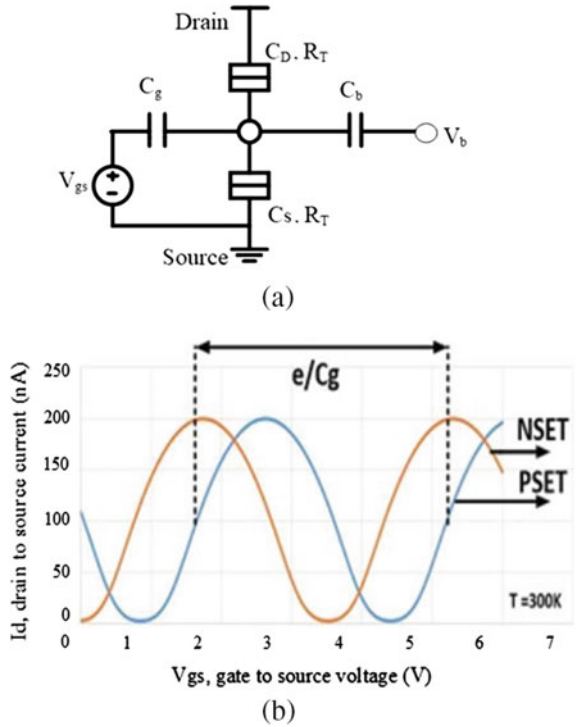
shown in Fig. 2b. Mantissa fields are multiplied to get the product, exponent fields are added, and bias is subtracted from the sum, then normalized and rounded to appropriate significant bits. Flag is set on the occurrence of underflow or overflow, and it is reset for normal operation.

2.1 Mantissa Block

Array multiplier has been used to multiply the mantissa field of floating point numbers as shown in Fig. 3. Multiplier circuit is based on add and shift algorithm. Each partial product is generated by multiplying the multiplicand with one multiplier bit. Partial product is shifted in accordance with their bit order and then added. Addition is performed using ripple carry adder. The Multiplier Block provides double precision output; that is, the mantissa field result will have double the number of bits as that of input mantissa field. The block diagram below represents the mantissa block of 32-bit FPM. $[a_0–a_{22}]$, $[b_0–b_{22}]$ represents normalized mantissa field of multiplicand and multiplier, leading one bit before the decimal point of multiplicand, multiplier is represented by $[a_{23}, b_{23}]$, $[p_0-p_{47}]$ represents multiplier result, and a_0b_0, a_0b_1 …
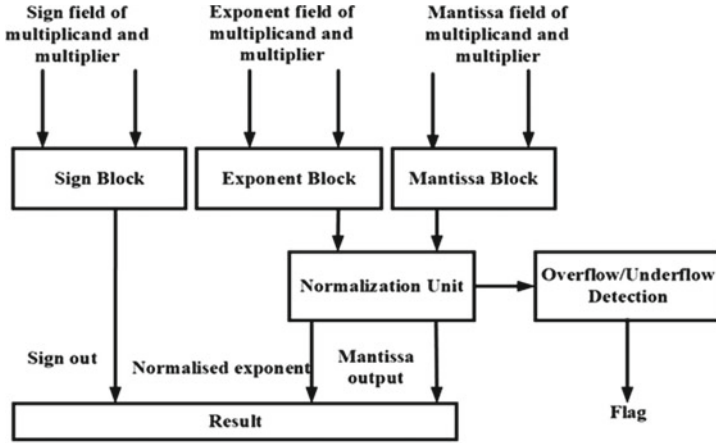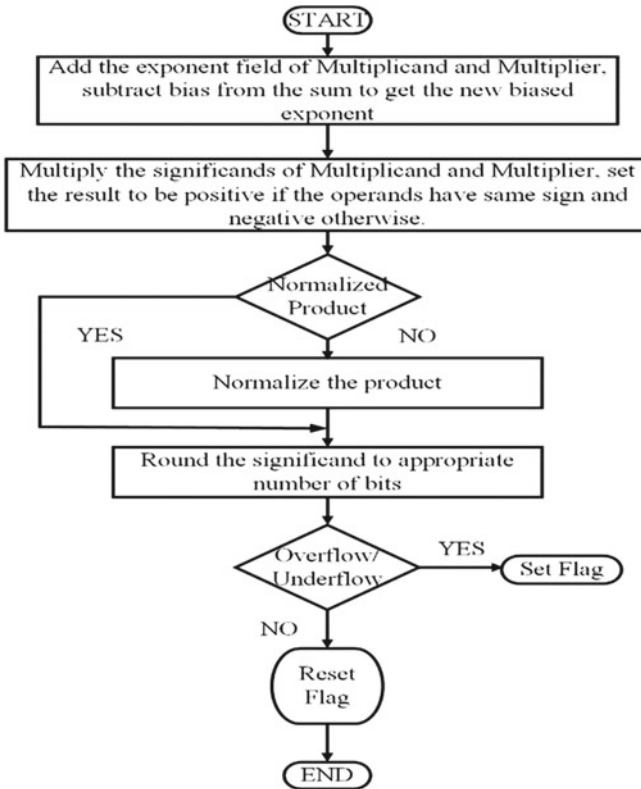
Fig. 2 Floating point multiplier **a** block diagram of FPM, **b** algorithm
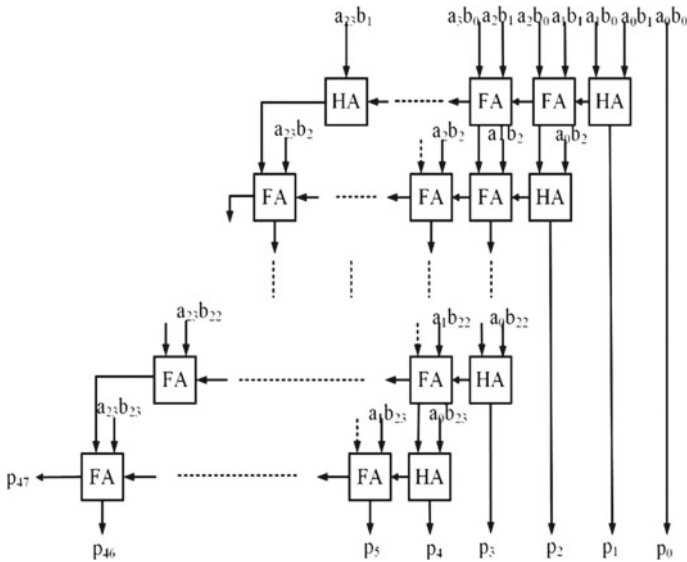
Fig. 3 Block diagram of mantissa block

$a_{23}b_{23}$ are partial products generated using AND operation of each bit of multiplicand and multiplier.

2.2 Exponent Block

This block adds the biased exponent field of two floating point numbers and removes the extra bias to get the original biased exponent of the result (E1 + E2−bias), where bias is 127. Ripple carry adder is used to add these exponents. Ripple borrow subtractor is used to subtract bias from sum. Figure 4 represents exponent block of 32-bit FPM. $[e_0$–$e_7]$, $[f_0$–$f_7]$ represents exponent field of multiplicand and multiplier, and $[bias_0$–$bias_7]$ represents bias.

2.3 Normalization Unit

The result of mantissa block must be normalized. A normalized number has only one 1 to the left of the decimal point. For 32-bit FPM, if the result has zero in P_{47} position and one in P_{46}, then the result is said to be in normalized form. If the result has one in P_{47} position irrespective of one or zero in $P_{46,}$ then the exponent is added by one to get the result in normalized form and the result is right shifted by one. For more accuracy, double precision output is used. Hence, for single precision FPM,
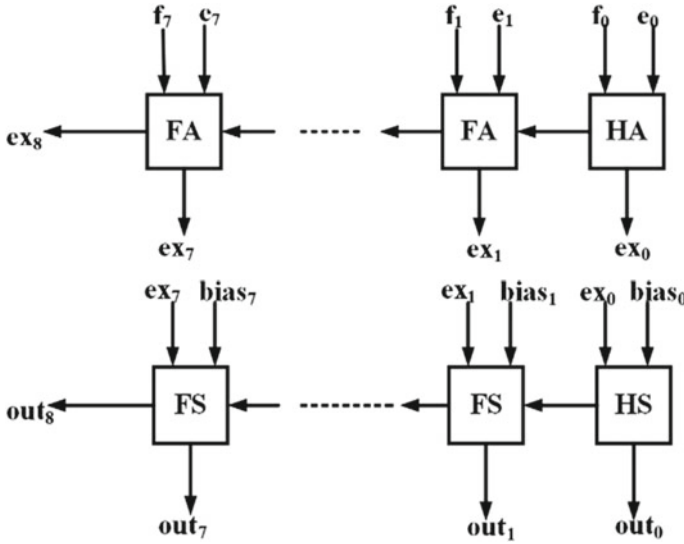
Fig. 4 Block diagram of exponent block

after normalization the result is rounded off to most significant 46 bit after decimal point. The block diagram of normalization unit is shown in Fig. 5a. Shifter block is designed using forty-six 2:1 multiplexer cells. Figure 5b shows the circuit diagram of 2:1 multiplexer using SET.

2.4 Overflow/Underflow Detection

Assuming exponent field of multiplicand and multiplier is valid values; flag is raised whenever underflow or overflow occurs or if the normalized exponent takes special values that is all zeros or all ones. For a 32-bit FPM, the size of biased exponent of the result with normalization must be 8 bits, which means the value must lie between 1 and 254 as shown in Table 1. Underflow or overflow is detected if 9th bit of normalized exponent is set.

2.5 Sign Block

Sign block provides sign bit of the result. It consists of one XOR gate. If the sign field of multiplicand and multiplier is same, the sign field of result will be zero, that is, positive else if the sign field of multiplicand and multiplier is different, the sign field of result will be one, that is negative.
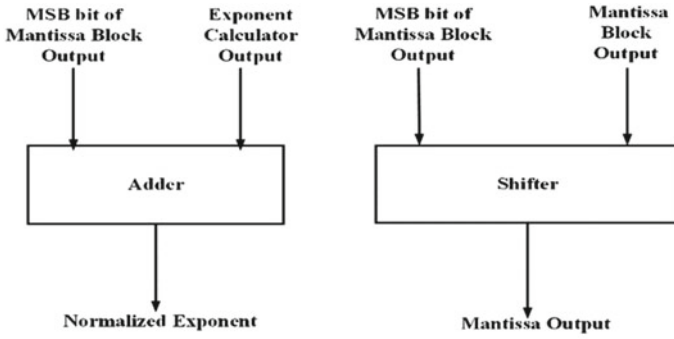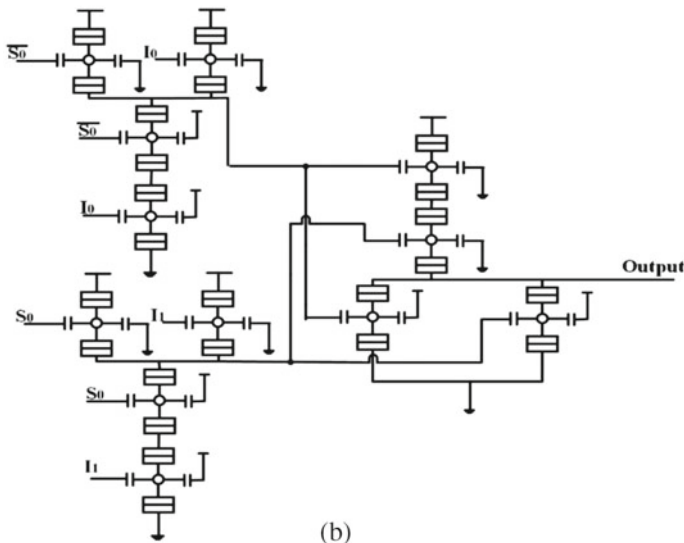
Fig. 5 **a** Block diagram of normalization unit, **b** circuit diagram of mux using SET symbol

Table 1 Conditions for overflow/underflow detection	$-125 \leq E_{exp} < 0$	Underflow
	$E_{exp} = 0$	May turn to normalize
	$1 \leq E_{exp} < 254$	Normalized number
	$E_{exp} \geq 255$	Overflow

3 Simulation Results

Simulation is performed using Cadence Virtuoso Environment that supports analog, digital and mixed signal devices at block and chip level. VerilogA library file is used

for SET implementation. MIB model is used for SET simulation, and parameters are for real fabricated SET according to [1]. In similar way for caring out stimulation for 16 nm CMOS PTM model is being implemented in Cadence Virtuoso [17]. FPM is implemented in 16 nm CMOS as well, and then, power and delay have been compared, as shown in Table 2. Figure 6 shows the simulation result of single precision floating point number using SET at supply voltage of 0.8 V. The electrical parameters used in this work for SET symbol are based on the previous work [18, 19]. This metallic SET performs better than 16 nm CMOS counterpart as shown in Table 2. This work has better performance of 32-bit SET with power 13.3 μw and delay 185 ps as compared to previous work which is power 173.72 μw and delay 29.72 ns, respectively, for 32-bit multiplier at 90 nm technology node [18]. In addition to this, in another work on single precision 32-bit FPM implemented with Modified Full Adder in divide and conquer approach with pipelining [20] reports delay and power of 17.266 ns and 158.94 mW, respectively, as compared to delay and power of SET-based FPM as 185 ps and 13.3 μW, respectively. For best comparison, the same design of SET has been implemented in this work with 16 nm CMOS and performance analysis is shown in Table 2. As shown, the delay and power of FPM at 16 nm CMOS are 1150 ps and 22.354 μW and SET is 185 ps and 13.3 μW, respectively. Hence, SET-based FPM outperforms CMOS technology.

The result as shown in Fig. 6 is represented in 55 bits. Since mantissa block provides double precision output, the 46 lower significant bits provide the mantissa field of result, the next 8 bits provide normalized exponent field of result, and the most significant bit provides the sign field of result. Considering the dashed box in Fig. 6, multiplier represents the value: $1.111001011001101110010110 \times 2^{-60}$, multiplicand represents value −

Table 2 Performance analysis of different multiplier

#Bits	SET		16 nm CMOS	
	Power (μW)	Delay (ps)	Power (μW)	Delay (ps)
8-Bit	0.36	35	1.37	741.5
16-Bit	1.33	170	12.7	1045
32-Bit	13.3	185	22.354	1150
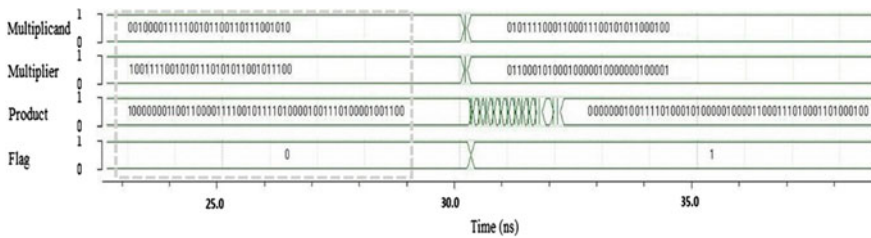
Fig. 6 Simulation waveform of SET-based 32-bit FPM

$1.1010111010101100101110 \times 2^{-67}$, and with normalization, result represents value: $-1.1001100001111001011110100001001110100001001100 \times 2^{-126}$. To determine the normalized exponent of result, bias of 127 is added to get exponent of result that is $(-126 + 127)$ one. Since the sign field is set, the result is negative.

4   Conclusion

Design and simulation of FPM have been performed using Cadence Virtuoso in this work. Results of every block have been checked and are found to be correct for transient analysis. Power is reduced by 40.5% for SET only-based design, and speed of SET-based design is 83.9% improved in comparison with 16 nm CMOS-based design. SET-based FPM is power efficient and has lesser delay. Based on results achieved, it is concluded that SET is better device for low power applications and high performance computing. With increase in number of bits in FPM, power and delay increase. It is a design tradeoff that can be decided based on application. Hence, SET-based low power logic can be stacked above a CMOS carrier which can result in increased footprint, reduced thermal budget and higher performance.

References

1. Parekh R, Beaumont A, Beauvais J, Drouin D (2012) Simulation and design methodology for hybrid SET-CMOS integrated logic at 22-nm room-temperature operation. IEEE Trans Electron Devices 59(4):918–923
2. Parekh R, Beauvais J, Drouin D (2014) SET logic driving capability and its enhancement in 3-D integrated SET–CMOS circuit. Microelectron J 45(8):1087–1092
3. Maeda K, Okabayashi N, Kano S, Takeshita S, Tanaka D, Sakamoto M, Teranishi T, Majima Y (2012) Logic operations of chemically assembled single-electron transistor. ACS Nano 6(3):2798–2803
4. Khan MH (2015) Single-electron transistor based implementation of NOT, Feynman, and Toffoli Gates. In: IEEE international symposium on multiple-valued logic 2015, pp 66–71. IEEE, Waterloo
5. Miralaie M, Mir A (2016) Performance analysis of single-electron transistor at room-temperature for periodic symmetric functions operation. J Eng 10:352–356
6. Inokawa H, Nishimura T, Singh A, Satoh H, Takahashi Y (2018) Ultrahigh-frequency characteristics of single-electron transistor. In: International conference on electron devices and solid state circuits (EDSSC) pp 1–2. IEEE, Shenzhen
7. Hasani M, Abbasian K, Karimian GH, Asadi MJ (2013) Design of a half-adder using silicon quantum dot-based single-electron transistor operating at room temperature. J Electron Devices 18:1505–1509
8. Ghosh A, Jain A, Sarkar SK (2019) Design and simulation of nanoelectronic data transfer system with an emphasis on reliability and stability analysis. Analog Integr Circ Sig Process 101(1):13–21
9. Rajasekaran S, Sundari G (2017) Analysis of flip flop design using nanoelectronic single electron transistor. Int J Nanoelectron Mater 10:21–28

10. Raut V, Dakhole PK (2014) Design and implementation of single electron transistor N-BIT multiplier. In: International conference on circuits, power and computing technologies (ICCPCT), pp 1099–1104. IEEE, Nagercoil
11. Eskandarian A, Rajeyan Z, Ebrahimnezhad H (2018) Analysis and simulation of single electron transistor as an analogue frequency doubler. Microelectron J 75:52–60
12. Tannu S, Sharma A (2012) Low power random number generator using single electron transistor. In: International conference on communication, information & computing technology (ICCICT), pp 1–4. IEEE, Mumbai
13. Miralaie M, Mir A (2018) Evaluation of room-temperature performance of ultra-small single-electron transistor-based analog-to-digital convertors. J Circuits Syst Comput 27(14):1850217
14. Parekh R (2019) Design and simulation of single electron transistor based SRAM and its memory controller at room temperature. Int J Integr Eng 11(6):186–195
15. Rajaraman V (2016) IEEE standard for floating point numbers. Resonance 21(1):11–30
16. Dubuc C, Beauvais J, Drouin D (2008) A nanodamascene process for advanced single-electron transistor fabrication. IEEE Trans Nanotechnol 7(1):68–73
17. Predictive Technology Model (PTM). http://ptm.asu.edu/. Accessed 08 Oct 2021
18. Sunesh NV, Sathishkumar P (2015) Design and implementation of fast floating point multiplier unit. In: International conference on VLSI systems, architecture, technology and applications (VLSI-SATA), pp 1–5. IEEE. Bengaluru
19. Gowreesrinivas KV, Samundiswary P (2017) Comparative performance analysis of multiplexer based single precision floating point multipliers. In: International conference of electronics, communication and aerospace technology (ICECA) vol 2, pp 430–435. IEEE, Coimbatore
20. Krishnan T, Saravanan S (2017) Design of low-area and high speed pipelined single precision floating point multiplier. In: 6th international conference on advanced computing and communication systems (ICACCS) (2020), pp 1259–1264. IEEE, Coimbatore

Comparison of Total Ionizing Dose Effect on Tolerance of SCL 180 nm Bulk and SOI CMOS Using TCAD Simulation

Shubham Anjankar and Rasika Dhavse

Abstract The long-term reliability of metal oxide semiconductor (MOS) devices in space technology depends on the total ionizing dose (TID) effect. In MOS technology, power consuming, expensive, and bulky triple modular redundancy and shielding techniques are required to address radiation related issues. In this work, we simulate Semi-Conductor Laboratory (SCL) 180 nm silicon on insulator (SOI) and Bulk NMOS device for comparative study of TID effects in space technology applications. Both devices after simulation show 0.42 V and 0.62 V threshold voltage, respectively. Devices are irradiated for 15 s to achieve doses of 100 K Rad, 200 K Rad, 500 K Rad, 800 K Rad, 1 M Rad, respectively with different dose rates. Bulk 180 nm NMOS was found to be more radiation-sensitive than SOI devices. Dose rate (DR) effect of 35 μV on a Bulk device and 16 μV on SOI was observed. 267% on Bulk and 256% on SOI leakage current shift observed due to radiation. Devices show the dose rate sensitivity with varying leakage current from the range of 1.8 to 3nA/um. In both the devices, leakage current is generated because of interface charge trapped due to radiation and charge trapped. Post radiation major shift transconductance characteristics are observed.

Keywords Total ionizing dose (TID) · Dose rate (DR) · Ionizing radiation · 180 nm NMOS · TCAD

1 Introduction

For modern electronic devices, the most important and challenging failure phenomenon is radiation-induced effects. Radiation is the process by which energy

S. Anjankar (✉)

Department of Electronics Engineering, Shree Ramdeobaba College of Engineering and Management, Nagpur, Maharashtra, India
e-mail: d17ec009@eced.svnit.ac.in

R. Dhavse

Department of Electronics Engineering, Sardar Vallabhbhai National Institute of Technology, Surat, Gujrat, India

is emitted as either particles or waves [1]. The radiation effect on devices is broadly classified in total ionizing dose (TID), single event upset, and displacement damage which is observed due to heavy dose and long dose duration, heavy dose but for a small duration, and due to low dose rate, respectively [2–4]. The main reason behind the TID is oxide trapped in the interface and silicon region. There are two dominant mechanisms associated with these effects, the generation of hole traps and interface states. Both of these mechanisms contribute to the overall device parametric degradation. The first effects are typically seen in the thick field isolation region and the second effects are in the gate region, under total irradiated dose exposure [5, 6]. TID effect is especially a concern for the long-term reliability of semiconductor devices [7].

The space environment induces TID degradation to a majority of electrical, electronic, and electromechanical (EEE) components employed in a spacecraft. A space mission's success relies on functional EEE components. TID testing is necessary to characterize the performance of a device in a space environment [8, 9].

Since both TID and SEE (single event effects) are the effect of ionizing radiation, hence it is important to address the important difference between these two concerning design and analysis [10, 11]. TID versus SEE which is long-term failure effect and instantaneous failure effect, respectively. As an analogy of failure: TID would be similar to the thread lifetime of the device, therefore, TID failure rate can be described by a mean time to failure (MTTF), but SEE must be expressed in terms of a random failure rate [12]. Clinical and medical laboratory equipment's also suffered TID but not up to the level of space radiation. TID challenges remain for low dose rate (<1Mrad), e.g., space environment and high dose rate (~1Mrad), e.g., high luminosity accelerator environment [13]. Shielding devices is also one of the ways to protect devices from the TID effect, but the implementation of these techniques is not cost-effective and puts the burden on system and power [8, 14–16]. Many authors worked on various TID effects on MOS devices but for deep study of TID effect on Bulk and SOI technology deep comparison study is required.

In CMOS technology, TID effect was observed due to reduced gate insulator thickness. However, TID effects for thick insulators are still a major concern [17, 18]. In the integrated circuit (IC), thick insulators are still present in the shallow trench isolation (STI) region, where oxide-charge trapping due to radiation still be observed [19]. These increases in oxide traps are responsible for effective increases in transistor leakage current [6]. Most of the radiation test study is performed on the device level, but due to the shrinking size of devices (as well as oxide layers) chip-level, TID study is essential. Due to node technology advancement more and more devices are accumulated in the same circuit chip [20–22]. This results in more ionizing radiation exposure to the number of devices than the previous chip/circuit level design causing effective degradation at the chip/circuit level. To overcome these failures, designers have relied on modular redundancy and multilevel shielding techniques. Modular redundancy makes the system area- and power-hungry [20, 23]. Due to controllable short-channel effects and reliability requirements for ≈10 years of lifetime, a 180 nm node is preferred in space technology [24, 25]. This work aims

to test TID effects on SOI and Bulk devices for space technology. SCL 180 nm SOI and Bulk technology will be used for all experimentation.

This paper is organized into three sections. Section 2 discusses the strategy for the simulation of 180 nm SOI and SCL Bulk NMOS. Section 3 examines the radiation effect on leakage current, threshold voltage, transconductance, output characteristics, on–off current, and subthreshold swing. Section 4 discusses the conclusion of this work.

2 Simulation of 180 nm SOI and SCL Bulk NMOS

SCL 180 nm simulated parameters are extracted from the SCL model file [26]. SCL 180 nm model parameters are shown in Table 1. The threshold voltage is calculated by using a constant current method, and a calculated threshold voltage is 0.42 V. SCL Bulk 180 nm NMOS device is simulated using Synopsys Sentaurus TCAD simulator. Polysilicon reoxidation is at 900 °C using oxygen gas is done to release stress before spacer formation. Figure 1 shows the SCL 180 nm simulation flow. Figure 2a shows the simulated SCL model parameters 180 nm NMOS.

SOI technology 180 nm NMOS device is simulated using Synopsys Sentaurus TCAD Sdevice simulator. 300 um SOI region is simulated with a 0.12 um oxide layer. Gate oxide of 40 e-10 is grown over the silicon region. Then, the polysilicon layer of

Table 1 Simulated and SCL model parameter comparison

SCL model parameter	SCL model values	Bulk NMOS simulated results	SOI NMOS simulated results	Description
N_{SUB}	6e16 cm^{-3}	6e16 cm^{-3}	1e16 cm^{-3}	Substrate doping concentration
N_{SD}	1e20 cm^{-3}	1.5e20 cm^{-3}	1.1e20 cm^{-3}	Source/drain doping concentration
XT	0.15 um	0.156 um	0.12 um	Doping depth
T_{OX}	40 Å	40.45 Å	40 Å	Oxide thickness
NLD	1e19 cm^{-3}	5e19 cm^{-3}	–	LDD/LDS doping density (>1e19: LDD/LDS treated as D/S extension)
NBH	1e17 cm^{-3}	7e17 cm^{-3}	–	Halo doping
G_L	177 nm	171 nm	165 nm	Effective gate length
B_{OX}	–	–	0.12 um	Buried oxide
V_{TH}	0.42 V	0.46 V	0.62 V	Threshold voltage (by constant current method)

Fig. 1 SCL 180 nm NMOS
simulation flow
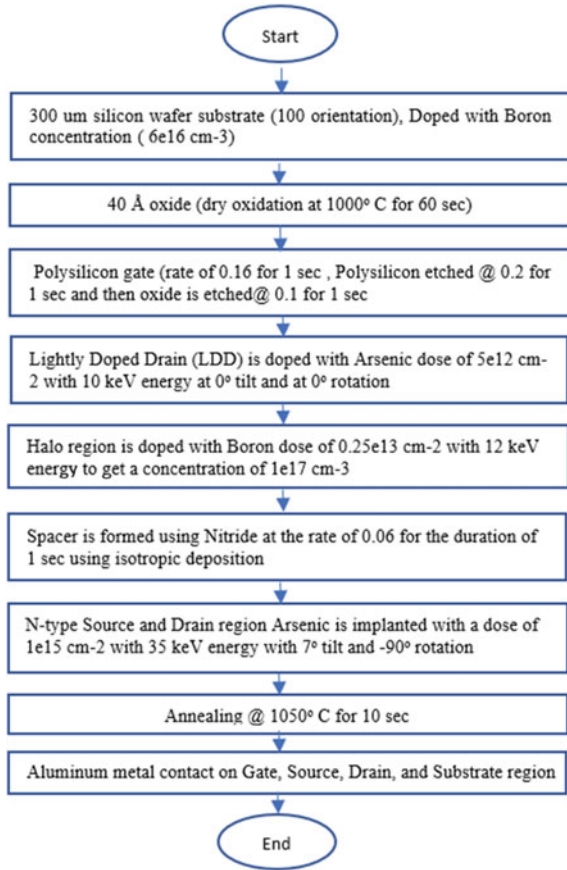
180 nm thickness is grown for generating gate region. Etching is done by masking the gate region. Source and drain are doped with arsenic with the concentration of 1e19 cm-3. The depth of source and drain obtained is 0.12 um. A spacer is created to isolate the gate region with the source and drain region with nitride. The effective gate length obtained is 165 nm. Figure 2b shows the simulated 180 nm SOI technology NMOS.

3   Result and Analyses

All testing's are carried out in the Sentaurus Sdevice model using the IN-SITU testing procedure [27]. All the parameters tested and data collected are during the radiation process. Mobility models which include doping dependence, high-field saturation (velocity saturation), and transverse field dependence are specified for
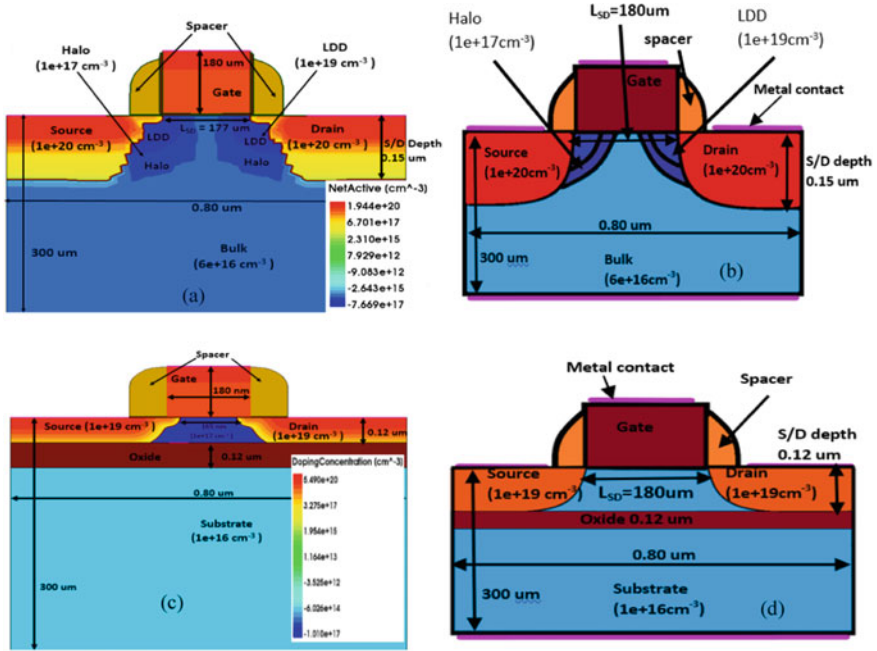
Fig. 2 180 nm model parameter **a** simulated bulk NMOS **b** proposed bulk NMOS **c** simulated SOI technology **d** proposed SOI technology

this simulation. The doping dependence of the Shockley–Read–Hall recombination (SRH) lifetimes is modeled in Sentaurus Device with the Scharfetter relation [28]:

$$\tau_{dop}(N_{A,0} + N_{D,0}) = \tau_{min} + \frac{\tau_{max} - \tau_{min}}{1 + \left(\frac{N_{A,0}+N_{d,0}}{N_{ref}}\right)} \tag{1}$$

Electric field dependent process-based generation of electron–hole pairs and is modeled as follows:

$$G_r = g_0 \, D.Y(F) \tag{2}$$

$$Y(F) = \left(\frac{F + E_0}{F + E_1}\right)^m \tag{3}$$

where D is the dose rate, g_0 is the generation rate of electron–hole pairs, E_0, E_1 and E_2 constants. $g = 7.6000e + 12$ [1/(rad $*$ cm^3)], $E0 = 0.1$ [V/cm], $E1 = 1.3500e + 06$ [V/cm], $m = 0.9$.

Electrical measurements are taken for threshold voltage, transconductance, output characteristics, subthreshold swing, I_{ON}, and I_{OFF}. Gamma radiation test is performed

on both of the devices as Gamma radiation is accepted as the standard for measuring any type of radiation [29, 30]. Then, radiation is started for 15 s to test the TID effect on both the Bulk and SOI technology with the same concentration. Radiation dose is varied from 100 kRad to 1 MRad. To study dose rate sensitivity dose rate of 7 kRad/s, 13 kRad/s, 33 kRad/s, 53 kRad/s, 70 kRad/s irradiated for 15 s to achieve does of 100 Rad, 200 Rad, 500 Rad, 800 Rad, 1 MRad, respectively. Post irradiation electrical measurement is done again for the same parameters to study pre- and post-TID effects on the devices.

3.1 Leakage Current

Figure 3a shows the post-radiation leakage current for irradiation time of 15 s for Bulk 180 nm NMOS. Initially, leakage current increases rapidly for radiation dose, after 3 s current goes into steady rise state. The device shows the dose rate sensitivity with varying leakage current from the range of 1.8 to 3nA/um. Irradiation is carried out keeping the gate terminal at ground potential (VG = 0 V). Below the threshold, with ground gate terminal Bulk NMOS is expected to show 0A current but post-radiation leakage current is noticeable. For higher drain voltage, dose rate effect is more. For VD = 1 V, 0.3 nA/μm change is observed, while for VD = 3 V, the current shift is 0.8 nA/um is observed.

For SOI technology, Fig. 3b is observed that with the increase in dose rate, leakage current is increasing. The same phenomena as Bulk MOS technology are observed for drain voltage to radiation dose relation and its leakage current. Difference due to radiation VD = 1 V is less than VD = 2 V and it is less than VD = 3 V for leakage current generation.
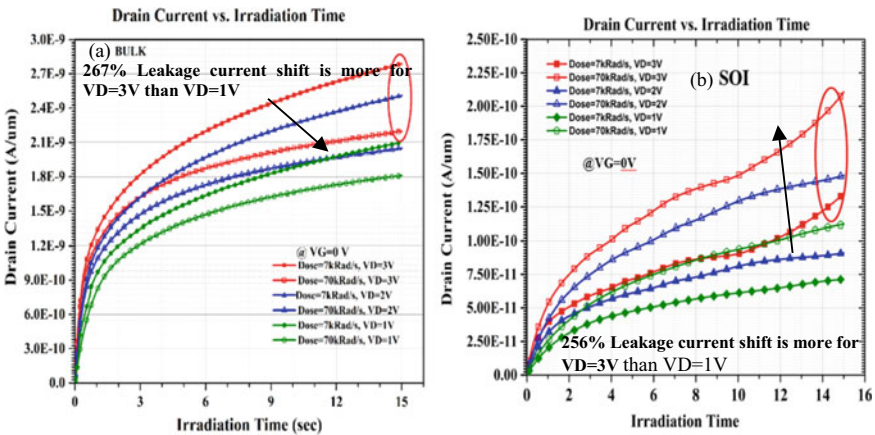
Fig. 3 Leakage current due to radiation on **a** bulk and **b** SOI 180 nm NMOS

In both the devices, leakage current is generated because of interface charge trapped due to radiation and charge trapped in silicon. In SOI technology due to charge trapped in buried oxide, the leakage current is generated but at the same time it works as an insulator for substrate, hence leakage current is less in SOI than Bulk technology.

3.2 Threshold Voltage Shift

Threshold voltage is one of the important parameters for the devices to decide the parameters like I_{ON}, $I_{OFF,}$ etc. Drain current versus gate voltage cure is plotted for Bulk and SOI technology. The desired SCL threshold voltage is 0.42 V and achieved threshold voltage through simulation for Bulk technology is 0.46 V and SOI threshold voltage, 0.62 V. The threshold voltage is calculated using the constant current method. $V_{T(ci)}$ can be calculated using

$$V_{T(ci)} = V_{GS}(\text{at } I_D = I_{D0}W/L) \tag{4}$$

where W and L are the gate width and gate length.

For 180 nm Bulk technology, 0.12 V threshold voltage shift is calculated after Gamma radiation in Fig. 4a. The dose rate effect is also observed on the threshold voltage. Different dose rates cause threshold voltage shifts in mV. From Fig. 5a, it is observed that with increasing dose rate threshold voltage shift is decreases due to displacement damage (DD) effect. The threshold voltage is a function of gate oxide thickness, and low dose radiations are not having enough energy to penetrate deep into the device, hence the causes radiation charge trapped near-surface and gate oxide interface.
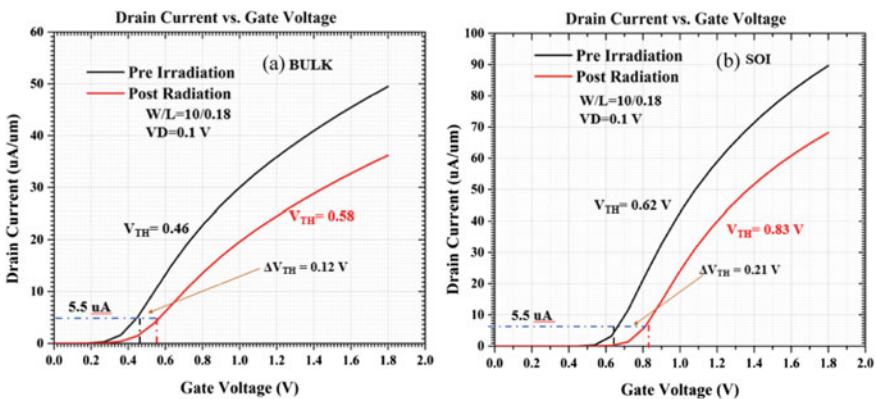
Fig. 4 Drain current verus gate voltage for pre- and post-radiation on **a** bulk **b** SOI 180 nm NMOS
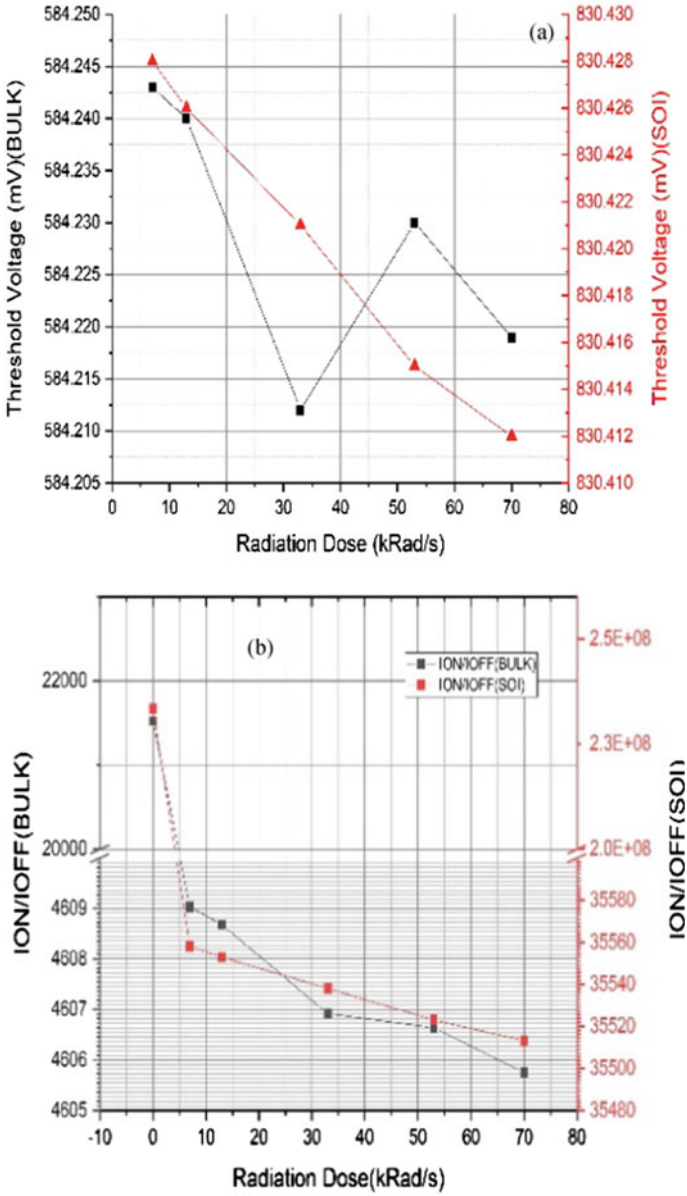
Fig. 5 **a** Threshold voltage shift as a function of radiation dose rate bulk and SOI 180nmNMOS **b** I_{ON}/I_{OFF} as a function of radiation dose rate on Bulk and SOI NMOS

For SOI-based NMOS, also drain current versus gate voltage is plotted in Fig. 4b. Using constant current source pre- and post-radiation threshold voltage is calculated. Pre-radiation threshold voltage is 0.62 V, and the post-radiation threshold voltage is 0.83 V. Shift of 0.21 V is occurred due to the TID effect. Dose rate sensitivity is also measured and observed the same phenomena as the Bulk NMOS technology, decrease in threshold voltage for higher dose rate due to displacement damage effect shows in Fig. 5a. Dose rate sensitivity of $16\,\mu V$ threshold voltage shift is observed for SOI technology, while $35\,\mu V$ threshold voltage shift is observed for Bulk technology.

3.3 On/off Current

More gate control leads to more I_{ON}/I_{OFF}. ON–OFF ratio should be as more as possible for better performance. A higher ratio means lower OFF current or higher ON current. After radiation, severe degradation in the ON/OFF ratio is observed which is a result of leakage current due to radiation leakage current. Figure 5b shows the degradation in ratio due to radiation-induced leakage current in SOI NMOS which is in the order of E-9. Figure 5b also shows the dose-dependent degradation in the Bulk NMOS due to leakage current. As threshold voltage is shifted due to radiation, it is obvious that the ON/OFF ratio has to be shifted.

3.4 Transconductance (Gm)

Transconductance is calculated by using following formula:

$$gm = \Delta I_D / \Delta V_{GS}|_{V_D=\text{constant}} \tag{5}$$

For Bulk MOS transconductance (gm), [31] initially decreases for low radiation dose. Figure 6 shows that gm and radiation dose are having a direct proportion, gm increases with the radiation dose but still, it is below the pre-radiation value. The same function is observed in figure for SOI device is showing more degradation than Bulk for transfer characteristics degradation. Due to trapped charges in buried oxide, the SOI technology is showing more degradation than Bulk technology. The degradation in the Bulk technology is observed due to the gate oxide and interface trapped charges, which form an extra barrier on the surface. g_m is directly related to the threshold voltage shift, and the same behavior is observed in graphs.
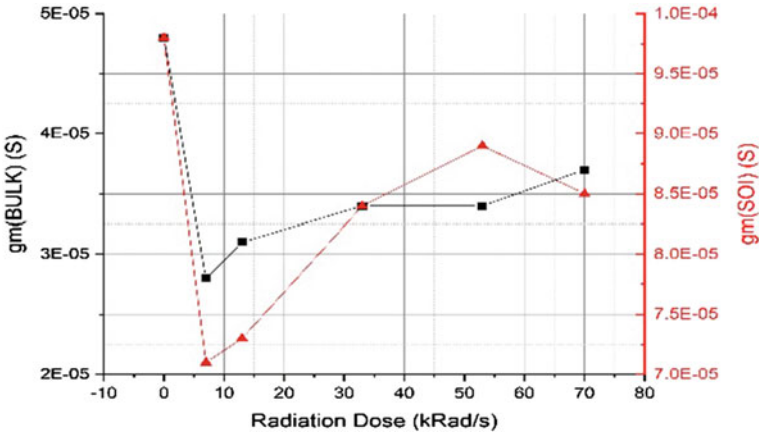
Fig. 6 Transconductance characteristics as a function of the radiation dose of bulk and SOI 180 nm NMOS

3.5 Output Characteristics

As the voltage on the top electrode increases further, electrons are attracted to the surface. In the MOS capacitor, the high density of electrons in the inversion layer is supplied by the electron–hole generation process within the depletion layer. The positive charge on the gate is balanced by the combination of negative charge in the inversion layer plus negative ionic acceptor charge in the depletion layer.

Figure 7a shows the increase in the saturation current due to radiation. The output resistance of the device is also increasing. The shift in the saturation and ohmic region of the characteristics is of the order of 0.04 V which is observable. Figure 7b shows the radiation effect on the output characteristics of the SOI device. For SOI devices, the saturation current decreases due to radiation, while for Bulk it is increasing. The shift in saturation current is 0.03 V which is equal to the Bulk device. SOI device goes into saturation early than Bulk because of buried oxide trapped charge which is not present in Bulk technology. The buried trapped charge provides an extra trapped hole and electrons. Table 2 shows the output resistance for Bulk and SOI technology. The output resistance is the function of the saturation region.

$$R(o/p) = (d(I_D)/d(\text{VD}))^{-1} \tag{6}$$

3.6 Subthreshold Swing

In the MOSFET, the subthreshold swing is limited to (kT/q) ln10 or 60 mV/dec at room temperature.
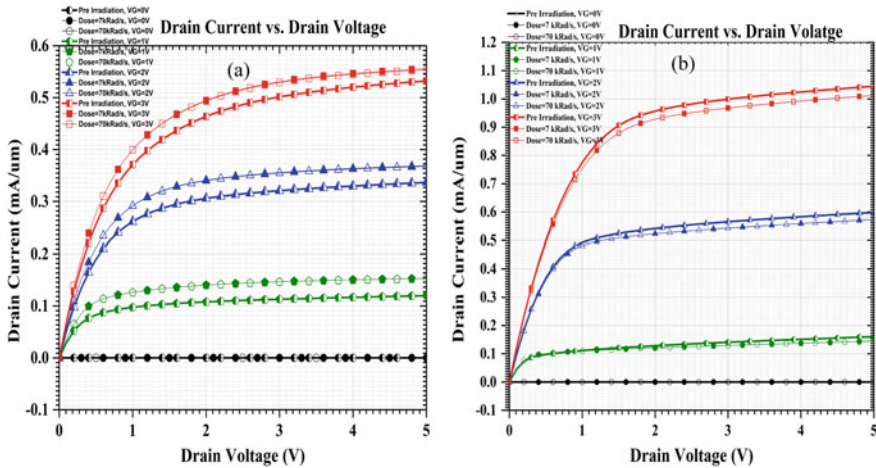
Fig. 7 Output characteristics of **a** bulk **b** SOI 180 nm NMOS

Table 2 Bulk technology output resistance

V_G (V)	d(Id) (Bulk)	R(o/p) (ohm) (Bulk)	d(Id) (SOI)	R(o/p) (ohm) (SOI)
0	1.33 E−09	2.26 E + 08	1.21 E−12	2.48 E + 11
1	3.58 E−06	8.37 E + 04	4.72 E−06	6.36 E + 04
2	1.07 E−05	2.82 E + 04	1.14 E−05	2.64 E + 04
3	2.33 E−05	1.29 E + 04	3.52 E−05	8.53E−03

$$\text{Subthreshold swing} = 1/\text{slope} \qquad (7)$$

where Slope $= d(V_{\text{GS}})/d(\log I_D)$, log I_D is noted for $V_{\text{GS=}}\ V_{\text{TH}}$, and $V_{\text{GS}} = 0$v. Subthreshold swing for Bulk and SOI technology is shown in Table 3, shows that Bulk technology NMOS shows more degradation for the subthreshold region due to large leakage and charge trapped in the silicon layer due to TID effect.

Table 4 shows a comparison of simulated SCL 180 nm NMOS with fabricated 180 nm NMOS. All comparisons were done with 180 nm NMOS only. ΔV_{TH} (V) for simulated and fabricated devices are showing approximately a similar shift. The shift in leakage current (ΔI_L) also showing a similar shift. The comparison shows the simulated device is in line with the fabricated device. When compared with other oxide technology threshold voltage is observed even if the area is decreased.

Table 3 Bulk versus SOI technology I_{ON}, I_{OFF} subthreshold slope(S), and subthreshold swing (mV/dec)

Dose in kRad/s	Bulk		SOI	
	Slope = dVg/dlogId	Swing = 1/slope (mV/dec)	Slope = dVg/dlogId	Swing = 1/slope (mV/dec)
–	8.46 E + 04	1.18 E−05	2.57 E + 05	3.89 E−06
7	1.10 E + 05	9.05 E−06	3.94 E + 05	2.54 E−06
13	1.10 E + 05	9.05 E−06	3.94 E + 05	2.54 E−06
33	1.11 E + 05	9.05 E−06	3.95 E + 05	2.53 E−06
53	1.10 E + 05	9.05 E−06	3.94 E + 05	2.54 E−06
70	1.10 E + 05	9.05 E−06	3.94 E + 05	2.54 E−06

Table 4 Comparison of simulated 180 nm with fabricated 180 nm NMOS

Device	$W/L(\mu m/\mu m)$	V_D (V)	ΔV_{TH} (V)	ΔI_L
180 NMOS transistor [32]	5/0.18	0.05	0.15	–
SCL 180 nm NMOS [33]	10/0.18	0.05	0.1	–
180 nm n-MOSFETs using BSIM3 [34]	10/0.18	0.1	0.1	10^3
180 nm core NMOS [35]	10/0.18	0.05	0.1	10^3
16-nm InGaAs FinFETs with HfO2/Al2O3 dielectrics [36]	1/0.016	50E−3	500E−3	10^2
Gate-length bulk and SOI FinFETs with SiO2/HfO2 gate dielectrics [37]	0.02/0.25	0.05	25E−3	–
SCL 180 nm simulated NMOS (Bulk)	10/0.18	0.1	0.12	10^3
SCL 180 nm simulated NMOS (SOI)	10/0.18	0.1	0.21	10^3

4 Conclusion

From the results, it can be concluded that Bulk technology is more sensitive to radiation than SOI technology. A cumulated comparative study was performed for a deep analysis of the TID effect on MOS devices. Interface trapped charges are the main reason behind the radiation sensitivity of the Bulk device. Buried oxide is working as a negative factor for SOI devices due to the trapping of oxide charge in it. Still, SOI technology is more hardened to radiation than Bulk technology. The Bulk device is showing more leakage current than SOI. The threshold voltage shift for the Bulk device is 0.12 V over 0.21 V of the SOI device. ON–OFF current shows a steady trend over SOI devices. For transconductance, same behavior is observed for both devices. Post-radiation drains current is increasing for the Bulk device while decreasing for SOI device. This work is part of radiation sensor designing for mitigation of space radiation effect on 180 nm devices.

References

1. Attix FH (1986) Introduction to radiological physics and radiation dosimetry. Wiley, New York
2. King MP et al (2017) Analysis of TID process, geometry, and bias condition dependence in 14-nm FinFETs and implications for RF and SRAM performance. IEEE Trans Nucl Sci 64(1):285–292. https://doi.org/10.1109/TNS.2016.2634538
3. Chen RM et al (2017) Effects of total-ionizing-dose Irradiation on SEU- and SET-induced soft errors in bulk 40-nm sequential circuits. IEEE Trans Nucl Sci 64(1):471–476. https://doi.org/10.1109/TNS.2016.2614963
4. Zhang L et al (2017) Single event upset sensitivity of d-flip flop: comparison of PDSOI with bulk Si at 130 nm technology node. IEEE Trans Nucl Sci 64(1):683–688. https://doi.org/10.1109/TNS.2016.2636338
5. Schwank JR et al (2000) Correlation between Co-60 and X-ray radiation-induced charge buildup in silicon-on-insulator buried oxides. IEEE Trans Nucl Sci 47(6):2175–2182
6. Jafari H, Feghhi SAH, Boorboor S (2015) The effect of interface trapped charge on threshold voltage shift estimation for gamma irradiated MOS device. Radiat Meas 73:69–77. https://doi.org/10.1016/j.radmeas.2014.12.008
7. Zhang CX et al (2014) Total-ionizing-dose effects and reliability of carbon nanotube FET devices. Microelectron Reliab 54(11):2355–2359. https://doi.org/10.1016/j.microrel.2014.05.011
8. Liu F et al (2017) Radiation-hardened CMOS negative voltage reference for aerospace application. IEEE Trans Nucl Sci 64(9):2505–2510. https://doi.org/10.1109/TNS.2017.2733738
9. Space Radiation Effects. https://www.xilinx.com/applications/aerospace-and-defense/space/radiation-effects.html. (Accessed 19 Nov 2017)
10. J. Benfica et al Analysis of SRAM-based FPGA SEU sensitivity to combined effects of conducted EMI and TID. In: Radiation and its effects on components and systems (RADECS), 2015 15th European conference on, pp 1–4
11. Zheng Q et al (2017) Total ionizing dose influence on the single-event upset sensitivity of 130-nm PD SOI SRAMs. IEEE Trans Nucl Sci 64(7):1897–1904. https://doi.org/10.1109/TNS.2017.2706287
12. Benfica J et al (2016) Analysis of SRAM-based FPGA SEU sensitivity to combined EMI and TID-imprinted effects. IEEE Trans Nucl Sci 63(2):1294–1300. https://doi.org/10.1109/TNS.2016.2523458
13. Fleetwood DM (2018) Evolution of total ionizing dose effects in MOS devices With Moore's law scaling. IEEE Trans Nucl Sci 65(8):1465–1481. https://doi.org/10.1109/TNS.2017.2786140
14. Ebrahimi M, Miremadi SG, Asadi H, Fazeli M (2013) Low-cost scan-chain-based technique to recover multiple errors in TMR systems. IEEE Trans Very Large Scale Integr (VLSI) Syst 21(8):1454–1468. https://doi.org/10.1109/TVLSI.2012.2213102
15. Ramamurthy C, Chellappa S, Vashishtha V, Gogulamudi A, Clark LT (2015) High performance low power pulse-clocked TMR circuits for soft-error hardness. IEEE Trans Nucl Sci 62(6):3040–3048. https://doi.org/10.1109/TNS.2015.2498919
16. Adell PC et al (2014) Radiation hardening of an SiGe BiCMOS Wilkinson ADC for distributed motor controller application. IEEE Trans Nucl Sci 61(3):1236–1242. https://doi.org/10.1109/TNS.2014.2323975
17. Barnaby HJ (2006) Total-ionizing-dose effects in modern CMOS technologies. IEEE Trans Nucl Sci 53(6):3103–3121. https://doi.org/10.1109/TNS.2006.885952
18. Li L et al (2020) A study on ionization damage effects of anode-short MOS-controlled thyristor. IEEE Trans Nucl Sci 67(9):2062–2072. https://doi.org/10.1109/TNS.2020.3012766
19. Colins K, Li L, Liu Y (2017) Analysis of a statistical relationship between dose and error tallies in semiconductor digital integrated circuits for application to radiation monitoring over a wireless sensor network. IEEE Trans Nucl Sci 64(5):1151–1158. https://doi.org/10.1109/TNS.2017.2687881

20. Goiffon V et al (2017) Radiation hardening of digital color CMOS camera-on-a-chip building blocks for multi-MGy total ionizing dose environments. IEEE Trans Nucl Sci 64(1):45–53. https://doi.org/10.1109/TNS.2016.2636566

21. Ren Z et al (2021) TID response and radiation-enhanced hot-carrier degradation in 65nm nMOSFETs: concerns on the layout dependent effects. IEEE Trans Nuclear Sci, pp 1–1. https://doi.org/10.1109/TNS.2021.3063137

22. Ren Z et al (2020) TID response of bulk Si PMOS FinFETs: bias, fin width, and orientation dependence. IEEE Trans Nucl Sci 67(7):1320–1325. https://doi.org/10.1109/TNS.2020.2979905

23. Witulski AF, Sternberg AL, Rowe JD, Schrimpf RD, Zydel J, Schaf J (2017) Ionizing dose-tolerant enhancement-mode cascode for high-voltage power devices. IEEE Trans Nucl Sci 64(1):382–387. https://doi.org/10.1109/TNS.2016.2636023

24. Faccio F (1999) Radiation effects in the electronics for CMS

25. Stassinopoulos EG, Raymond JP (1988) The space radiation environment for electronics. Proc IEEE 76(11):1423–1442

26. Drs2 0018sl Scl Manual|Mosfet|Spice—Documents. https://usdocument.net/the-philosophy-of-money.html?utm_source=drs2-0018sl-scl-manual-mosfet-spice. (Accessed 29 May 2018)

27. Hofman J, Jaksic A, Sharp R, Vasovic N, Haze J (2017) In-situ measurement of total ionising dose induced changes in threshold voltage and temperature coefficients of RADFETs. IEEE Trans Nucl Sci 64(1):582–586. https://doi.org/10.1109/TNS.2016.2630275

28. Anjum A, Vinayakprasanna NH, Pradeep TM, Pushpa N, Krishna JBM, Prakash APG A comparison of 4MeV proton and Co-60 gamma irradiation induced degradation in the electrical characteristics of N-channel MOSFETs. Nucl Instrum Methods Phys Res Sect B: Beam Interact Mater Atoms 379, no. Supplement C, pp 265–271, Jul. 2016. https://doi.org/10.1016/j.nimb.2016.04.023

29. Cangialosi C et al (2016) On-line characterization of gamma radiation effects on single-ended Raman based distributed fiber optic sensor. IEEE Trans Nucl Sci 63(4):2051–2057. https://doi.org/10.1109/TNS.2016.2528584

30. Gao L, Holbert K, Yu S (2017) Total ionizing dose effects of gamma-ray radiation on NbOx based selector devices for crossbar array memory. IEEE Trans Nuclear Sci, pp 1–1. https://doi.org/10.1109/TNS.2017.2700434.

31. Neamen DA (2003) Semiconductor physics and devices: basic principles, 3rd edn. McGraw-Hill, Boston

32. He B, Wang Z, Sheng J, Huang S (2016) Total ionizing dose radiation effects on NMOS parasitic transistors in advanced bulk CMOS technology devices. J Semicond 37(12):124003. https://doi.org/10.1088/1674-4926/37/12/124003

33. Aditya K et al (2019) Effect of post radiation annealing on the TID response of $0.18\mu m$ bulk NFETs. In: 2019 electron devices technology and manufacturing conference (EDTM), Singapore, Singapore, Mar 2019, pp 336–338. https://doi.org/10.1109/EDTM.2019.8731170

34. Ilik S, Kabaoglu A, Solmaz NS, Yelten MB (2019) Modeling of total ionizing dose degradation on 180-nm n-MOSFETs using BSIM3. IEEE Trans Electron Devices 66(11):4617–4622. https://doi.org/10.1109/TED.2019.2926931

35. Hu Z et al (2011) Comprehensive study on the total dose effects in a 180-nm CMOS technology. IEEE Trans Nucl Sci 58(3):1347–1354. https://doi.org/10.1109/TNS.2011.2132145

36. Bonaldo S et al (2020) Total-ionizing-dose effects and low-frequency noise in 16-nm InGaAs FinFETs with HfO_2/Al_2O_3 dielectrics. IEEE Trans Nucl Sci 67(1):210–220. https://doi.org/10.1109/TNS.2019.2957028

37. Gorchichko M et al (2020) Total-ionizing-dose effects and low-frequency noise in 30-nm gate-length bulk and SOI FinFETs with SiO_2/HfO_2 gate dielectrics. IEEE Trans Nucl Sci 67(1):245–252. https://doi.org/10.1109/TNS.2019.2960815

Communication

Performance Analysis of Corrugated Horn Antenna for Liquid Level Measurement Application

Amit Patel, Alpesh Vala, Keyur Mahant, Pujita Bhatt, Jitendra Chaudhari, and Hiren Mewada

Abstract In this paper, we have proposed the design and performance analysis of corrugated horn antenna for non-contact liquid level measurement applications. The performance of corrugated horn antenna is dependent on corrugation profile, depth and period of corrugations. It gives higher gain, wide bandwidth, low side lobe level and better isolation from cross-polarization component. One of the best merits of the profiled corrugated horn antenna compared to rectangular or circular horn antenna is in compact size. The proposed design is simulated using computer simulation technology (CST)-microwave studio software based on finite integration technique. The simulation results show that it gives very narrow beam width and better isolation value in operating band.

Keywords Corrugated horn antenna · Horizontal and vertical grooves · Mode pattern · Return loss · Gain and radiation pattern

1 Introduction

Nowadays, profiled corrugated horn antennas are mainly used in the field of space, radio detection and ranging (RADAR) (radio altimeter application) and land telecommunications since they are fairly short and low weight with excellent radiation features [1–4]. It also plays a crucial role as feed for reflector antennas [5]. In particular liquid and solid level measurement, plants are mainly used pulsed RADAR or frequency modulated continuous wave RADAR for non-contact measurements. There are several bands allocated for the RADAR frequencies like 5.8 GHz,

A. Patel · A. Vala (✉) · K. Mahant · P. Bhatt · J. Chaudhari
CHARUSAT Space Research and Technology Center, V.T Patel Department of Electronics and Communication, Chandubhai S. Patel Institute of Technology, Charotar University of Science and Technology, Changa, Anand, Nadiad, India
e-mail: Alpeshvala.ec@charusat.ac.in

H. Mewada
Electrical Engineering Department, Prince Mohammad Bin Fahd University, Al Khobar, Saudi Arabia

26.5 GHz, etc. For these types of applications, the performance of antenna plays a crucial role so the selection of antenna is very important. Rectangular or circular horn and dielectric rod antennas are mainly used for these types of applications due to their simple construction and higher gain value. However, at lower frequency the size of antenna becomes more and weight is also large. Moreover, they give low isolation from cross-polar component. So another antenna has been proposed which is based on corrugation. Due to corrugations, it provides high impedance for surface current and creates the electric field value zero on the surface so it reduces the ohmic loss. Another merit of this antenna is giving better cross-polar isolation and higher gain value.

Various corrugated profile horn antennas have been presented [6–8]. The performances of the profiled corrugation horn antenna are totally dependence on the depth and width of corrugations, arrangements of corrugations and smoothness of variations in corrugation depths. A number of different techniques have been proposed for the profiled of corrugated horn antenna like linear and nonlinear profile, gaussian profiled horn antenna (GPHA), etc. Out of them, GPHA gives better performance in terms of gain, side lobe level and isolation from cross-polar component. However, GPHA is longer in length compared to nonlinear corrugated profiled horn antenna. Another design has been proposed based on a choked gaussian horn antenna consisting of separate horizontal and vertical corrugations [6]. It gives mode compact structure than the GPHA while the same performance is maintained.

In this paper, we have proposed the various design techniques and their performance analysis for the corrugated horn antenna at 5.8 GHz is based on separate horizontal and vertical grooves and alternative combinations of horizontal and vertical groove of corrugation. The organization of the paper is as follows: Sect. 1 contains the introductory part. Theory and design of the proposed antenna are described in Sect. 2. The proposed structure is simulated using CST software, and its results are shown in Sect. 3. Comparison and discussion of the different design methodology are shown in Sect. 4 and finally the concluding remarks at the end.

2 Theory

In the design of corrugation horn antenna, the role of corrugated wall, profile of corrugation and the flare angle are principle parameters which control the electromagnetic field flow inside the antenna. Figure 1 shows the basic corrugation wall, in which p, d and w indicate period of corrugation, depth of groove and width of groove. The impedance of the corrugated wall is given as [9]

$$Z = \frac{w}{p} \frac{\tan(k \cdot d)}{1 + \frac{\tan(k \cdot d)}{2ka}} \tag{1}$$

Fig. 1 The proposed design of separate arrangement of horizontal and vertical grooves in horn antenna
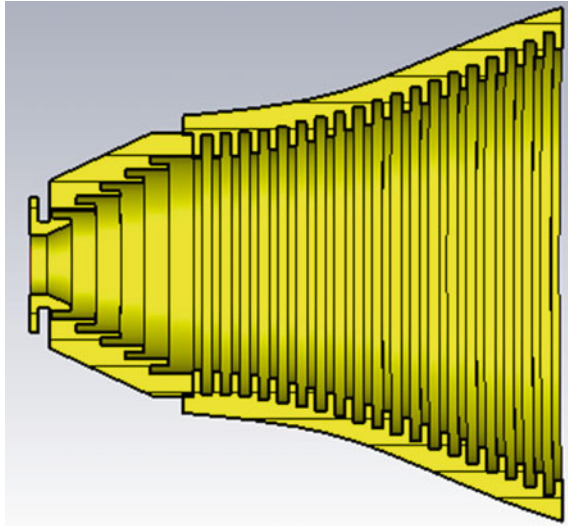
where *a* indicates the radius of circular waveguide and k is the wave number. The ratio $\frac{w}{p}$ indicates that if the width of corrugation is small, it reduces reactance. Therefore, the width of corrugated wall should be kept around 0.3λ to 0.4λ[9]. Moreover, if the depth of corrugation is $\frac{\lambda}{4}$, slots act as short circuit transmission line because of tan(*k.d*) term. As a result, axial current is zero which is generated by azimuthal magnetic field component. Many of the researchers design the corrugated horn antenna based on TE11 to HE11 mode converter, in which corrugation depth varies from $\frac{\lambda}{2}$ to $\frac{\lambda}{4}$ achieving higher gain and better isolation from cross-polar component.

Another important parameter is the selection of corrugation profile. There are two profiles mentioned in literature: (i) linear and (ii) nonlinear. Nonlinear (as specially gaussian) profile of horn antenna has been given by [7]

$$r(z) = a\left[1 + \left(\frac{2.z}{k.w_0^2}\right)^2\right]^{\frac{1}{2}} \tag{2}$$

where *r*(z) is the nonlinear profile, *a* is the waveguide radius, w_0 is the beam waist size, and *k* is the wave number.

3   Design and Simulation Results

As shown in Figs. 1 and 2, we have proposed two corrugation antennas based on the arrangement of corrugation grooves: (i) separate group of horizontal and vertical
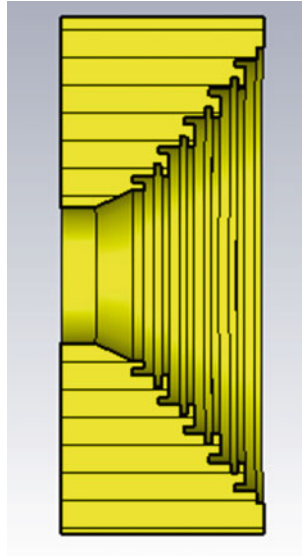
Fig. 2 Corrugated horn antenna (horizontal and vertical grooves are separated)

(SHV) and (ii) alternate position of horizontal and vertical (AHV). The electric field flow inside the proposed design is shown in Fig. 2. Majority of field is concentrated at center axis; various at surface field becomes zero due to high impedance.

As shown in Fig. 3, it is excited by TE_{11} mode and the output mode HE_{11} is generated which is hybrid mode (combination of TE and TM modes) for both the proposed design shown in Fig. 4b and c. Compared to SHV, AHV gives better mode purity as shown in Fig. 4. The return loss for both the proposed design is shown in Fig. 5 that shows both of them give more than 10 dB. The radiation plot for the proposed designs is shown in Fig. 6. It shows that SHV give much higher gain compared to AHV design. Moreover, its beam width is very narrow that is an ideal for liquid level measurement application. However, AHV gives better isolation from cross-polar component compared to SHV design.

4 Comparison and Discussion

We have compared and tabulated in Table 1, the different design methodology of profile corrugated horn antennas in terms of gain, beam width, side lobe level and isolation from cross-polar component. It shows that SHV corrugations give narrow beam width and higher gain compared to AHV. However, AHV corrugated horn antenna gives compact design and better isolation from cross-polar component.
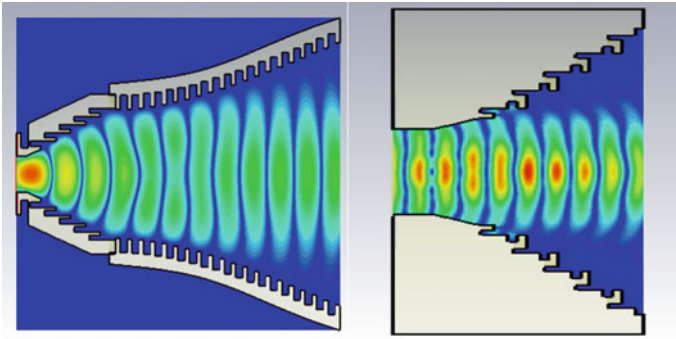
Fig. 3 The electric field flow inside the proposed corrugated horn antennas

(a)   (b)   (c)
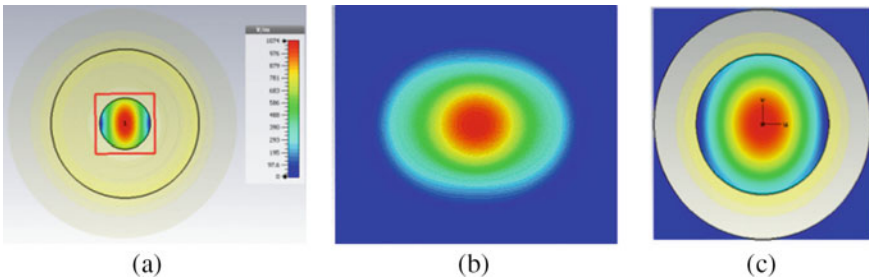
Fig. 4 Mode pattern at **a** input, **b** output SHV and **c** output AHV

Fig. 5 Return loss of various proposed design
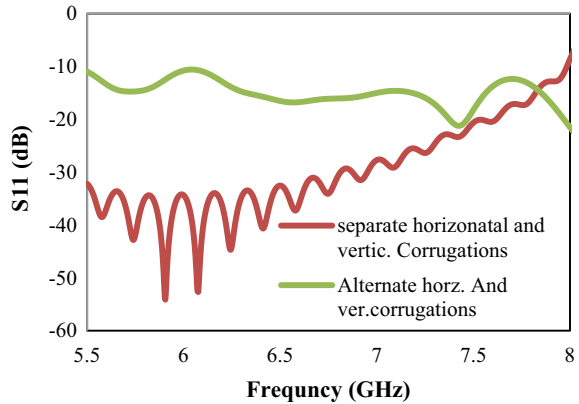
5 Conclusion

In this paper, we have proposed various horn antennas based on corrugation groove arrangement for performance analysis. Placements of grooves inside the horn antenna

Fig. 6 Radiation pattern of
the proposed corrugated horn
antennas
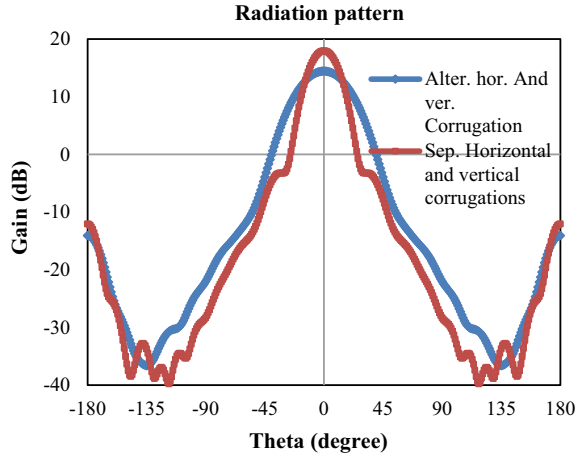
Table 1 Comparison of various proposed horn antenna

Parameter	Standard horn antenna	Sep. horizontal and vertical corrugations	Alt. vertical and horizontal corrugation
Slope of profile (degree)	> 20	25	45
Period and width of corrugation groove (mm)	Not applicable	17 and 10	17 and 10
Overall length (mm)	260	204	150
Return loss (dB) @ 5.8 GHz	18	35	15
Gain (dB)	15	21.6	16
Beamwidth (degree)	28	21.9	26
Side lobe level (dB)	20	40.5	38

improve the performance in terms of higher gain and compact design. Moreover, they
give better isolation from side lobe level and cross-polar component. Mode purity
of this type of antenna is quite good. However, an arrangement of horizontal and
vertical grooves separately gives low cross-polar component isolation and longer
length compared to alternate arrangement of grooves.

References

1. Addamo G, Peverini OA, Tascone R, Virone G, Cecchini P, Orta R (2009) A Ku-K dual-band compact circular corrugated horn for satellite communications. IEEE Antennas Wirel Propag Lett 8:1418–1421
2. Li H, Li J-Y, Wang H-Y, Li T-M, Zhou Y-H (2009) Design of the high efficiency circular horn feed for high-power microwave system. Prog Electromagnet Res C 8:1–12
3. Mallahzadeh AR, Karshenas F (2009) Modified TEM horn antenna for broadband applications. Prog Electromagnet Res 90:105–119
4. Balanis CA (2011) Modern antenna handbook, Wiley, New York, NY, chapter-3
5. Olver AD, Clarricoats PB, Kishk AA, Shafai L (1994) Microwave horns and feeds. IEEE Electromagnetic waves series 39, The Institution of Electrical Engineers
6. Soares P, Pinho P, Gonçalves R (2014) Corrugated horn antenna for CosmoGal satellite with reduced dimensions. In: IEEE international symposium on antennas and propagation USNC-URSI. Memphis, Tennessee, pp 1648–1649
7. Zhang TL, Yan ZH, Fan FF, Li B (2011) Design of a Ku-band compact corrugated horn with high Gaussian beam efficiency. J Electromagnet Waves Appl 25(1):123–129
8. Soares PA, Pinho P, Wuensche CA (2014) High performance corrugated horn antennas for CosmoGal satellite. Procedia Technol 17:667–673
9. Thumm M (1985) Design of short high-power TE_{11}-HE_{11} mode converters in highly overmoded corrugated waveguides. IEEE Trans Microw Theory Tech 39:577–597

Quad-Element with Penta-Band MIMO Antenna for 5G Millimeter-Wave Applications

Amrees Pandey, Jamshed Aslam Ansari, Iqra Masroor, and Piyush Kr. Mishra

Abstract A compact ($32 \times 32 \times 1.6$ mm^3) quad-element with penta-band key-shaped Multiple-Input-Multiple-Output (MIMO) antenna is proposed having a wide bandwidth for targeting Ku, K and Ka band applications and to be used for 5G millimeter-wave applications. Four antenna designs (Ant-1, Ant-2, Ant-3 and Ant-4) are methodically investigated in terms of simulated gain, return loss, radiation efficiency, radiation pattern, envelope correlation coefficient (ECC), diversity gain (DG) and total active reflection coefficient (TARC). The design parameters of Ant-4 have been optimized for desired performance parameters and operation. Simulated isolation < -17 dB, ECC <0.08, DG between 9.979–9.999 (dB), TARC <0 dB and radiation efficiency $> 70\%$ are obtained.

Keywords MIMO · Radiating patch · Radiation efficiency · Diversity gain · Envelope correlation coefficient · TARC

1 Introduction

Recently, Fifth Generation (5G) has acquired a huge attention in wireless communication domain. The rapid increase in mobile phone traffic, demanding a higher data rate and bandwidth, is the reason behind the great interest toward the development of the 5G technology [1]. The execution up to 4G technology has been achieved this far. However, these advancements could not fulfill the demand of modern technology in terms of higher bandwidth and data rate [2]. Huge mobile data traffic is generated from social applications, video streaming, cloud services etc. [3]. Hence, research work on the Fifth Generation (5G) technology has gained momentum. In order to solve these limitations, the Multiple-Input-Multiple-Output (MIMO) technologies having wide bandwidth characteristics are being developed to improve the spectrum efficiency and channel capacity by utilizing the multipath property with no need for increasing the input power [4, 5]. Also, MIMO systems should exhibit high element

A. Pandey (✉) · J. A. Ansari · I. Masroor · P. Kr. Mishra
Department of Electronics and Communication, University of Allahabad, Prayagraj, India
e-mail: amrishpandey19@gmail.com

isolation and broadband so as to contribute toward fulfilling performance [6, 7]. The throughput of the MIMO antenna system is affected by high mutual coupling between the MIMO antenna elements [8, 9]. Therefore, designing a MIMO antenna system with high element isolation is also a major challenge. Centimeter and millimeter-wave spectrum (3–300 GHz) has been mostly targeted by the 5G technology. This can enable to achieve higher bandwidth with up to several Gigabit-per-second (Gbps) data rate up to [10, 11]. MIMO technology is helpful in developing spectral efficiency to manage higher data rates and is capable of increasing the accuracy along with desired range without using additional bandwidth. Services like 4G and 5G applications demand higher data rates [12, 13].

In this paper, we are proposing a quad-element with penta-band key-shaped MIMO antenna by using FR4 as a substrate, bearing a wide bandwidth, operating in the millimeter-wave spectrum, which is suitable for Ku, K and Ka band applications and, specifically, for 5G communications. Key-shaped MIMO antenna is designed and simulated by using electromagnetic simulation tool High Frequency Structure Simulator (HFSS) version 13. HFSS uses mathematical formulations of finite element method (FEM). In Sect. 2, antenna design and evolution of the proposed antenna structure are presented followed by results and discussion in Sect. 3 and conclusion in Sect. 4.

2 Antenna Design and Evolution of the Proposed Antenna Structure

Front (green color) and back (orange color) view of the Ant-1, Ant-2, Ant-3 and Ant-4 (proposed) is shown in Fig. 1, and the proposed antenna (Ant-4) geometry wherein patch side (green color-front view), ground side (orange color-back view) and specifications or dimensions are in millimeter scale (mm) is shown in Fig. 2 [14].

The systematic growth for Ant-1, Ant-2, Ant-3 and Ant-4 (proposed) is presented in Fig. 1.The ground plane (orange color-back view) of all these antennas (Ant-1, Ant-2, Ant-3 and Ant-4) is same.

| Ant-1 | Ant-2 | Ant-3 | Ant-4 (Proposed) |
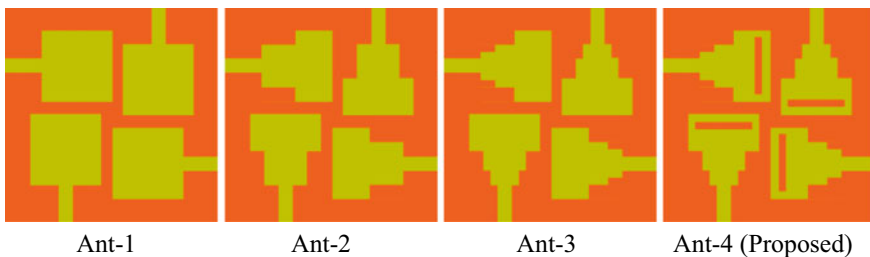
Fig. 1 Step-wise evolution of the Ant-1, Ant-2, Ant-3 and Ant-4 (proposed)

Fig. 2 Front (green color) and back (orange color) view layout of the proposed antenna
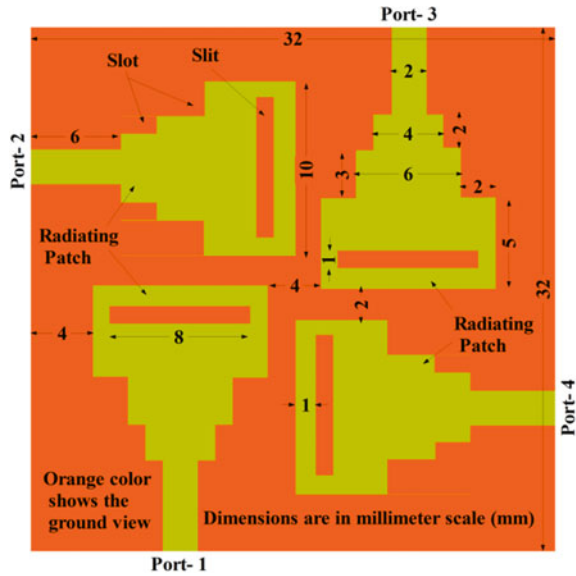
Ant-1 is introduced by four rectangular patches (green color) that are symmetrical with ground (orange color) structure (cf. Figure 1). Ant-2 is obtained from Ant-1, in which two parallel slots of dimension 5×2 mm^2 are cut in the radiating patch and the slots are also symmetrical (cf. Figure 1) [14, 15].

Ant-3 is obtained from Ant-2, in which two more symmetrical parallel slots of dimension 2×1 mm^2 are again cut in the radiating patch (cf. Figure 1). Ant-4 (proposed antenna) is obtained from Ant-3, in which one slit of dimension 8×1 mm^2 is made in the radiating patch (cf. Figs. 1 and 2).

The reason behind etching of slot/slit in radiating patch is to achieve variations in isolation, bandwidth and total antenna gain [15].

FR4 epoxy material is used to design the proposed antenna structure having $\varepsilon = 4.4$ and h = 1.6 mm. The performance parameters of antenna such as return loss, gain, radiation patterns, ECC (envelope correlation coefficient), DG (diversity gain), TARC (total active reflection coefficient) and radiation efficiency are investigated using HFSS version 13 simulation tools [15].

3   Results and Discussion

The proposed design is examined for performance parameters, namely return loss, gain, mutual coupling (isolation), radiation patterns, ECC (envelope correlation coefficient), DG (diversity gain), TARC (total active reflection coefficient) and radiation efficiency.

Table 1 represents the data of Ant-1, Ant-2, Ant-3 and Ant-4 (proposed), respectively, at all ports, i.e., port-1, port-2, port-3 and port-4 for ready reference. Table 1 depicts the operating band frequency and its impedance bandwidth in percentage, frequency of resonance (in GHz) in the concerned band, reflection coefficient (in dB) and peak gain (in dBi) [14].

$|S_{11}|$, $|S_{22}|$, $|S_{33}|$ and $|S_{44}|$ (in dB versus frequency is as shown in Table 1), gain (in dBi) and isolation/mutual coupling (in dB) are illustrated in Figs. 3 and 4, respectively.

A read-through of Table 1 and Figs. 3 and 4 clearly shows that the operating band and gain characteristics of Ant-1, Ant-2, Ant-3 and Ant-4 are identical at all ports (port-1, port-2, port-3 and port-4) with marginal variation. For 5G mm-wave applications, required significant return loss (<-10 dB), operating bandwidth (in Europe 24.25–27.5 GHz, China 24.25–27.25, Japan 27.5–28.28 GHz, Korea 26.5–29.5 GHz, USA 24.25–28.35 GHz and India 24.5–29.5 GHz), gain (>0 dBi) and element isolation (<-15 dB) [7], although variation of the proposed MIMO antenna (Ant-4) in expressions of return loss (<-10 dB), element isolation(<-15 dB), operating bandwidth (mm band of all over country is also being covered, cf. Table 1) and peak gain(>0 dBi) with larger values as compared to Ant-1, Ant-2 and Ant-3. These mentioned parameters of proposed design are making suitable and potential for 5G mm-wave applications.

ECC is a main recital parameter of MIMO systems considered by Eqs. (1), (2), (3) and (4). ECC has been succeeded as 0–0.08 (< 0.08) among the ports 1–2, ports 1–3 and ports 1–4 at the accessible operating band frequencies (cf. Fig. 4d). Diversity gain specifies the transmission power and is calculated by applying Eq. (5); DG has been obtained in the desired range between the ports 1–2, ports 1–3 and ports 1–4 of 9.979–9.999 dB at the presented operating band frequencies (cf. Fig. 4b). Figure 4c depicts the plots of simulated TARC and simulated radiation efficiency as a function of frequency. The radiation efficiency is perceived to be greater than 70% for the preferred operating band. TARC value less than 0 dB is vital for the efficient transmission of MIMO antenna, and it is deliberate using Eq. (6). The TARC is a vital parameters for scheming the bandwidth and the efficiency of the MIMO antennas for the N-element MIMO system. It can be construed as the ratio of the summation of the reflected signal strength square root the power fed to antenna square root. MIMO systems have the b_i and a_i characteristics of the reflected power and the incident power fed to the antenna related as: b = [S]a. Equation (6) can be used to define the rate of TARC for the MIMO system. The isolation value is < -17 dB Fig. 3f for the proposed bandwidth [14].

$$\text{ECC} = \frac{\left|\left|\iint_{4\pi} F1(\theta,\, \emptyset)\, .F_2(\theta,\, \emptyset)\mathrm{d}\Omega])\right|^2\right|}{\iint_{4\pi} |F1(\theta,\, \emptyset)|^2 d\Omega \iint_{4\pi} |F2(\theta,\, \emptyset)|^2 \mathrm{d}\Omega} \tag{1}$$

$$\text{ECC}_{12} = \frac{|S_{11} * S_{12} + S_{21} * S_{22} * S_{13} * S_{32} + S_{41} * S_{42}|^2}{\left(1 - |S_{11}|^2 - |S_{12}|^2\right)\left(|S_{13}|^2 + |S_{14}|^2\right)} \tag{2}$$

Table 1 Port characteristics of the Ant-1, Ant-2, Ant-3 and Ant-4 (proposed)

Antenna	Port No.	Operating band (GHz)/Impedance bandwidth (in %)	Resonant frequency (GHz)/Reflection coefficients (dB)	Peak gain (dBi)	Antenna	Port No.	Operating band (GHz)/Impedance bandwidth (in %)	Resonant frequency (GHz)/Reflection coefficients (dB)	Peak gain (dBi)
Antenna-1	Port-1	13.02–15.23/16.22 18.67–19.88/6.27 21.56–25.45/16.54 26.49–34.82/27.17	13.50/–16.79 14.76/–16.69 19.16/–12.86 22.60/–24.75 27.77/–31.63 30.09/–31.63	–3.08 3.9 –3.1 0.98 –3.2 –3.9	Antenna-2	Port-1	18.17–19.43/6.70 22.39–28.03/22.37 31.64–33.38/5.35	18.76/–12.46 23.46/–37.13 26.86/–19.36 32.66/–12.55	1.52 2.79 –11.63 1.95
	Port-2	13.02–15.19/15.38 18.59–19.87/6.65 21.76–33.46/42.37	13.46/–21.61 14.46/–19.54 19.11/–14.23 23.46/–26.81 27.86/–22.88 30.86/–14.24	–3.89 1.74 –3.2 –2.7 –3.38 –1.8		Port-2	18.09–19.51/7.5 22.39–28.09/22.58	18.66/–13.70 23.46/–30.05 27.30/–16.70 32.66/–16.44	1.51 2.79 –7.77 1.95
	Port-3	13.02–15.19/15.38 18.87–19.95/5.5 21.84–32.18/38.28	13.56/–17.68 14.66/–16.11 19.56/–11.59 23.46/–23.96 27.86/–23.96 30.86/–14.04	–3.88 1.74 –0.64 –2.74 –3.39 –1.82		Port-3	18.13–19.44/6.97 22.39–27.82/21.62 31.05–34.40/10.23	18.76/–12.28 23.56/–31.29 26.56/–19.62 32.16/–13.34	1.52 2.81 –2.03 2.03
	Port-4	13.02–15.19/15.38 18.75–19.71/5 21.64–25.49/16.34 26.25–30.78/15.88	13.50/–19.84 14.36/–17.09 19.16/–11.29 23/–28.38 27.86/–18.66	–3.08 1.70 –3.2 –1.98 –3.35		Port-4	18.21–19.43/9.45 22.31–27.95/22.44 29.81–33.10/10.46	18.66/–12.37 23.46/–32.26 26.86/–17.59 32.16/–12.90	1.45 2.79 –11.63 2.03

(continued)

Table 1 (continued)

Antenna	Port No.	Operating band (GHz)/Impedance bandwidth (in %)	Resonant frequency (GHz)/Reflection coefficients (dB)	Peak gain (dBi)
Antenna-3	Port-1	14.38–15.43/7.04 16.79–18.79/11.24 19.03–23.44/20.76 25.21–27.97/10.37 29.93–33.38/10.91	14.86/−26.12 17.36/−21.86 20.46/−14.83 22.66/−24.95 26.56/−22.49 32.56/−17.68	2.83 −1.15 1.70 0.38 2.61 −6.38
	Port-2	14.34–15.31/6.54 16.83–18.75/10.79 21.64–23.44/7.98 25.57–27.97/8.96 31.34–33.62/7.01	14.86/−24.95 17.46/−18.86 22.66/−25.63 26.46/−22.69 33.02/−14.34	2.83 −1.15 0.38 2.61 −7.75
	Port-3	14.38–15.43/7.04 16.87–18.43/8.83 21.76–23.44/7.43 25.45–27.93/9.29 31.58–33.66/6.37	14.76/−28.78 17.36/−18.27 22.66/−25.44 26.46/−20.43 32.96/−15.22	2.79 −1.15 0.38 2.61 −6.38
	Port-4	14.34–15.35/6.80 16.75–18.39/9.33 19.63–23.44/17.69 25.73–27.97/8.34 31.82–33.70/5.73	14.86/−26.12 17.46/−22 20.46/−13.45 22.56/−27.40 26.86/−21.02 30.06/−13.65	2.83 −1.15 1.70 0.38 2.92 −0.31
Antenna-4 (proposed)	Port-1	14.34–15.23/6.02 16.87–18.43/8.83 19.79–23.48/17.05 25.45–27.89/9.14 31.86–34.14/6.90	14.86/−21.51 17.46/−21.11 20.46/−12.47 22.66/−20.82 26.56/−28.29 33.02/−23.67	1.98 5.25 1.61 1.53 4.39 4.2
	Port-2	14.34–15.39/3.53 16.79–18.75/11.02 18.87–23.44/21.60 25.33–27.81/9.33 31.70–33.58/5.75	14.76/−21.11 17.46/−34.28 22.66/−26.52 26.56/−23.28 32.56/−16.0.60	1.58 5.25 1.53 4.39 4.77
	Port-3	14.18–15.27/7.40 16.75–18.55/10.19 19.47–23.32/18 25.53–28.21/9.97 31.42–33.94/7.71	14.86/−16.50 17.36/−25.44 20.46/−14.44 22.66/−20.53 26.76/−23.47 32.66/−21.11	1.98 5.25 1.61 1.53 4.43 4.77
	Port-4	14.30–15.31/6.82 16.83–18.59/9.93 19.19–23.44/19.94 25.37–27.89/9.46 31.02–33.82/8.63	14.86/−20.92 17.46/−19.94 20.46/−13.85 22.60/−20.62 26.56/−23.67 32.86/−18.17	1.98 5.25 1.61 1.55 4.39 4.77

Fig. 3 **a** |S$_{11}$|, **b** |S$_{22}$|, **c** |S$_{33}$|, **d** |S$_{44}$|, **e** gain versus frequency of Ant-1, Ant-2, Ant-3 and Ant-4 and **f** mutual coupling (between the port) of the proposed antenna (Ant-4)
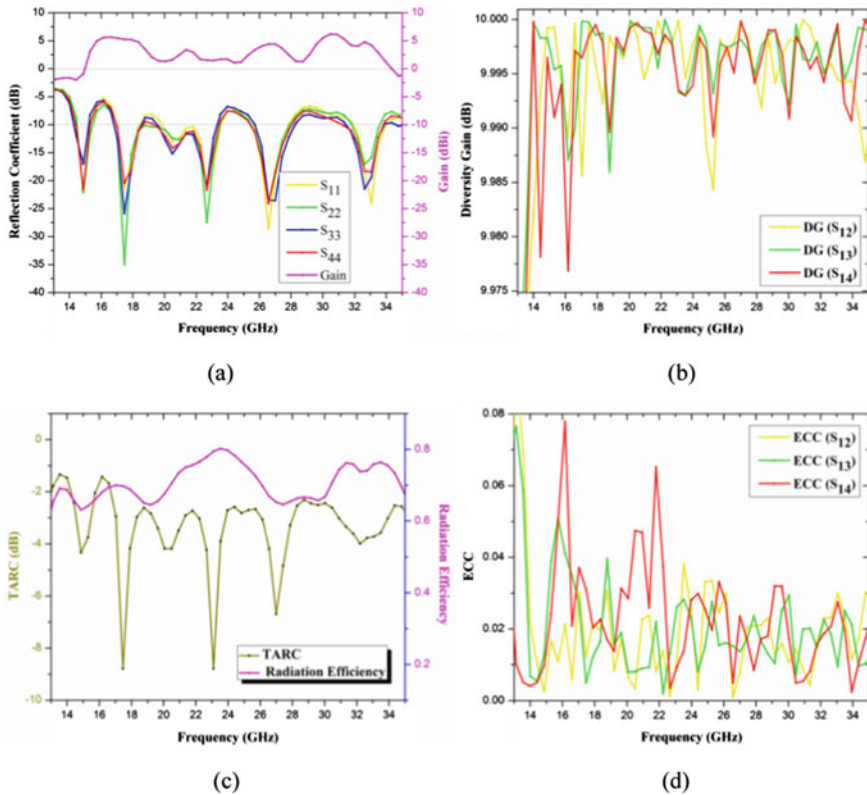
Fig. 4 Simulated **a** $S_{11}|$, $S_{22}|$, $S_{33}|$, $S_{44}|$ and gain, **b** DG, **c** TARC and radiation efficiency and **d** ECC versus frequency plot of the Ant-4 (proposed)

$$\text{ECC}_{13} = \frac{|S_{11} * S_{13} + S_{12} * S_{23} * S_{13} * S_{33} + S_{14} * S_{43}|^2}{\left(1 - |S_{11}|^2 - |S_{12}|^2\right)\left(|S_{13}|^2 + |S_{14}|^2\right)} \tag{3}$$

$$\text{ECC}_{14} = \frac{|S_{11} * S_{14} + S_{24} * S_{13} * S_{34} + S_{14} * S_{44}|^2}{\left(1 - |S_{11}|^2 - |S_{12}|^2\right)\left(|S_{13}|^2 + |S_{14}|^2\right)} \tag{4}$$

$$\text{Diversity Gain} = 10 \times \sqrt{1 - \text{ECC}^2} \tag{5}$$

$$\Gamma_a^t = \frac{\sqrt{\sum_{i=1}^{N} |b_i|}^2}{\sqrt{\sum_{i=1}^{N} |a_i|^2}} \tag{6}$$

The simulated E- and H-plane far-field radiation patterns of the proposed antenna are as presented in Fig. 5a, b, c, d, e and f at 14.86 GHz, 17.46 GHz, 20.46 GHz, 22.66 GHz, 26.56, and 33.02 GHz, respectively, at port-1. The proposed antenna for all resonating frequencies shows omnidirectional broad radiation pattern characteristics.

4 Conclusion

In this paper, a quad-element with penta-band key-shaped MIMO antenna is demonstrated which can be utilized for Ku, K and Ka band applications and in particular for 5G millimeter-wave applications. The operating band of the proposed antenna covers from 13 to 34 GHz and provides a maximum impedance bandwidth (17.05% at port-1, 21.60% at port-2, 18% at port-3 and 19.94% at port-4) and maximum peak gain (5.25 dBi at port-1, port-2, port-3 and port-4). In proposed antenna, ECC obtained between ports 1–2, ports 1–3 and ports 1–4 is < 0.08, diversity gain is between 9.979–9.999 (dB), TARC < 0 dB, isolation is < −17 dB, and radiation efficiency is observed to be above 70% of the desired millimeter-wave frequencies. The proposed MIMO antenna operates efficiently with a significant return loss, high gain and high element isolation, which make it a potential for 5G mm-wave applications. The foremost advantage of MIMO systems is advanced rate and advanced reliability without the necessity of additional power and bandwidth.
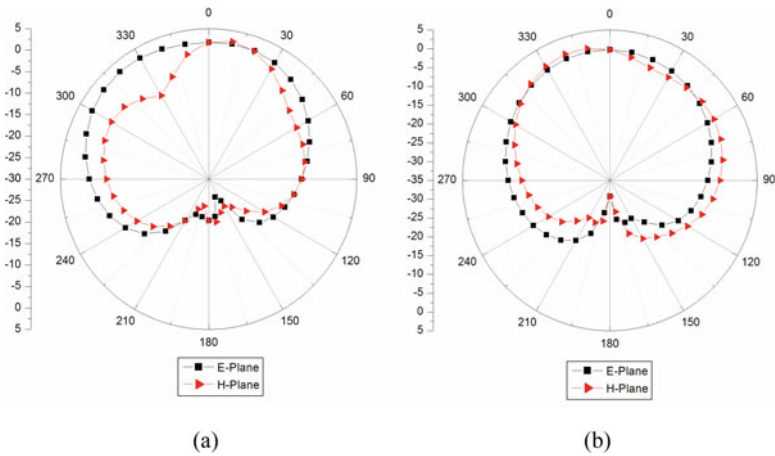
Fig. 5 Radiation pattern in E- and H-plane at port-1 for **a** 14.86 GHz, **b** 17.46 GHz, **c** 20.46 GHz, **d** 22.66 GHz, **e** 26.56 GHz and **f** 33.02 GHz
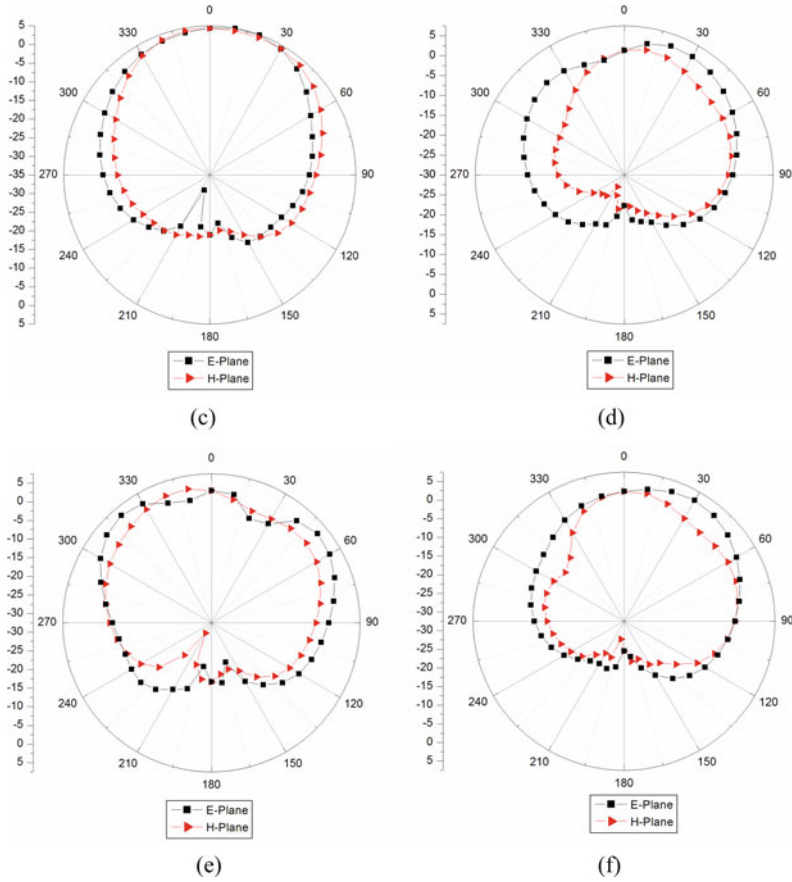
Fig. 5 (continued)

References

1. Haroon MS, Muhammad F, Abbas G, Abbas ZH, Kamal A, Waqas M, Kim S (2020) Interference management in ultra-dense 5g networks with excessive drone usage. IEEE Access 2020, pp 1–10
2. Khan J, Sehrai DA, Ali U (2019) Design of dual band 5G antenna array with SAR analysis for future mobile handsets. J Electr Eng Technol 14:809–816
3. Pervez MM, Abbas ZH, Muhammad F, Jiao L (2017) Location-based coverage and capacity analysis of a two tier HetNet. IET Commun 11:1067–1073
4. Abdullah M, Kiani SH, Iqbal A (2019) Eight element multiple-input multiple-output (MIMO) antenna for 5G mobile applications. IEEE Access 7:134488–134495
5. Yuan X, He W, Hong K, Han C, Chen Z, Yuan T (2020) Ultra-wideband MIMO antenna system with high element-isolation for 5G smartphone application. IEEE Access 8:56281–56289
6. Altaf A, Alsunaidi MA, Arvas E A novel EBG structure to improve isolation in MIMO antenna. In: Proceedings of the IEEE USNC-URSI radio science meeting (joint with AP-S symposium), San Diego, CA, USA, 9–14 July 2017; pp 105–106

7. Wang F, Duan Z, Wang X, Zhou Q, Gong Y (2019) High isolation millimeter-wave wideband MIMO antenna for 5G communication. Int J Antennas Propag 2019:4283010
8. Abdullah M, Kiani SH, Abdulrazak LF, Iqbal A, Bashir MA, Khan S, Kim S (2019) High-performance multiple-input multiple-output antenna system for 5G mobile terminals. Electronics 8:1090
9. Haroon MS, Abbas ZH, Abbas G, Muhammad F (2020) SIR analysis for non-uniform HetNets with Joint decoupled association and interference management. Comput Commun 155:48–57
10. Haroon MS, Abbas ZH, Muhammad F, Abbas G (2019) Coverage analysis of cell edge users in heterogeneous wireless networks using stienen's model and RFA scheme. Int J Commun Syst 33:e4147
11. Sharaf MH, Zaki AI, Hamad RK, Omar MMM (2015) A novel dual-band (38/60 GHz) patch antenna for 5G mobile handsets. Sensors 20:2541
12. Ullah S, Yeo WH, Kim H (2020) Development of 60-GHz millimeter wave, electromagnetic band-gap ground planes for multiple-input multiple-output antenna applications. Sci Rep 10:8541–8553
13. Kumar S, Lee GH, Kim DH, Mohyuddin W, Choi HC, Kim KW (2020) A compact four-port UWB MIMO antenna with connected ground and wide axial ratio bandwidth. Int J Microw Wirel Technol 20(19):1–11
14. Pandey A, Singh AK, Yadav V, Singh S, Singh R (2021) An ultra-wideband (UWB) MIMO Antenna for 5G Applications. In: 6th international conference on communication and electronics systems, pp 420–425
15. Pandey A, Ansari JA, Masroor I, Mishra PK (2021) Microstrip line-fed based quad-port wideband MIMO antenna for K band application. ICTACT J Commun Technol, December 2021, 12, 04, pp 2229–6948
16. Sun L, Li Y, Zhang Z, Feng Z (2020) Wideband 5G MIMO antenna with integrated orthogonal-mode dual-antenna pairs for metal-rimmed smartphones. IEEE Trans Antennas Propag 68:2494–2503
17. Singh AK, Pandey A, Singh S, Yadav V and Singh R (2021) quad-port circularly polarized MIMO antenna for K band applications. In: 6th international conference on communication and electronics systems, pp. 405–410

Quad Band Planar Monopole Antenna with Polarization Diversity for FSS and SAR Application

Reshmi Dhara

Abstract Here, a simple, planar monopole antenna with polarization diversity for quad band application using a single feed mechanism has been reported. The design antenna which is proposed here involves two L-shaped radiators with two asymmetric cross slots within it creating mutual coupling to attain dual circularly polarized (CP) bands. To generate quad impedance bandwidth (IBW), defective ground plane is utilized on the bottom portion on the substrate. The antenna which is proposed covered the quad simulated IBs that are from 3.631–4.167 GHz (535.6 MHz, f_{rc1} = 3.9 GHz, 13.73%), 6.542–8.494 GHz (1951.8 MHz, f_{rc2} = 7.52 GHz, 25.96%), 8.859–10.253 GHz (1134.3 MHz, f_{rc3} = 9.56 GHz, 14.59%) and 10.8494–beyond 15 GHz (4150.6 MHz, f_{rc4} = 12.92 GHz, 32.19%), respectively. The simulated dual ARBWs span over 3.865–4.069 GHz (203.7 MHz, f_{cp1} = 3.97 GHz, 5.14%) within 1st IB and 8.888–9.785 GHz (897.3 MHz, f_{cp2} = 9.34 GHz, 9.6%) within 3rd IB. The simulated peak gain between 2.2 and 6.01dBi span throughout IBW region makes the dual CP bands appropriate for some part of S- and X-band, particularly fixed-satellite service (FSS) and synthetic aperture radar (SAR) applications.

Keywords Quad band · Polarization diversity · Axial ratio bandwidth · Impedance bandwidth · FSS · SAR

1 Introduction

Recently, multiband antennas with polarization diversity have satisfied multiple necessities of many devices in wireless communication systems. In personal global position system (GPS) appliances and mobile, antennas through omnidirectional radiation are particularly suitable. On the other hand, several communication devices,

R. Dhara (✉)

Department of Electronics and Communication Engineering, National Institute of Technology Sikkim, South Sikkim, Gangtok, Ravangla PIN 737 139, India
e-mail: reshmidhara@nitsikkim.ac.in

different satellite communication systems, and antennas having unidirectional radiation patterns are growing by means of an integral technology. To generate vertically/horizontally omnidirectional dual-polarized radiation, it is needed to superimpose two radiation from a monopole antenna which is vertically polarized and a loop antenna which is horizontally polarized. Now in communication system where the astronomical research is the main attention, several uses communication devices are essential as a substitute to single communication typical device. As a consequence of the striking characteristics like lower footprint, simpler geometry, and lighter in weight, planar monopole antennas help as an utmost suitable practice. This is known to all that a conventional monopole antenna in longitudinal direction creates linearly polarized (LP) wave. But the foremost drawbacks of linear polarized wave expected at dual-band process are lower sensitivity and multipath fading towards the positioning between the antenna which are transmitting and receiving, lower mobility, and like that [1–3]. This might be overwhelmed to a great scope for antennas which consume the circular polarization. Henceforth, dual-band antennas by means of two different frequency bands instantaneously functioning dual circular polarization (left-hand circular polarization (LHCP) and right-hand circular polarization (RHCP)) are significantly widespread compared to dual-band antennas with two quadrature (vertically/horizontally) linear polarizations. The requirement of multiple antennas decreases due to using a multiband antenna by means of dual-polarization features. The CP antenna is very attractive for many wireless systems as no strict alignment is required among antenna which is transmitting and receiving and encountering interference. To fulfil these necessities of multiband antenna presentation together with linear and circular polarization, various methodologies have been used by many researchers [4–8].

Inspired by the aforementioned whole thing, a simple quad band monopole antenna with LHCP in 1st band, LP in 2nd, LHCP in 3rd, and LP in 4th bands is proposed in this paper. The proposed design can support 3.631–4.167 GHz, 6.542–8.494 GHz, 8.859–10.253 GHz, and 10.8494 beyond 15 GHz. To design a quad antenna, it has been appropriately improved in method so that it can sustain together with linear and circular polarizations.

An actual good reflection coefficient, widespread ARBW and dependable radiation features are gained for the implemented antenna. It became apparent that the implemented antenna is simple and makes available for wider LP and CP frequency bands.

This paper is represented like Sect. 2: Design Procedure of Antenna; Sect. 3: Simulation Justifications and Discussions; and lastly Sect. 4: Conclusion.

2 Design Procedure of Antenna

An antenna with Quad band with polarization diversity can gratify the several purposes for changed device; they are generally used in wireless communication systems [9].

The designed antenna simulated structures are depicted in Fig. 1a and b. The size of the microstrip antenna is $70 \times 60 mm^2$ (70×60 mm^2, i.e. $1.378 \times 1.181 \lambda_g^2$, λ_g = guided wavelength at 3.6 GHz). Commonly available, low-cost workable FR4-epoxy substrate thickness of 1.6 mm, having effective permittivity $\varepsilon r = 4.4$ and $tan\delta = 0.02$ (loss tangent), is utilized to simulate the implemented antenna. Comprehensive optimal dimensions are recorded in Table 1.

The progress steps of the implemented antenna are represented in Fig. 2. Figure 3a and b demonstrates the reflection coefficient and axial ratio bandwidth progress plots of the designed antenna. First, Antenna.1 is designed at a resonating frequency 3.6 GHz using a rectangular radiator and a ground plane rectangular in size on the reverse side of the substrate for FSS application. Here, a centre feed microstrip line is utilized to feed the antenna. But the IBW is very poor at this frequency and also got a CP in the higher frequency region (12.8 GHz). To progress the IBW and to satisfy the multiband characteristics by using the same dimension of the antenna, it is needed to create additional current paths. For that reason, two L-shaped radiators are used by modifying the rectangular-shaped radiator. The gap between two radiators creates a

(a) Top View   (b) Bottom View
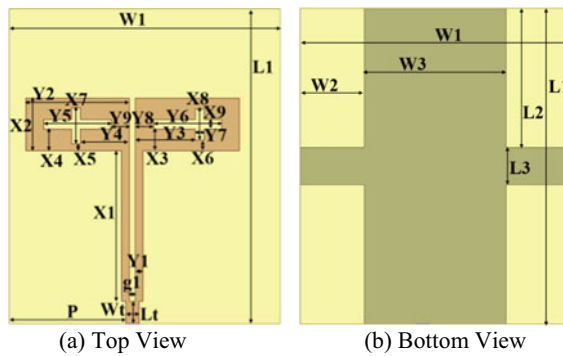
Fig. 1 Dimension of proposed antenna

Table 1 Proposed antenna optimal dimension

Parameter	Value (mm)	Parameter	Value (mm)	Parameter	Value (mm)
L1	70	L2	30.9	L3	8.2
W1	60	W2	14.3	W3	31.4
Lt	5	Wt	3	g1	1.4
X1	33.5	X2	11.7	X3	4.8
X4	4.8	X5	1.7	X6	2.0
X7	7.8	X8	7.0	X9	2.1
Y1	1.7	Y2	23	Y3	13.2
Y4	10.8	Y5 = Y6	15	Y7	2.0
Y8 = Y9	4	P	25.8	h	1.6

coupling effect due to generation of capacitance between them. This gap creates additional current path that increases IBW in addition to improve ARBW performance compared to earlier stage. To improve ARBW performance more, also an asymmetric feed [8] is used in this step. Better impedance matching network can be performed by this feeding structure. Here, using defective ground plane improves the IBW performance of the implemented antenna [9]. But this Antenna.2 generates only a small CP (13.8 GHz) band. In the next stage to improve ARBW more <3dB, two slots asymmetric in size [10–12] are edged from two L-shaped radiator gives Antenna.3. These two slots generate two CP bands resonating at frequency 3.97 GHz and 9.34 GHz, respectively. These asymmetric slots [10, 11] create two orthogonal electric fields with equal amplitude at these two-resonating frequencies. This Antenna.3 helps to achieve quad impedance band resonating at 3.9 GHz, 7.52 GHz, 9.56 GHz, and >12.92 GHz, respectively. Since it satisfied our purpose, it definite to select finalized this design and analysed its performance.
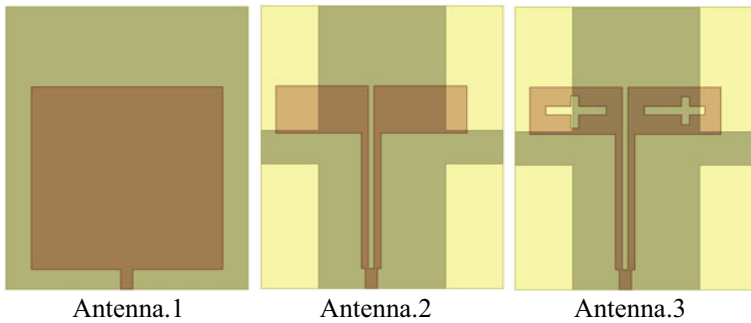
Fig. 2   Improvement of implemented antenna
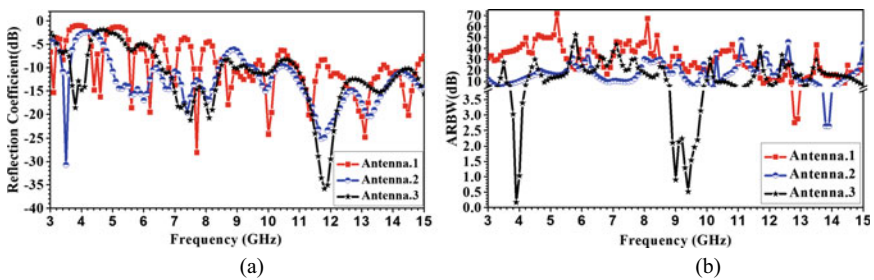
Fig. 3   Evaluation of **a** reflection coefficient (dB) and **b** ARBW (dB) for antennas. 1–3

3 Simulation Justifications and Discussions

To design the antenna, use Ansys Electronics Desktop 2020 R1 simulation software. The designed antenna enclosed the quad simulated IBW ranged from 3.631–4.167 GHz (535.6 MHz, f_{rc1} = 3.9 GHz, 13.73%), 6.542–8.494 GHz (1951.8 MHz, f_{rc2} = 7.52 GHz, 25.96%), 8.859–10.253 GHz (1134.3 MHz, f_{rc3} = 9.56 GHz, 14.59%), and 10.8494–beyond 15 GHz (4150.6 MHz, f_{rc4} = 12.92 GHz, 32.19%) is depicted in Fig. 4a.

Figure 4b also depicts the simulated ARBW of the implemented antenna. The simulated dual ARBWs span over 3.865–4.069 GHz (203.7 MHz, f_{cp1} = 3.97 GHz, 5.14%) within 1st IB and 8.888–9.785 GHz (897.3 MHz, f_{cp2} = 9.34 GHz, 9.6%) within 3rd IB.

Figure 4b, simulated input impedance, is depicting at 50Ω microstrip feed line for the real (resistance) and imaginary (reactance) parts. Within the matching of IBs is fine because the resistance part of the impedance is closer to 50Ω, and the reactance part is closer to 0Ω.

From Fig. 4c, using Smith chart, one can see that on resonance frequency 3.7, 3.9, 7.5, 9.6, 12.92, and 15.0 GHz the normalized impedance (Z11) values are close to 1, whereas the complex reflection coefficient magnitude (Γ) values are also very small. So above values depict that best matching can occur on resonance frequencies because real part of Z11 approaches to 50Ω and imaginary part tends to 0Ω. Also,

Name	Freq	Ang	Mag	RX	Q	VSWR
m1	3.70	69.96	0.20	1.06 + 0.42i	0.40	1.51
m2	3.90	100.84	0.23	0.83 + 0.39i	0.47	1.59
m3	7.50	15.32	0.09	1.18 + 0.05i	0.05	1.19
m4	9.60	-88.42	0.28	0.87 − 0.53i	0.61	1.78
m5	12.92	-173.53	0.23	0.62 − 0.03i	0.06	1.61
m6	15.00	-18.90	0.17	1.36 − 0.15i	0.11	1.40
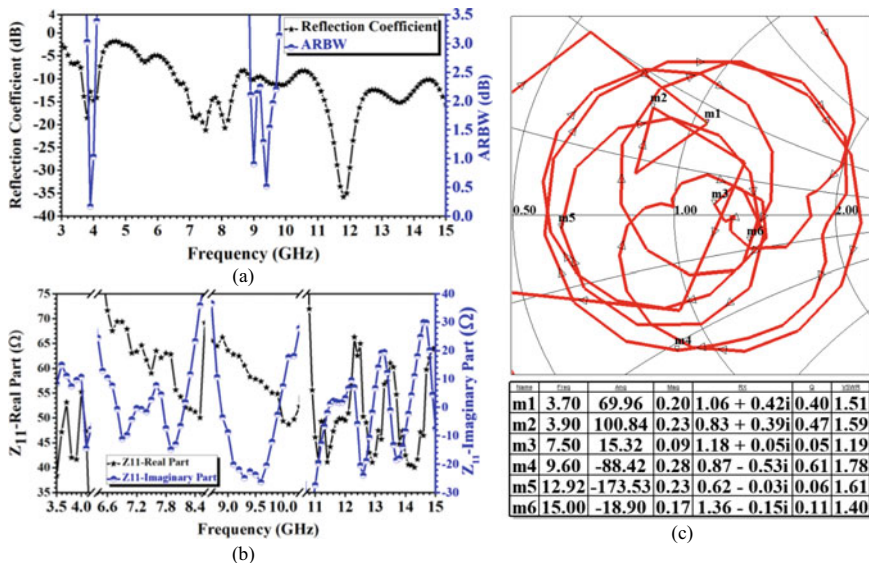
Fig. 4 **a** Simulated reflection coefficient and ARBW curves comparisons, **b** simulated impedance (real and imaginary) vs. frequency curves, **c** results of the effect of complex reflection coefficient (Γ), normalized input impedance (Z11), Q-factor, and VSWR using Smith chart for the implemented antenna
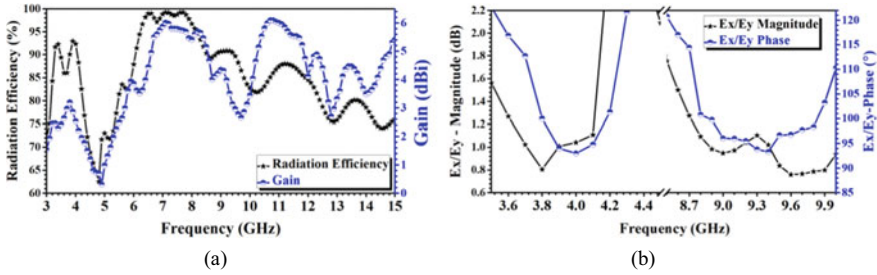
Fig. 5 Proposed antenna **a** radiation efficiency and gain, **b** E_X/E_Y—magnitude and E_X/E_Y—phase plot versus frequency

VSWR value on those frequencies is also <2. The Q-value on those lower resonating frequencies in addition to higher resonating frequencies is also very small. That signifies widest IBW can occur due to small Q-factor. From this Smith chart, it is also clear that the graph rotates four times nearly equal to kick point (SWR = 1) which proves quad impedance bands are generated by using the same structure.

Figure 5a represents the radiation efficiency curve. The ranges of radiation efficiencies are between 74 and 99% for the quad IBs. The maximum efficiency is 99.17% at 7.1 GHz. Figure 5a also depicts the peak gains respecting frequency. The gain is within 2.20–6.01 dBi for quad IBs, and the peak gain is maximum 6.01 dBi at 7.1 GHz.

Figure 5b depicts the Ex/Ey magnitude is closely equal to 1 or 0 dB within the dual CP bands, and the difference of phase among them is also nearly 90°. That demonstrates that the dual bands gratify CP conditions [13].

Well-defined LHCP and RHCP are detected in Fig. 6a, c and b, d which illustrate at f_{cp1} = 3.97 GHz and f_{cp2} = 9.34 GHz resonating frequencies, the radiation patterns for φ = 0° (XZ) and φ = 90° (YZ) plane. At broadside direction on two CP resonating frequencies, the radiations observed are LHCP, whereas the polarization (co and cross) difference is 32.47 dBi and 22.57 dBi, correspondingly. Because of the asymmetric inset feeding radiator, the distribution of current is productive, due to that reason radiation is somewhat slanting from its broadside direction.

To understanding the generation of the dual CP modes at 3.97 and 9.34 GHz, a general studies are depicted in Figs. 7a and b. The normalized currents distribution from the below figures is observed that at four separate time moments (wherever T is the total time period for one cycle), dual CP modes could be accomplished at f_{cp1} = 3.97 GHz and f_{cp2} = 9.34 GHz which are LHCP.

The simulated axial ratio beam width at f_{cp1} = 3.97 and f_{cp2} = 9.34 GHz is plotted versus θ° in Fig. 8a and b. The simulated results at f_{cp1} the implemented antenna has a 3 dB axial ratio beam width with respect to vertical θ angle of about 17° at XZ (φ = 0°) plane and 89° at YZ (φ = 90°) plane. So, at broadside direction, the difference between co- and cross-plane for simulated 3 dB AR beam width is 72° at f_{cp1} = 3.97 GHz. Similarly, at f_{cp2}, the implemented antenna has a 3 dB axial ratio beam width over vertical θ angle of around 5° at XZ (φ = 0°) plane also 35° at YZ (φ =

Frequency= 3.97 GHz   Frequency= 9.34 GHz

(a) XZ plane   (b) YZ plane   (c) XZ plane   (d) YZ plane
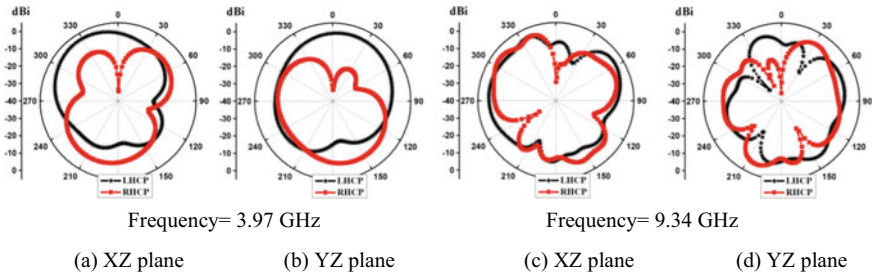
Fig. 6 Radiation patterns for (LHCP and RHCP) in the **a**, **c** XZ ($\varphi = 0°$) and **b**, **d** YZ ($\varphi = 90°$) planes

(a) t=0   t=T/4   t=3T/4   t=T f_{cp1}=3.97 GHz

(b) t=0   t=T/4   t=3T/4   t=T f_{cp2}=9.34 GHz
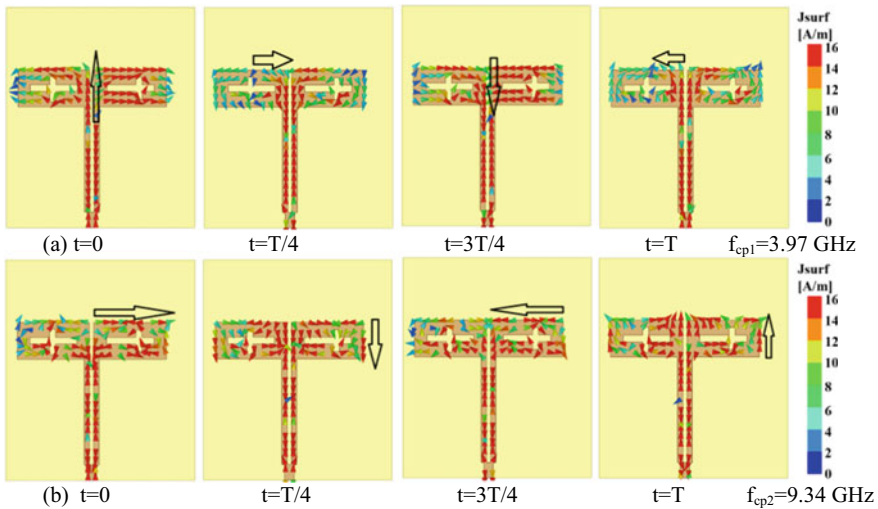
Fig. 7 Simulated current distribution at $f_{cp1} = 3.97$ and at $f_{cp2} = 9.34$ GHz

90°) plane. So, at broadside direction, the difference between co- and cross-plane for simulated 3 dB AR beam width is 30° at $f_{cp2} = 9.34$ GHz (Table 2).

4   Conclusion

A quad band antenna with polarization diversity characteristics bandwidth showing LHCP in 1st IB, LP in 2nd IB, LHCP in 3rd IB, and LP in 4th IB is comprehended by employing changes in ground plane and asymmetric feeding system of two L-shaped planar monopole antenna with two asymmetric cross-shaped slots. The proposed antenna (size 70×60 mm^2, i.e. 1.378×1.181 λ_g^2, λ_g = guided wavelength at 3.6 GHz) gives quad IBWs are 13.97, 25.96, 14.59, and 32.19% resonating at 3.9,
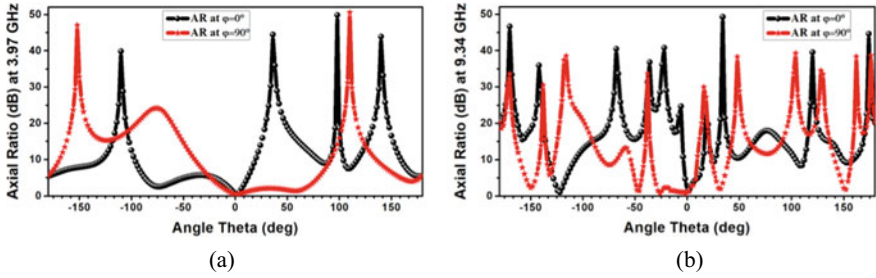
Fig. 8 Axial ratio beam width versus $\theta°$ at XZ plane ($\varphi = 0°$) and YZ plane ($\varphi = 90°$) **c** $f_{cp1} =$ 3.94 GHz, **b** $f_{cp2} = 9.34$ GHz for the proposed antenna

Table 2 Comparative study through related multiband antennas and proposed antenna

Ref. (year)	Polarization	IBW (%), f_{rc} (GHz)	ARBW (%), f_c (GHz)
4 (2011)	RHCP; LP	74; 39, 2.725; 7.15	16, 2.35
5 (2017)	RHCP; LP	3.93; 29.45, 5.845; 8.08	2.57, 5.84
6 (2019)	LP; LHCP	20.57; 68.74, 2.43; 7.39	18.5
7 (2020)	RHCP; LP	30.43; 14.94, 4.6; 8.1	27.89
8 (2021)	LP; RHCP	10.66; 61.18, 6.19; 10.445	41.41; 4.85, 9.105; 11.96
Proposed antenna	LHCP, LP, LHCP, LP	13.73; 25.96, 14.59; 32.19, 3.9, 7.52, 9.56, 12.92	5.14; 9.6, 3.97, 9.34

7.52, 9.56, and 12.92 GHz, respectively. The dual CP bands of this antenna can support S- and X-band specially FSS and SAR applications in a single device.

References

1. Toh BY, Cahill R, Fusco VF (2003) Understanding and measuring circular polarization. IEEE Trans Educ 46(3):313–318. https://doi.org/10.1109/TE.2003.813519
2. Yu D, Gong SX, Xu Y, Wan YT (2015) Dual-band dual-polarized circular microstrip patch antenna with the curved slots on the ground. Prog Electromagnet Res 51:27–31. https://doi.org/10.2528/PIERL14112004
3. Langston WL, Jackson DR (2004) Impedance, axial-ratio, and receive-power bandwidths of microstrip antennas. IEEE Trans Antennas Propag 52(10):2769–2774
4. Bao XL, Ammann MJ (2011) Wideband dual-frequency dual-polarized dipole-like antenna. IEEE Antennas Wirel Propag Lett 10:831–834. https://doi.org/10.1109/LAWP.2011.2164609

5. Ding K, Gao C, Wu Y, Qu D, Zhang B, Wang Y (2017) Dual-band and dual-polarized antenna with endfire radiation. IET Microwaves Antennas Propag 11(13):1823–1828. https://doi.org/10.1049/iet-map.2017.0124

6. Bag B, Biswas P, Biswas S, Sarkar PP (2019) Wide-bandwidth multifrequency circularly polarized monopole antenna for wireless communication applications. Int J RF Microwave Comput Aided Eng 29(3):e21631. https://doi.org/10.1002/mmce.21631

7. Madaka KCR, Muthusamy P Mode investigation of parasitic annular ring loaded dual band coplanar waveguide antenna with polarization diversity characteristics. Int J RF Microwave Comput-Aided Eng, pp e22119. https://doi.org/10.1002/mmce.22119

8. Dhara R (2021) A compact dual band dual polarized monopole antenna with enhanced bandwidth for C, X, and Ku band applications. Prog Electromagnet Res Lett 96:65–72. https://doi.org/10.2528/PIERL20121903

9. Dhara R, Jana SK, Mitra M (2020) Tri-band circularly polarized monopole antenna for wireless communication application. Radioelectron Commun Syst 63(4):213–222. https://doi.org/10.3103/S0735272720040044

10. Singh AK, Patil S, Kanaujia BK, Pandey VK (2020) A novel printed circularly polarized asymmetric wide slot antenna for digital cellular system. Microw Opt Technol Lett 62(3):1438–1447. https://doi.org/10.1002/mop.32177

11. Ellis MS, Effah FB, Ahmed AR, Kponyo JJ, Nourinia J, Ghobadi C, Mohammadi B (2020) Asymmetric circularly polarized open-slot antenna. Int J RF Microwave Comput Aided Eng 30(5):e22141. https://doi.org/10.1002/mmce.22141

12. Dhara R, Yadav S, Sharma MM, Jana SK, Govil MC (2021) A circularly polarized quad-band annular ring antenna with asymmetric ground plane using theory of characteristic modes. Prog Electromagnet Res 100:51–68. https://doi.org/10.2528/PIERM20102006

13. Dhara R, Mitra M (2020) A triple-band circularly polarized annular ring antenna with asymmetric ground plane for wireless applications. Eng Reports 2(4): e12150. https://doi.org/10.1002/eng2.12150

Design and Comparative Analysis of Reconfigurable Antenna with Compound Reconfigurability

Sanket Patil and S. P. Mahajan

Abstract In recent times, reconfigurable antennas become essential components of communication and radar systems because of their capability to adapt to changing system requirements or environmental conditions. Reconfigurability is a factor that changes the characteristics of a particular antenna for obtaining additional functionalities for any system. These antennas are low profile and low priced resulting in a good performance. Moreover, one single antenna can deliver the same purpose of more than one traditional single functionality antenna. Mainly reconfigurable antennas possess the ability to change the properties of antenna such as polarization, pattern, and frequency dynamically. The proposed antenna design is desirable for emerging wireless communication systems. The design consists of a rectangular patch. L-shaped stubs are used between patch and ground using PIN diodes as switches. By changing the states of PIN diode switches, an antenna can be made reconfigurable. The substrate used is FR4 having 1.6 mm thickness and a 4.4 dielectric constant. This antenna is analyzed using HFSS 15.0 simulation software. The proposed structure can produce all three reconfiguration properties.

Keywords Reconfigurable antenna · Frequency shifting · Pattern diversity · Polarization reconfigurability

1 Introduction

Antennas are imperative and essential components for emerging wireless communication and radar systems. A variety of antennas are being used for these systems in the past few years, such as loop antennas, slot antennas, microstrip antennas, and helical antennas. All these antennas have fixed characteristics. Reconfigurability is a

S. Patil (✉) · S. P. Mahajan
Department of Electronics and Tele-Communication Engineering, College of Engineering Pune (COEP), Pune, India
e-mail: patilss19.extc@coep.ac.in

S. P. Mahajan
e-mail: spm.extc@coep.ac.in

factor that changes the characteristics of a particular antenna for obtaining additional functionalities for any system.

Reconfigurable antennas possess the ability to change the properties of antennas such as polarization, radiation, and frequency dynamically. To do it, they make use of many components like PIN diodes, varactors, radiofrequency microelectromechanical systems (RF-MEMS), field-effect transistors (FETs), parasitic pixel coating, photoconductive components, mechanical actuators, metamaterials, ferrites, and liquid crystals. By using such components they not only alter their geometry but also the performance in response to changes in surrounding conditions. Due to the rapid growth of wireless communication systems, as well as the great need for integration of wireless standards into a single platform, it is highly desirable to reconfigure the frequency, radiation pattern, and polarization of antennas. But it is not as simple as that. Modifying the properties of an antenna by applying various techniques to have reconfigurability is a challenging and complex task. To make the antenna reconfigurable, we must consider several factors like gain, spectral efficiency, impedance match, and radiation pattern. All these factors should attain the desirable response throughout the antenna's operation stages. Based on properties that we are adjusting dynamically, reconfigurable antennas can be classified as follow:

- Frequency reconfigurable antennas
- Pattern reconfiguration antenna
- Polarization reconfiguration antenna.

There is one more type of reconfigurable antenna called compound reconfigurable antenna which is the combination of either of two or three above-mentioned types. The application areas of reconfigurable antenna include cognitive radio systems, MIMO systems, satellite applications, and biomedical applications. Thus, the antennas which can adapt to the reconfigurable capabilities are very essential and useful for the advancements of emerging wireless technologies.

A pattern and polarization reconfigurable antenna is designed for WLAN applications in [1]. In this, four PIN diodes are used with a circular ring patch. A defective ground surface is introduced in ground plane for gain improvement. The majority of previous research has concentrated on tweaking a single antenna property rather than numerous attributes. To achieve broad impedance and axial ratio bandwidths, proximity coupled triangular tapered feed is employed to feed the structure in [2]. The structure is complex as for connection/disconnection five switches are used. In a single antenna [3], two distinct metamaterial-inspired reconfigurable structures are built and integrated. For switching purpose, six varactor diodes are used. The loss character of the p-i-n diode is used to provide a steady gain performance [5].

By properly switching shorting pins, eight discrete operating frequency bands can be achieved, and by adjusting perturbation segments, three polarization states, namely left-hand circularly polarization (LHCP), right-hand circularly polarization (RHCP), and linearly polarization (LP), can be realized simultaneously. In [6], a flexible antenna with frequency shifting and pattern steering capabilities for 1.9 and 2.4 G is suggested. However, due to its complicated construction (more RF diodes) and huge size, the antenna is not appropriate for emerging radar systems [9, 10]

describe a slot antenna with pattern and frequency diversity using PIN diodes. The complexity is more resulting in insertion losses due to a large number of RF PINs. A two-element array antenna with frequency and pattern reconfigurability based on a stub-loaded design is shown in [12]. Varactor diodes with open stubs are used to construct the frequency-tuning process and two separate bias voltages allow pattern reconfigurability. But, the size is very large limiting its use in emerging wireless technology.

This paper provides an optimum approach for communication system configurations where the frequency, pattern, and polarization of the system can be independently reconfigured. The design specifications and detailed geometry of the proposed structure are discussed in Sect. 2. The performance evaluation and comparative analysis are studied in Sect. 3. At last, the conclusion is stated in Sect. 4.

2 Proposed Antenna Geometry

The expeditious growth in communication and radar systems necessitates layouts in which the system's frequency, pattern, and polarization can be independently adjusted. The primary goal of this study is to combine all of these designs into a single antenna.

A. *Design Specifications*

The proposed antenna is going to be used for frequency, pattern, and polarization reconfigurability purpose. For that, the basic antenna structure used is a microstrip rectangular patch. The three most important factors to consider while designing a rectangular microstrip patch antenna are:

- Frequency of operation (f_0): The resonant frequency of the antenna must be selected appropriately.
- The dielectric constant of the substrate (ε_r): The dielectric material selected for my design is FR-4 which has a dielectric constant of 4.4. An antenna with high dielectric constant shrinks in size.
- Height of dielectric substrate (h): The height of the dielectric substrate is selected as 1.6 mm.

Thus, the resulting geometry of the antenna is 25 mm * 33 mm * 1.6 mm having a microstrip line feed of 3.3 mm wide and 50 ohms characteristic impedance.

B. Geometry of Designed Antenna

The structural dimensions and geometry of the proposed antenna are shown in Fig. 1. The simulation is performed using lossy FR4 substrate. The proposed antenna is having a small compact size. The dimensions of the antenna are 25 mm * 33 mm * 1.6 mm. The microstrip feed line is 3 mm wide resulting in 50 ohms characteristic impedance.

The length of the radiating element is calculated using the following formula:

Fig. 1 Geometry of the
antenna
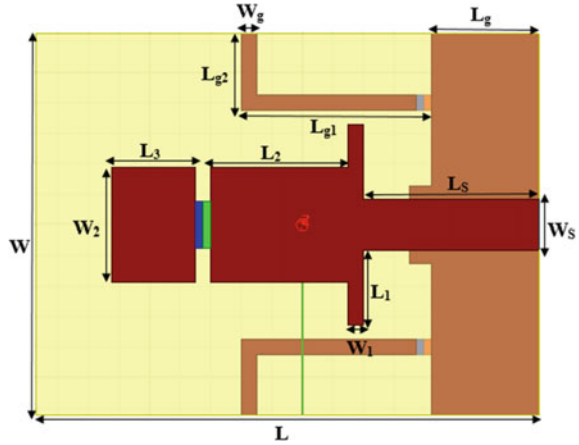
$$L_{f_r} = \frac{C/4f_r}{\sqrt{\epsilon_{\text{eff}}}}$$

where

$$\epsilon_{\text{eff}} = \frac{\epsilon_r + 1}{2} + \frac{\epsilon_r - 1}{2}\left[1 + 12\frac{h}{W}\right]^{\frac{-1}{2}}$$

where c is the speed of light, w is the width of the substrate, and h is the thickness
of the substrate.

So, the calculated length using the above formula is 13.9 mm. However, the noted
optimal length will be (L2 + L3) 14.5 mm. Table 1 lists the values of key parameters
used in the proposed antenna structure.

The L-shaped stubs are introduced in the ground plane. Total three lumped
switches (PIN diodes) are used. One is for the patch, and the remaining two are
used in the ground plane. Thus, the proposed antenna is low profile.

Table 1 Antenna parameters
and corresponding values

Parameters	Values (mm)	Parameters	Values (mm)
W	25	L_g	7.2
L	33	L_{g1}	11.5
L_1	4.9	L_{g2}	5
L_2	9	W_g	1
L_3	5.5	L_s	11.5
W_1	1	W_s	3.3
W_2	7.5		

An inductor (L) and a resistor (R) make up the equivalent circuits of the PIN diode's ON and OFF states (R). The diode is forward biased when the inductor and resistor (R) are connected in series; i.e., the diode is ON. The diode is reverse biased when the inductor is connected with a parallel combination resistor (R) and capacitor (C); i.e., the diode is OFF.

The equivalent ON and OFF state circuits of the PIN diode are as shown in Fig. 2. The values used for ON and OFF states of the PIN diode are illustrated in Table 2.

Thus, the ON and OFF states of the PIN diode are analyzed as RL and RLC circuits, respectively.

Fig. 2 Equivalent circuit of PIN diode

| C | 0.04 pF |

Lumped RLC Boundary

Switch ON   Switch OFF
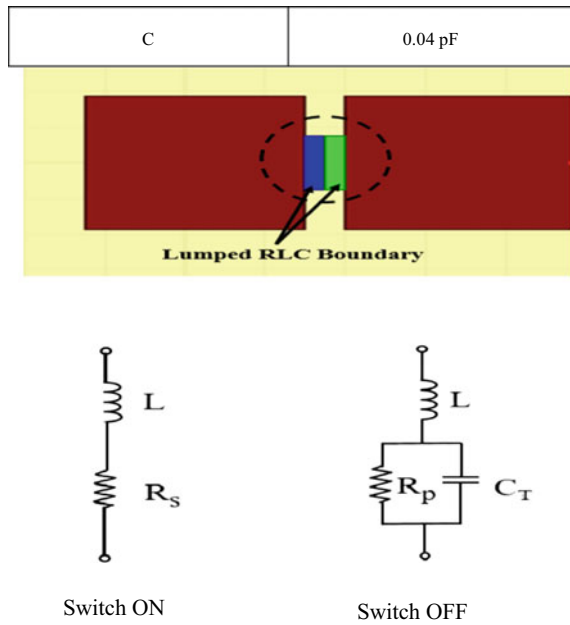
Table 2 Values used for equivalent circuits of PIN diodes

Parameters	Values
L	0.02 nH
R_{ON}	1 Ω
R_{OFF}	5 megaΩ
C	0.04 pF

3   Results and Comparative Analysis

To have frequency reconfigurability, switch 1 is kept on and off for two cases, and the
remaining two switches are kept off in both cases. In case1, the antenna is resonating at
3.31 GHz having 1.47 GHz bandwidth, and at 5.97 GHz having 735 MHz bandwidth.
In case 2, the antenna is resonating at 3.975 GHz having 1.4 GHz bandwidth, and at
6.705 GHz having 630 MHz bandwidth. This is shown in Fig. 3. Table 3 shows the
frequency shifting cases.

Now, for radiation pattern and polarization reconfigurability, we are keeping diode
1 in the ON state and switching the states of diode 2 and diode 3. The insertion of
an L-shaped stub into the ground has a significant influence on radiation properties.
Depending on it, we are getting four cases. The polarization diversity is observed at
3.31 GHz. The pattern reconfigurability results are obtained at frequencies 3.31 GHz
and 5.97 GHz both at phi $= 0^0$ and phi $= 90^0$.

Figure 4a, b, c, d represents the pattern shifting in cases 1 to 4, respectively.
Figure 5 represents the polarization reconfigurability in all four cases. The axial
ratio at 3.31 GHz observed is 8.90 dB for case 1. This shows that when only diode
1 is ON and the remaining diodes are OFF, the antenna is elliptically polarized.
The axial ratio at 3.31 GHz observed is 1.12 dB for case 2. This shows that when
only diode 1 and diode 3 are ON and the remaining diodes are OFF, the antenna is
circularly polarized. Moreover, when the surface current distribution is observed, the
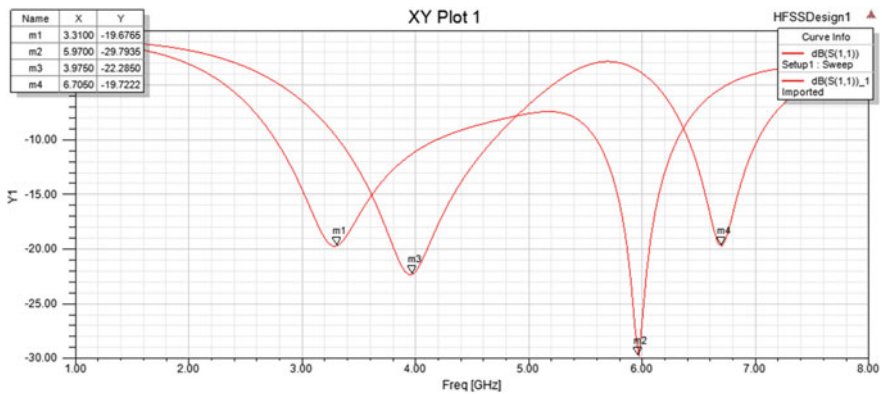
Fig. 3 Frequency shifting

Table 3 Frequency shifting cases

Case	Switch 1	Switch 2	Switch 3	Frequency	Bandwidth	Applications
1	ON	OFF	OFF	3.31 GHz 5.97 GHz	1.47 GHz 735 MHz	WiMAX GPS WLAN
2	OFF	OFF	OFF	3.94 GHz 6.705 GHz	1.4 GHz 630 MHz	

direction of current flow is anti-clockwise which shows that it is LHCP. For case 3, the axial ratio at 3.31 GHz observed is 2.90 dB. This shows that when only diode 1 and diode 2 are ON and the remaining diodes are OFF, the antenna is circularly polarized. Moreover, when the surface current distribution is observed, the direction of current flow is clockwise which shows that it is RHCP. For case 4, the axial ratio at 3.31 GHz observed is 34.48 dB. This shows that when all the diodes are ON, the antenna is linearly polarized. Table 4 illustrates beam steering and polarization diversity cases.

(a)   At f=3.31 GHz for phi=0⁰ and 90⁰ and at f=5.97 GHz for phi=0⁰ and 90⁰ respectively

(b)   At f=3.31 GHz for phi=0⁰ and 90⁰ and at f=5.97 GHz for phi=0⁰ and 90⁰ respectively

(c)   At f=3.31 GHz for phi=0⁰ and 90⁰ and at f=5.97 GHz for phi=0⁰ and 90⁰ respectively

(d)   At f=3.31 GHz for phi=0⁰ and 90⁰ and at f=5.97 GHz for phi=0⁰ and 90⁰ respectively
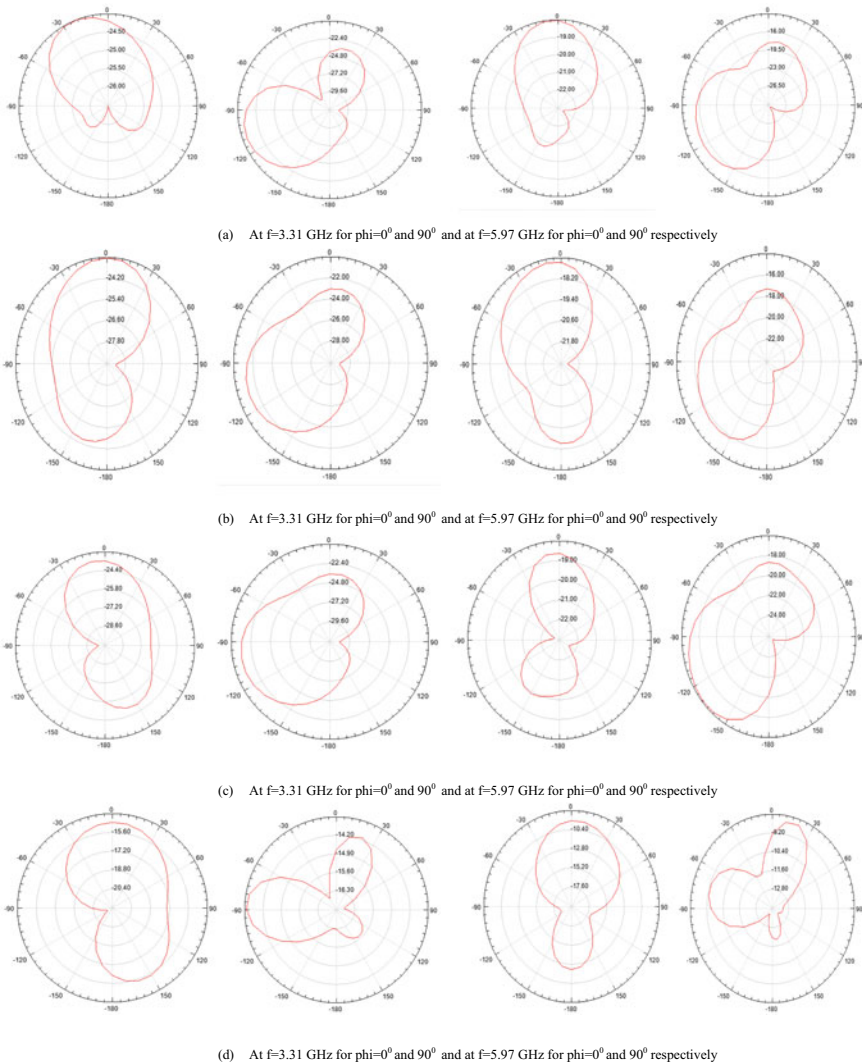
Fig. 4 Pattern shifting **a** case 1 **b** case 2 **c** case 3 **d** case 4
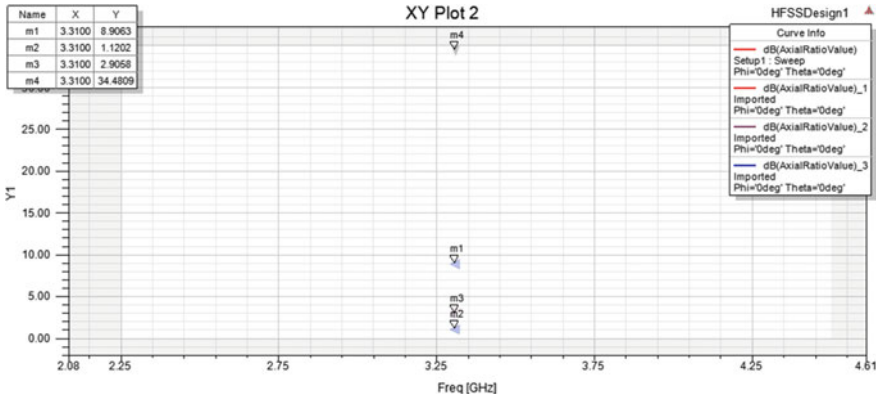
Fig. 5 Pattern diversity

Table 4 Beam steering and polarization reconfigurability

Case	Switch 1	Switch 2	Switch 3	Main lobe direction at phi = 0^0 for 3.31 GHz	Main lobe direction at phi = 0^0 for 5.97 GHz	Axial ratio (in dB) At 3.31 GHz	Polarization
1	ON	OFF	OFF	-30^0	0^0	8.90	EP
2	ON	OFF	ON	0^0 and -150^0	-15^0	1.12	LHCP
3	ON	ON	OFF	-15^0 and 150^0	0^0	2.90	RHCP
4	ON	ON	ON	0^0 and 150^0	0^0	34.48	LP

As shown in Figure 6, the current density is larger in the lower portion than the remaining part of the structure. Depending upon which switch is ON and which switch is OFF among the diode 2 and diode 3, the current will flow through either in left-sided stub or right-sided stub in cases 2 and 3. Depending upon this current distribution the beam will steer from case to case as depicted in Table 4. The novelty of the proposed antenna lies in its simple, compact, low-profile structure and capability to reconfigure the properties through different switching conditions. In all cases, the average gain observed is about 2 dBi. Thus, the antenna is suitable for emerging wireless systems due to its compactness, low profile, and less use of switching elements. The comparison of the proposed antenna concerning existing structures is shown in Table 5.

As we can see from Table 5, the proposed antenna structure has a very small size as compared to others. Moreover, the switching elements used are very few compared to others resulting in less complexity while designing. The bandwidth is better. Also, the proposed antenna is capable of having all three reconfigurability in a single configuration. Thus, the antenna is very efficient and cost-effective.

Case 1   Case 2   Case 3   Case 4
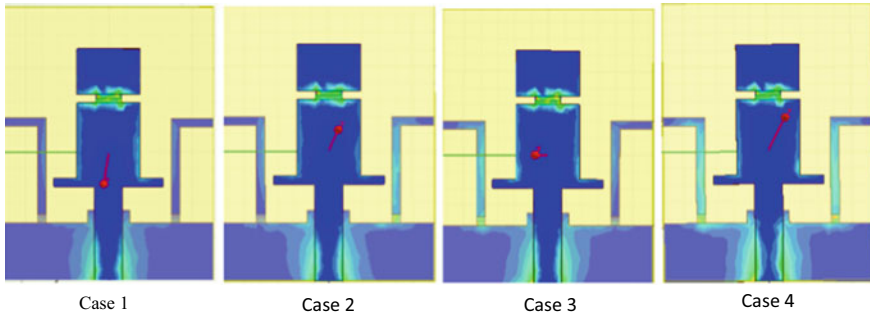
Fig. 6 Current distribution in various cases

Table 5 Comparison with previous work

Ref. No.	Size (mm^3)	Reconfiguration	Switches	Bandwidth (MHz)
1	60 * 65 * 1.6	Pattern and Polarization	4 PIN diodes	170/130
2	58 * 58 * 1.53	Frequency and polarization	5 PIN diodes	4930
6	42 * 44 * 1.6	Frequency and pattern	8 PIN diodes	160/220
9	130 * 160 * 1.6	Frequency and pattern	11 PIN diodes	200/150/150
10	80 * 45.8 * 1.6	Frequency and pattern	5 PIN diodes	580/290
12	160.9 * 151.5 * 1.6	Frequency and pattern	2 varactor diodes	230
3	120 * 120 * 1.6	Frequency, pattern, and polarization	6 varactor diodes	> 25
7	60 * 50 * 1.6	Frequency, pattern, and polarization	9 PIN diodes	200
This work	25 * 33 * 1.6	Frequency, pattern, and polarization	3 PIN diodes	1470/730

4 Conclusion

In this work, three leading reconfigurable antenna research aspects are addressed. For that purpose, at first, these antenna's existing structures are discussed, classified depending upon the configurations, observed the various switching techniques used, and their applications are reviewed. After the detailed survey, the design process of the proposed antenna is commenced. A low-profile printed antenna capable of frequency shifting, beam steering as well as polarization reconfigurability is successfully designed and validated. The proposed antenna gives distinct results depending

upon the states of switching elements. Keeping switch 2 and switch 3 in OFF state and varying the state of switch 1, we are able to achieve frequency shifting. For beam steering and polarization diversity, we kept switch 1 ON and varied the states of the remaining two switches. After that, the comparative analysis is done with the previously existing structures. Thus, a compact, simple-to-design, efficient, cost-effective which can have good impedance bandwidth reconfigurable antenna is designed.

References

1. Niture DV, Gurame SS, Mahajan SP (2018) A pattern and polarization reconfigurable antenna for WLAN application. In: IEEE 8th International Advance Computing Conference (IACC)
2. Singh RK, Basu A, Koul SK (2020) Reconfigurable microstrip patch antenna with polarization switching in three switchable frequency bands. IEEE Access 8
3. Zhang J, Yan S, Vandenbosch GAE (2019) A low-profile frequency reconfigurable antenna with polarization and pattern diversity. In: IEEE MTT-S international conference on microwaves for intelligent mobility (ICMIM)
4. Iqbal A, Smida A, Mallat NK, Ghayoula R, Elfergani I, Rodriguez J, Kim S (2019) Frequency and pattern reconfigurable antenna for emerging wireless communication systems. Electronics 8:407
5. Hu J, Hao Z-C (2018) Design of a frequency and polarization reconfigurable patch antenna with a stable gain. IEEE Access 6
6. Zhu Z, Wang P, You S, Gao P (2018) A flexible frequency and pattern reconfigurable antenna for wireless systems. Progress Electromagnet Res Letters 76:63–70
7. Selvam YP, Elumalai L, Alsath MGN, Kanagasabai M, Subbaraj S, Kingsly S (2017) Novel frequency-and pattern-reconfigurable rhombic patch antenna with switchable polarization. IEEE Antennas Wirel Propag. Lett 16
8. Costantine J et al (2015) Reconfigurable antennas: design and applications. In: Proceedings of the IEEE 103.3, pp 424–437
9. Majid HA, Rahim MKA, Hamid MR, Ismail MF (2014) Frequency and pattern reconfigurable slot antenna. IEEE Trans Antennas Propag 62(10)
10. Li PK, Shao ZH, Wang Q, Cheng YJ (2013) Frequency and pattern reconfigurable antenna for multi-standard wireless applications. IEEE Antennas Wirel Propag Lett
11. Xiao M, Cui Y, Li R (2019) A reconfigurable circularring patch antenna with pattern and polarization diversities, 978-1-7281-2168-0/19/$31.00 ©2019 IEEE
12. Zainarry SNM, Nguyen-Trong N, Fumeaux C (2018) A frequency-and pattern-reconfigurable two-element array antenna. IEEE Antennas Wirel Propag Lett
13. Niture DV, Govind PA, Mahajan SP (2016) Frequency and polarisation reconfigurable square ring antenna for wireless application. IEEE region 10 conference (TENCON)

Fractal CSRR Metamaterial-Based Wearable Antenna for IoT Application

Anand Kumar Singh and Kirti Inamdar

Abstract IoT applications have opened up new avenues of research in all domains of electronics engineering. Antenna designing is one of them. This paper presents the design of a wearable antenna designed for IoT applications like medical healthcare and home automation. The design covers the W-BAN applications. The antenna design uses combination of Minkowski fractal and CSRR metamaterial-based antenna design on flexible materials like Jeans and polyimide used as a substrate. The antenna gives a gain of 4.6031 dB at 3.9 GHz using Jeans as a substrate and its performance remains good under bent conditions also.

Keywords CSRR · Fractal · Metamaterials · Minkowski · Wearable antennas

1 Introduction

Antenna design is an advanced subject of study; as a result, it is special for a new technique to emerge in light of old approaches for application in current communication systems. Antennas used to have a basic shape based on Euclidean geometry. A multitude of novel and creative antenna designs have resulted from recent attempts by various scholars across the world's earliest attempt to merge fractal geometry and metamaterials with the electromagnetic theory [1].

Wearable antennas are a new technology that has got a lot of interest in recent years because of its appealing characteristics. Wearable devices are frequently utilized for tracking, navigation, mobile computing, and data collecting activities in the medical, monitoring, firefighting, and military sectors [2, 3]. The reduction in size is a key consideration in the design of wearable antennas, primarily those which resonate at single or multiband frequencies [4].

FRACTALS: The most basic definition of a fractal is an entity that seems self-similar at various magnifications and, as a result, has symmetry across dimension, with each little portion of the object reproducing the structure of the entire thing [1]

A. K. Singh · K. Inamdar (✉)
S.V. National Institute of Technology, Surat, Gujarat 395007, India
e-mail: kki@eced.svnit.ac.in

with multiband features, the self-similarity property of the fractal geometry may be utilized to reduce the size [5, 6]. The large proportion of corner and tips in all of these designs helps to increase antenna performance. The fractal designs like Hilbert curve, Sierpinski gaskets, Koch curves, Minkowski curves, and Sierpinski carpets are some of the self-symmetric geometries extensively utilized in antenna design to create multiband miniaturized antenna [7, 8]. The fractal loops have ability to fill space means that greater electrical length could be packed into a relatively smaller region [9].

METAMATERIALS: Metamaterials with simultaneous negative permeability and permittivity have a negative index of refraction, which bends electromagnetic waves to the same side of the normal as the incident wave, giving them the name left-handed materials. Veselago published a theoretical study on the concept of meta-material in 1968 [10]. The designed structures, rather than the material composition, give metamaterial negative μ and negative ε characteristics. These characteristics aren't seen in natural resources. The usage of an MTM in the near context of a patch antenna has been observed to improve antenna performance, and the idea of CSRR has been proposed (complementary slip ring resonator) and discuss in [5, 11, 12]. For the verification of MTM property, there are four prominent methods: Nicolson-Ross-Wier (NRW), NIST iteration methodology, new non-iterative methodology, and short circuit method. The transmission and reflection S-parameters derived from simulation or measurement data are necessary for validation in all of these procedures [13, 14].

In this paper, the design and analysis of the characteristics of the MTM structure, as well as the performance of a Minkowski fractal antenna with and without the MTM utilizing various types of flexible material is discussed.

2 Antenna Design

The antenna design consists of Minkowski fractal design on the patch and a CSRR MTM as a ground defect. A square initiator structure is used in the creation of the Minkowski fractal antenna. The following equation is used to estimate the starting size when iterated to a lower scale:

$$W1^{(n+1)} = a1 \times \text{Ln} \tag{1}$$

$$W2^{(n+1)} = a2 \times \text{Ln} \tag{2}$$

where n denotes the number of iterations, $W1$ is the width of the center segment, and $W2$ is the width of the indentation. The ratio of $W1/\text{Ln}$ gives a1, while the ratio of $W2/\text{Ln}$ gives the value of $a2$ (to avoid overlapping $a1$ must be less than $a2$). A common micro strip patch calculation formula yields the starting value of the square
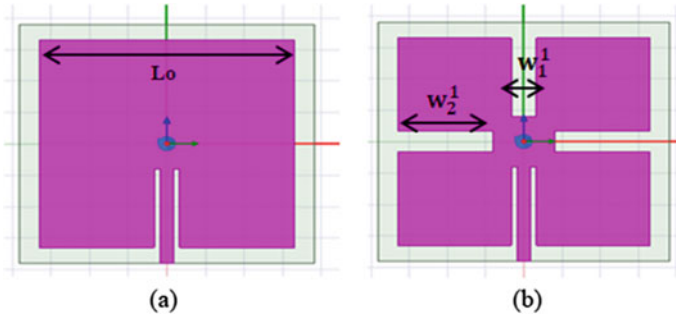
Fig. 1 **a** Basic square patch, **b** first order iteration of fractal

length Lo. An iteration length, Ln, is used to build the suggested second iteration fractal antenna.

The formula is as follows:

$$\text{Ln} = 2L_{(n+1)} + W1^{(n+1)} + 2W2^{(n+2)} \tag{3}$$

The initiator in this design is a standard square patch antenna with dimensions of 46 mm x 46 mm, as illustrated in Fig. 1a. The initiator is divided into four equal tiny squares shaped structures with $w_1^1 = 12.5$ mm, $w_2^1 = 16$ mm, and $a_1 = 0.27$, $a_2 = 0.35$ to achieve the first order iteration illustrated in Fig. 1b. To get the second order iteration, the same process is repeated for each of the squares generated in the first order iteration. As the number of repetitions inside the specified region increases, the length of the perimeter grows. Furthermore, the fractal construction occupies less metal than a traditional square patch antenna.

The antenna is designed on a Jeans substrate with a dielectric permittivity of 1.6 with dimensions of 64 mm × 64 mm and a height of 3 mm, as illustrated in Fig. 2. It is a Minkowski shaped fractal structure with copper layer of thickness 0.035 mm. Micro strip line feed structure is used for feeding which is positioned at the center point with 12 mm × 25 mm area. The feeding length and breadth of the antenna is optimized to improve the antenna performance and to obtain the better matching.

The required MTM structure in this case is CSRR, which is shown in Fig. 3b. For MTM testing, this structure is created independently on another jeans substrate of the same kind. Finally, the Minkowski fractal antenna is mounted on top of the substrate, with CSRR replacing the ground on the bottom side as shown in Fig. 3a. The Minkowski fractal antenna uses this CSRR as a defective ground plane. The dimensions of the CSRR shaped metamaterial structure of 46 mm × 46 mm is built-in the ground plane of the antenna. The separation width between the rings is 2 mm and the width of each ring is 1 mm and the gap is 0.5 mm.

Parameter extraction of the metamaterial is done either by applying PEC-PMC boundary conditions or master slave boundary conditions. In HFSS, if we use Master–slave boundary conditions then the parameters ε and μ can be extracted by scripting
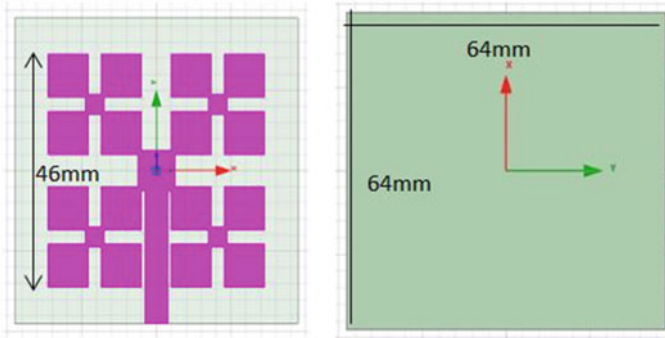
Fig. 2 Proposed second order iteration minkowskifractal antenna geometry

(a) Top view   (b) Bottom view
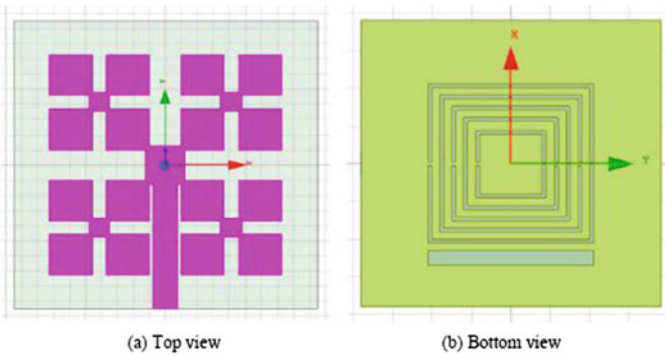
Fig. 3 Proposed fractal antenna with CSRR MTM ground plane

the standard equations in the output variable form. Floquet ports excitation is used in the case of master–slave boundary and wave port is assigned if PEC-PMC boundary is applied. In this design we have used output variable method for parameter extraction.

The medium's parameter ε and μ are linked to S-parameters by the Equations.

$$n = \frac{1}{\mathrm{kd}} \cos^{-1}\left[\frac{1}{2S_{21}}\left(1 - S_{11}^2 + S_{21}^2\right)\right],$$

$$z = \sqrt{\frac{(1 + S_{11})^2 - S_{21}^2}{(1 - S_{11})^2 - S_{21}^2}} \tag{4}$$

ε and μ can be obtained as follows:

$$\mu = n/z \tag{5}$$

$$\varepsilon = n * z \tag{6}$$

3   Simulated Results and Analysis

For the purpose of designing and simulating the proposed Minkowski fractal antenna, the CSRR structure and the CSRR loaded Minkowski fractal antenna, the Ansys HFSS electromagnetic Simulation software is used in this study. In each case, the simulation is swept across a frequency range of 1 to 10 GHz.

Flexible substrate materials are used to design wearable antennas, which are made up of textile and electro textile materials. These textile materials must be affordable, pleasant, lossless, and widely available. Many researchers have constructed flexible wearable antennas utilizing various textile materials such denim cotton, poly cotton, and polyester cotton. As a substrate material, jeans and polyimide are chosen here as flexible material for analysis and simulation of proposed design for wearable application (Fig. 4).

The designed antenna is fractal in shape, this is the reason behind its multi-resonant response. From the simulated results shown in Fig. 5, it is inferred that the antenna after second iteration operates at two frequencies 4.02 GHz and 4.58 GHz and the return loss (RL) at these frequencies are −15.1832 dB and −30.6892 dB, respectively (Table 1).

It can be seen from the graph that the VSWR value is significantly greater than 2 indicates poor matching of the antenna at desired frequencies (Fig. 6).

At 3.9 GHz and 4.28 GHz, the antenna's maximum gain value is −5.1575 dB and −4.698 dB, respectively, as shown in Fig. 7. The gain is calculated at phi = 0º for both the frequencies (Fig. 7).

After adding the MTM, the antenna works over the 3.78 to 4 GHz band, 4.24 to 4.36 GHz band, and 4.65 to 5.05 GHz band with left shift, as indicated by the
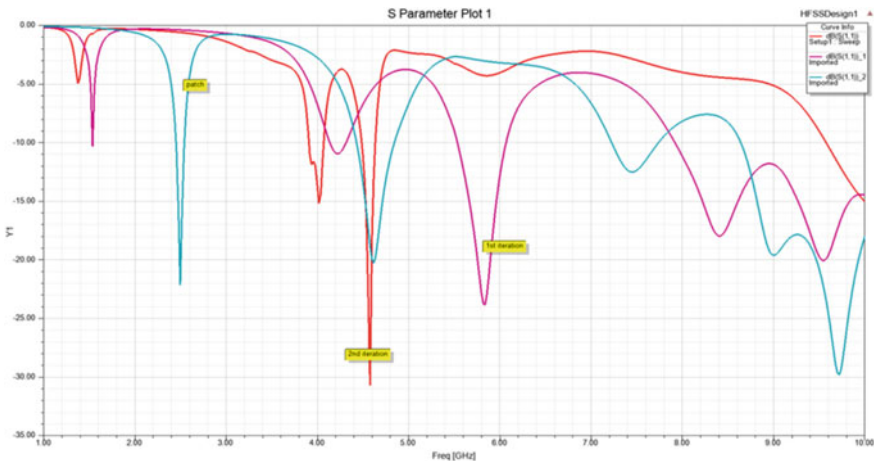
Fig. 4 S11 response of fractal antenna without MTM using jeans as a substrate
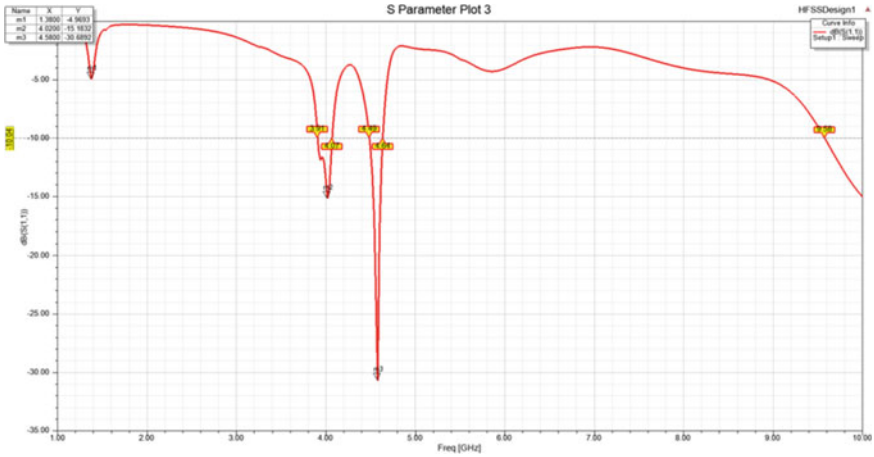
Fig. 5 S11 response of the fractal antenna for second order iteration

Table 1 Frequency and S11 of Fractal iterations without MTM

Geometry	Frequency (GHz)	S11 (dB)
Basic square patch	2.42, 4.58, 7.25	$-22, -20.012, -12.227$
First iteration	1.58, 4.21,5.82	$-10.5, -11, -23.98$
Second iteration	4.02, 4.58	$-15.1832, -30.6892$
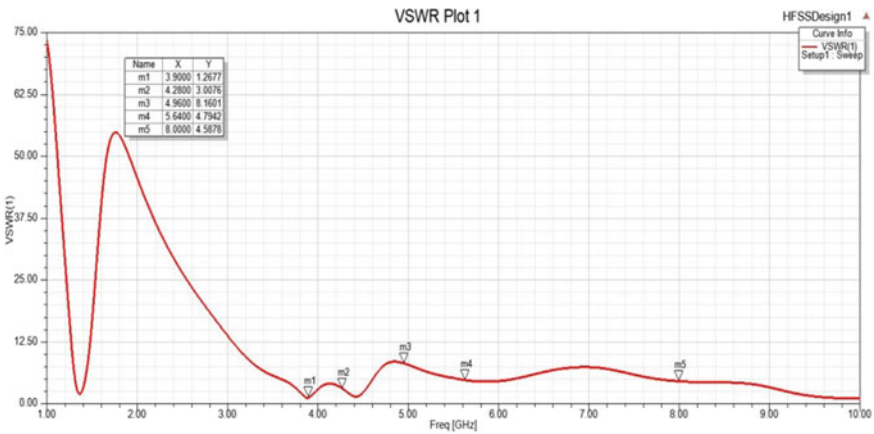
Fig. 6 VSWR of the fractal antenna without MTM

(a)   (b)
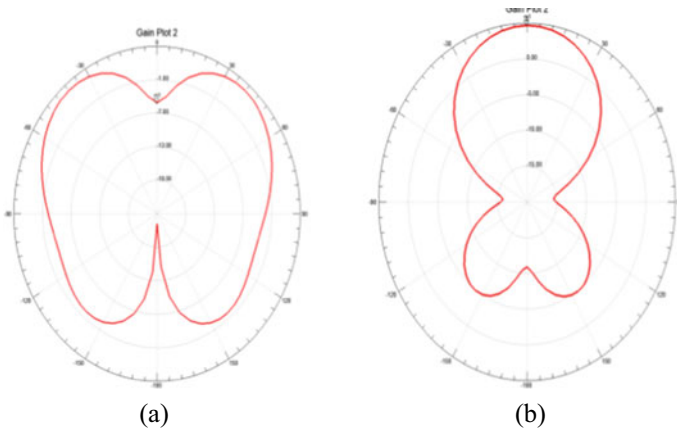
Fig. 7 Gain plot of fractal antenna without MTM at **a** 3.9 GHz **b** 4.28 GHz

simulated S-parameter results shown in Fig. 8. In this range of frequency, MTM is also showing negative property shown in Fig. 9.

As discussed previously, the parameters ε and μ are extracted directly from the HFSS tool using output variable expressions. The structure is meant to work at frequency range from 3.8 to 4.74 GHz, 4.82 to 4.96, and 8.24 to 9.34 GHz. In this frequency range, both permittivity (ε) and permeability (μ) are negative, as seen in Fig. 9.

As illustrated in Fig. 10a and b, at 3.9 GHz, the antenna's maximum gain is 4.6031 dB, and its maximum directivity is 5.7398 dB with MTM, which is higher than the antenna without MTM.
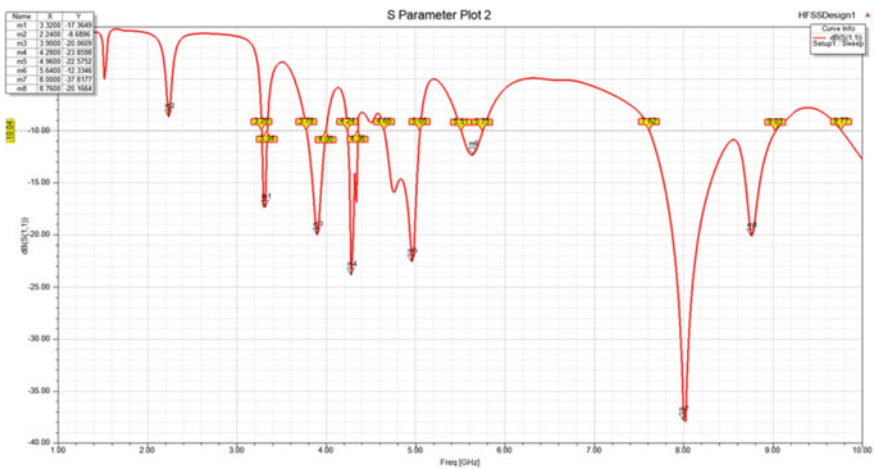
Fig. 8 Simulated S11 parameter with MTM
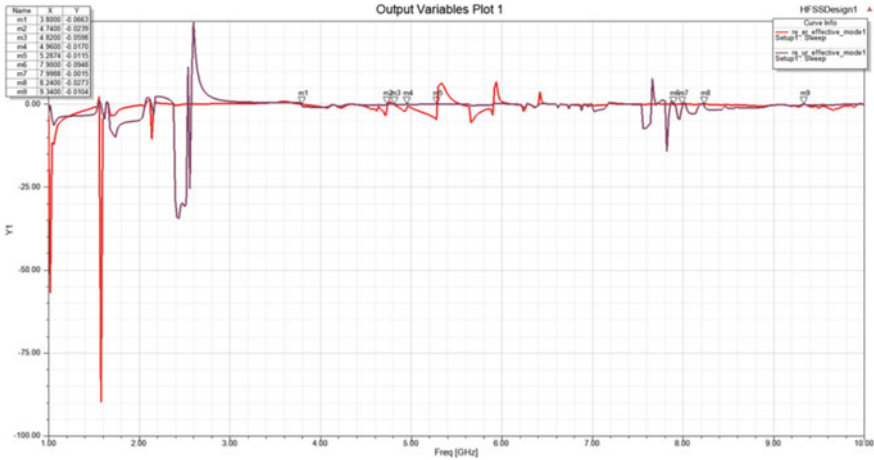
Fig. 9 Real ε and μ value obtained from the simulation using output variable method

4 Antenna Performance Under Bending Condition

Antennas constructed of flexible fabrics may alter in size and shape as a result of conformability with the body's surface, such as when put on a curved portion of the body like the leg or arm. The performance of a wearable antenna is decreased when it is incorporated into clothes owing to bending. As a result, it's critical to investigate the wearable antenna's performance under bending conditions. Employing the antenna on a cylindrical shape with varying radii R, such as 30 cm and 40 cm, as illustrated in Fig. 11a and b, produces a fractal antenna bending effect. Figures 12a and b illustrate the antenna's return loss characteristics under various bending situations.

It is clearly seen from the simulated result shown in Fig. 12a and b that as the degree of bending rises, the antenna's performance degrades owing to the variation in electrical length.

5 SAR Calculations

The SAR is a unit for measuring how much energy is absorbed by human body cells. The SAR must be within the stated limitations for wearable antenna applications. Here in this design, we are using a four-layer rectangular body phantom model, designed in HFSS software to analyze the SAR value. The human body phantom model is seen in Fig. 13.

As illustrated in Fig. 13, the designed antenna is positioned below the body phantom model with the ground plane facing the human body modal at a distance D. The distance D varies between 10 and 50 mm. Before starting the simulation, the desired frequency for measuring SAR is chosen.
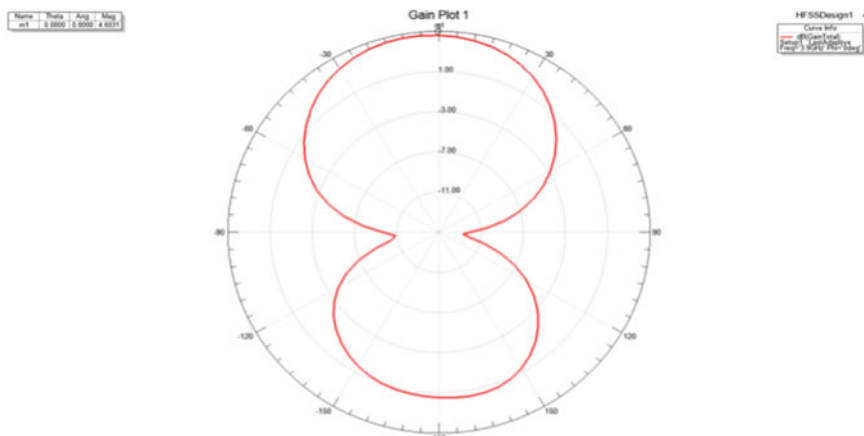
(a)
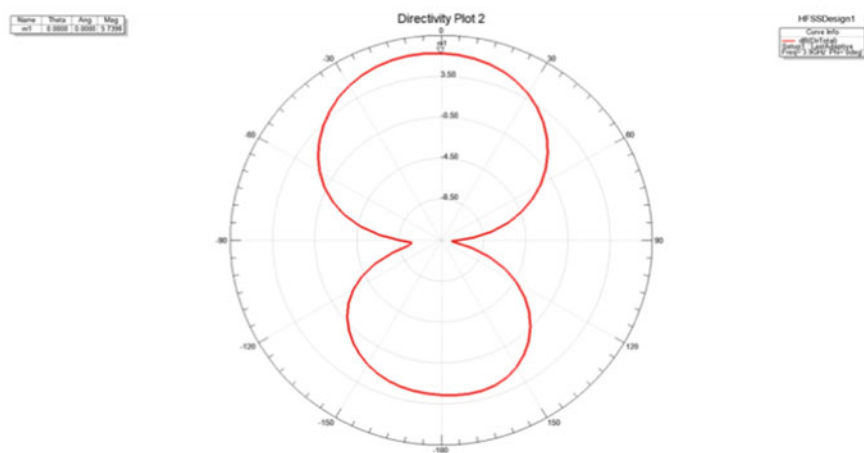
(b)

Fig. 10 **a** Gain plot with MTM at 3.9 GHz, **b** directivity at 3.9 GHz with MTM

Fig. 11 Bending of antenna with MTM at **a** 30 cm and **b** 40 cm

(a)   (b)
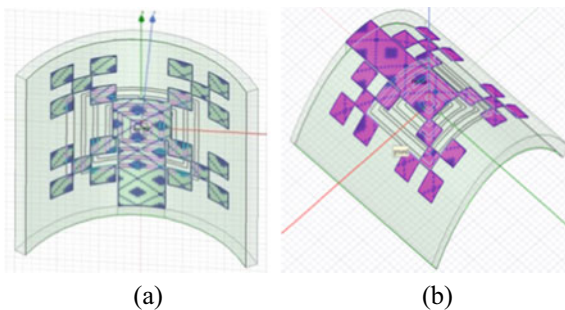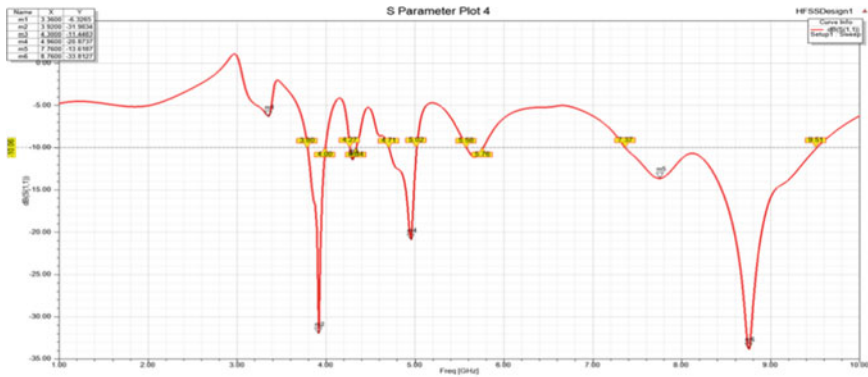
(a)
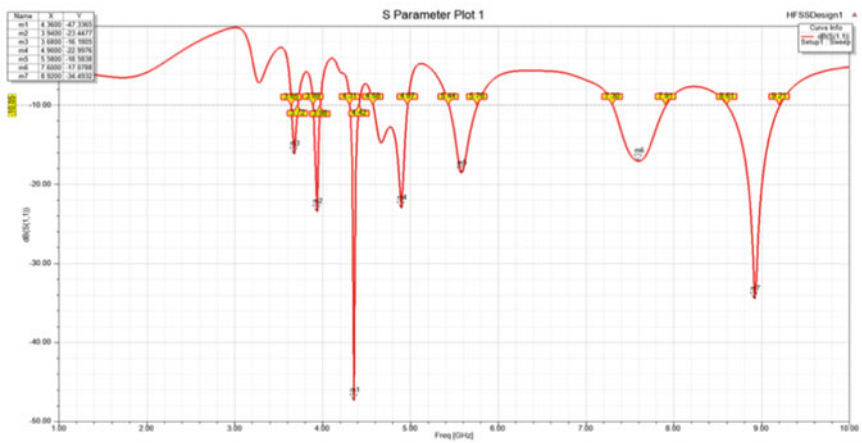
(b)

Fig. 12 Simulated S11 in dB of the fractal antenna for bending at **a** 30 cm and **b** 40 cm

At 3.9 GHz, the maximum average value of SAR is 4.45 W/Kg, as shown in Fig. 14, which is more than 1.6 W/Kg for 1 g of tissue at a distance of 10 mm ranging up to 50 mm from the antenna. As a result, the proposed antenna unable to be utilized for wearable applications because of the SAR value produced does not meet the FCC's required limitations (1.6 W/Kg). MTM is also added to the antenna's ground plane to make it acceptable for wearable applications and to lower the SAR value.

And the result obtain with MTM is shown in Fig. 15 the maximum average value of SAR at 3.9 GHz after inserting MTM in the antenna's ground plane is 0.1157 W/Kg which is below the FCC's (1.6 W/Kg) stated limitations (Table 2).
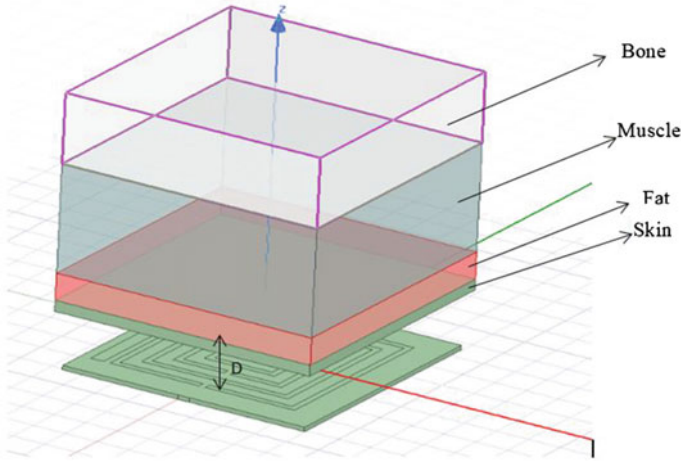
Fig. 13 Body phantom modal for SAR calculation
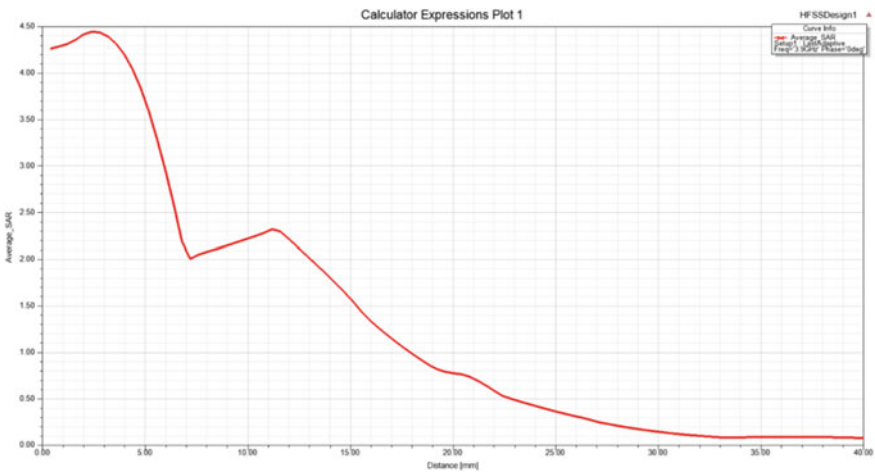
Fig. 14 SAR of fractal antenna without MTM at 3.9 GHz

6 Conclusion

In this paper, a design of metamaterial-based wearable fractal antenna has been proposed. CSRR metamaterial is used in the ground plane of second iteration Minkowski fractal antenna. Jeans and polyimide as flexible material are used for analysis and simulation of proposed design for wearable application. After inserting the CSRR shaped metamaterial in the antenna's ground plane, the second iteration Minkowski fractal antenna has improved in VSWR, directivity, gain, and is tuned
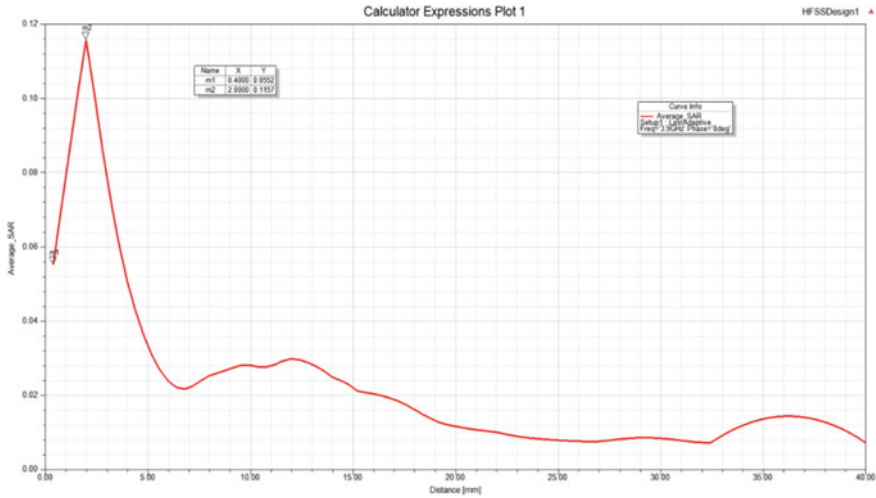
Fig. 15 SAR of fractal antenna with MTM at 3.9 GHz

Table 2 Comparison of various parameter of antenna using different substrate

Parameter	Frequency (GHz) Using jeans as substrate		Frequency (GHz) Using polyimide as substrate	
	3.9	4.28	2.74	8.36
S11(dB) with MTM	−20.0609	−23.8598	−38.1299	−27.6643
VSWR without MTM	1.2677	3.0076	38.5770	30.8031
VSWR with MTM	1.7415	1.0710	0.2155	0.7192
Gain(dB) without MTM	−5.1575	4.6982	−11.1714	−1.3056
Gain with MTM	4.6031	3.2410	1.5926	4.2829
Directivity without MTM	−2.7753	7.4803	4.8760	4.4250
Directivity with MTM	5.7398	5.3901	3.8705	5.8373
SAR(w/kg) without MTM	4.45	1.77	29.6473	7.0596
SAR with MTM	0.1157	0.1452	0.0071	0.0759
S11 with 30 cm bending	−31.9834	−11.4483	−12.3936	−8.6125
S11 with 40 cm bending	−23.4477	−8.5211	−7.5161	−14.9421
Application	WiMAX		S band, fixed mobile and mobile satellite and X band	

to the necessary frequency range. The SAR value was determined at a distance of 10 mm ranging up to 50 mm without MTM in the ground plane and found to be less than 1.6 W/kg with MTM, which is within the range allowed by the FCC, which has a maximum value of 1.6 W/kg used for 1 g of tissue. A detailed calculation method for systematic design at a specific desired frequency is demonstrated. Bending of antenna

at 30 and 40 cm is also performed to analyze the effect of bending while using in wearable application. The proposed antenna is desirable for Wimax, S band, fixed mobile, mobile satellite, and X band applications. This design can be used for IoT applications like health monitoring, office and home automation, secured payments, driving assistance etc. where the antennas are placed in proximity to human body.

References

1. Krzysztofik WJ (2013) Fractal geometry in electromagnetics applications-from antenna to metamaterials. Microwave Rev
2. Jalil ME, Rahim MKA, Samsuri NA, Murad NA (2012) Triple band fractal koch antenna for wearable application. In: Progress in electromagnetics research symposium proceedings, March 2012
3. Paracha KN, Rahim SKA, Soh PJ, Khalily M (2019) Wearable antennas: a review of materials, structures, and innovative features for autonomous communication and sensing. IEEE Access 7
4. Singh A, Singh MK (2014) Design and simulation of miniaturized minkowski fractal antennas for microwave applications. Int J Adv Res Comput Commun Eng 3(1), January 2014
5. Majid HA, Rahim MKA, Masri T (2009) Microstrip Antenna's gain enhancement using left-handed metamaterial structure. Progress Electromagnet Res M 8:235–247
6. Gianviff JP, Rahmat-Samii Y (2002) A novel antenna miniaturization technique and applications. IEEE Antenna's Propag Mag 44(1), February 2002
7. Poonkuzhali R, Alex ZC, Balakrishnan T (2016) Miniaturized wearable fractal antenna for military applications at VHF band. Prog Electromagnet Res C 62:179–190
8. Roy S, ChakrabortyU (2019) Metamaterial based dual wideband wearable antenna for wireless applications. Wirel Pers Commun
9. Lee EC, Soh PJ, Hashim NBM, Vandenbosch GAE, Volski V, Adam I, Mirza H, Aziz MZAA Design and fabrication of a flexible minkowski fractal antenna for VHF applications
10. Veselago VG (1968) The electrodynamics of substances with simultaneously negative values of μ and ε. Sov Phys Uspekhi 10(4):509–514
11. Mishra P, Pattnaik SS, Dhaliwal BS (2017) Square-shaped fractal antenna under metamaterial loaded condition for bandwidth enhancement. Prog Electromagnet Res C 78:183–192
12. Pattnaik SS, Joshi JG, Devi S, Lohokare MR (2010) Electrically small rectangular microstrip patch antenna loaded with metamaterial. IEEE
13. Suganthi S, Raghava S, Kumar D, Thilagar SH (2012) A compact hilbert curve fractal antenna on metamaterial using CSRR. In: PIERS proceedings, March 2012
14. Numan AB, Sharawi MS (2013) Extraction of material parameters for metamaterials using a full-wave simulator. IEEE Antennas Propag Mag 55(5), October 2013

GUI Development of IRNSS Receiver

Rashi Gautam, Vaisvik Chaudhary, and Sachin Gajjar

Abstract The satellite navigation system is the most important asset for any country in the world. Global navigation satellite system (GNSS) encompasses all global satellite positioning systems like global positioning system (GPS) from the USA, global navigation satellite system (GLONASS) from Russia, Galileo from Europe and BeiDou from China, regional Navigation systems like Quasi-Zenith Satellite System (QZSS) from Japan, and Indian Regional Navigation Satellite System (IRNSS) from India. The Indian Regional Navigation Satellite System (IRNSS) by Indian Space Research Organization (ISRO) consist of a group of seven satellites that cover the Indian boundary and 1500 km extended area near the border. The aim of this work is to develop graphical user interface (GUI) for IRNSS receiver that can use the navigation files in excel format, process it and provide position, velocity, time (PVT) information. It can also plot PVT data and display the coordinates on Google Maps. The GUI is developed with using Python 3.6 with Python Tkinter toolkit. Plot facility of the GUI takes navigation file as input and plots it into six kinds of information, i.e., ground track, position, velocity, altitude, clock bias, and intersystem bias. It also allows to save the plots at desirable locations in the computer. Google Maps facility provides the receiver location on Google Maps with the coordinates.

Keywords IRNSS · GNSS · ISRO · GLONASS · GUI · RTKLIB · RINEX · CSV · PVT · SPP

R. Gautam · V. Chaudhary · S. Gajjar (✉)
Institute of Technology, Nirma University, Ahmedabad, India
e-mail: sachin.gajjar@nirmauni.ac.in

R. Gautam
e-mail: 17bec031@nirmauni.ac.in

V. Chaudhary
e-mail: 16bec025@nirmauni.ac.in

1 Introduction

During the Kargil war, the Indian military faced difficulties because foreign countries refused to provide assistance for its navigation system. The Indian government then decided to have India's Navigation System under the Indian Space Research Organization (ISRO) to avoid consequences occurring due to the unavailability of navigation technology in the future. Indian Regional Navigation Satellite System (IRNSS) project started in 2006 with development of IRNSS, a group of seven satellites that covers the geographic area of India. Services provided by IRNSS system are standard positioning service (SPS) that is available to all the users (L5 and S frequency band) and restricted service (RS) is an encoded facility available only to authorized users (L5). ISRO has successfully launched seven IRNSS satellites till 2018. IRNSS receiver requires software tool which can extract and process received data to make it useful for navigation. Navigation systems like GPS (USA), BEIDOU (China), GALILEO (Europe), and GLONASS (Russia) have their own software to process the raw data. Software like RTKLIB [1], GPSTK [2, 3], Bernese [4–6] support multi GNSS systems but none of them support the IRNSS system. However, these software do not support IRNSS. Hence, this work aims to develop GUI based software for IRNSS that can perform the following functionalities:

- Identify and extract relevant data from raw IRNSS receiver files.
- Convert data from the raw IRNSS receiver files to formats required for plotting
- Plot information like ground track, position, velocity, altitude, clock bias, and intersystem bias
- Provide location of receiver on Google Maps with the coordinates.

  The methodology adopted to develop the GUI-based software for IRNSS is below:

- Basics of GNSS were studied including navigation satellites orbits frequencies, distance from earth surface, message frames, subframes, etc.
- Basics of the software of various navigation systems were studied including the file formats and facilities available
- Difference between IRNSS and GNSS systems like the number of satellites, coverage area, frequencies, message frames-sub frames, etc. were studied
- Various programming languages, tools and associated libraries to develop the GUI for IRNSS were studied and compared to identify the appropriate language for the software development
- The various information fields from the raw files from IRNSS receiver was studied
- Data from raw files was extracted and converted to format required for plotting
- Location of receiver was extracted from RAW files, GUI was integrated with Google Maps, and the location coordinates of the receiver was plotted on the Google Maps.

  Rest of the paper is organized as follows. Literature review is presented in Sect. 2. Section 3 discusses the GUI development process along with the software modules developed and tested. Paper is concluded in Sect. 4.

2 Literature Survey

2.1 Infrastructure

The infrastructure of IRNSS receivers consists of three segments [7]. The first segment is space segment that consists of seven satellites present in the space at various positions. Second segment is ground segment consists of: (i) spacecraft control center (SCC) that manages and maintains the satellite constellation, (ii) IRNSS telemetry and command stations and (iii) CDMA ranging stations. The third segment is user segment which consists of a specially designed dual frequency receiver.

A satellite navigation system with a global coverage is termed as a global navigation satellite system (GNSS). GPS [8], GLONASS [9], BeiDou [10], and Galileo [11] are examples of such GNSS systems. IRNSS is regional navigation satellite system (RNSS) system that cover the Indian boundary and 1500 km extended area near the border. To evaluate the performance of any navigation system a software tool is required. Popular GNSS software tools are RTKLIB [1], GPSTk [2, 3], gLAB [12] [13] and Bernese [4]. A comparison of these software tools based on their features, support for different GNSS system, support for file formats, and support for operating system platform is presented in Table 1.

The major applications of this tools are for (i) identify and extract relevant data from raw the receiver files, (ii) converting the receiver files containing the raw data files to appropriate formats for plotting, and (iii) plot information like ground track, position, velocity, altitude, clock bias, and intersystem bias.

As seen in the Table 1, none of the navigation software supports the IRNSS receiver.

Table 1 Navigation systems and associated software

System	IRNSS	GPS	BeiDou	GLONASS	Galileo
Country	India	USA	China	Russia	Europe
Coverage	Regional	Global	Global	Global	Global
Satellites	7	24	23	24	26
Frequency	L5-1.176 GHz S-2.492 GHz	L1-1.563 GHz L2-1.215 GHz L5-1.164 GHz	B1-1.561 GHz B2-1.201 GHz B3-1.268 GHz	G1-1.593 GHz G2-1.237 GHz G3-1.89 GHz	E1-1.559 GHz E2-1.164 GHz E6-1.260 GHz
Coding	CDMA	CDMA	CDMA	CDMA	CDMA
Precision (m)	20	5	10	4.5–7.5	1
Software	None	Bernese, RTKLIB. gLAB	TEQC, RTKLIB	Bernese, RTKLIB, gLAB	Bernese, RTKLIB, gLAB

Further, from among the software surveyed it is found that RTKLIB is a constantly evolving open source software and is best suited for processing receiver files as it supports a number of file formats, protocols, positioning algorithms and modes. Hence, the major aim of this work is to develop graphical user interface (GUI)-based software. The software will be similar to RTKLIB and will be for IRNSS receiver. It will use the navigation files in excel format, process it and provide position, velocity, and time (PVT) information. It can also plot PVT data and display the coordinates on Google Maps.

2.2   RTKLIB

RTKLIB is developed at Tokyo University Marine Science and Technology by Tomoji Takasu and Akio Yasuda [14, 15]. RTKLIB is for standard and precise positioning with GNSS. RTKLIB package consists of a portable program library and several application programming interfaces (API) utilizing the library. Users can use the APIs, install or link the libraries with their own program and modify the source codes according to the requirements of applications [1, 14, 15].

Some of the noteworthy features of RTKLIB are [1, 14, 15]:

- It supports standard and precise positioning algorithms for GPS, GLONASS, Galileo, BeiDou, SBAS [12] and QZSS [16] navigation systems
- It supports Single, DGPS/DGNSS, Kinematic, Static, Moving-Baseline, Fixed, PPP-Kinematic, PPP-Static and PPP-Fixed positioning modes with GNSS to create GUI using Python Tkinter. Different for both real-time and post-processing
- It supports RINEX, RTCM, BINEX, NTRIP, NMEA, SP3-c, ANTEX, IONEX, NGS PCV, and EMS formats and protocols for GNSS.
- It supports NovAtel, Hemisphere, u-blox, SkyTraq, JAVAD, Furuno, and NVS receiver's proprietary messages
- It supports serial, TCP/IP, NTRIP, and FTP/HTTP based external communication.

3   GUI Development and Results

As discussed in Sect. 2, the software tools available for GNSS are RTKLIB, GPSTk, gLAB, and Bernese. Out of these software RTKLIB supports GPS, GLONASS, Galileo, BeiDou, SBAS, and QZSS. GPSTk supports GPS, Bernese supports GPS, GLONASS and gLAB supports GPS, GLONASS, and Galileo. Even though RTKLIB supports most of the systems, it does not support IRNSS. IRNSS requires a new software as the existing software tool are not available to support it. A typical software tool for navigational system must have functions to identify and extract relevant data from raw receiver files, convert data from the raw receiver file to various file formats required for plotting, derive coordinates from the file and locate them on maps. In this work, a software like RTIKLIB that would support IRNSS is developed and tested.

The Python language is selected for developing GUI because python is simple, portable, object oriented and supports a number of graphical libraries. The code written in Python is easy to read, understand and debug. Above all, compared to other object-oriented languages Python code is 5–10 times shorter than C++ and 2–3 times shorter than Java which will be very beneficial when working on a big project such as software for navigational systems [17].

The IDE used for developing GUI is Visual Studio. It is freeware source code editor developed by Microsoft for Windows, macOS and Linux [18]. The features are support for debugging, syntax highlighting, intelligent code completion, snippets, code refactoring, and embedded Git. It supports various languages such as Java, JavaScript, Go, Node.js, Python and C++ . The version used for developing GUI is 1.54.3 for 64 bit with Python extensions. Python interpreter used is Python 3.9.1 64-bit [17].

In python to develop a GUI a special toolkit is required called Tkinter. Tkinter provides 'standard' toolkit, it is included in the base Python distribution and Tkinter code runs on any system with Python installed. Plotting options like scatter plot, bar plot, and plotting in HTML file is available in Python-Tkinter. Python Tkinter provides library for buttons, radio buttons, scroll, file dialog, processing tab, cascade windows, adjustment and position of the windows and buttons. It provides option to select color of the GUI windows. Libraries like ttk, filedialog, button, ImageTk, image, date and time, and Pandas are also used for developing various features in the GUI [19].

3.1   Results and Discussion

Figure 1 shows the main window of the GUI-based software. As seen in the figure, the major functions Plot and Google maps are developed in the GUI.

Main window displays the information in forms of labels. There are two button which will open pop-up windows. There is also a date and time stamp given at the bottom of the window.

Figure 2 shows the pop up window when button "Plot" is clicked. Next when a solution file (raw IRNSS receiver file) is selected, it is processed and converted to format required for plotting by the software. Next using buttons "GNDTRK", "POSITION", "VELOCITY", "ALTITUDE", "CLOCK BIAS", AND "INTER SYSTEM BIAS" different plots can be generated. The plots have option to be saved at desired location in the computer system.

As shown in Fig. 3, the first button is GND TRK which is a ground track in which the position, latitude and longitude have been tracked and plotted as longitude against latitude on the graph. The next button is the POSITION button, where the user position (X, Y, Z coordinates) is plotted with reference to time.

Figure 4 shows the VELOCITY button displays the velocities in X, Y and Z direction over the period of time. The ALTITUDE button plots the altitude of the receiver/user with respect to time.
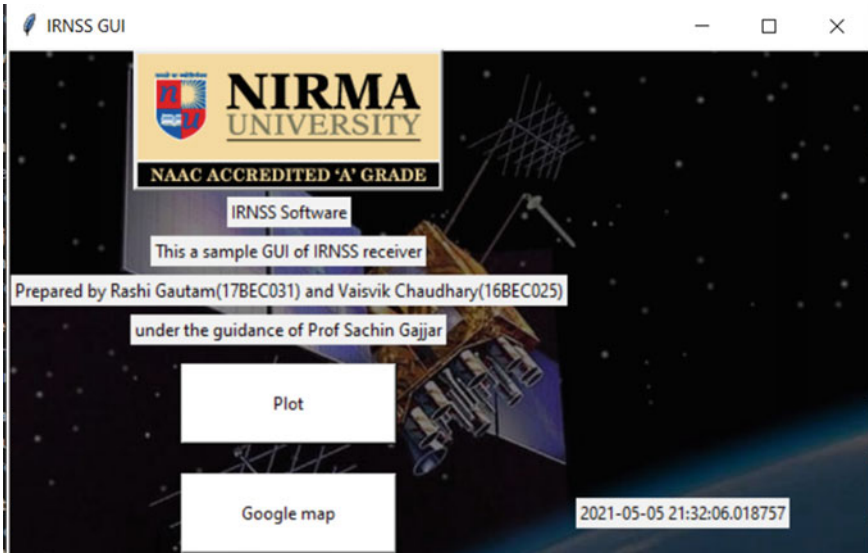
Fig. 1 Main window
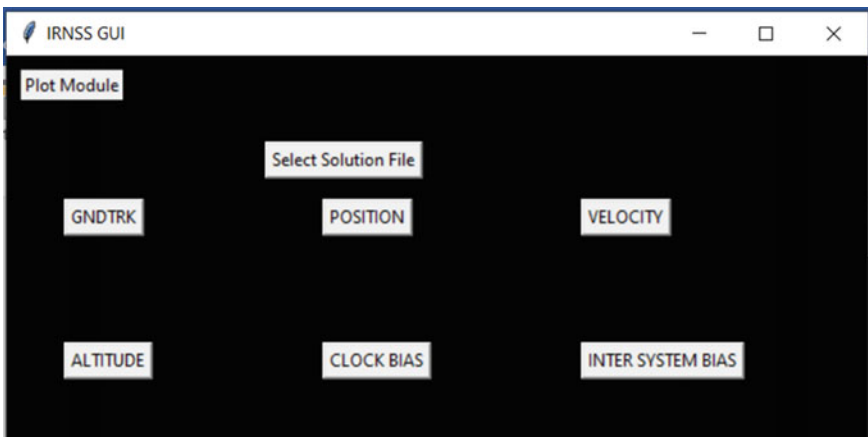
Fig. 2 Plot module

The CLOCK BIAS button gives the clock bias value of the receiver over the time. This is the difference between the receiver clock and the satellite clock. The INTER SYSTEM BIAS button gives the plot between Inter System Bias against the time as seen in Fig. 5.

As shown in the Fig. 6, when button "Google Map" is clicked, it pops a new window which opens Google Maps in browser. In the maps the co-ordinates are shown which were obtained by processing solution file.
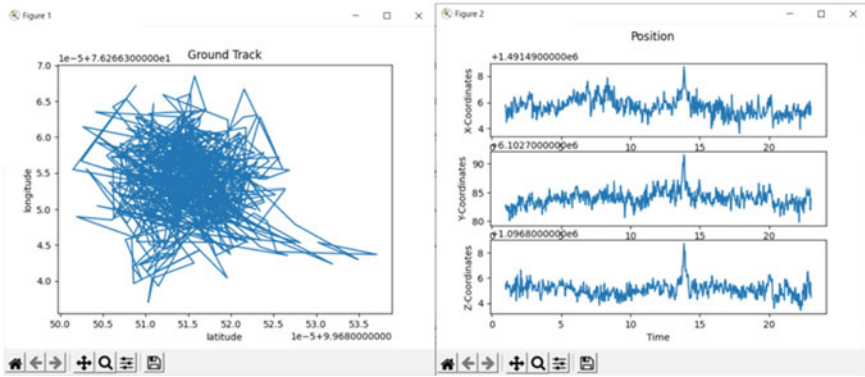
Fig. 3 Ground track and position plots
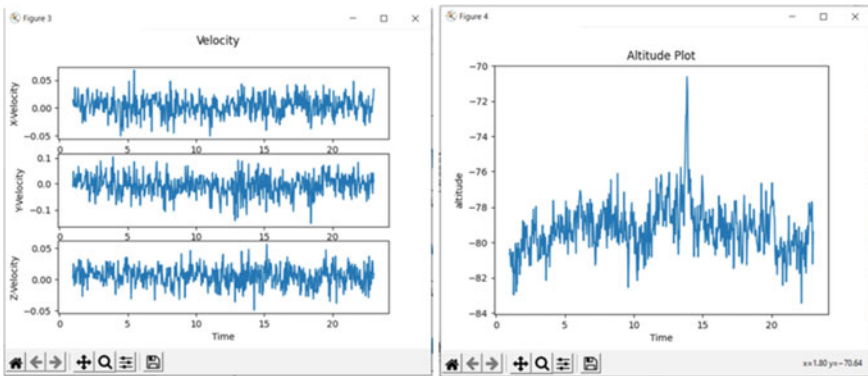
Fig. 4 Velocity and altitude plot
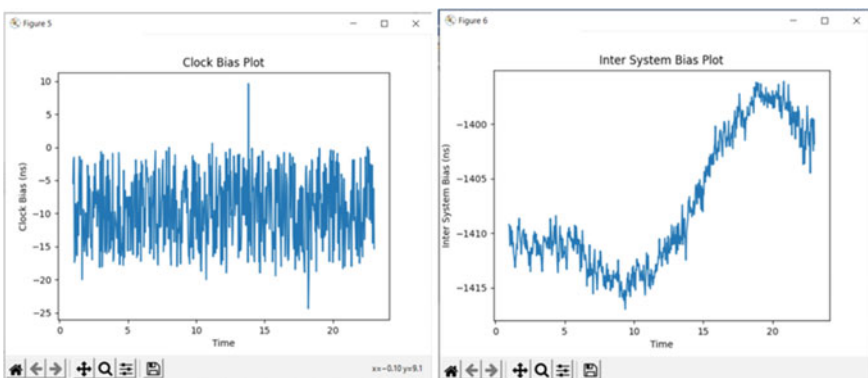
Fig. 5 Clock bias and inter system bias plots
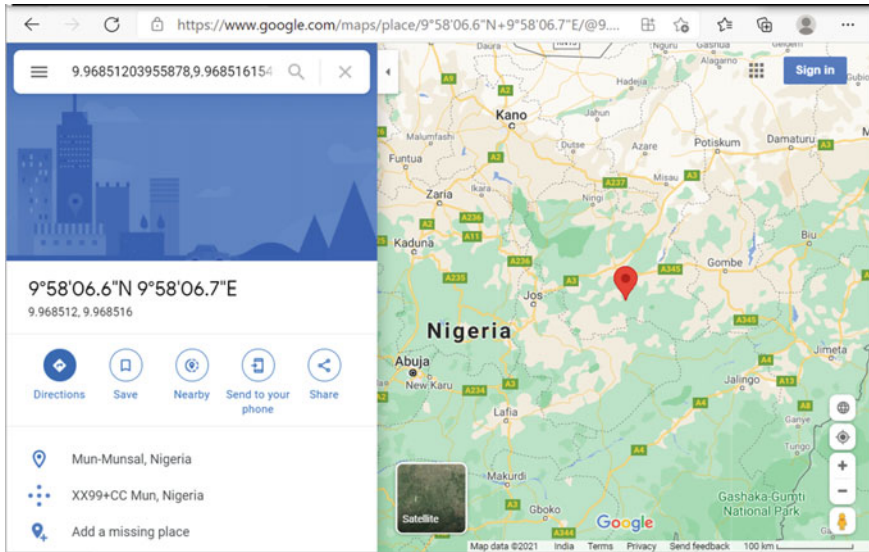
Fig. 6 Google maps in browser

4   Conclusion and Discussion

Software is a vital part of any navigation system and commonly used by researchers and scientists for processing the raw navigation system receiver files. The software tools features are used for analyzing and enhancing the positioning performance by performing experiments. The popular GNSS software tools available are RTKLIB, GPSTk, Bernese, and gLAB. RTKLIB supports almost all GNSS systems including GPS, Galileo, GLONASS, BeiDou, and QZSS. However, it does not support the IRNSS. The paper describes the GUI that is developed using Python with Tkinter library using Visual Studio IDE. GUI has two main modules (i) Plot and (ii) Google Maps. Plot module processes the data from raw IRNSS receiver files and plots the essential parameters. The plots are "gndtrk", "position", "velocity", "altitude", "clock bias", and "inter system bias". These plots can be saved on desirable locations in computer system. Google Maps module opens the browser and displays the coordinates of the locations on the Google Maps.

References

1. RTKLIB: An open source program package for GNSS positioning. http://www.rtklib.com/. Last accessed May 1 2021
2. The GPS toolkit—applied research laboratories. https://github.com/SGL-UT/GPSTk/. Last accessed May 1 2021

3. Conn T, Gaussian T, Harris J, Mach J, Munton D, Renfro B, Tolman B, Craddock T (2012) GPS toolkit: user guide for scientist, engineers and students. Department of Surveying, Helsinki University of Technology

4. Bernese: GPS/GNSS post-processing tools. https://www.unavco.org/software/data-processing/postprocessing/bernese/bernese.html. Last accessed May 1 2021

5. Subirana J, Zornoza J, Pajares M (2013) GNSS data processing: fundamentals and algorithms, European space agency communications

6. Geospatial world-What are the various GNSS systems. https://www.geospatialworld.net/blogs/what-are-the-various-gnss-systems/. Last accessed, May 1 2021

7. Indian Regional Navigation Satellite System (IRNSS). https://www.isro.gov.in/irnss-programme. Last accessed May 1 2021

8. U.S. Space Force, GPS: The global positioning system. https://www.gps.gov/systems/gps. Last accessed May 1 2021

9. Information and analysis center for positioning, navigation and timing, Russia, global navigation satellite system Glonass open service performance standard. https://glonass-iac.ru/en. Last accessed May 1 2021

10. BeiDou Navigation Satellite System (BDS). http://en.beidou.gov.cn. Last accessed May 1 2021

11. Galileo: The European global satellite-based navigation system, https://www.gsa.europa.eu/european-gnss/galileo. Last accessed May 1 2021

12. Ibanez D, Rovira-Garcia A, Sanz J, Juan J, Gonzalez-Casado G, Jimenez-Banos D, Lopez-Echazarreta C, Lapin I (2018) The GNSS laboratory tool suite (gLAB) updates: SBAS, DGNSS and global monitoring system. In: 9th ESA workshop on satellite navigation technologies and European workshop on GNSS Signals and Signal Processing, pp 1–10, IEEE, Netherlands

13. Sanz J, Rovira-Garcia A, Heranndez-Pajares M, Juan J, Ventura-Traveset J. Lopez-Echazarreta C, Hein G (2012) The ESA/UPC GNSS-Lab Tool (gLAB) an advanced educational and professional package for GNSS data processing and analysis

14. RTKLIB ver. 2.4.2 Manual. http://www.rtklib.com/prog/manual_2.4.2.pdf. Last accessed May 1 2021

15. An Introduction to RTKLIB open source GNSS processing software. https://www.oicrf.org/an-introduction-to-rtklib-open-source-gnss-processing-software. Last accessed May 1 2021

16. Quasi-Zenith Satellite System (QZSS). https://qzss.go.jp/en/. Last accessed May 1 2021

17. Python Software Foundation documentation. https://docs.python.org/3/. Last accessed May 1 2021

18. Microsoft Visual Studio Documentation. https://visualstudio.microsoft.com/downloads/. Last accessed May 1 2021

19. Tkinter—Python interface to Tcl/Tk. https://docs.python.org/3/library/tkinter.html. Last accessed May 1 2021

A 1 Gbps VLC System Based on Daylight and Intensity Modulator

Poonam Devi and Ravi Kr. Maddila

Abstract Visible light communication is a fast-growing technology that is being explored as a prominent option for future communication. It solves the problem of RF spectrum crunch with a license-free spectrum by reducing the cost of the communication system. A transmitter architecture including an external modulator is proposed in this article which can be employed in the indoor environment. The calculated BER at 1 Gbps data rate is 5.6×10^{-5}.

Keywords Visible light communication · Intensity modulator · Optical filter · BER

1 Introduction

Visible light communication (VLC) has been a very popular communication technology for decades and is still in the developing phase. It is a very well-known topic in the industry because of LEDs as LEDs can be used as the optical source and illuminance source in VLC system [1, 2]. The growth of LED has been recommendable due to its lifetime, efficiency, or energy-saving behavior. The fast switching characteristics of LED made it convenient for communication systems as optical source [3]. Although, some problems are caused due to switching of LED as flickering. VLC also needs dimming support because the optical source used in VLC is also used as an illumination source in the room [4]. VLC could also solve the problem of a limited RF spectrum.

Many VLC systems are reported using multiple modulation schemes with additional circuits for dimming support. The modulation techniques reported for VLC systems have their pros and cons, but the major problem with these schemes is the limitation on data rate [5, 6]. LED has fast switching characteristics. The continuous

P. Devi (✉) · R. Kr. Maddila
Department of Electronics and Communication, Malviya National Institute of Technology Jaipur, Rajasthan, India
e-mail: 2018rec9022@mnit.ac.in

switching of LED creates flickering which can be noticeable by human eyes and harmful to it. An external modulator can be employed which can increase the data rate, remove the dimming support circuit, and reduce the flickering problem.

This article is organized into four sections. The first section introduces VLC and the need for an external modulator in VLC. The existing VLC systems are explained in [7]. The proposed VLC setup is explained in Sect. 2 with transmitter and receiver components. As explained in [7], the VLC system consists of an information source, LED, dimming control circuit, channel, filter, and photodetector. An external modulator is introduced in this article while replacing LED with daylight optical source and removing dimming control circuit. The receiver link is the same as the existing link. Section 3 enlightens the simulation results. The conclusion of the paper and the future of work are summarized in the last section.

2 Proposed VLC System

Visible light communication (VLC) can be considered for indoor and outdoor applications. VLC system consists of a transmitter, channel, and receiver. Several modules are defined in the transmitter and receiver. Some important modules are the optical source, optical filter, optical concentrator, modulator, and photodetector. The proposed structure of the transmitter, receiver, and channel is explained in the following sections with their numerical modeling.

2.1 Block Diagram of Proposed Transmitter

Figure 1 shows the architecture of the transmitter used for the proposed system. It contains an optical source, optical concentrator, optical filter, and electro-optic intensity modulator. Detailed analysis is done for all modules in the following subsections.

2.1.1 Optical Source

LED is used as a conventional optical source in VLC systems but in this article, daylight is proposed as an optical source for VLC. The location plays an important role in the variation of solar spectrum throughout the day. There is a standard reference spectrum which is defined for academic research purpose. The data of solar spectrum falling directly on earth surfaces is AM 1.5 direct (+circular) which is provided by NREL transforming agency. The data includes solar spectral irradiance with respect to wavelength which is plotted in MATLAB, shown in Fig. 2 and can be used for optical signal processing.

Solar irradiance is defined as power received per unit area which electromagnetic radiation of sun. The power of solar spectrum can be calculated from this data and can
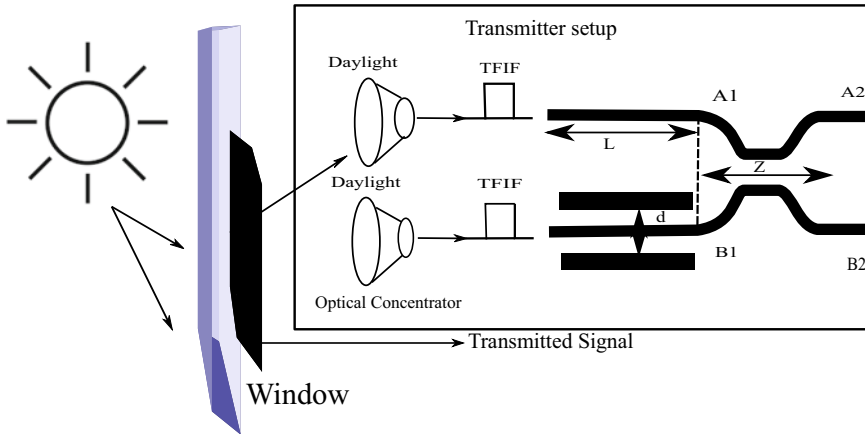
Fig. 1 Architecture of VLC transmitter
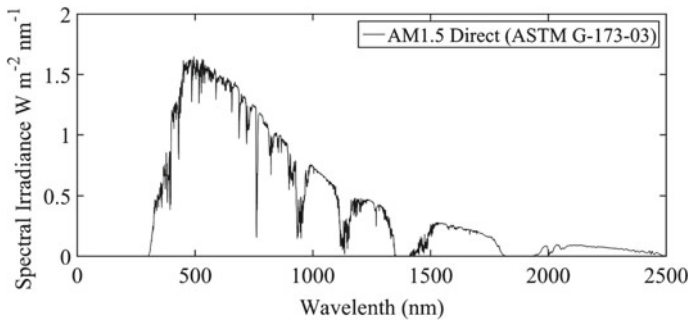
Fig. 2 Solar spectrum (solar irradiance wrt wavelength)

be processed for further communication process as an optical source. The spectrum has all the wavelength but modulator works in particular wavelength which can be extracted using an optical filter in this article.

2.1.2 Optical Concentrator

The capacity of VLC systems depends on the signal-to-noise ratio at the receiver end and channel bandwidth. But small bandwidth of LEDs limits the speed of data transmission. Similarly, the high-speed receiver or photo-detector used in the VLC system has a very small active area to receive an optical signal which affects the collection of optical signal and signal-to-noise ratio. The optical concentrator is used to increase the collected power on the receiver side which also increases the SNR and improves the capacity of the VLC system [8]. The optical concentrator is a device that is used to concentrate optical power over a confined space. Basic concepts for solar
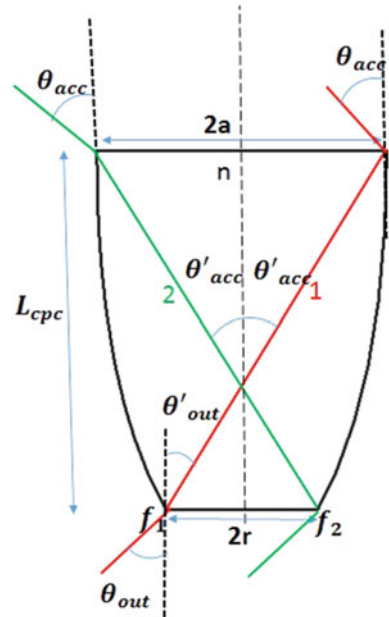
concentrators include used optics, principle characteristics, shapes of concentrators, etc. In non-imaging optics, the concentration of emitted radiation is focused instead of creating imaging. The difference between non-imaging and imaging optics is shown in the figure. In the figure, optical system is not focusing on farming images, and emitted radiation including radiation from intermediate zones is falling on the all-over surface of the receiver which is just the opposite of imaging optics. The principal characteristics of an optical concentrator are explained by geometrical concentration ratio, acceptance angle, optical efficiency, and homogeneity of the illumination flux.

Compound parabolic concentrator (CPC) has gained the interest of academic researchers and industrialists because of its efficient solar energy collection. CPC belongs to non-imaging optics. The basic principle of CPC is explained through the edge ray principle of the string method. The shape of CPC concentrator is same as rotation of the parabola about the concentrator axis.

The CPC can be designed considering 2D and 3D structure, dielectric-filled CPC, and special shapes of CPC. The range of acceptance angle can be increased using a dielectric material in CPC. The geometry of CPC could be asymmetric, seashell, lens walled, and CPC with the convex absorber. The structure of CPC can be decided based on applications. It could be made with reflective materials on the sidewalls or filled with dielectric materials. Some materials like stainless steel, aluminum plating, nickel gold plating, etc., with high reflectivity are used in making sidewalls (Fig. 3).

The geometrical parameters pf CPC are internal and external acceptance angles, length, input radius, and exit radius. All these parameters are related with each other and can be calculated using following equations [9]:
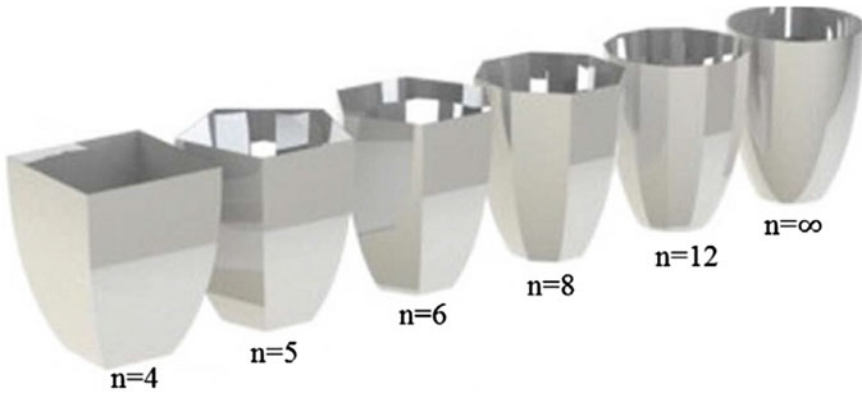
Fig. 4 3D polygon CPCs with sides and revolved CPC ($n = \infty$) [10]

$$a \quad = nr\sin(\theta_{\mathrm{acc}}) \tag{1}$$

$$L = (a + r)\cos(\theta_{\mathrm{acc'}}) \tag{2}$$

where a is input radius, r is exit radius, L is length, θ_{acc} is external acceptance angle, and θ_{acc} is internal acceptance angle.

In our VLC system, we have considered CPC with an acceptance angle $20°$ and exit angle $90°$. Its exit diameter is $63\,\mathrm{mm}$ and height is $68.84\,\mathrm{mm}$ with geometrical concentration 2. Author has proved that performance of CPC can be improved by increasing the no of facets. The number of facets can be 4, 5, 6, 8 12 or as shown in Fig. 4. The circular CPC can achieve 100% optical efficiency. CPC with circular facet is used in proposed VLC. The optical efficiency of used CPC could be 92%.

Concentration ratio of solar concentrator is defined as the "ratio of solar radiation entering the collector to solar radiation received by the receiver." It shows the concentrating ability of system. Due to variation in the intensity of solar radiation, it is hard to obtain concentration ratio using Eq. 3. To solve above problem, geometric concentration ratio is introduced. It is ratio of the light aperture area to the receiver area. The diameter of entry surface can be calculated using Eq. 4 [11].

$$C = I_{\mathrm{ap}}/I_{\mathrm{abs}} \tag{3}$$

$$C_{\mathrm{geo}} = A_{ap}/A_{\mathrm{abs}} \tag{4}$$

where A_{ap} is area of light aperture and A_{abs} is area of receiver.

The area of surface on which solar light is falling, i.e., circular, can be calculated using πr^2 which is $6231.27\ \mathrm{mm}^2$. Unit of solar irradiance is watt/m^2. So the power

of incident light can be calculated by multiplying the respective area. Total amount of power at exit area can be calculated using optical efficiency which is given by following Eq. 5 [12]—

$$\eta = P_{\text{out}}/P_{\text{in}} \tag{5}$$

where P_{out} is exit power at the system and P_{in} is power at the system entrance.

2.1.3   Optical Interference Band Pass Filters and Intensity Modulator

An optical filter is employed before intensity modulator to extract the desired operating wavelength of modulator. The intensity modulator which is proposed in this article is shown in Fig. 5. Solar energy is applied at the input of intensity modulator which travels through the straight arms which are made of electro-optic material LiNbO_3. The working principal of intensity modulator is same as MZM except the first 3 dB power splitter. The detailed analysis of optical interference band pass filters and intensity modulator is done in our previous article [13]. But the modulator which has been proposed here has different physical characteristics. It is miniaturized version of the previous intensity modulator. The equations to calculate A_1, A_2, B_1 and B_2 are explained in article [13].

ER is figure of merit of EO modulator, which is calculated using Eq. 6. In this case, two powers are P_{on} and P_{off} which represents power at output port 1 in presence and absence of electrical signal at electrode representing '1' and '0' message bit, respectively [14]. This ratio should be as large as possible to differentiate input signal at receiver side.

$$ER = 10 \log \frac{P_{\text{on}}}{P_{\text{off}}} \tag{6}$$

IL is defined as the fraction of signal power attenuated due to propagation through the device. It is a combination of coupling loss, waveguide propagation loss, and other losses. It must be as small as possible and generally measured in decibel (dB). Ideally, it should be 0 dB for a loss-less path. It can be calculated by using equation given below-

Fig. 5 Proposed modulator design
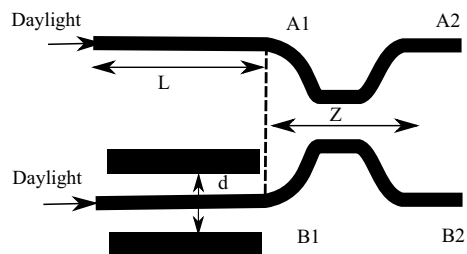
Table 1 Designing parameters

Parameters	Numerical value
Width of waveguide (a)	1.5
Distance between electrode in μm (d)	3.6
Operating wavelength in nm (λ)	520
Length of interferometric arm in mm (L)	1.5
Applied voltage in Volts (V)	5.3357
Coupling length of second coupler in mm (z)	2.5
Total length of device in mm (L_T)	4

$$IL = 10 \log \frac{P_{\text{on}}}{P_{\text{in}}} \tag{7}$$

where P_{in} is input power.

The designing parameter of proposed intensity modulator is (Table 1).

These parameters are used in both simulation, optical and numerical. The ER of the proposed modulator is **15.8375 dB** and IL is **0.0212 dB** and these results are calculated using Eqs. 6 and 7. The ER and IL are used to calculate the total power transmitted through the modulator.

2.2 Block Diagram of Proposed Receiver

The signal is transmitted through a channel where random noise is added. In the proposed system, additive white Gaussian noise (AWGN) is considered. There is an optical filter, photodetector, and matched filter. The optical filter removes the other signals and selects the desired wavelength signal. The received signal is compared with the transmitted signal and BER is calculated. The photodetector converts the optical signal into electrical signal, matched filter maximize the received signal peak, and decode message bits based on the energy level (Fig. 6).
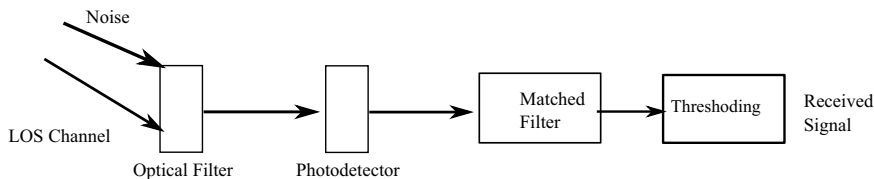
Fig. 6 Proposed receiver block diagram

3 Simulation Results

In error analysis, few assumptions are made as follows:

- The transmitter is in line of sight (LOS) of receiver and the channel imposes no multipath dispersion and no path loss.
- The only source for noise is shot noise which is assumed as a white Gaussian.
- Interference of other light source is not considered here (Fig. 7).

The proposed transmitter and receiver are simulated in MATLAB. Here, we did not consider factors as light reflected from walls, interference from ambient light, and other factors. We have considered photodiode with responsivity 1. The responsivity of any photodiode is the output signal (typically voltage or current) of the detector produced in response to a given incident radiant power falling on the detector. The signal length is 10^7 and the data rate is fixed at 1 Gbps. The bit error rate (BER) is calculated at a 1 Gbps data rate. The fig. ref shows the BER vs. SNR graph. As the SNR is increased, BER started decreasing because the signal power is increased in comparison with noise power. Calculated BER is in the range 10^{-5}. In [15], an optical concentrator is considered at the receiver side which will increase the SNR. In [16], the considered SNR is in the range of 90–135 dB. In both references, authors have reported BER is in the range of 10^{-4}–10^{-6}. The BER for the proposed design falls in this range only without considering higher SNR (1–12 dB) and any optical concentrator at the receiver side.
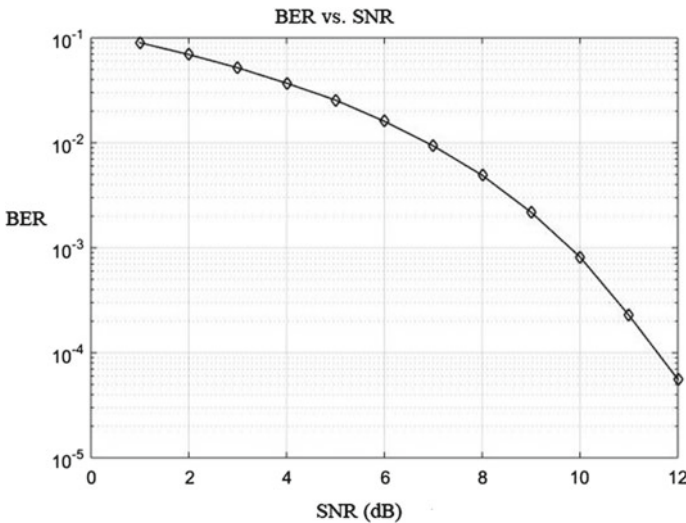
Fig. 7 BER versus SNR

4   Conclusion and Future Work

The VLC is enhancing its domain. It is widely employed in indoor communication, under water communication, and vehicle communication [1–3]. VLC is also reported for 5G communication [17, 18]. So the efficiency of VLC system in real-life communication matters. The modulation plays an important role in sending data efficiently and deciding data rate in optical wireless communication system. The article has proposed a VLC system which is simulated in MATLAB and results indicate it to be an efficient system although other factors like channel modulation and ambient light interferences need to be considered in real-life implementation.

References

1. Matheus LEM, Vieira AB, Vieira LFM, Vieira MAM, Gnawali O (2019) Visible light communication: concepts, applications and challenges. IEEE Commun Surv Tutor 21:3204–3237. https://doi.org/10.1109/COMST.2019.2913348
2. Khan LU (2017) Visible light communication: applications, architecture, standardization and research challenges. Digital Commun Netw 3:78–88. https://doi.org/10.1016/j.dcan.2016.07.004
3. Rehman SUU, Chong S, Yongchareon PHJ, Komosny S (2019) Visible light communication: a system perspective-overview and challenges. Sensors 19:1153. https://doi.org/10.3390/s19051153
4. Rajagopal S, Roberts RD, Lim S-K (2012) IEEE 802.15.7 visible light communication: modulation schemes and dimming support. IEEE Commun Mag 50:72–82. https://doi.org/10.1109/MCOM.2012.6163585
5. Zafar F, Karunatilaka D, Parthiban R (2015) Dimming schemes for visible light communication: the state of research. IEEE Wirel Commun 22(2):29–35. https://doi.org/10.1109/MWC.2015.7096282
6. Aliaberi A, Sofotasios PC, Muhaidat S (2019) Modulation schemes for visible light communications. In: 2019 international conference on advanced communication technologies and networking (CommNet), pp 1–10. https://doi.org/10.1109/COMMNET.2019.8742376
7. Popoola W, Rajbhandari S, Ghassemlooy Z (2017) Optical wireless communications: system and channel modelling with MATLAB, CRC Press, United States. https://books.google.co.in/books?id=xR8uDwAAQBAJ
8. Riaz A, Collins S (2019) A slab fluorescent concentrator for visible light communications. In: 2019 2nd IEEE Middle East and North Africa COMMunications conference (MENACOMM), pp 1–4. https://doi.org/10.1109/MENACOMM46666.2019.8988526
9. Himer E, Ayane SE, Yahyaoui SE, Salvestrini S, Ahaitouf JE, Ali (2020) Photovoltaic concentration: research and development. Energies 13(21):5721. https://doi.org/10.3390/en13215721
10. Tian M, Su Y, Zheng H, Pei G, Li G, Riffat S (2018) A review on the recent research progress in the compound parabolic concentrator (CPC) for solar energy applications. Renew Sustain Energy Rev 82, Part 1:1272–1296. https://doi.org/10.1016/j.rser.2017.09.050
11. Ochieng RM, Onyango FN (2009) Investigation of the geometric concentration ratio of a modified cone concentrator generated from a compound parabolic concentrator (CPC) by use of configurational geometry. Int J Energy Environ Econ 17(1):11–27. https://doi.org/030003.10.1063/1.5053502
12. Himer SE, Ahaitouf A, El-Yahyaoui S, Mechaqrane A, Ouagazzaden A (2012) A comparative of four secondary optical elements for CPV systems. AIP Conf Proc. https://doi.org/030003.10.1063/1.5053502

13. Devi P, Maddila RK (2020) Energy saving visible light communication with daylight. In: 2020 IEEE international conference on electronics, computing and communication technologies (CONECCT), pp 1–4. https://doi.org/10.1109/CONECCT50063.2020.9198331

14. Wooten EL, Kissa KM, Yi-Yan A, Murphy EJ, Lafaw DA, Hallemeier PF, Maack D, Attanasio DV, Fritz DJ, McBrien GJ, Bossi DE (2000) A review of lithium niobate modulators for fiber-optic communications systems. IEEE J Sel Topics Quantum Electron 6:69–82. https://doi.org/10.1109/2944.826874

15. Riaz A, Collins S (2019) A slab fluorescent concentrator for visible light communications. In: 2019 2nd IEEE Middle East and North Africa communications conference (MENACOMM). Manama, Bahrain, pp 1–4.https://doi.org/10.1109/MENACOMM46666.2019.8988526

16. Liu X, Chen Z, Wang Y, Zhou F, Luo Y, Hu RQ (2019) BER analysis of NOMA-enabled visible light communication systems with different modulations. IEEE Trans Veh Technol 68(11):10807–10821.https://doi.org/10.1109/TVT.2019.2938909

17. Idris S, Mohammed U, Sanusi J, Thomas S (2019) Visible light communication: a potential 5G and beyond communication technology. In: 2019 15th international conference on electronics, computer and computation (ICECCO), pp 1–6. https://doi.org/10.1109/ICECCO48375.2019.9043201

18. Feng L, Hu RQ, Wang J, Xu P, Qian Y (2016) Applying VLC in 5G networks: architectures and key technologies. IEEE Netw 30(6):77–83. https://doi.org/10.1109/MNET.2016.1500236RP

Performance of MISO Systems with Alamaouti Transmit Diversity and Antenna Selection in TDD and FDD

Dehit H. Trivedi, Neel N. Joshi, and Y. N. Trivedi

Abstract In this paper, the focus is to obtain performance of a multiple input and single output (MISO) wireless communication system in a real-time scenarios of time division duplex (TDD) and frequency division duplex (FDD). We consider a MISO system equipped with $2N$ transmit antennas. In the total N pairs of antenna, there is a spatial correlation in each pair (two antennas) only. We assume quasi-static Rayleigh fading channels. We select one pair of antennas with the highest channel power gain. In case of FDD, we assume antenna selection and detection, both based on imperfect channel state information (CSI), whereas in case of TDD, detection is based on imperfect CSI, but antenna selection is to be done using perfect CSI. Finally, we use Alamouti transmit diversity. For this system, we present the performance in terms of bit error rate (BER) versus avg. signal-to-noise ratio (SNR) and outage probability versus avg. SNR using Monte Carlo simulations. We have seen the adverse effect of spatial correlation and imperfect CSI on the performance. We conclude that TDD outperforms the FDD due to higher antenna selection gain.

Keywords Alamouti transmit diversity · Transmit antenna selection (TAS) · Spatial channel correlation · Imperfect channel state information (CSI)

1 Introduction

The next generation mobile communication is demanding for high data rate, which can be accomplished by using techniques such as higher-order adaptive modulation and adaptive channel coding, multi-carrier modulation and multiple antenna systems [1]. In which multi-antenna systems, popularly known as multiple input multiple

D. H. Trivedi (✉) · N. N. Joshi · Y. N. Trivedi
Department of Electronic and Communication Engineering, Institute of Technology, Nirma University, Ahmedabad 382481, India
e-mail: dehit.trivedi@gmail.com

Y. N. Trivedi
e-mail: yogesh.trivedi@nirmauni.ac.in

output (MIMO) is adopted in standards such as LTE and WiMAX due to high spectral efficiency [2], measured in bits per hertz . However, this can be fulfilled by adding complexity such as radio frequency chains (RFC) corresponding to each transmit or receive antenna. The power consumption and space requirements increase with number of RFC. Therefore, antenna selection is used, in which full diversity can be exploited with reduced number of RFC [3]. However, to exploit the benefits of MIMO systems with antenna selection, channel state information (CSI) is to be estimated perfectly. Unfortunately, in the real-time scenario, it is not possible always to have perfect CSI. Therefore, detection with imperfect CSI results in error floor in the BER versus SNR performance [4]. Furthermore, antenna selection with imperfect CSI results in loss of diversity gain [5]. Another paper [6] proposed similar system model, as ours, of selecting subset of transmit antennas from the given set, however, only accounting for perfect CSI. The second issue in real-time scenario is spatial correlation [7] between adjacent antennas due to limited spacing between antennas. The spatial correlation reduces the diversity gain [8].

In the next generation wireless communication, the variance of data rate is very high. Some applications are based on fast broadband communication such as real-time gaming, where target is high spectral efficiency. On the other hand, some applications may require low data rate communication with tolerable delay such as Internet of Things (IoT) or communication in low power sensor network, where the target is higher energy efficiency. In both the cases, base station uses either time division duplex (TDD) or frequency division duplex (FDD). Both the duplex schemes have pros and cons over other [9]. For example, FDD supports high data rate communication with double the spectrum compared to TDD. In case of FDD, two separate channels are required for Uplink and Downlink, whereas in TDD, the same channel is used for Uplink as well as for Downlink in different time slots, which restricts the data rate due to limited time slot in TDD.

In case of MIMO, where CSI is also required at the transmitter, the TDD has a benefit over FDD. During the first time slot, BS estimates the channel and then uses the same channel for transmit beamforming or transmit antenna selection. In this case, the chances of perfect antenna selection are high as the BS can estimate the channel well due to high onboard resources. If we consider a case of FDD, then Uplink and Downlink channels are separate. Hence, the user will estimate the Downlink channel and then feed it back to the transmitter for antenna selection at the BS. In this case, channel estimation quality may be low at the user because of the limited resources and erroneous feedback channel. There, in FDD, antenna selection may not be perfect compared to antenna selection in TDD.

In this paper, we have considered a MISO system with a real-time practical scenario with FDD or TDD. We have assumed $2N \times 1$ MISO system, where imperfect CSI is available at the receiver (user side). In case of FDD, we assume antenna selection based on imperfect CSI, and in case of TDD, we assume antenna selection based on perfect CSI. The correlation between actual CSI and the imperfect CSI is denoted by ρ. At the BS, we assume N pairs of antennas, where in each pair, there are two antennas. There is a spatial correlation η in each pair of antennas, however, there is no correlation between two pairs of antennas. Based on the perfect (in case of TDD)

or imperfect (in case of FDD) CSI, one pair of antennas is selected among all the pairs. Then, we use full Alamouti transmit diversity for the equivalent 2×1 system [10]. The detection at the receiver is assumed using imperfect CSI. We present the performance of the system in terms of BER versus SNR and outage probability versus SNR using simulations. We have presented the performance for different values of ρ and η for both FDD and TDD. We have seen that the performance of TDD is better than the performance of FDD as expected.

The rest of the paper is organized as followed. Section 2 describes the system model. Section 3 presents the BER and outage probability performance of the considered system for different values of ρ and η. Finally, Sect. 4 concludes the paper.

2   System Model

We consider a MISO system with $2N \times 1$ antennas or at the transmitter, total N pairs of antennas are there and each pair has two antennas. The underlying fading channels are assumed to be complex Gaussian with mean zero and variance one.

As shown in Fig. 1, the channel coefficients from first pair to the receiver are h_1 and h_2. Similarly, the channel coefficients between the last Nth pair and the receiver are h_{2N-1} and h_{2N}. Thus, channel coefficients between kth pair and receive antenna are h_{2k-1} and h_{2k}. In each pair, the spatial correlation is η. Thus,

$$E[h_{2k-1}^* h_{2k}] = \eta, \quad 1 \leq k \leq N, \ \ 0 \leq \eta \leq 1 \tag{1}$$
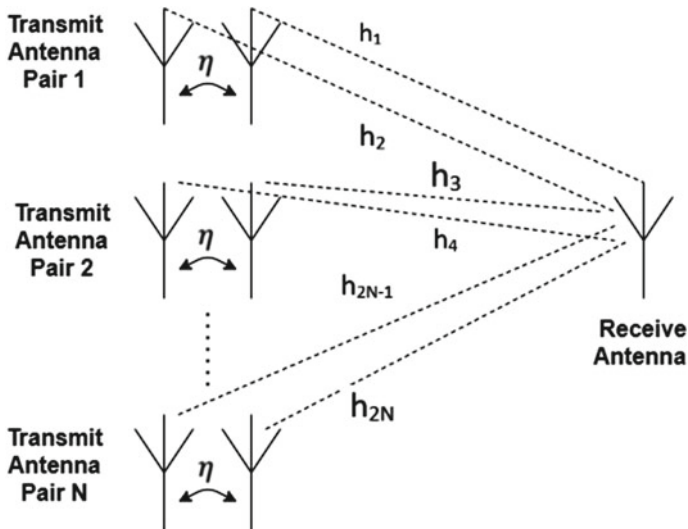
Fig. 1 Considered MISO system

Thus, h_{2k} is generated from h_{2k-1} using first-order Gauss–Markov model as follows.

$$h_{2k} = \eta h_{2k-1} + \sqrt{1 - \eta^2}\mu_{2k-1}, \leq k \leq N \qquad (2)$$

where h_{2k-1} and μ_{2k-1} are independent and identically distributed complex Gaussian random variables with mean zero and variance one. There is no correlation in between two pairs. At the receiver, imperfect CSI g_k is available instead of h_k, which is generated using first-order Gauss–Markov model as follows

$$g_k = \rho h_k + \sqrt{1 - \rho^2}\delta_k, \quad 1 \leq k \leq 2N, \ 0 \leq \rho \leq 1 \qquad (3)$$

where δ_k is complex Gaussian random variable with mean zero and variance one. Further, δ_k is independent of h_k.

Subsequently, we select the mth pair of antennas, which has the highest summation of the two channel power gain as shown below. For FDD, the mth pair is selected based on imprefect CSI, hence

$$m = \arg \max_{1 \leq k \leq N} \{|g_{2k-1}|^2 + |g_{2k}|^2\} \qquad (4)$$

In case of TDD, the mth pair is elected based on the perfect CSI, hence

$$m = \arg \max_{1 \leq k \leq N} \{|h_{2k-1}|^2 + |h_{2k}|^2\} \qquad (5)$$

We use g_k for detection in both the FDD and TDD. After selecting the two transmit antennas, we use Alamouti transmit diversity scheme. Hence, the received symbols y_1 and y_2 for two consecutive instants can be expressed as

$$\begin{bmatrix} y_1 \\ y_2^* \end{bmatrix} = \begin{bmatrix} h_{2m-1} & h_{2m} \\ h_{2m}^* & -h_{2m-1}^* \end{bmatrix} \begin{bmatrix} x_1 \\ x_2 \end{bmatrix} + \begin{bmatrix} n_1 \\ n_{2*} \end{bmatrix}$$

Here, x_1 and x_2 are assumed to be BPSK symbols with average power E_s, whereas n_1 and n_2 are i.i.d. complex Gaussian with mean zero and variance N_0. Thus, average SNR per symbol is denoted by $\gamma_c = E_s/N_0$.

Now, for both FDD and TDD, the detection variables $\hat{x}_1$ and $\hat{x}_2$ corresponding to x_1 and x_2, respectively, can be expressed

$$\hat{x}_1 = \begin{bmatrix} g_{2m-1}^* & g_{2m} \end{bmatrix} \begin{bmatrix} y_1 \\ y_2^* \end{bmatrix}$$

$$\hat{x}_2 = \begin{bmatrix} g_{2m}^* & -g_{2m-1} \end{bmatrix} \begin{bmatrix} y_1 \\ y_2^* \end{bmatrix}$$

As x_1 and x_2 are equi-probable binary symbols, the BER can be expressed as

$$P_e = \text{Prob}\{\hat{x}_1 \neq x_1\} \tag{6}$$

The outage probability P_o can be expressed as

$$P_o = \text{Prob}\{\gamma \leq \gamma_{th}\}$$

Here, γ can be expressed as

$$\gamma = \frac{|g_{2m-1}^* h_{2m-1} + g_{2m} h_{2m}^*|^2 \gamma_c}{|g_{2m-1}^* h_{2m} - g_{2m} h_{2m-1}^*|^2 \gamma_c + 2(|g_{2m-1}|^2 + |g_{2m}|^2)} \tag{7}$$

It can be seen that for perfect CSI, i.e., $g_{2m-1} = h_{2m-1}$ and $g_{2m} = h_{2m}$, (7) is reduced to $\gamma = (|h_{2m-1}|^2 + |h_{2m}|^2)\gamma_c/2$. In case of imperfect CSI, the presence of γ_c in the denominator of (7) results in error floor.

3 Results

In this section, we present the performance of the considered system in terms of BER versus avg. SNR and probability of outage versus avg. SNR for different values of spatial correlation ρ and imperfect CSI in terms of ρ. We have referred the case of imperfect antenna selection and perfect antenna selection as FDD and TDD respectively. We have assumed BPSK constellation and number of pair of antennas $N = 2$ or 3 for simulations.

Figure 2 presents BER versus avg. SNR for TDD taking $\eta = 0.5$ for different values of ρ such as 0.9 and 0.6. As expected, by increasing N, the performance improves due to better antenna selection gain and performance degrades when ρ reduces from 0.9 to 0.6. For $\rho = 0.9$, the error floor is also visible. Figure 3 presents BER versus avg. SNR for FDD taking $\eta = 0.5$ for different values of ρ such as 0.9 and 0.6. The same trend is visible for FDD also. In the outage probability, also the same trend is visible for both FDD and TDD.

Figure 4 presents BER versus avg. SNR for TDD taking $\rho = 0.9$ for different values of η such as 0.3 and 0.9. As expected, by increasing N, the performance improves due to better antenna selection gain and performance degrades when η increases from 0.3 to 0.9. The reason of the error floor is due to $\rho = 0.9$ (not having perfect CSI for detection or $\rho \neq 1$). Figure 5 presents BER versus avg. SNR for FDD taking $\rho = 0.9$ for different values of η such as 0.3 and 0.9. The same trend is visible for FDD also. In the outage probability, also the same trend is visible for both FDD and TDD.

Figure 6 presents BER versus avg. SNR for both FDD and TDD taking $\rho = 0.6$, $\eta = 0.5$. It can be seen that the TDD outperforms the FDD, as expected due to better antenna selection gain. It shows that in real-time scenario, if the BER degrades due to η and/or ρ, the mode can be changed from FDD to TDD.
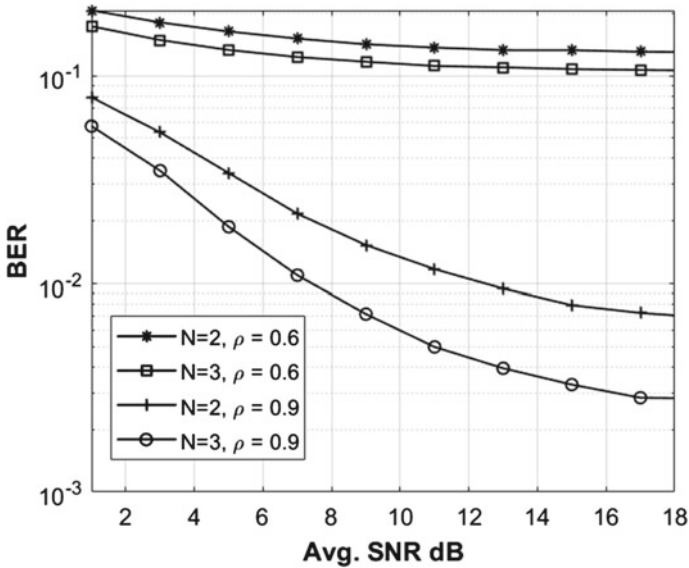
Fig. 2 BER versus avg. SNR, TDD, $\eta = 0.5$

In Fig. 7, we have shown the outage probability versus avg. SNR taking $\rho = 0.6$, $\eta = 0.5$, $N = 3$ and $\gamma_{th} = 3$ dB for FDD and TDD. The similar trend of BER can be seen in case of outage probability also. It is to be noted that the coverage probability of BS, $P_c = 1 - P_o$. Thus, P_c is more in case of TDD. For example, at the SNR of 11 dB, the $P_c = 0.66$ and 0.619 for TDD and FDD, respectively. Hence, the mobile can be switched from FDD to TDD to stay in coverage or to prevent it to go to the state of outage.

4 Conclusion

In this paper, we considered a MISO system with N pairs of antennas and in each pair two antennas are there. We assume spatially uncorrelated, however correlated in each pair with coefficient η, Rayleigh fading channels. We performed selection of the pair of antennas with highest channel power gain using imperfect CSI (referred as FDD) or using perfect CSI (referred as TDD). Finally, we used Alamouti transmit diversity and detection with the imperfect CSI. The imperfection in the CSI is referred by ρ for antenna selection (for FDD) and detection (for FDD and TDD). For the considered system, we presented BER versus avg. SNR and outage probability versus avg. SNR using simulations for $N = 2$ and 3. We conclude that the performance degrades, when ρ is reducing from 1 to 0 or/and η is increasing from 0 to 1, and N is decreasing from 3 to 2. The TDD outperforms FDD due to perfect antenna selection. Hence, the
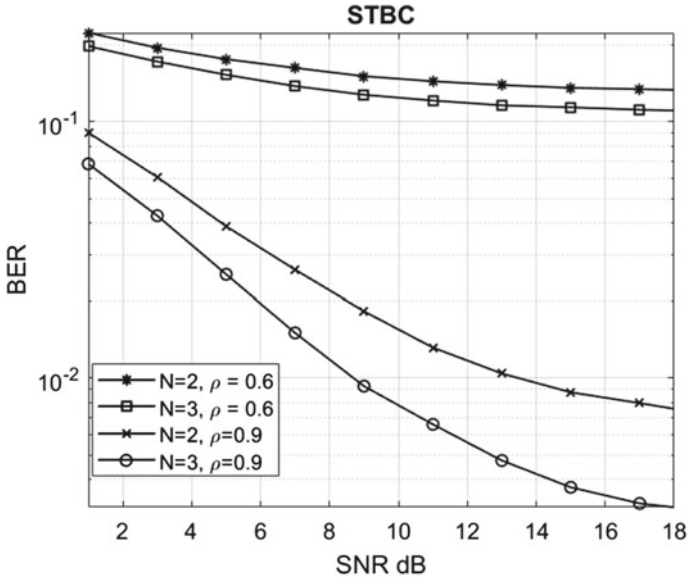
Fig. 3 BER versus avg. SNR, FDD, $\eta = 0.5$
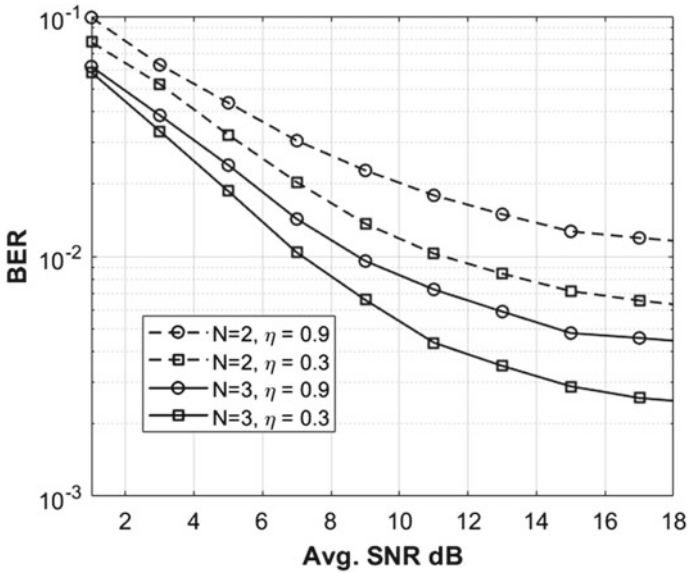
Fig. 4 BER versus avg. SNR, TDD, $\rho = 0.9$
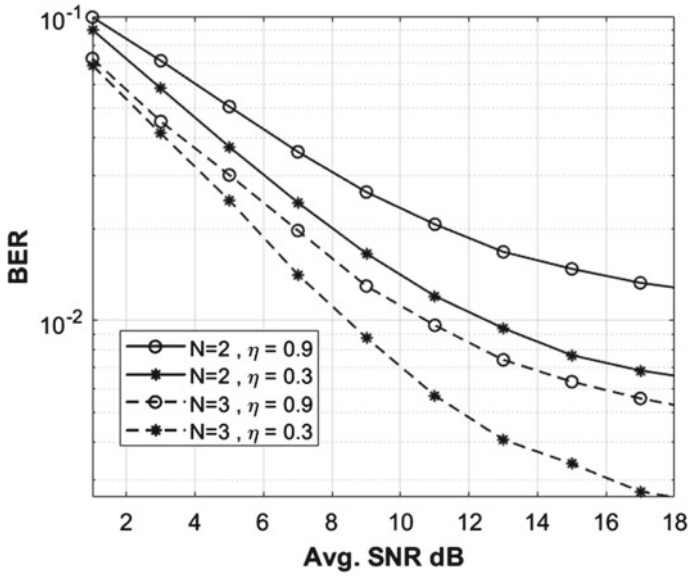
Fig. 5 BER versus avg. SNR, FDD, $\rho = 0.9$
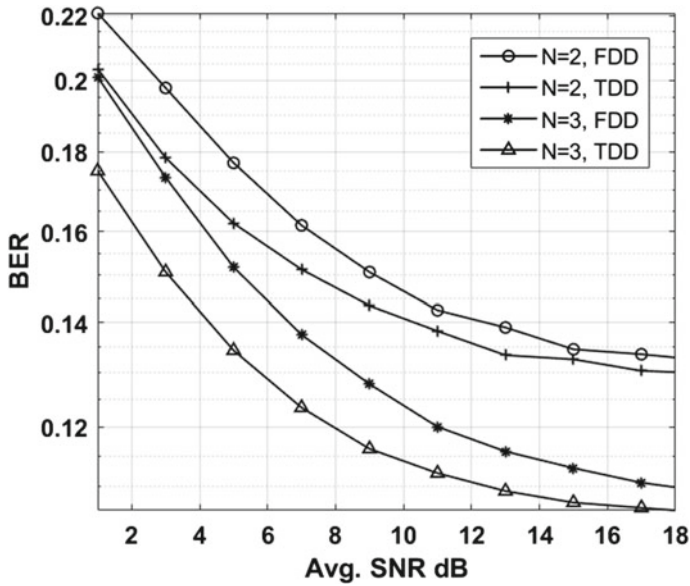
Fig. 6 BER versus avg. SNR, FDD and TDD comparison, $\eta = 0.5$, $\rho = 0.6$
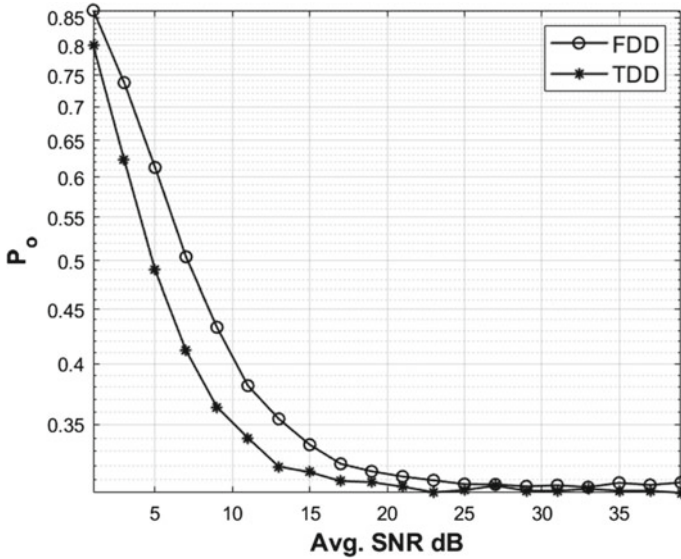
Fig. 7 P_o vs avg. SNR, FDD and TDD comparison for $\gamma_{th} = 3$ dB

operating mode can be switched from FDD to TDD, when the received SNR may drop, so that user may not suffer outage.

References

1. Tse D, Viswanath P (2005) Fundamentals of wireless communication. Cambridge University Press
2. Gheorghe C, Dragomir R, Alexandru Stoichescu D Massive MIMO technology for 5G adaptive networks. In: 2019 11th international conference on electronics, computers and artificial intelligence (ECAI)
3. Chen Z, Collings IB, Zhou Z, Vucetic B (2009) Transmit antenna selection schemes with reduced feedback rate. IEEE Trans Wirel Commun 8(2):1006–1016. https://doi.org/10.1109/TWC.2009.080296
4. Dietrich FA, Utschick W (2005) Impact of imperfect channel knowledge on transmit processing concepts. In: IEEE international conference on communications, vol 3. ICC, pp 1916–1921. https://doi.org/10.1109/ICC.2005.1494673
5. Yu X, Xu W, Leung S-H, Wang J (2018) Unified performance analysis of transmit antenna selection with OSTBC and imperfect CSI over Nakagami-m fading channels. IEEE Trans Veh Technol 67(1)
6. Chen Z, Collings IB, Zhou Z, Vucetic B (2009) Transmit antenna selection schemes with reduced feedback rate. IEEE Trans Wirel Commun 8(2):1006–1016. https://doi.org/10.1109/TWC.2009.080296
7. Sanguinetti L, Björnson E, Hoydis J (2020) Toward massive MIMO 2.0: understanding spatial correlation, interference suppression, and pilot contamination. in IEEE Trans Commun 68(1)

8. Chakravarti JM, Trivedi YN (2015) Performance analysis of MISO systems with antenna selection over correlated channels. In: Twenty first national conference on communications (NCC), pp 1–5. https://doi.org/10.1109/NCC.2015.7084837

9. Proakis JG (2001) Digital communication, 4 ed, MH

10. Alamouti SM (1998) A simple transmit diversity technique for wireless communications. IEEE J Sel Areas Commun 16(8):1451–1458. https://doi.org/10.1109/49.730453

Performance Analysis of OFDM-Based Optical Wireless Communication System

Aishwarya Medpalliwar, Abhishek Tripathi, and Shilpi Gupta

Abstract The Free Space Optics (FSO) is one of the best solutions for ever-increasing demand of higher bandwidth requirements. As in the FSO, the transmitted optical signal passes through the free space channel where the atmospheric attenuation due to fog and rainfall considerably decreases the performance of the system. In our analysis, link range of 1 km is considered in 64 QAM-OFDM system with a data rate of 10 Gbps, where the system is analyzed under different atmospheric conditions of rainfall and fog. Results show that the optical beam cannot prolong beyond 1 km as the atmospheric conditions worsens.

Keywords Power law parameters · Free space optics · Tropical climate

1 Introduction

The principle of Free Space Optics (FSO) is same as the optical fiber communication system, but the only difference is of the channel; here, the channel is free space instead of optical fiber. FSO is a line of sight communication technology, where the optical signal is transmitted through the free space channel [1]. The FSO system principle is that the narrow beam of laser which transfers the modulated information signal to the receiving end through the channel. The growth of internet traffic in conjunction with an increase in the number and range of new services has placed pressure on radio networks operating on low-speed infrastructure [2]. As the FSO system has higher bandwidth, thus, it can support higher data rate transmission. Besides the various advantages of the FSO system, it suffers from the main issue, i.e., the atmospheric attenuation. Thus, inclusion of the atmospheric parameters is must while designing of the system. The FSO link equation is as follows [2]:

A. Medpalliwar (✉) · A. Tripathi · S. Gupta
Department of Electronics Engineering, Sardar Vallabhbhai National Institute of Technology, Surat, Gujarat 395007, India
e-mail: Aishwarya.medpalliwar2611@gmail.com

S. Gupta
e-mail: sgupta@svnit.ac.in

$$P_R = P_T \frac{d_R^2}{(d_T + \theta R)^2} 10^{-\alpha R}/10 \qquad (1)$$

where P_R is received power, P_T is transmitted power, d_R and d_T are receiver and transmitter aperture diameter, respectively, θ is beam divergence, R is link range, and α is atmospheric attenuation.

In order to reduce the multipath fading, significant efforts are required. OFDM is a multi-carrier modulation technology in which the data is distributed over many subcarriers thus mitigating the problems such as multi-path interference and inter-symbol interference. In OFDM, the spectrum is efficiently used as the subcarriers are overlapping and orthogonal to each other, making it bandwidth efficient [3]. Thus, OFDM is the best choice for optical communication system. The use of OFDM makes the system secure, higher data rate support and high speed.

The atmosphere consists of many gases and microparticles such as aerosols, dust, smoke. Along with these small particles, large precipitation because of rain, haze, fog and snow is present in the channel. Out of all environmental factors, the attenuation caused by fog is adverse as the size of fog particle is comparable with the operating wavelength [4]. It thus changes the characteristics of the beam or can completely block the passage of beam because of absorption, scattering and reflection. To calculate the specific attenuation caused by fog, the relationship between visibility (V) and attenuation (α) must be known. The attenuation due to fog faces Mie scattering, but it includes complex calculations and requires information about the fog condition. Another approach is based on using visibility data, where the attenuation caused due to foggy weather is calculated using empirical method. The 550 nm wavelength is generally chosen as the reference wavelength. Equation (2) gives us the specific attenuation of fog by common empirical model for Mie scattering [5]:

$$\alpha(V) = \frac{13}{V}\left(\frac{\lambda}{550}\right)^{-q(V)} \qquad (2)$$

where V (km) is visibility, λ (nm) is the operating wavelength, $q(V)$ the scattering size distribution coefficient.

By Kim model, $q(V)$ is given as [5]:

$$q(V) = \begin{cases} 1.6 & \text{for } V > 50 \text{ km} \\ 1.3 & \text{for } 6 < V < 50 \text{ km} \\ 0.585 \, v^{1/3} & \text{for } 0 < V < 6 \text{ km} \end{cases} \qquad (3)$$

By Kruse model, $q(V)$ is given as [5]:

$$q(V) = \begin{cases} 1.6 & \text{for } V > 50 \text{ km} \\ 1.3 & \text{for } 6 < V < 50 \text{ km} \\ 0.16\,v + 0.34 & \text{for } 1 < V < 6 \text{ km} \\ v - 0.5 & \text{for } 0.5 < V < 1 \text{ km} \\ 0 & \text{for } V < 0.5 \text{ km} \end{cases} \qquad (4)$$

The visibility of weather condition is low during thick fog, and operating wavelength has less effect on the attenuation due to light fog and haze. If visibility is high, the attenuation is very less for 1550 nm as compared to 850 and 950 nm. As visibility range increases, such as in clear weather, dependence of the attenuation on the operating wavelength reduces.

Rainfall is an important factor causing attenuation of transmitted optical signal. Heavy rain is the main limiting factor for FSO link availability. The drop size distribution of rain and its intensities are required to understand the effect of rainfall on FSO link. These parameters are not mostly available or not easy to quantify. Hence, a general empirical relation between the specific rain attenuation (RSA) and rain rate is derived in decibel scale as follows [6]:

$$\gamma \left(\text{dB}/\text{km} \right) \, = \, k\, R^{\alpha} \qquad (5)$$

where R is the rain intensity (mm/h) and k and α are power law parameters which depend on frequency, microstructure of rain and temperature. In Eq. (5), we can easily calculate the RSA when the intensity data is available in mm/h. In FSO, there are many power law models for calculating specific rain attenuation. Carbonneau's model can be used to calculate the RSA. The measurement done however is for low R compared with the tropical region [7]. The Japan model made calculations for R values around 80 and 90 mm/h. Both of these models are suggested by ITU-R to calculate the RSA. One more model was also proposed in temperate region to calculate rain attenuation for rain rate of up to 100 mm/h in Prague. In tropical climatic conditions, model developed in Malaysia KL used ITU-R approach which is based on the relationship between the equal probability of experimental rain rate and rainfall attenuation. The commonly known drop size distribution based on Marshal-Palmer and Joss models in microwave systems is also now commonly used in FSO link. The specific attenuation of rainfall can be evaluated by the power law Eq. (5). The values of the parameters for k and α are arranged in Table 1.

The paper is organized as follows: Sect. 2 describes the simulation setup for 64 QAM-OFDM-based FSO system, and Sect. 3 describes the results and discussion. The paper is concluded in Sect. 4.

Table 1 k and α values of RSA models of FSO

Model	k	α	Region
Carbonneau (ITU-R)	1.076	0.67	Temperate
Japan (ITU-R)	1.58	0.63	Temperate
Prague	0.231	0.7	Temperate
Marshal and Palmer	0.365	0.63	Temperate
Malaysia (KL)	0.4195	0.8486	Tropical
Malaysia (Johar)	2.03	0.74	Tropical
Malaysia (Suriza)	0.3988	0.7601	Tropical

2 System Description

The system under test is designed by the use of OptiSystem™ 17, and the schematic layout is shown in Fig. 1. Here, the OFDM modulated data is converted into an optical signal and then transmitted through free space. The complete system is comprised by the transmitter, atmospheric channel and receiver. The information or message signal gets processed through many stages, viz., generation, conversion into electrical signals, and then passes through free space in the form of optical signal. As the transmitted optical beam gets severely affected by the atmospheric conditions, thus considering the parameters is important before system design. Here, the system is analyzed under the effect of rainfall and fog.
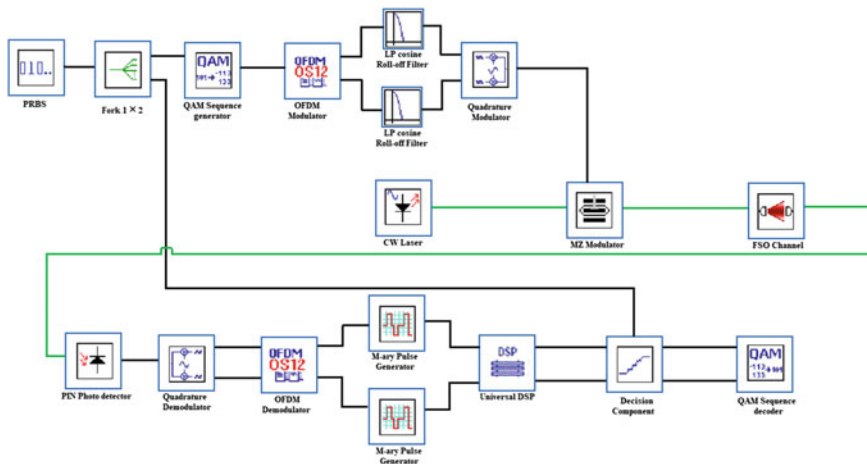
Fig. 1 Schematic block diagram of OFDM-FSO communication system

2.1 Rainfall Analysis

Proper knowledge of rainfall attenuation is essential for the design of the new wireless optical communication system. RSA is calculated using the existing available attenuation models, but they are suitable in the temperate regions as the highest R is less than compared to the tropical regions. According to the ITU-R P.1814 [8], the precipitation rate of 0.25 mm/h is for drizzle, 2.5 mm/h for light rain, 12.5 mm/h for moderate rain, 25 mm/h for strong rain and 100 mm/h for stormy rainfall. Tropical and subtropical Indian regions experience heavy rain up to 300 mm/h, and hence, understanding of rainfall statistics is important before designing the FSO link. Rainfall data for four consecutive years from the Indian metrological department is considered in Table 2. India is home of a verity of extraordinary climate region, and there exists regional and temporal variation in the rainfall distribution [9].

According to the rainfall data recorded by Indian Meteorological Department (IMD), the heaviest rainfall may reach 600 mm in a day. To have knowledge of all this data is important for worst case analysis. To get the highest average rainfall data for four years similar analysis is done for four consecutive years, i.e., 2015, 2016,

Table 2 Meteorological subdivision-wise heaviest one-day rainfall—SW monsoon 2015, 2016, 2017 and 2018 and their average per hour rainfall rate [10–12]

Met subdivision	Highest one-day recorded rainfall				Four years averaged monsoon rainfall	Average per hour rainfall rate
	R (mm/h) 2015	R (mm/h) 2016	R (mm/h) 2017	R (mm/h) 2018		
Assam and Meghalaya	745	549	638	384	579	289.5
Saurashtra and Kutch	636	341	450	496	480.75	240.3
Gujrat region	495	348	497	316	414	207
Konkan and Goa	475	528	468	491	490.5	245.25
West Madhya Pradesh	387	302	261	336	321.5	160.75
Odisha	330	240	395	622	396.75	198.375
Arunachal Pradesh	278	321	263	150	253	126.5
Vidarbha	270	300	342	282	298.5	149.25
Kerala	228	269	235	398	282.5	141.25
East Madhya Pradesh	221	340	190	299	262.5	131.4
West Uttar Pradesh	189	310	284	226	252.25	126.25
Uttarakhand	159	318	245	277	249.75	124.8

Table 3 Rainfall specific attenuation values for different weather conditions

Weather conditions	Precipitation or R (mm/h)	RSA (dB/km) $2.03R^{0.74}$
Storm	100	61.305
Strong rain	25	21.977
Average rain	12.5	13.158
Light rain	2.5	3.999
Drizzle	0.25	0.727

2017 and 2018. I considered worst analysis, the heaviest rain data of day is available, and it is necessary to make certain assumption for the analysis. As from the power law equation, we require rainfall rate in mm/h, and this data is not available; thus, it is required to convert rainfall rate from mm/day to mm/h, which can be carried out in two ways.

(1) The traditional mathematical procedure, i.e., dividing per day data by total hours in a day.
(2) More real approach and do probable assumptions.

By using the values of *R*, we can calculate the *RSA* in dB/km using the models available. As from the above analysis, it is clear that India experience heavy rainfall, and the models suggested by ITU-R have considered very less rainfall values for their calculation of power law parameters. Thus, we have considered the parameters (Malaysia-Johor) available for tropical region. By considering the rainfall categories depending on the ITU-R P.1814 as shown in Table 3, we have calculated the RSA value by considering the parameters available for tropical region.

2.2 Fog Analysis

Fog is made of minute water droplets present in air, and its diameter is less than 100 μm. It is admitted in theory that there is fog when visibility is reduced to less than 1 km, and the relative humidity of the air reaches the saturation level (relative humidity close to 100%) [5]. Due to the atmospheric constituents, there is decrease in power level, i.e., attenuation of laser beam caused by several factors, including absorption and Rayleigh or Mie scattering. Out of all these factors, the attenuation caused by fog is considered adverse as fog particle size is comparable with the operating wavelength in FSO link. It changes the characteristics of the transmitted light, or it may completely block the passage of beam because of absorption, scattering and reflection. The values of attenuation with their corresponding visibilities are considered in Table 4.

The attenuation due to fog is dependent on the visibility conditions, and the transmitted optical signal encounters interference due to the fog particles. Table 5 shows the parameters that are considered for analyzing the system.

Table 4 Specific attenuation value for different fog weather condition

Fog conditions	Attenuation (dB/km)
Thick fog	65
Moderate fog	26
Light fog	7.743
Haze	1.177

Table 5 OFDM-based FSO system parameters for performance analysis

Parameters	Values	Units
Wavelength	1550	nm
Power	3–10	mW
Link range	200–1000	meters
Total bit rate	10	Gbps
Bits per symbol	6	Bits/symbol
No. of subcarriers	Variable	–
D_T	2.5	cm
D_R	8	cm
Baseband modulation	64-QAM	–
Responsivity	1	A/W
Attenuation	Variable	dB/km
Refractive index structure parameter (C_n^2)	1×10^{-14}	$m^{-2/3}$
Beam divergence	1	mrad

3 Results and Discussion

3.1 System Analysis Under Rainfall

About 10 Gbps data is generated using 64 QAM sequence generator using 6 bits per symbol. Before modulated at 7.5 GHz using a quadrature modulator, the QAM data is modulated by an OFDM modulator using 64 and 128 subcarriers. This signal is modulated by using LiNb-MZM modulator. We have RF-OFDM signal which is then transformed to optical form by using RF to optical-up converter. The QAM-OFDM signal is transmitted by means of a continuous wave (CW) laser with wavelength of 1550 nm having power of 10 mW.

At the receiver, the signal is recovered using a PIN photodetector and the output is given to the QM demodulator which is followed by the OFDM block and QAM sequence decoder to get the original 10 Gbps data successfully. Figure 2 shows the measured received power for increasing link range under different weather condition. The different values of attenuation considered are 0.727 dB/km for drizzle, 3.999 dB/km for light rain, 13.158 dB/km for average rain, 21.977 dB/km for strong

rain and 61.305 dB/km for storm. Table 6 shows the value for total power for different link ranges of FSO transmission link under all rainfall conditions. Figure 2 depicts the measurement of total received power against different link range under different rainfall weather conditions. It can be seen that the stormy weather deteriorates the power performance of the systems when compared to other rainfall conditions.

I have built a 10Gbit/s 64QAM-OFDM-based FSO transmission system and investigated the performance of signals with different subcarriers. The signals with 64 and 128 subcarriers are transmitted over 1 km. Firstly, I have compared the number of symbols in error for 64 subcarriers and 128 subcarriers over a distance of 1 km. Table 7 shows the values of no. of symbols in error for 64 and 128 subcarriers-based proposed system under the light and strong rainfall condition with the RSA value of 3.99 dB/km for light rainfall and 21.97 dB/km for strong rainfall, respectively.

From Fig. 3, we can see that the no. of symbols that are in error using 64 subcarriers is very less compared to 128 subcarriers. For instance, let us consider at a link range of 1000 m under light rainfall, the difference is of 189 symbols which is huge. Also
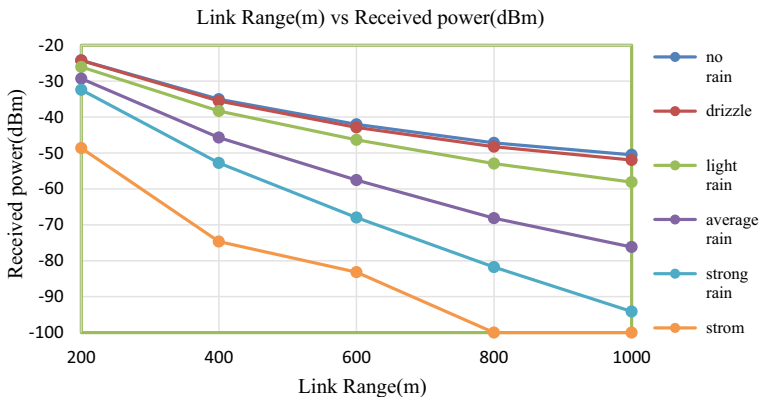
Fig. 2 Evaluation link range versus received power under different rainfall conditions for 64 QAM-OFDM-FSO system

Table 6 Evaluation for link range versus received power under different rainfall conditions

Link range (m)	No rain	Drizzle	Light rain	Average rain	Strong rain	Storm
	Power (dBm)	Power (dBm)	Power (dBm)	Power (dBm)	Power (dBm)	Power (dBm)
200	− 24.20	− 24.23	− 26.03	− 29.31	− 32.41	− 48.64
400	− 35.00	− 35.50	− 38.31	− 45.70	− 52.77	− 74.66
600	− 42.02	− 42.87	− 46.32	− 57.54	− 67.99	− 83.18
800	− 47.19	− 48.23	− 52.95	− 68.15	− 81.75	− 100
1000	− 50.50	− 51.96	− 58.10	− 76.17	− 94.15	− 100

Table 7 Evaluation of link range versus no. of symbols in error under different rainfall conditions

Link range (m)	Number of symbols in error			
	64 subcarriers		128 subcarriers	
	Light rain	Strong rain	Light rain	Strong rain
200	39	36	206	258
400	48	59	212	270
600	51	65	224	283
800	56	89	233	293
1000	61	102	250	319

for strong rainfall condition, complete received symbols are in error with a difference of 217.

The results show that as the number of subcarriers increases here 64 to 128, the value of error symbols will gradually increase and the quality of the received optical signals will deteriorate. Thus, we can conclude that the error performance of with 64 subcarriers is better than 128 subcarriers. Hence for further analysis, I have considered 64 subcarriers for the given system. When an optical information signal propagates through the channel, random variations in air temperature and pressure lead to refractive index inhomogeneity; this results in affecting the amplitude and phase of the signal. Further, we have studied the EVM (%) and symbol numbers in error for light and strong rainfall with turbulence and without turbulence condition. In Table 8, we have considered the gamma–gamma turbulence model for the channel with refractive index structure parameter value of $C_n^2 = 1 \times 10^{-14}$ m$^{-2/3}$.

From Fig. 4, we can see that with increase in the link range, there is reduction in error performance of the system under the influence of rainfall with turbulence. For
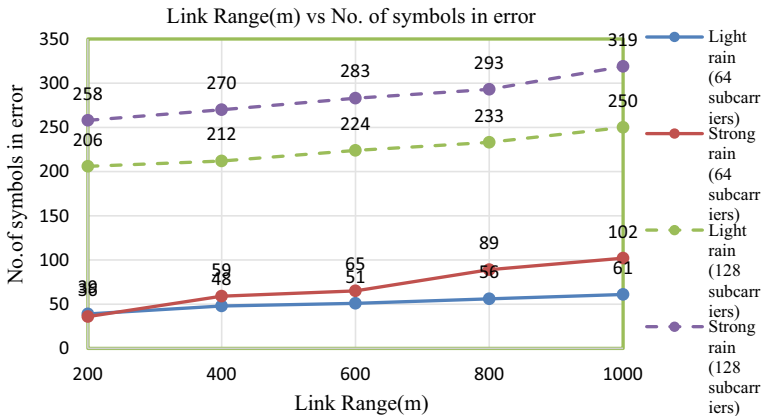
Fig. 3 Evaluation of error symbols against link range under strong and light rainfall with 64 and 128 subcarriers for the proposed system

Table 8 Evaluation error symbols and EVM (%) against link range under different rainfall conditions for 64 subcarrier

Link range (m)	Without turbulence				With turbulence			
	Light rain (3.99 dB/km)		Strong rain (21.97 dB/km)		Light rain (3.99 dB/km)		Strong rain (21.97 dB/km)	
	Error symbols	EVM (%)	Error symbols	EVM (%)	Error symbols	EVM (%)	Error symbols	EVM (%)
200	39	8.446	36	8.377	62	10.832	101	11.031
400	48	8.950	59	8.953	102	10.794	106	11.757
600	51	10.321	65	9.632	128	11.442	139	12.136
800	56	9.236	89	11.310	153	12.239	211	13.025
1000	61	10.031	102	11.354	202	12.886	246	12.742

instance, there is an increase in the symbol error of about 141 when comparing light rainfall with and without turbulence. From Fig. 4, we can see that as we increase the link range, the error vector magnitude increases. The EVM is a measure of modulation quality and error performance which is mathematically denoted as the root mean square value of the difference between the ideal symbol that is transmitted and received symbols in I/Q plane.

The plot of EVM (%) for light and strong rainfall conditions is shown in Fig. 5. There is a difference of ~2.85% (without turbulence) and ~1.6% (with turbulence) in the EVM %. Thus with increase in attenuation due to atmosphere, there is chance that constellation points deviate from its ideal position.

In Fig. 5, the plotted graphs of the EVM (%) against link range for light and strong rainfall condition (with/without turbulence) are given; it is found that the
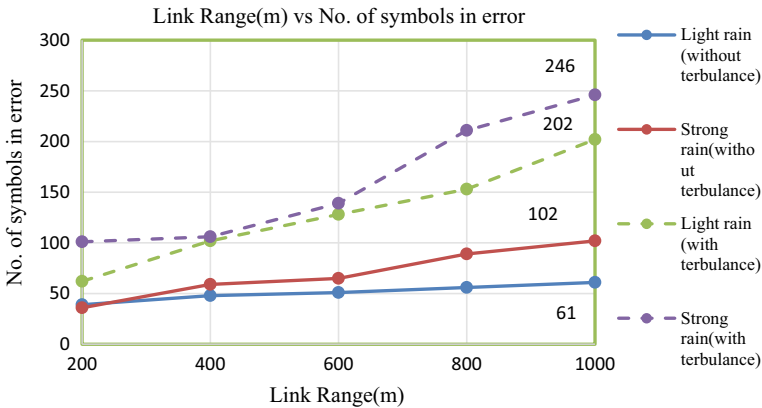
Fig. 4 Error symbols versus link range under the effect of strong and light rainfall conditions with and without turbulence for proposed system
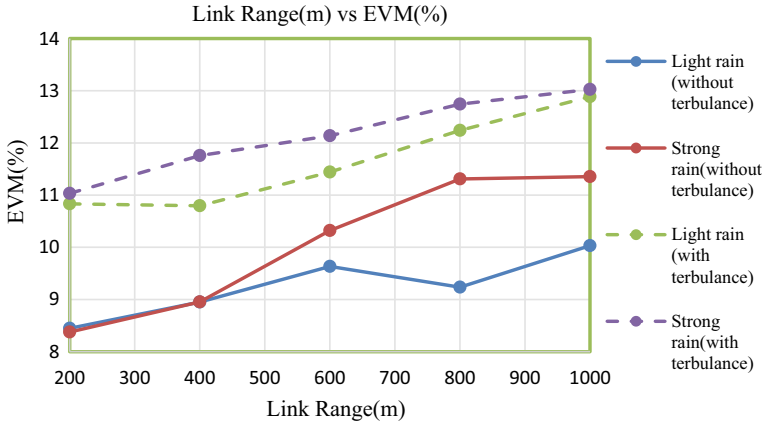
Fig. 5 EVM (%) as a function of link range under strong and light rainfall conditions with and without turbulence for simulative system

strong rainfall (in presence of turbulence) causes more error symbols compared to strong rainfall (in absence of turbulence).

3.2 System Analysis Under Fog Condition

Fog is considered as one of the most deteriorating factors in FSO communication systems. Foggy weather condition is classified on the basis of visibility conditions. The specific attenuation due to fog is dependent on the operating wavelength, visibility and the value of $q(V)$ based on either Kim or Kruse model. In the analysis, we have considered Kruse model (Eq. 7) for calculating $q(V)$. The values of attenuation (dB/km) considered for analyzing the system are given in Table 9. As from Fig. 3, we concluded that the error performance by considering 64 subcarriers is better than considering 128 subcarriers for proposed communication system, and thus the fog analysis is done by considering 64 subcarriers. The signal is transmitted by means of a continuous wave (CW) laser with wavelength of 1550 nm and power 3 mW. In this analysis, the free space channel introduces attenuation by fog.

At the receiver end, the OFDM signals are detected using a PIN photodetector, and the output of photodetector is given to the QM demodulator and then by the OFDM demodulator and QAM sequence decoder in order to recover the original transmitted 10 Gbps data successfully. Figure 6 shows the measured received power for different link range under different atmospheric weather condition. The fog is categorized to haze, light fog, moderate and thick fog. When the visibility is very low, the attenuation caused due to fog is very high. The different values of attenuation considered are 1.17 dB/km for haze, 7.74 dB/km for light fog, 26 dB/km for moderate

Table 9 Obtained values of received power versus link range under different foggy conditions

Link range	Haze Power (dBm)	Light fog Power (dBm)	Moderate fog Power (dBm)	Thick fog Power (dBm)
200	− 46.69	− 39.5	− 48.91	− 63.93
400	− 49.84	− 54.67	− 69.45	− 76.12
600	− 51.08	− 60.89	− 79.98	− 100
800	− 62.14	− 70.36	− 83.61	− 100
1000	− 63.76	− 78.38	− 100	− 100

and 65 dB/km for thick fog. Table 9 describes the values for received power in dBm for different ranges of transmission link range under different foggy conditions.

As the attenuation due to fog is dependent on visibility conditions, it greatly effects the transmitted optical signal. Figure 6 shows the link range versus received power under different atmospheric conditions and link ranges. From Fig. 6, it can be concluded that at a link range of 1000 m, the effect of thick fog is more when compared to haze, light and moderate fog condition. Also from Fig. 6, we can conclude that the fog degrades the system performance, as the received power is very low when the link range is increasing from 200 to 1000 m.

The impact of the fog can further be analyzed by studying error vector magnitude (EVM). The EVM is commonly used to analyze the error performance of the wireless system. As the optical signal is transmitted through free space, it faces attenuation due to various effects. Fog is considered as the most performance deteriorating factor as it can completely block the transmitted optical signal. Table 10 shows the EVM and error symbols against link range for different weather condition.

Thus with the increase in the attenuation due to fog, the error performance of the system deteriorates. From Fig. 7, it can be concluded that performance is better in case of light fog at a distance of 1000 m as compared to thick fog for the same link
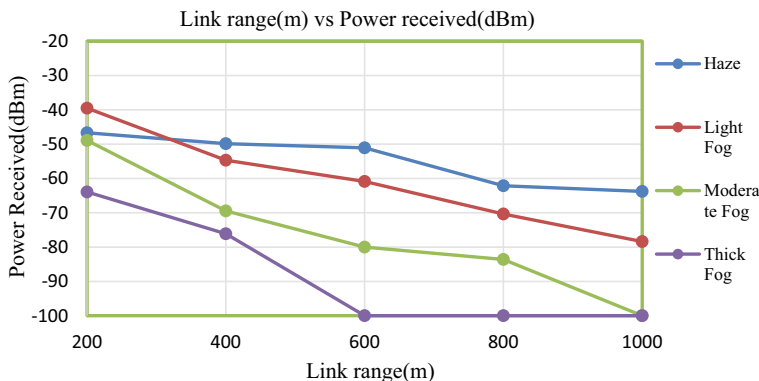
Fig. 6 Evaluation of received power a function of link range under different foggy conditions for the given system

Table 10 Evaluation of the EVM (%) and error symbols under different foggy conditions

Link range (m)	Haze		Light fog		Moderate fog		Thick fog	
	Error symbols	EVM (%)	Error symbols	EVM (%)	Error symbols	EVM (%)	Error symbols	EVM (%)
200	29	8.643	39	9.578	41	7.626	45	9.896
400	32	8.729	41	8.768	48	9.804	55	9.218
600	47	8.57182	48	10.523	54	9.13004	61	8.78524
800	52	10.2857	59	10.3043	60	8.83982	88	10.9544
1000	57	9.63882	66	10.9753	71	10.4506	101	10.9945
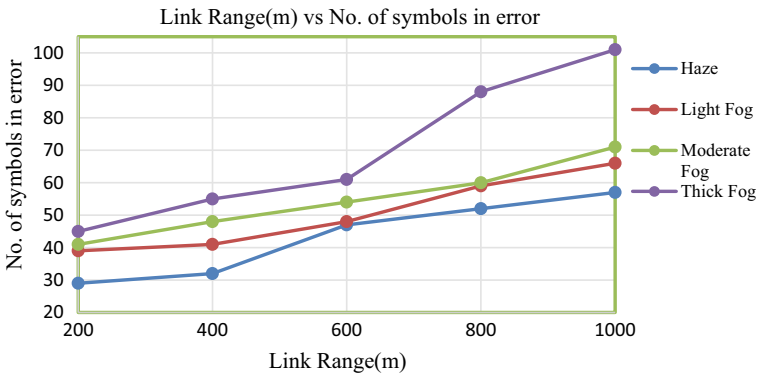
Fig. 7 Evaluation of error symbols against link range under the impact of different foggy conditions for given system

range. This statement can be further be supported by Fig. 8, where EVM is plotted against link range. The link range increases, the system performance decreases for different weather conditions, and the error symbols also increase.

4 Conclusions and Future Scope

Atmospheric turbulence is the major obstacle in FSO communication system and thus blocking its use in extended applications. The OFDM scheme gives an effective solution for high information rate, increased link range for adverse weather condition like fog, haze, rainfall, etc. With OFDM, high spectral efficiency is achieved as the information is distributed over large number of subcarriers. Immunity against intersymbol and intercarriers interference is the major benefit by enhancing factor in FSO. The FSO link is affected by the attenuation caused due to atmospheric effects. The attenuation caused due to fog is more adverse compared to rainfall as it decreases the link availability and increases the error rate. The error caused by
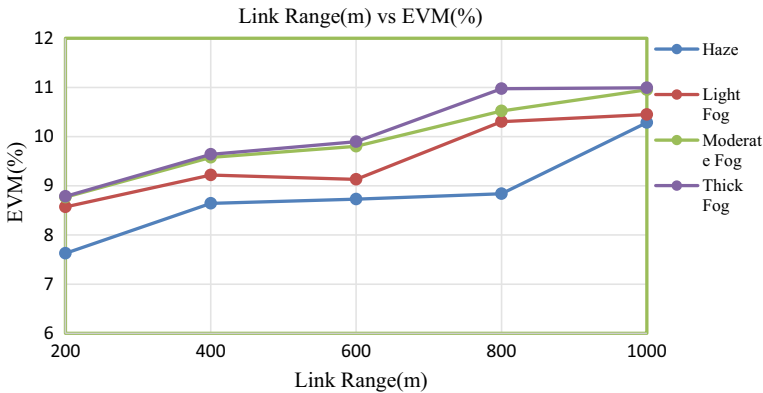
Fig. 8 EVM (%) against link range under different foggy conditions for the proposed system

stormy weather drastically reduces the performance of the system compared to light rainfall condition. The results show that the link cannot be prolonged beyond 1 km range for effective transmission of optical link.

In the future scope of the mentioned work, improvement in the system can be achieved by incorporating several mitigation techniques. As the attenuation caused by weather effect decreases the link range and increasing of transmitted power is not enough, incorporation of proper amplifiers can do the work. Also further improvement in the system can be achieved by doing channel estimation for analyzing the attenuation caused by the channel and then tuning the gain of amplifier accordingly.

References

1. Tripathi A, Gupta S, Mandloi A (2020) Orthogonally polarized and 60 GHz dual-channel based 18 × 2.5 Gb/s DWDM-interleaved hybrid FSO system under atmospheric turbulence. Opt Quant Electron 52(4):1–12. https://doi.org/10.1007/s11082-020-02324-6
2. Chaudhary S, Amphawan A, Nisar K (2014) Realization of free space optics with OFDM under atmospheric turbulence. Opt 125(18):5196–5198. https://doi.org/10.1016/j.ijleo.2014.05.036
3. Tripathi A, Gupta S, Mandloi A (2021) Performance of orthogonal frequency division multiplexing based 60-GHz transmission over turbulent free-space optical link. J Opt Commun. https://doi.org/10.1515/joc-2020-0242
4. Tripathi A, Gupta S, Mandloi A (2021) Investigation of weather effects toward convergence of wired and wireless gigabit services over hybrid free-space optical link. Opt Eng 60(2):026102. https://doi.org/10.1117/1.OE.60.2.026102
5. Kaushal H, Jain VK, Kar S (2017) Free-space optical channel models. In: Free space optical communication. Springer, New Delhi, pp 41–89. https://doi.org/10.1007/978-81-322-3691-7_2
6. Basahel AA, Islam MR, Zabidi SA, Habaebi MH (2017) Availability assessment of free-space-optics links with rain data from tropical climates. J Lightwave Technol 35(19):4282–4288. https://doi.org/10.1109/JLT.2017.2732459
7. Suriza AZ, Rafiqul IM, Wajdi AK, Naji AW (2013) Proposed parameters of specific rain attenuation prediction for free space optics link operating in tropical region. J Atmos Solar Terr Phys 94:93–99. https://doi.org/10.1016/j.jastp.2012.11.008

8. Soni G, Mandloi A, Gupta S (2019) Feasibility analysis of optical wireless communication for Indian tropical and subtropical climates. J Opt Commun. https://doi.org/10.1515/joc-2019-0235

9. Prediction methods required for the design of terrestrial free-space optical links (Recommendation P.1814–0 (08/2007). www.itu.int/rec/R-REC-P.1814-0-200708-I/en

10. Rainfall Statistics of India (2016) India meteorological department (Ministry of earth sciences) Report No. ESSO/IMD/HS/R. F. Report/04(2016)/22

11. Rainfall Statistics of India (2017) India meteorological department (Ministry of earth sciences) Report No. ESSO/IMD/HS/R. F. Report/01(2017)/2

12. Rainfall Statistics of India (2020) India meteorological department (Ministry of earth sciences) Report No. ESSO/IMD/HS/R. F. Report/30(2020)/54

Performance Comparison of Different Diversity and Combining Techniques Over Gamma–Gamma FSO Link

Hardik Joshi and Shilpi Gupta

Abstract Free space optical communication (FSO) is featured as a solution to the massive demand for large bandwidth and last-mile connectivity. However, the link performance degrades due to atmospheric turbulence. Like RF wireless communication link, the diversity and combining techniques were found effective in FSO link too. This paper compares BER performance of various diversity and combining techniques. We have simulated maximum ratio transmission (MRT) and transmit aperture selection (TAS) technique as transmit diversity scheme. For the receive diversity techniques, we have used selection combining (SC), maximal ratio combining (MRC), and equal gain combining (EGC). We have also considered MIMO configuration and wavelength diversity. These all techniques are compared for various diversity orders and different strengths of atmospheric turbulence. We found that maximum ratio combining and maximum ratio transmission schemes have the best BER performance among all diversity techniques. However, the MRT technique requires additional resources to make CSI information available at the transmitter.

Keywords Free space optical communication · Diversity and combining · Maximal ratio combining · Equal gain combining · Selection combining · Wavelength diversity · Maximum ratio transmission · Transmit aperture selection

1 Introduction

Due to various advantages like large bandwidth, unlicensed spectrum, high directivity, less power, and high security, the FSO is seen as one of the solutions for the demand for huge data rate and last-mile connectivity. However, the performance of

H. Joshi (✉)
Nirma University, Ahmedabad, Gujarat 382481, India
e-mail: hardik.joshi@nirmauni.ac.in

S. Gupta
S.V. National Institute of Technology, Surat, Gujarat, India
e-mail: sgupta@eced.svnit.ac.in

the FSO system is degraded due to various atmospheric effects and misalignment between transmitter and receiver. Atmospheric turbulence is one factor that plays a significant role in the degradation of signal quality [1]. Due to atmospheric turbulence, received irradiance has spatial and temporal fluctuations, called turbulence-induced fading or scintillation. Scintillation is a significant factor that leads to an increase in bit error rate and outage probability.

Various turbulence mitigation techniques like modulation and detection, error-correcting codes, aperture averaging, diversity, and combining are available. Out of those techniques, diversity and combining is one of the robust solutions against atmospheric turbulence. The most simple and low-cost modulation scheme for FSO is on-off keying (OOK). Nevertheless, the receiver required an adaptive threshold for reliable detection due to contentious change in atmospheric effect. In subcarrier intensity modulation (SIM), no such adaptive threshold plus SIM is more bandwidth efficient than OOK.

In [2], and [3], the SC, EGC, and MRC techniques are discussed. However, the transmit diversity, MIMO configurations, and wavelength diversity are not covered. This paper demonstrates the simulated results of various transmit and receive diversity techniques like selection combining, equal gain combining, maximum ratio transmission, maximal ratio combining, and wavelength diversity. For simulation, SIM with QPSK modulation scheme is considered with intensity modulation/direct detection (IM/DD).

The organization of the paper is as follows. Section 1 contains the introduction. In Sect. 2, the gamma-gamma channel model is presented. In sections three and four, the system model with different diversity and combining techniques is discussed. Simulation results are demonstrated in Sect. 5. In Sect. 6, we concluded the article.

2 Channel Model

The physical experimentation in wireless and optical communication is quite expensive and time-consuming. Statistical channel models allow us to perform various experiments in less time and cost. In literature, different channel models are described like log-normal, gamma–gamma [4], K channel, Malaga [5] and negative exponential, exponentiated Weibull [6], etc. Among this, gamma–gamma channel model is widely accepted because its best fit to moderate to strong turbulence.

The gamma–gamma model is derived by modulation process between the large-scale turbulent eddies and small-scale turbulent eddies, considering both have gamma distribution. The PDF of irradiance fluctuation is distributed as gamma–gamma distribution is [4].

$$f_I(I) = \frac{2(\alpha\beta)^{\frac{\alpha+\beta}{2}}}{\Gamma(\alpha)\Gamma(\beta)} \, I^{\frac{\alpha+\beta}{2}-1} K_{\alpha-\beta}\left(2\sqrt{\alpha\beta I}\right); \; I > 0 \tag{1}$$

The value of α and β is related to strength of atmospheric turbulence. Γ and $K()$ are gamma function modified Bessel function of second kind, respectively. α and β

are defined in [4] as.

$$\alpha = \left[\exp\left(\frac{0.49\chi^2}{\left(1 + 0.18d^2 + 0.56\,\chi^{12/5}\right)^{7/6}}\right) - 1\right]^{-1} \tag{2}$$

$$\beta = \left[\exp\left(\frac{1 + 0.51x^2\left(1 + 0.69\chi^{12/5}\right)^{-5/6}}{\left(1 + 0.9d^2 + 0.62d^2\chi^{12/5}\right)^{5/6}}\right) - 1\right]^{-1} \tag{3}$$

where Rytov variance $\chi 2 \triangleq 0.5\,C_n^2 k^{7/6} L^{11/6}$, $d \triangleq \left(kD^2/4L\right)^{1/2}$, and $k = 2\pi/\lambda i$ is wave number. λ, D, L, and C_n^2 are the wavelength, the diameter of receiver's aperture, link distance, and the refractive index structure parameter, respectively. Gamma–gamma distribution fits well for all kind of turbulence but best fit to moderate to strong turbulence [4].

3 System Model

As shown in Fig. 1, we are considering the MIMO FSO link with M LASER sources and N photodetectors. The received signal matrix is represented by [7].

$$Y = \frac{1}{M}\eta WGIx + n \tag{4}$$

where x is transmitted QPSK symbol, η is photodetector responsivity, I is an irradiance fluctuation distributed as gamma–gamma distribution, n is AWGN noise vector having dimension $N \times 1$. The value of M, N, beam-forming matrix or precoding matrix W, and combiner matrix G depends on the type of diversity techniques applied. The W is the unity matrix for all other techniques except MRT, and G is the unity matrix for all other schemes expect MRC. The factor $\frac{1}{M}$ is used to keep the total transmitted power the same as SISO for a fair comparison. Further, a per-
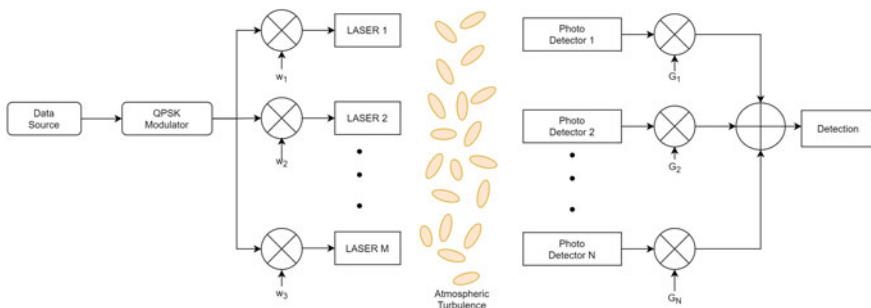
Fig. 1 MIMO FSO system

fect line of sight or negligible tracking and pointing errors between transmitter and receiver is assumed.

3.1 Detection Rule

Assuming accurate CSI available at the receiver side, using maximum likelihood detection, received symbols can be estimated by

$$\hat{s} = \underset{s \in \mathcal{A}}{\mathrm{argmax}} |y_{xx} - \sqrt{\gamma} I s|^2 \tag{5}$$

where $\mathcal{A}$ is set of QPSK constellations. y_{xx} and γ are received signal and SNR after applying diversity and combining techniques.

4 Diversity and Combining Techniques

4.1 SISO

In SISO, the $M = N = 1$, i.e., single LASER transmitter and single receiver photodetector, is used.

4.2 Transmitter Diversity

For all transmit diversity scheme, no. of photodetectors $N = 1$.

4.2.1 Maximal Ratio Transmission

In MRT, we use a precoding matrix at the transmitter to maximize the SNR at the receiver side. For that matrix, W is $w_{ij} = \frac{I_{ij}^H}{\|I\|}$, where $[\ ]^H$ represents a hermitian operation [8]. So for MRT, we need exact channel state information at the transmitter side, which requires an additional feedback channel.

4.2.2 Transmit Aperture Selection

There are multiple transmitter apertures in this scheme, and the single or set of transmitter apertures are selected, giving maximum channel gain. TAS also needs a feedback channel for CSI availability at the transmitter.

4.3 Receive Diversity

For all receiver diversity techniques, no of transmitter $M = 1$.

4.3.1 Selection Combining

In the SC, signal with the best SNR is selected out of signals available from multiple receiver photodetectors. So, the received signal can be given by $y_{sc} = y_m$ and $m = \underset{1 \leq k \leq N}{\mathrm{argmax}} \; I_k^2$.

4.3.2 Equal Gain Combining

In EGC receiver, all symbols received by receiver aperture are added with equal weight. Considering all weights are equal to unity, the combined signal y_{EGC} is given by sum of all received signals.

$$y_{EGC} = \sum_{i=1}^{N} y_i = \eta \sum_{i=1}^{N} \sum_{j=1}^{M} I_{ij}s + \sum_{i=1}^{N} n_i \tag{6}$$

4.3.3 Maximum Ratio Combining

For maximum ratio combining receiver, the received signal by each antenna is multiplied with some weight such that the SNR of the combined signal is maximized. This scheme is an optimal scheme to maximize the received signal SNR so it is also called optimal combining. The combined signal y_{MRC} is

$$\begin{aligned} y_{MRC} &= \eta \sum_{i=1}^{N} \sum_{j=1}^{M} I_{ij} y_i \\ &= \eta^2 \sum_{i=1}^{N} \left(\sum_{j=1}^{M} I_{ij} \right)^2 x + \eta \sum_{i=1}^{N} \sum_{j=1}^{M} I_{ij} n_i \end{aligned} \tag{7}$$

4.4 MIMO Systems

In MIMO FSO systems, multiple transmission aperture and multiple receiver photodetectors are there. At the transmitter side, the repetitive coding is used, i.e., the

same symbol is transmitted through all apertures. At receiver, signal received by the different photodetector can be combined using different combining techniques like SC, EGC, and MRC.

4.5 Wavelength Diversity

In wavelength diversity, a signal is transmitted over multiple wavelengths. Separate receivers receive different wavelengths. We can use all the combining techniques discussed above at the receiver side [9, 10]. On the receiver side, we have used the MRC technique for best performance.

The signal received by aperture i is given by

$$y_i = \eta \sum_{j=1}^{n} I_i x + n_i; i = j \tag{8}$$

5 Simulation Results

In this section, the results of the Monte Carlo simulation are demonstrated. The simulation flow is shown in Fig. 2 In Monte Carlo simulation, QPSK symbols are generated for 2×10^7 random data bits. The gamma–gamma channel is generated by the multiplication of two gamma random numbers. The parameters α and β are calculated from Eqs. 2 and 3. Different diversity techniques have been applied, and maximum likelihood detection is used for the detection of symbols. The bit error rate can be calculated by BER = No of erroneous bits/Total no of bits. The summary of simulation parameters is given in Table 1, which are taken from various reputed publications [1, 10, 11].
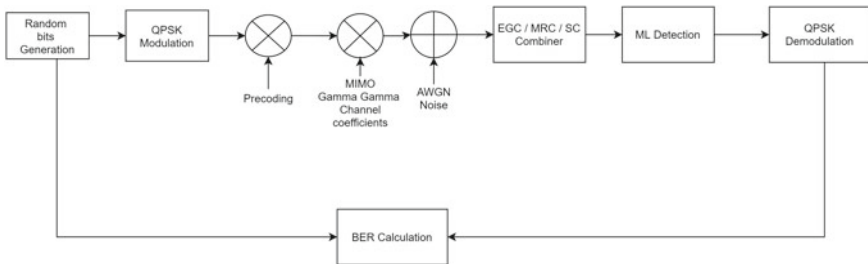
Fig. 2 Simulation steps for the Monte Carlo simulation of BER performance analysis of FSO system

Table 1 Link parameters considered for simulation

Parameters	Value
Link distance (L)	1000 mm
Wavelength (λ)	1.5 μm
Receiver aperture diameter (D)	0.01 m
Reflective index structure parameter (C_n^2)	WT: 9×10^{-15} m$^{-2/3}$
	MT: 6×10^{-14} m$^{-2/3}$
	ST: 2×10^{-13} m$^{-2/3}$
Modulation scheme	SIM-QPSK
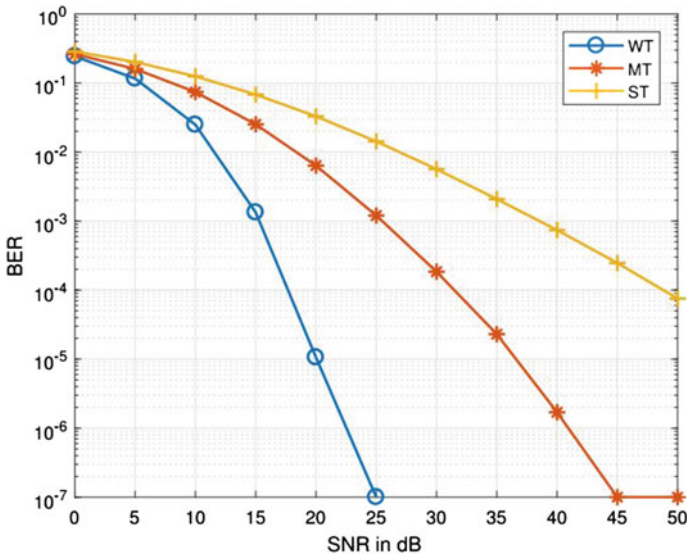
Fig. 3 BER versus SNR of SISO FSO link with QPSK modulation in different strength of turbulence

Figure 3 shows BER performance comparison of FSO link over different strengths of atmospheric turbulence. The simulation parameters are summarized in the Table 1. It is clear that by changing the atmospheric turbulence from weak to strong, the BER performance degrades. The performance is worst in the case of strong turbulence.

Performance of different transmit diversity schemes is demonstrated in Fig. 4. The performance of MRT is better than TAS for all kinds of turbulence. The increasing strength of turbulence will degrade the FSO link performance for both MRT and TAS. For moderate turbulence, different transmit diversity scheme is compared in Fig. 5. The performance of MRT is better than TAS for both 2×1 and 3×1 link.

Figure 6 shows BER performance of 1×2 SIMO FSO link with different receive diversity scheme. The performance of the MRC technique is slightly better than the performance of EGC. EGC and MRC both outperform the selection combining for
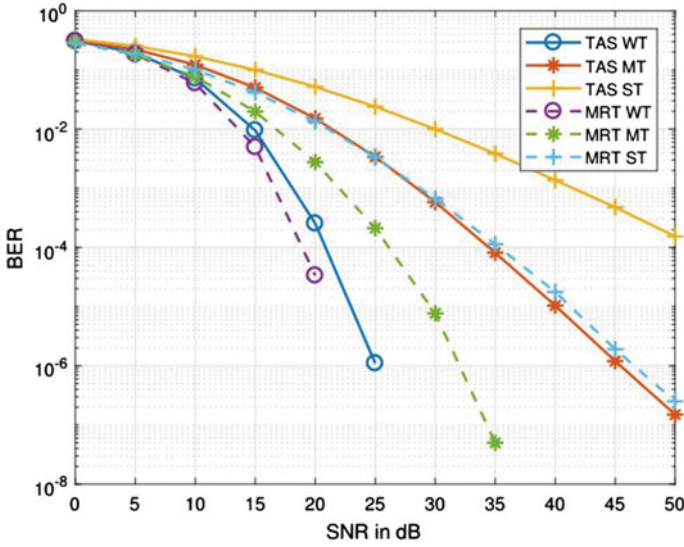
Fig. 4 BER performance comparison of 2×1 transmit aperture selection (TAS) and maximum ratio transmission (MRT) MISO FSO link in different atmospheric turbulence

all kinds of turbulence. The effect of increasing no of the receiver is shown in Fig. 7. The performance of the 1×3 SIMO scheme is better than the 1×2 SIMO scheme and SISO link for all the combining techniques.

BER performance of wavelength diversity is demonstrated in Figs. 8 and 9. For diversity order 1 ($\lambda_1 = 1.55\,\mu\text{m}$), for diversity order 2 ($\lambda_1 = 1.55\,\mu\text{m}$ *and* $\lambda_2 = 0.85\,\mu\text{m}$), and for order 3 ($\lambda_1 = 1.55\,\mu\text{m}$, $\lambda_2 = 1.31\,\mu\text{m}$ *and* $\lambda_3 = 0.85\,\mu\text{m}$), wavelengths are considered. Figure 8 demonstrates the BER performance of wavelength diversity in different strengths of atmospheric turbulence. Reducing the strength of turbulence, the BER performance improves. Figure 9 demonstrates the effect of diversity order on BER performance in moderate turbulence. As increase the diversity order from 2 to 3, the BER performance gets improved.

The BER performance of best among transmit diversity and receive diversity scheme, i.e., MRT and MRCare compared in Fig. 10. 2×1 MRT, 1×2 MRC, 2×2 MRC, and 2×2 wavelength diversity link for moderate atmospheric turbulence is shown in Fig. 10. In 2×2 MIMO link at transmitter side repetitive, code is used as it is most simple configuration. The receive diversity gives better BER performance than transmit diversity scheme. The 2×2 MIMO configuration is best among all diversity techniques.
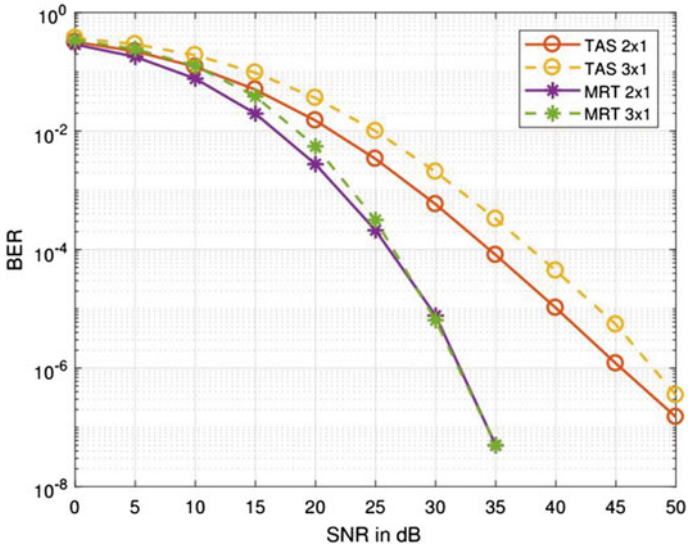
Fig. 5 BER performance comparison of TAS and MRT MISO FSO link for different diversity order in moderate turbulence scenario
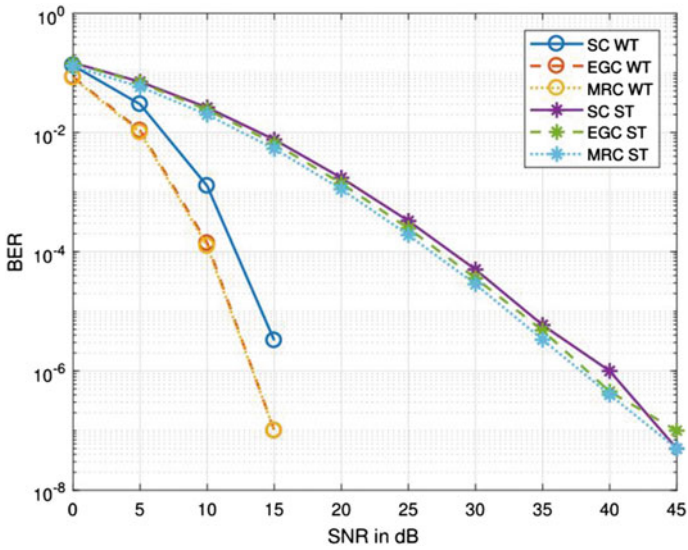
Fig. 6 BER performance of 1×2 SIMO FSO link using different receive diversity techniques in weak and strong atmospheric turbulence
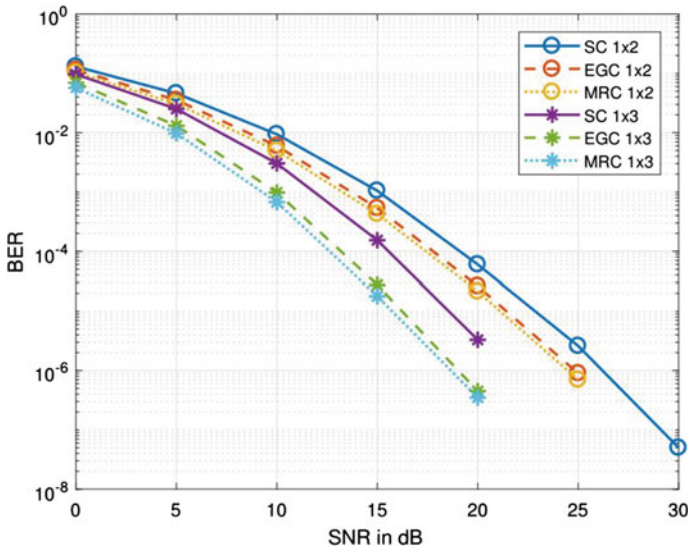
Fig. 7 BER performance comparison of SC, EGC, and MRC MISO FSO link for diversity order 1×2 and 1×3 in moderate atmospheric turbulence
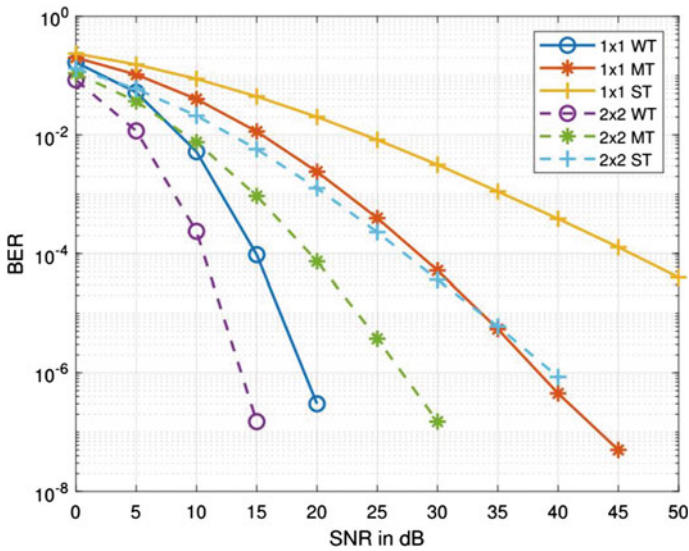
Fig. 8 BER performance of FSO link using wavelength diversity with diversity order $m = 1(\lambda_1 = 1.5\,\mu\text{m})$, $m = 2(\lambda_1 = 1.5\,\mu\text{m}, \lambda_2 = 0.85\,\mu\text{m})$ for all kind of atmospheric turbulence
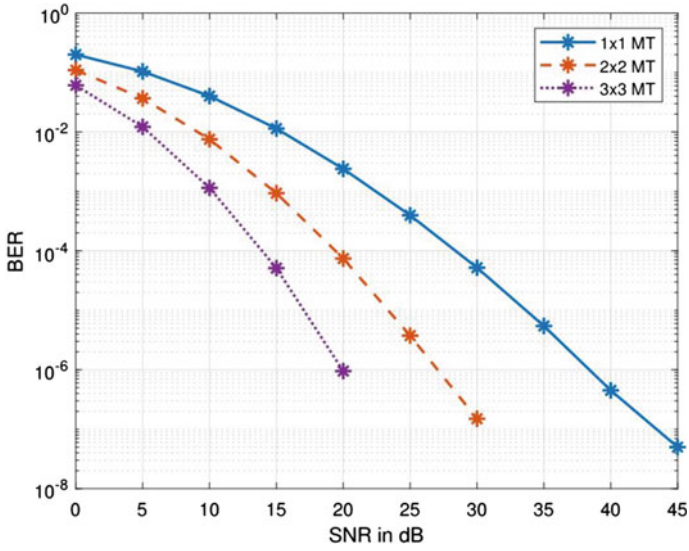
Fig. 9 Effect of wavelength diversity order on BER performance of FSO link in moderate atmospheric turbulence scenario
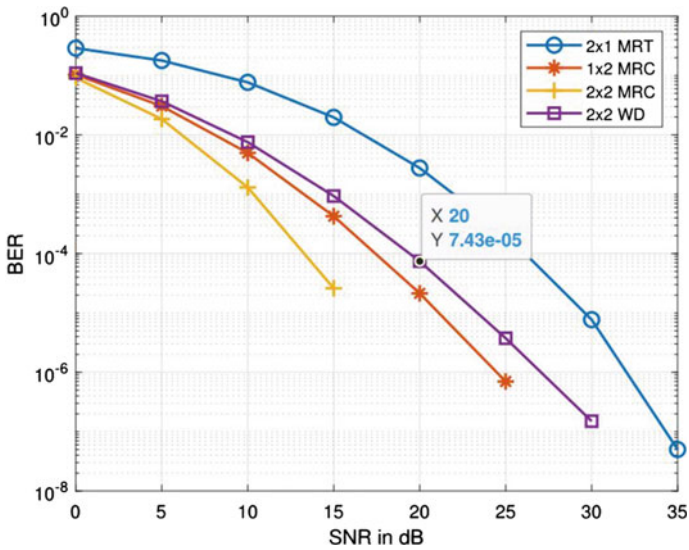
Fig. 10 BER performance of 2×1 MRT, 1×2 MRC, 2×2 MRC, and 2×2 wavelength diversity link for moderate atmospheric turbulence

6   Conclusion

BER performance of different diversity techniques for the gamma–gamma FSO channel was simulated and compared. The use of transmit diversity schemes like maximal ratio transmission and transmit aperture selection enhances the performance of the FSO link in a different atmospheric turbulent scenario. However, both techniques need a perfect knowledge of CSI at the transmitter side, which requires an additional feedback channel. The receive diversity also improves the BER performance of the FSO link. The maximum ratio combining technique gives the best performance, but it has a complex receiver structure. On another side, equal gain combining gives a slightly higher BER than MRC, but it is simpler than MRC. The wavelength diversity also gives better performance in all kinds of atmospheric turbulence.

The MRC and MRT give the best performance overall diversity techniques. However, MRT needs an additional feedback channel for CSI knowledge at the transmitter side. So, MRC technique is suitable to achieve the best BER performance at a lower cost.

References

1. Khalighi MA, Uysal M (2014) Survey on free space optical communication: a communication theory perspective. IEEE Commun Surv Tutor 16(4):2231–2258
2. Saeed RA, Abbas EB (2018) Performance evaluation of mimo fso communication with gamma-gamma turbulence channel using diversity techniques. In: 2018 international conference on computer, control, electrical, and electronics engineering (ICCCEEE). IEEE, pp 1–5
3. Kaur K, Miglani R, Malhotra JS (2016) The gamma-gamma channel model-a survey. Indian J Sci Technol 9(47)
4. Al-Habash A, Andrews LC, Phillips RL (2001) Mathematical model for the irradiance probability density function of a laser beam propagating through turbulent media. Opt Eng 40(8):1554–1563
5. Jurado-Navas A, Garrido-Balsells JM, Paris JF, Puerta-Notario A, Awrejcewicz J (2011) A unifying statistical model for atmospheric optical scintillation. Numer Simul Phys Eng Process 181
6. Barrios R, Dios F (2012) Exponentiated Weibull distribution family under aperture averaging for gaussian beam waves. Opt Express 20(12):13,055–13,064
7. Bayaki E, Schober R, Mallik RK (2009) Performance analysis of mimo free-space optical systems in gamma-gamma fading. IEEE Trans Commun 57(11):3415–3424
8. Bhatnagar MR (2015) A one bit feedback based beamforming scheme for fso miso system over gamma-gamma fading. IEEE Trans Commun 63(4):1306–1318
9. Shah D, Kothari D, Ghosh A (2016) Performance of free-space optical link with wavelength diversity over exponentiated Weibull channel. Opt Eng 55(11):116,112
10. Nistazakis HE, Tombras GS (2012) On the use of wavelength and time diversity in optical wireless communication systems over gamma-gamma turbulence channels. Opt Laser Technol 44(7):2088–2094
11. Navidpour SM, Uysal M, Kavehrad M (2007) BER performance of free-space optical transmission with spatial diversity. IEEE Trans Wirel Commun 6(8):2813–2819

Abstract Data Models and System Design for Big Data Geospatial Analytics

Vimal Sheoran and Jai Prakash Verma

Abstract The objective of this research is to design an abstract framework that can be used to represent and visualize any kind of geographical phenomena. The framework aims to be generalized in nature so that it can be applicable to all different kinds of geographical phenomena. There are three different proposed abstractions, namely *objects*, *events* and *processes*. We also propose a generic system design framework for developing a big data geospatial analytics application. The system design proposed provides a brief overview of what a usual big data geospatial analytics system might look like. The design highlights a few important aspects of the system like data ingestion and data store selection.

Keywords Geospatial analytics · Geographic information systems · Big data · Data models · Data analytics · Geographical data analysis

1 Introduction

There exist a plethora of GIS tools and services that help people to analyze and visualize their geospatial data; however, there is also a need for a generalized platform that provides users with an abstract representation of all kinds of geographical phenomena. There is a need for a system that can be used to analyze rainfalls, earthquakes, spread of a city, etc., all in a single place. Based on the literature review, this project proposes three abstract classes of geographical phenomena, namely *objects*, *fields* and *processes* [1, 2] and proposes data models [3] based on these abstractions. The research also recommends a generic design for designing a system that incorporates and scales with the challenges of big data and is aimed toward solving problems that include a huge amount of geospatial data. The end goal of this system would

V. Sheoran (✉) · J. P. Verma
Institute of Technology, Nirma University, Ahmedabad, India
e-mail: 20mced15@nirmauni.ac.in

J. P. Verma
e-mail: jaiprakash.verma@nirmauni.ac.in

be to allow the user to load some geospatial data, define abstractions based on the specific kind of analysis the user wishes to perform and then have the system that returns the desired data for the analysis.

1.1   Need Analysis

The main motivation from this work comes from studying and analyzing current state-of-the-art systems which are designed in the recent times to study and analyze geographical phenomena. Briefly speaking, these systems were designed to monitor and/or analyze specific geographical phenomena. These systems fail to generalize when dealing with different types of geographical phenomena. In the recent years, we have seen an explosion in geospatial data from sensors, satellite images, GPS data, etc. In order to properly understand this data, researchers are continuously making effort to analyze this vast amount of data and make important decisions based on it. Due to scale of this data, we categorize it under big data. Due to this scale, this data cannot be handled on regular computing architectures; hence, we shift to technologies used by the paradigm of big data. Some of the current system designs do not consider this large volume of data. This prevents these systems from scaling over a period of time when multiple phenomena have to be analyzed at once.

Two of the systems we studied provided solutions to predict local rainfall [4, 5]. This was done primarily by collecting data in the form of sensor input and/or scraping internet archives. One of the major issues we noticed is how the work did not talk about how the entire data infrastructure is designed. Both [4, 5] collected certain amount of data from a point location either by a data logger [4] or from a meteorological station [5]. It was not clear whether the system will be able to scale well and generalize for scenarios where there can be multiple locations whose rainfall has to be predicted. The system also fails to address the total amount of data that was collected and for how long was the data collected. The system collects data and uses it for rainfall prediction, but the collected parameters may also be used for some other kind of analysis. The suggested design does not talk about how the system can be generalized.

We also studied other systems that provided solutions for landslide identification [6, 7]. One of the systems for landslide detection used different kinds of data, i.e., topographical, geological and rainfall and established different databases based on previous landslide data. This is one of the systems which talks about utilizing different types of data for a single type of analysis; hence, it hints toward a possible general data layer, where different kinds of data can be stored and then they could be pre-processed and pulled according to the needs of a particular analysis. Even if the data layer for this system in particular is generalized, it still processes data to provide only a single kind of analysis and hence does not provide a general approach for analyzing any kind of geographical phenomena. The other landslide detection system [7] however does not present such approaches. Like [4, 5], it also does not generalize well for analysis of any geographical phenomena.

The systems designed should also be able to include the need for geospatial big data. Due to this scale of data, we need to think about handling this data in a big data context. Existing big data technologies like Hadoop [8] and Spark [9] can be used with their geospatial extensions like SpatialHadoop [10]. We can also leverage existing database technologies like PostgreSQL and MongoDB for handling this kind of data. The choice of underlying data systems is completely dependent on the requirements of the user and requires further research; however, a general framework for designing such a system can be proposed.

From this survey of recent literature, we concluded that it was necessary to think about a generalized system that can be used for storage of geospatial big data and analysis of any kind of geographical phenomena. In the next section, we talk about the recent systems that were used for handling of geospatial big data and in the sections following that we talk about how we can represent any general kind of geographical phenomena using simple abstractions.

2 Related Work

2.1 Data Models

To design a general kind of system that can be used to analyze any kind of geographical phenomena, we need to design meaningful abstractions on top of our data so that they can be used to encapsulate a geographical phenomenon.

There are two classical approaches to representing geographical phenomena. The first is an *object-based* representation, and the other is a *field-based* representation. Objects can be viewed as discrete phenomena that are spatially homogeneous and have defined spatial boundaries such as buildings, trees, whereas fields are representative of a single-value geographical variable related to a geographical phenomenon distributed over a spatial region [1].

One of the most prominent works in modeling geospatial and temporal data adopts an object based approach for modeling geospatial phenomena. The information space is viewed as being populated by self-encapsulating objects that represent state and behavior. It also focuses on solving the problem of event and database time duality. This duality occurs when the time at which an event is projected to occur (*event time*) is different from the time at which the event is recorded in the database (*database time*). This leads to a loss of information about time when the event actually occurred. The problem is described by using the example of a land parcel that has been changing boundaries and changing ownership over time. A similar example is also discussed in [11]. The work uses concepts of *bi-temporal elements (BTE)* [12] to represent geospatial information along two orthogonal temporal dimensions of database time and event time. The work furthers into handling spatiotemporal information as *ST Simplexes* and *ST Complexes* which have their own querying algebra for retrieving information. The model described here lays a foundation of how to design a better

spatiotemporal database that can be used to store spatial and temporal data in a way that there is no loss in temporal information and also provides the required algebra to query the data stored within this database [3].

Pequet and Duan [1] also proposes an event-based data model for analyzing geographical data along the temporal dimension. Their model is called the *event-based spatiotemporal data model* or *ESTDM* for short. The model aims to answer three fundamental types of queries (1) retrieving locations that have changed at a given point in time, (2) retrieving locations that have changed over a given time interval and (3) calculation in change of a total area over a given time interval. Changes to a spatial region over time can be naively represented by a *snapshot model* where at each time instance, a snapshot of the region is stored. However, this is not a very efficient way of storing the state. Another proposed model for the same is to use a *grid model* where the spatial region is divided into grids and changes to a grid are stored separately. A model similar to the grid model is proposed by Langran [13]. The ESTDM model proposes a time-based approach where specific events in time, events being described as manifestation of a spatiotemporal process, become the organizational basis of storing change. A single-dimensional timeline is used to store the location of events as they happened. Each event can store the set of locations and geospatial features that changed at that particular point in time and their new values. The authors describe this method of recording changes when they occur as opposed to at every tick of a clock as *temporal run length encoding*.

The two models discussed so far provide a way of handling geospatial and temporal data and modeling it, but these systems are implemented within an existing database system. Over the years, a lot of database systems have come out in the commercial as well as in research space that accommodate even better models to handle storage and retrieval of geospatial and temporal data. The next step to this is to design abstractions on top of geospatial and temporal data that is stored inside these databases and data stores. These abstractions are important to interpret any kind of geospatial data that is stored inside the data store and hence provide a general model to analyze any kind of spatiotemporal data. Yuan [2] talks about two abstractions for geospatial data: (1) events and (2) processes. Events are defined as an occurrence of something significant, and a process is a sequence of dynamically related states that shows how something evolves in time and space. In this work, we build upon the work done by Yuan and better define these abstractions and demonstrate the use of these abstractions with some real-world examples.

2.2 Analysis and Design of Geospatial Big Data Systems

Even with the prevalence of big data geospatial systems, the user sometimes is restricted to using a regular database as the primary storage and querying mechanism for the underlying geospatial data. Given the unstructured nature of geospatial data, a common approach is to store this data in document-oriented databases. MongoDB is a prime example of a document-oriented database with geospatial storage and querying

support. GeoYCSB is described as a framework for evaluating database performance with geospatial workloads as presented in [14]. The framework is based on the Yahoo YCSB framework [15] for database evaluation. Using similar frameworks allows the users to evaluate their chosen data storage system for geospatial big data use-cases.

In terms of using big data systems for geospatial analytics, the work done in [16] compares performance of SpatialHadoop and GeoSpark in terms of data compression and index performance. These parameters are extremely important when considering a system for storing and querying large amounts of data. [17] describes a geospatial big data system designed using MapReduce [17] and HBase [18] for storing shape-files. The system uses HBase tables as indexes on top of HDFS which stored the actual data. This review of literature tells us that there exists a lot of options both in terms of systems and strategies when it comes to designing a big data geospatial analytics system. Providing a generalized framework for designing such a system would serve as a guide and provide a brief understanding of what the final system should look like, for the people designing the system.

3 Data Abstractions for Geographic Phenomena

3.1 Objects

We define *objects* as geographical phenomena that are bound to a static location, and their parameters do not change over a large range of time. Examples of *objects* could be light poles, buildings, trees, etc. *Objects* also give us a way to represent point attributes such as height of a building, number of road accidents over a given location. The existence of an *object* rarely changes over a long period of time, i.e., a decade or half a decade. Neither do the parameters of an *object* (e.g., height of an object) change frequently over time. Due to this behavior, we do not often need to measure the data for an object over a temporal dimension. However, later in this section, we will see a special case of objects, where its state changes over small time intervals. The change in state of an object can be related to an event, e.g., the demolition (*event*) of a building (*object*) affects its existence.

Object Data Model

Object

```
1              struct {
2                  float latitude;
3                  float longitude;
4                  char ∗ name;
5                  struct Parameters ∗ params;
6              } Object;
```

Parameter

```
1              struct {
2              float height;
3              float area;
4              int building no;
                        –
5              } Parameter;
```

For the representation of an object, it is compulsory to have a latitude and a longitude field. There can be additional required fields that can be defined by the programmer, e.g., name in this case. All the fields that are not required can be represented as parameters.

Sample Object Data Figure 1 represents the visualization of trees in the SF area on a map of San Francisco. Each hexagon in the plot represents a tree; the position of the hexagon is defined by the *latitude* and the *longitude* fields. The height and the color of the hexagon can represent other parameters that need to be visualized (Table 1).

Visualization of Objects
See Fig. 1.
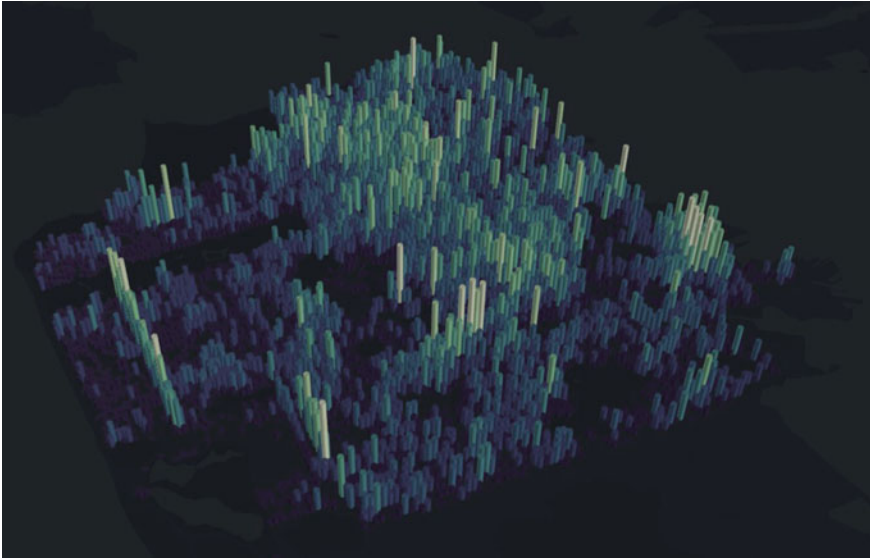
Fig. 1 Representation of trees in the SF area as objects

Table 1 San Francisco street tree data [20]

qSpecies	Latitude	Longitude	Age
Fraxinus uhdei:: Shamel Ash: Evergreen Ash	37.77448101	− 122.4691091	0
Lophostemon confertus:: Brisbane Box	37.80468521	− 122.4402315	6
Arbutus'Marina':: Hybrid Strawberry Tree	37.75995923	− 122.4866885	
Podocarpus gracilor:: Fern Pine	37.77353367	− 122.4169045	
Podocarpus gracilor:: Fern Pine	37.77353367	− 122.4169045	
Agonis flexuosa:: Peppermint Willow	37.76026555	− 122.4705695	
Hakea suaveolens:: Sweet Hakea Tree	37.75778273	− 122.4993677	1
Lophostemon confertus:: Brisbane Box	37.72954822	− 122.3926894	3
Platanus x hispanica:: Sycamore: London Plane	37.80304673	− 122.4250636	25
Prunus cerasifera:: Cherry Plum	37.7528239	− 122.4366208	17
Tree(s)	37.77300994	− 122.4355982	0
Platanus x hispanica:: Sycamore: London Plane	37.80797069	− 122.4158502	11
Acacia melanoxylon:: Blackwood Acacia	37.73901484	− 122.381104	
Pyrus calleryana:: Ornamental Pear	37.77310137	− 122.4173585	
Acacia melanoxylon:: Blackwood Acacia	37.78136501	− 122.4248636	
Lophostemon confertus:: Brisbane Box	37.73743182	− 122.3840631	
Platanus x hispanica:: Sycamore: London Plane	37.79059396	− 122.4198251	
Prunus serrulata 'Kwanzan':: Kwanzan Flowering Cherry	37.77473647	− 122.4213262	
Myoporum laetum:: Myoporum	37.73970633	− 122.4828998	0
Platanus x hispanica:: Sycamore: London Plane	37.79448363	− 122.3950546	Height

3.2 Events

Events are geographical phenomena that occur at discrete points in time and at discrete geographical locations. *Events* are discrete both in terms of time and geographical space. The *event* data type has a great abstract significance since the occurrence of an *event* represents a sudden change in the state of geography in and around the location where the *event* has occurred. *Events* are usually short-lived in nature, i.e., the events would occur for a very small timeframe when considered from the perspective of the surroundings of the geographical phenomena. *Events* are special in nature since they are related to both *objects* and *processes*.

Event Data Model

```
    Events
1          struct {
2          float latitude;
3          float longitude;
4          timestamp datetime;
```

```
5              char ∗ type;
6              struct Parameters ∗ params;
       }
    Parameters
1              struct {
2              float impact area;
3              float duration;
       }
```

For the representation of an event, it is compulsory to have a latitude, a longitude and a datetime or timestamp field. There can be additional required fields that can be defined by the programmer, e.g., type in this case. All the fields that are not required can be represented as parameters.

Sample Event Data
See Table 2.

Visualization of Events
See Figs. 2, 3 and 4.

Figures 2, 3 and 4 represent earthquakes occurring in California over three different time periods, 1990–1995, 2000–2005 and 2005–2010. The purple dots represent the location where the event occurred, and using a time-based filter, we are able to isolate events within a given timeframe, e.g., from January 1, 1990, to December 31, 1995, in case of Fig. 2. The size and the color of an individual dot can be used to depict other parameters related to that particular event, e.g., depth and magnitude.

3.3 Processes

Processes can be viewed as a change in geographical state variables in a fixed geographical region over a given period of time. During the occurrence of a *process*, state is viewed as continuous as opposed to events that occur at discrete points in time. A *process* is observed over a geographical location with well-defined boundaries. A *process* can also be viewed as a sequence of *events* occurring at various time-steps during the observation of a geographical location. *Processes* are generally used to monitor changes in attributes over a given geographical landscape over a given frame of time in order to make predictions about the state that follows, e.g., monitoring wind speed and air pressure over oceans to predict cyclone.

Process Data Model

Processes
struct {
     float latitude;

Table 2 California earthquake data [21]

Datetime	Latitude	Longitude	Depth	Magnitude
1967/08/01 10:33:50.47	36.08000	− 121.07083	80.339	2.50
1967/08/02 02:49:12.55	35.63433	− 120.75716	3.980	2.60
1967/08/03 05:55:26.73	36.37967	− 121.00850	39.609	2.70
1967/08/03 06:57:01.25	36.39550	− 121.01667	40.159	2.70
1967/08/03 20:21:26.52	36.54350	− 121.17216	5.945	2.60
1967/08/09 04:53:59.73	35.40150	− 120.58783	4.060	2.60
1967/08/09 07:27:32.82	36.15567	− 121.09367	68.790	2.70
1967/08/13 20:29:14.27	35.41950	− 121.10900	4.050	2.70
1967/08/15 16:53:24.26	35.48417	− 121.01167	4.585	2.90
1967/08/22 08:04:34.06	37.65333	− 122.42950	39.675	2.50
1967/08/22 08:29:47.47	36.40050	− 120.98650	36.357	3.00
1967/08/22 08:37:42.51	36.39767	− 120.99983	37.267	2.90
1967/08/22 08:38:29.57	36.40117	− 120.99050	36.627	2.60
1967/08/26 10:35:05.61	36.53867	− 121.16033	4.277	3.30
1967/08/27 13:20:08.75	36.51083	− 121.14500	1.386	3.60
1967/08/27 23:32:41.57	36.53717	− 121.15567	2.417	2.50
1968/01/12 22:19:10.35	36.64533	− 121.24966	6.578	3.00
1968/01/26 16:15:06.33	36.96717	− 121.46384	5.485	2.50
1968/02/09 13:42:37.05	37.15267	− 121.54483	8.256	3.00
1968/02/11 10:26:13.89	36.98217	− 121.47767	4.503	2.80
1968/02/21 14:39:48.10	37.17833	− 121.57800	6.716	3.80
1968/03/02 04:25:53.94	36.83433	− 121.54467	5.143	3.00
1968/03/02 13:12:15.29	37.27550	− 121.66450	40.231	2.63

```
        float longitude;
        timestamp datetime;
        struct Parameters* params;
    } Process;

    Parameters
    struct {
        // Example parameter.
        float windspeed;
        float air_pressure;
    } Parameters;
```

For the representation of a *process,* it is compulsory to have a *latitude*, a *longitude* and a *datetime* or *timestamp* field. There can be additional required fields that can be defined by the programmer. All the fields that are not required can be represented as *parameters*. As one can see that this model is quite similar to the *Event* model,
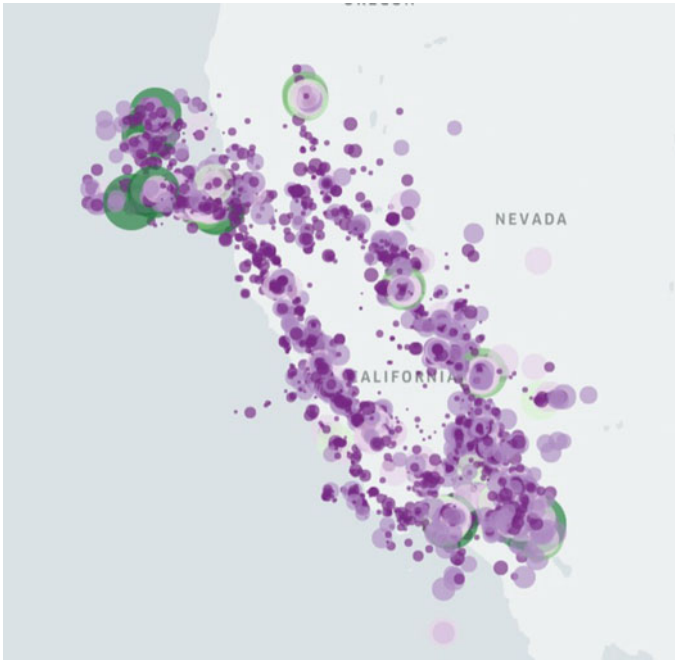
Fig. 2 Representation of earthquakes in California from 1991 to 1995

however, the major difference is that the *latitude* and *longitude* values for a given process will be derived from a fixed set of values that can be specified by using geographical bounds. These sets of value recur at every time-step.

Sample Process Data
See Table 3.

Visualization of a Process Figure 5 represents the spread of bush fire in and around Kakadu National Park in Australia. As we can clearly see, this can be defined as a *process* monitoring the places within the areas that are affected by fire and how the fire in these locations changes. It can thus be seen as a collection of various discrete fire events over a time period and over a given geographical area.

3.4 Relation Among Objects, Events and Processes

- The change in an object can often be described/explained by the occurrence of an event.
- Events can be viewed as discrete objects over a large interval of time.

Fig. 3 Representation of earthquakes in California from 2000 to 2005
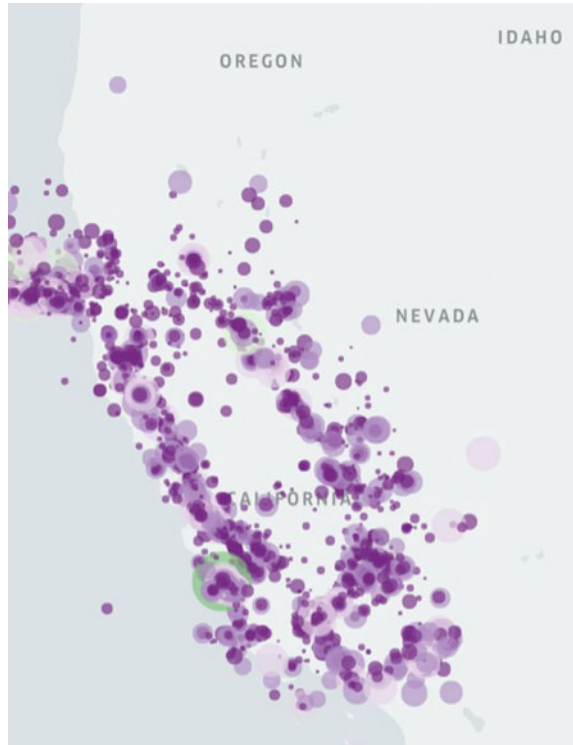
- Processes can be described as a collection of events over a fixed geography and a given time interval (Fig. 6)

4 General Design of Big Data Geospatial Analytics System

A general way to design a geospatial big data analysis system is described in the Fig. 7.

4.1 Importing Data and Storing Raw Data

Raw geospatial data exists in many formats and places. You might have an application where you may have proprietary access to geospatial data or you might be using some third-party data archive or APIs for regularly accessing geospatial data. Importing the data into your system depends upon how your system consumes data. If the data is available in large batches with large time intervals between subsequent batches, one can opt for a batch processing-based consumption approach. The data could
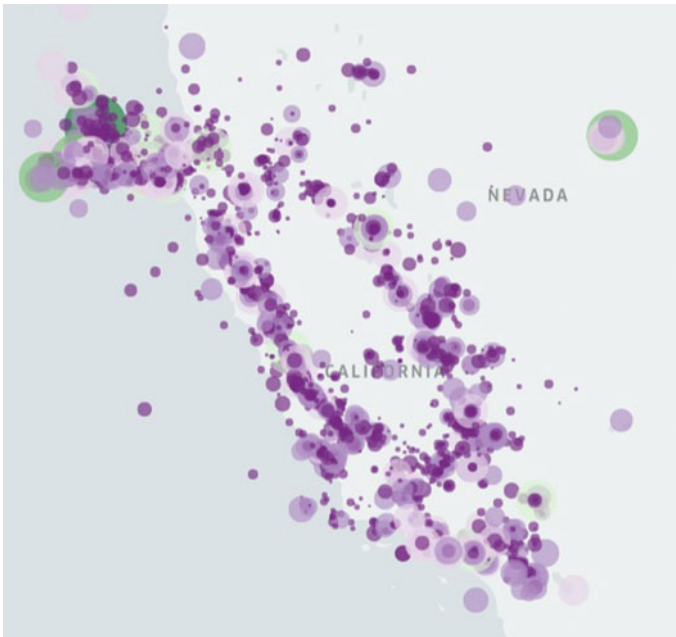
Fig. 4 Representation of earthquakes in California from 2005 to 2010

also be available in real time, and in that case, one could opt for stream processing approaches for processing the data.

Pre-processing the raw data is important for numerous reasons. There are multiple different available file formats and data formats for storing geospatial kind of data. The available raw data might be available in one format, and the designed system might desire a different kind of data format. This becomes one of the reasons why pre-processing the data is important. Additional processing is also required in order to divide the data into the *objects*, *processes* and *events*-based abstraction.

There are two common strategies for storing and processing incoming data, one could be to dump all the raw data into an initial data store, then process the data from that data store into a main data store which will interface with your analytics application. The other common strategy is to process the data in the initial store itself and use it as your main store.

4.2 Common Considerations for Data Stores

PostgreSQL Postgres is one of the most advanced relational databases in the world. Postgres is open sourced and was developed from the Ingres database system developed at UC Berkeley. Postgres does not directly support geospatial data; to introduce

Table 3 Australian bush fire data [22]

Datetime	Latitude	Longitude	Brightness	Confidence
2019-08-01 0:56	− 11.807	142.0583	313.0	48
2019-08-01 0:56	− 11.7924	142.085	319.3	71
2019-08-01 0:57	− 12.8398	132.8744	311.6	42
2019-08-01 0:57	− 14.4306	143.3035	310.1	33
2019-08-01 0:57	− 12.4953	131.4897	310.3	36
2019-08-01 0:57	− 12.6191	142.1998	314.8	68
2019-08-01 0:57	− 14.3655	143.5682	305.4	24
2019-08-01 0:57	− 14.3195	143.5198	322.9	79
2019-08-01 0:57	− 13.1654	141.9715	317.2	72
2019-08-01 0:57	− 11.5473	132.6796	311.5	40
2019-08-01 0:57	− 11.5417	132.649	312.2	42
2019-08-01 0:57	− 11.5471	132.6538	316.0	65
2019-08-01 0:57	− 12.7626	142.1759	335.2	88
2019-08-01 0:57	− 12.705	133.907	311.7	57
2019-08-01 0:57	− 13.1092	134.1848	315.9	67
2019-08-01 0:57	− 14.0539	142.3327	316.0	52
2019-08-01 0:57	− 12.6996	133.9138	310.9	55
2019-08-01 0:57	− 12.7499	134.5251	314.8	66
2019-08-01 0:57	− 12.7141	134.3991	313.9	64
2019-08-01 0:57	− 12.7061	134.4077	314.0	64
2019-08-01 0:57	− 13.8656	141.9771	315.7	69

support for geospatial data objects into Postgres, one needs to install the PostGIS extension that allows Postgres to handle geospatial information. PostGIS stores the data in the form of well-known binary (WKB) and well-known text (WKT) as specified by the OpenGIS standards. Within these formats, one has the freedom to express geospatial data as a.

- POINT
- POINT Z
- POINT ZM
- LINESTRING
- POLYGON
- MULTIPOINT
- MULTIPOINT Z
- MULTILINESTRING
- MULTIPOLYGON
- GEOMETRY COLLECTION
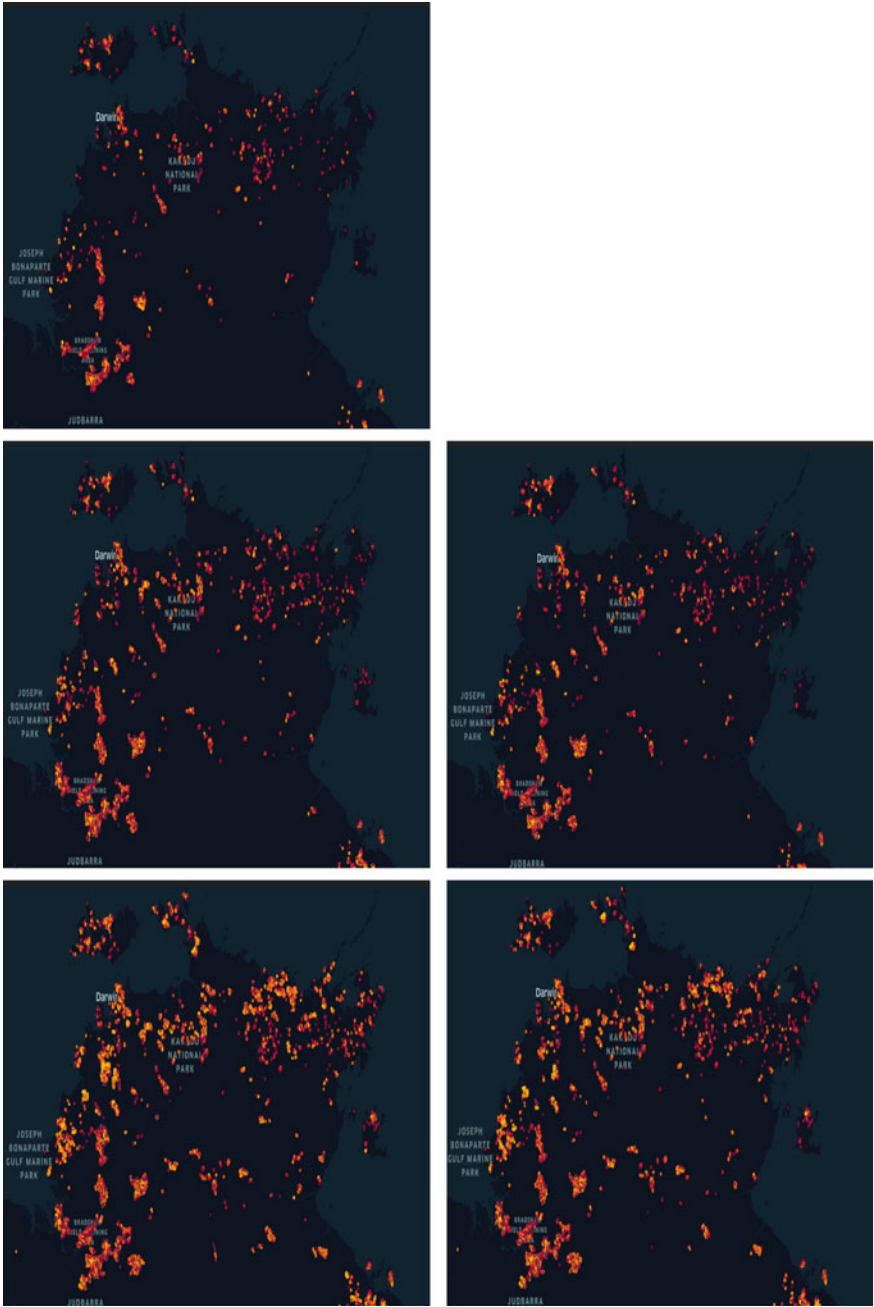
Fig. 5 Spread of bush fire in and around Kakadu National Park, Australia
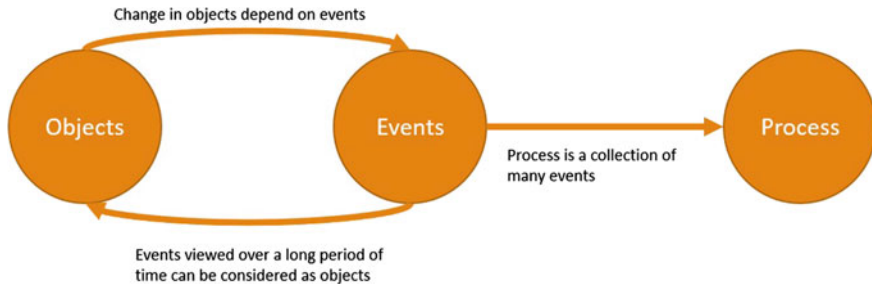
Fig.6 Relation among objects, events and processes
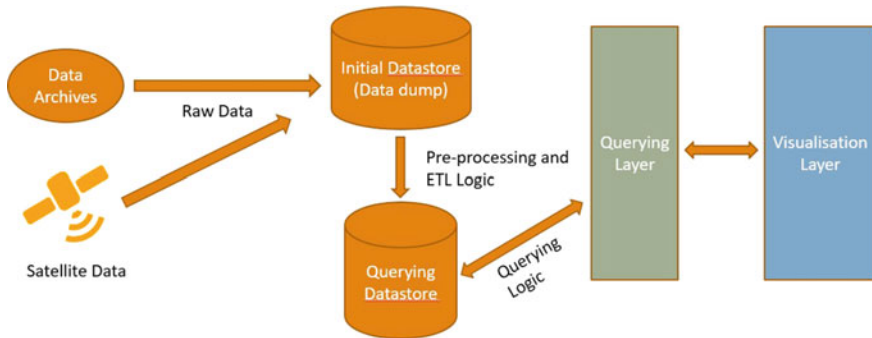
Fig. 7 Sample big data geospatial analytics system

The geospatial queries are expressed under the ST family of queries written as ST INTERSECT, ST AREA, ST LENGTH, etc. [19].

MongoDB is a NoSQL, document-oriented, distributed, general-purpose database. MongoDB is one of the most popular document-oriented databases in terms of preference [23]. MongoDB supports geospatial data in form of GeoJSON objects and uses Euclidean geometry to calculate the geospatial queries. It provides 2D sphere and 2D indexes for indexing geospatial data. One of the major advantages of using MongoDB is that it provides the ability to operate on schema-less data. Since not all geospatial data is relational in nature and most of the geospatial data available out there is non-relational in nature, processing it in relational databases makes it difficult to pre-process data in a relational format. However, MongoDB specifically supports only GeoJSON objects and not any other kind of data like raster or vector. This means that one needs to convert data to GeoJSON in order to make it compatible with MongoDB [24].

Big Data Solutions Big data platforms perform better when it comes to analyzing geospatial big data since they are designed to handle voluminous data and are flexible in terms of the kind of data that can be stored on them. They also exhibit high performance in terms of processing speed on large amounts of data. Most popular

big data systems come with plugins for geospatial support like SpatialHadoop [10] and GeoSpark [25].

5 Conclusion and Future Work

5.1 Summary

We conducted a survey of existing literature to understand the needs for developing a generalized abstract framework for representation and visualization of data related to geographical phenomena. We proposed three different abstractions, namely *objects*, *events* and *processes*. We also demonstrated the use of each of these abstractions along with relevant data and visualizations. We also proposed a generic system architecture that can be used to design a system for analysis and visualization of geographical big data. In this proposed architecture, we discussed the different ways to ingest geospatial data and gave a brief overview about batch and stream processing-based approaches. We also talked about different data store solutions that one could opt for while deciding how to store their geospatial big data.

5.2 Conclusion and Future Work

We have concluded that abstractions such as *objects*, *events* and *processes* provide us a reliable method for representing, analyzing and visualization of geospatial data. Not only do abstractions like these make it easier to understand the geospatial data at hand but, also increase interoperability between different domains utilizing geospatial data. The abstractions being generic can be used for multiple use-cases and across domains. We also proposed a generic system design for a geospatial big data analytics system. We would like to work more on exploring how these proposed abstractions could be applied to a variety of use-cases. We would also like to work along the system design aspect of the system and see how we can focus more on the finer aspects of the design and deliver a more detailed system design. This can include writing software libraries as well as architecture documents related to the overall system design and developing a software ecosystem around these applications.

References

1. Peuquet DJ, Duan N (1995) An event-based spatiotemporal data model (ESTDM) for temporal analysis of geographical data. Int J Geogr Inf Syst 9(1):7–24
2. Yuan M (2001) Representing complex geographic phenomena in GIS. Cartogr Geogr Inf Sci 28(2):83–96
3. Worboys MF (1994) A unified model for spatial and temporal information. Comput J 37(1):26–34
4. Kashiwao T, Nakayama K, Ando S, Ikeda K, Lee M, Bahadori A (2017) A neural network-based local rainfall prediction system using meteorological data on the internet: a case study using data from the japan meteorological agency. Appl Soft Comput 56:317–330
5. Hernández E, Sanchez-Anguix V, Julian V, Palanca J, Duque N (2016) Rainfall prediction: a deep learning approach. In: International conference on hybrid artificial intelligence systems. Springer, Cham pp 151–162
6. Wang H, Zhang L, Yin K, Luo H, Li J (2021) Landslide identification using machine learning. Geosci Front 12(1):351–364
7. Ma Z, Mei G, Piccialli F (2020) Machine learning for landslides prevention: a survey. Neural Comput Appl 1–27
8. Beakta R (2015) Big data and Hadoop: a review paper. Int J Comput Sci Inf Technol
9. Zaharia M, Xin R, Wendell P, Das T, Armbrust M, Dave A, Meng X, Rosen J, Venkataraman S, Franklin M, Ghodsi A, Gonzalez J, Shenker S, Stoica I (2016) Apache spark: a unified engine for big data processing. Commun ACM 59(11):56–65
10. Eldawy A (2014) SpatialHadoop: towards flexible and scalable spatial processing using MapReduce. SIGMOD, ACM, pp 46–50
11. Egenhofer MJ, Al-Taha KK (1992) Reasoning about gradual changes of topological relationships
12. Snodgrass RT (1992) Temporal databases
13. Langran G (1988) Temporal GIS design tradeoffs. GIS/LIS 2:890–899
14. Kim S, Kanwar YS (2019) Geoycsb: a benchmark framework for the performance and scalability evaluation of NoSQL databases for geospatial workloads. In: 2019 IEEE international conference on big data (big data). IEEE, Los Angeles, CA, USA pp 3666–3675
15. Cooper BF, Silberstein A, Tam E, Ramakrishnan R, Sears R (2010) Benchmarking cloud serving systems with YCSB. In: Proceedings of the 1st ACM symposium on cloud computing. Association for computing machinery pp 143–154
16. More NP, Nikam VB, Sen SS (2018) Experimental survey of geospatial big data platforms. In: 2018 IEEE 25th international conference on high performance computing workshops (HiPCW). IEEE, Bengaluru, India pp 137–143
17. Dean J, Ghemawat S (2004) Mapreduce: simplified data processing on large clusters. In: Proceedings of the 6th conference on symposium on operating systems design implementation. USENIX Association
18. Patel H (2017) HBase: a NoSQL database
19. Obe R, Hsu L (2011) PostGIS in action. Manning Publications Co
20. San Francisco Street Tree data. Data SF. https://data.sfgov.org/City-Infrastructure/Street-Tree-List/tkzw-k3nq/data
21. Uber and USGS California earthquake data. https://rawgithubusercontent.com/uber-web/kepler.gl-data/master/earthquakes/data.csv
22. Kaggle Fires from space: Australia and New Zealand. https://www.kaggle.com/datasets/carlosparadis/fires-from-space-australia-and-new-zeland
23. Chauhan A (2019) A review on various aspects of MongoDB databases. Int J Eng Res Technol (IJERT) 8
24. MongoDB MongoDB official documentation. https://docs.mongodb.com/manual/
25. Yu J, Wu J, Sarwat M (2015) Geospark: a cluster computing framework for processing large-scale spatial data. In: Proceedings of the 23rd SIGSPATIAL international conference on advances in geographic information systems. Association for computing machinery

Circularly Polarized Sector Patch Antenna with Fractal Defected Ground Structure

R. Ramya and Shilpi Gupta

Abstract A sector-shaped circularly polarized (CP) corporate feed inspired fractal defected ground structure (FDGS) antenna is proposed in this paper. Fine-tuning the ground plane's defected ground structure (DGS) dimensions to aid CP radiation with enhanced axial-ratio bandwidth. Comparative analysis of the fine-tuned fractal structure with the conventional patch is provided. The higher iterations of the FDGS help achieve good polarization purity with axial ratio enhanced bandwidth compared to traditional sector antenna. The proposed sector patch antenna illustrates an impedance bandwidth of around 110 MHz (1.75–1.86 GHz), while its 3 dB axial-ratio bandwidth is 40 MHz (1.78–1.82 GHz). The gain ranges from 3.39 to 3.75 dBi across the axial-ratio bandwidth.

Keywords Circular polarization · Defected ground structure (DGS) · Fractal structure · Microstrip antenna

1   Introduction

Compact and broadband antennas are becoming increasingly important [1] In addition, wireless systems with circularly polarized (CP) antennas can provide more significant aid without any polarization misalliance between transmitter and receiver [2]. Over the last few decades, there has been a tremendous increase in the research and use of CP planar antennas. Many applications that require low-cost, multi-band, frequency, and reconfigurable polarization antennas prefer microstrip patch antennas (MSA). A sector-shaped microstrip antenna is studied experimentally in [3]. Right-hand or left-hand CP radiation was easily acquired using a single probe feed for specific flare angles ranging from $65°$ to $70°$. The letter presented in [4] depicts an

R. Ramya (✉) · S. Gupta
Sardar Vallabhbhai National Institute of Technology, Surat, Gujarat 395007, India
e-mail: ramyaraki9@gmail.com

S. Gupta
e-mail: sgupta@eced.svnit.ac.in

innovative method for designing a single feed CP microstrip antenna with FDGS. This strategy not only produces circular polarization but also improves the cross-polar levels. The second and third iterative CP microstrip antennas showed significant improvement in achieving CP. A dual-band dual-polarized antenna is presented [5], utilizing a portion of a sector. The sector disk shape is cut into the shape of the fan to make it further compact and facilitate multi-band ability. The antenna shows resonance with circular and linear polarization in UMTS (1920–2170 MHz) and WiMAX (3.4–3.7 GHz) bands. A compact CP microstrip antenna (1.492–1.518 GHz) utilized in the mobile satellite communications band is presented in [6]. Kim and Park [7] initially worked on the concept of DGS to characterize the single unit of the defect of the dumbbell pattern. In [8], a chronology of its development is presented in a structured manner. Due to its compact structure and ease of implementation, DGS has emerged as a promising alternative to EBG for various applications. The circular patch of CP radiation is imprinted with two asymmetric length rectangular-shaped slots perpendicular to each other. Koch's fractal DGS in [6] aids size reduction by 44.74%, improved bandwidth of AR by 62.73%, impedance bandwidth by 70.74%, and radiation effectiveness by 4.03% compared to conventional patch antennas. A 90-degree flare angular sector-shaped broadband antenna is depicted in [7]. Square notches on the side lengths contribute to the tuning and bandwidth improvement of the axial ratio. The same element, stacked as a parasitic patch with 0.8 mm height substrate material, improved the gain considerably. A single feed E-shaped patch with inclined fractal defected ground structure (IFDGS) is proposed in this article [8]. Like the traditional patches that use notches to generate CP in [9], a similar idea has been implemented to produce CP with sector patches. Some miniaturization has been achieved, was extended to make an array of patches to improve the gain. It is evident from the experimental results that this strategy significantly enhanced the impedance bandwidth, axial-ratio (AR) bandwidth, and gain of the antenna. An inclined FDGS has been discussed in [10] and [11], here the CP is achieved by the fractal DGS embedded in the ground plane inclined along the diagonal axis. The work in [12] gives a detailed understanding of the fractal structure used in the paper with a square patch. The generation of the degenerate modes with an in-depth analysis with the help of resonant curves and current distributions are clearly explained.

Single-feed microstrip antennas to produce circular polarization are used considerably to reduce the bulkiness and make a compact antenna. More shapes like sector, hexagonal, pentagonal, etc., are explored due to their ease of incorporation with a single feed configuration. Circular polarization can be generated by embedding diagonal slots, perturbing the edges, cutting corners, adding tabs, etc. Sector patch antennas help produce circular polarization by controlling the flare angle and providing an offset feed position. CP radiation can also be achieved by using a specific segment of the circular patch, such as a sector-shaped microstrip patch with a certain angle of flare shown in Fig. 1. The proposed design includes a sector-shaped CP antenna with fractal DGS and specific flare angles to achieve circular polarization. Compared to the traditional sector patch antenna, the axial-ratio bandwidth also improves using fractal DGS.
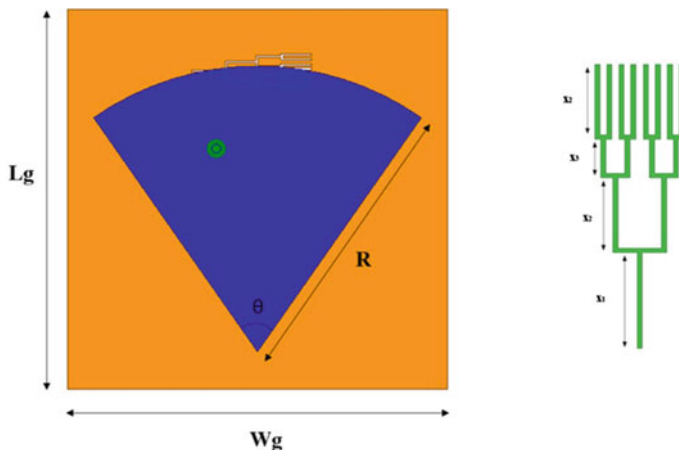
Fig. 1 Coaxial probe fed circular disk sector patch antenna with fractal DGS ($L_g = W_g = 60$, $R = 45$, $h = 3.18$ (all in mm), $\theta = 70°$ and $\varepsilon r = 4.4$)

2 Antenna Design and Geometry

The sector segment of the patch with the radius of R and flare angle of θ is etched on a substrate material of thickness h and relative permittivity εr. Near degenerate modes with the same amplitudes and 90° out of phase, these components are excited by slightly making the lengths of the corresponding surface current paths on the patch in the orthogonal directions different. The coaxial point was positioned at an end where the two orthogonal modes TM_{10} and TM_{01} are excited around 1.8 GHz at near degenerate frequencies. The precise flare angle at which these modes are excited was obtained through HFSS simulation. An FR4 dielectric substrate with $\varepsilon r = 4.4$, the dielectric height of 3.18 mm, and ground plane dimensions are $W_g \times L_g$ mm. An impedance bandwidth at which S_{11} magnitude is below -10 dB is obtained from (1.75–1.86 GHz), i.e., 110 MHz with the addition of fractal DGS. The axial-ratio characteristics show a *CP* bandwidth of 40 MHz. Furthermore, there is a substantial decrease in the antenna size as the ground plane dimension is 60 × 60 mm, keeping the flare angle 70° and radius as 45 mm compared to the conventional sector-shaped patch antenna.

2.1 Mathematical Modeling of the Proposed Antenna

The dimensions of the proposed sector antenna depicted in Fig. 1 are approximated [2] and optimized by using the formulae in Eq. (1)
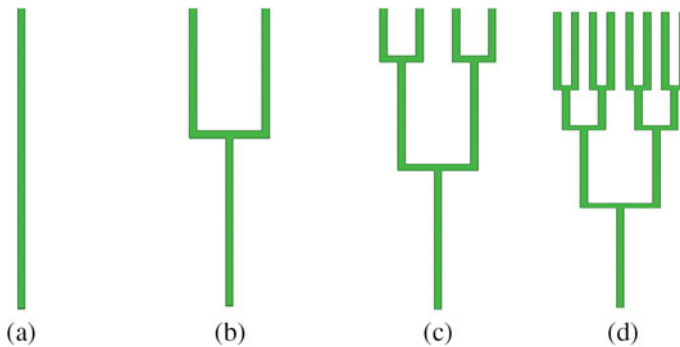
Fig. 2 Evolution of fractal geometries **a** Iteration zero **b** Iteration one **c** Iteration two **d** Iteration three

$$\text{Radius} = \frac{2c}{2 * F\sqrt{\varepsilon r}} \tag{1}$$

where c = speed of light

F = frequency of operation.

Figure 2 shows the geometry of the considered fractal assemblies with zero to the third iteration. As shown in Fig. 2a, zeroth iterative basic fractal structure. The fractal structure with the first iteration is attained by considering a U-shaped layout embedded with a straight line, as illustrated in Fig. 2b. The first fractal iterative structure is also considered the fundamental fractal unit. The second iterative structure evolved from the first iterative structure by adding small U-shaped structures onto the arms of the first fractal unit, as shown in Fig. 2c The third iterative fractal structure is developed by repeating four sections of the first iterative fractal structure U-shaped unit cell, as shown in Fig. 2d. By repetition of this procedure, higher iterations of the fractal structure are attained.

2.2 The Design Evolution of the Proposed Antenna

In stage I, the zeroth iteration is carried out. The design is depicted in Fig. 3. In the stage I, zeroth iteration is carried out. The structure is illustrated in Fig. 3. The first fractal unit is positioned at 9.3 mm from the feed center with $x_1 = 5.25$ mm. The return loss shows a good resonance, but the axial ratio is not yielded, so the circular polarization was not obtained in this case. In stage II, the first iteration is implemented. The design is shown in Fig. 3. It is now divided into two more fractals of lengths $x_1 = 5.25$ mm, $x_2 = 8.3$ mm, $y_1 = 2.7$ mm, and $g = 0.3$ mm. The return losses shown in Fig. 4 imply a good bandwidth, but the axial ratio is not tuned and shows poor polarization purity, i.e., it is not yielding circular polarization. There was no considerable change in the cross-polar level when observing the radiation patterns
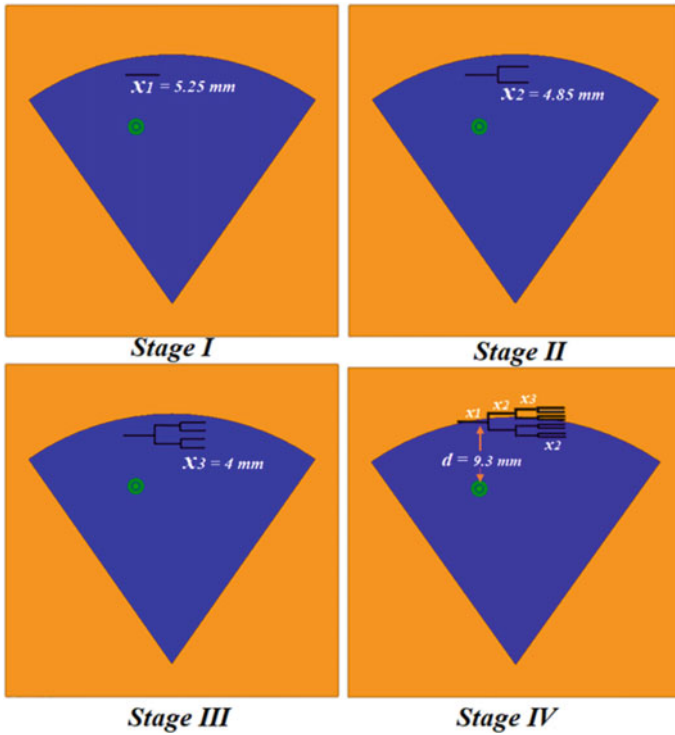
Fig. 3 Different stages of antenna development from zeroth iteration to the third iteration

at this stage. Stage 3 shows parameter values of the second iteration design are: $x_1 =$ 5.25 mm, $x_2 = 4.85$ mm, $x_3 = 4$ mm, $y_1= 2.7$ mm, $y_2 = 1.26$ mm, and $g = 0.3$ mm. The antenna design is depicted in Fig. 3. The return loss for the second iteration, as in Fig. 4, gives a bandwidth of 100 MHz, and the axial ratio needs to be tuned further. In stage IV, the antenna yields a good axial-ratio bandwidth and polarization purity. The kink in the return loss plot in Fig. 4 indicates that degenerate modes are perfectly tuned.

3   Results

The parameter values of the third iteration design are: $x_1 = 5.25$ mm, $x_2 = 4.85$ mm, $x_3 = 4$ mm, $x_4 = 4.85$ mm, $y_1 = 2.7$ mm, $y_2 = 1.26$ mm, $y_3 = 0.36$ mm, and $g = 0.3$ mm. The antenna design is depicted in Fig. 1. The third iterative FDGS, unlike the first two, helps to produce circular polarization. The frequency plot also indicates that a quite good axial ratio below 3 dB has been obtained. An axial ratio of less
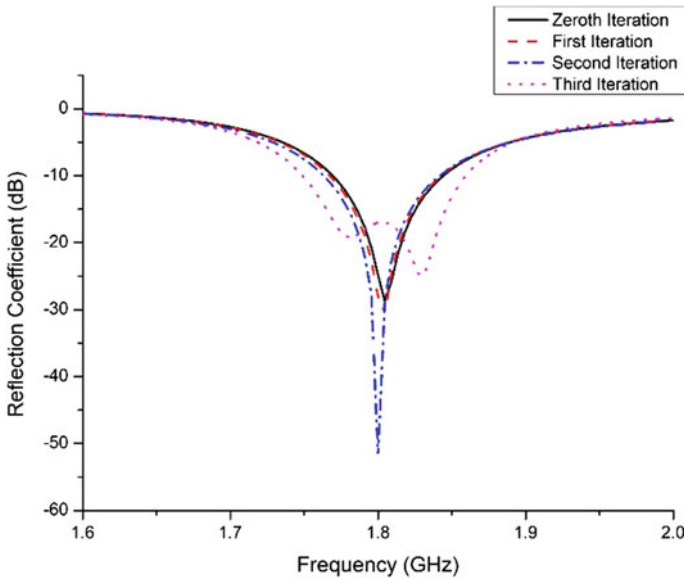
Fig. 4 Return loss plots from zeroth iteration to the third iteration

than 1 dB is seen in Fig. 6, indicating a pure CP at 1.8 GHz frequency. Fractals aid in producing long current lines providing a slow wave effect.

The addition of fractal DGS induced an impedance bandwidth of 1.75–1.86 GHz (110 MHz) is obtained as shown in Fig. 5, which is wider when compared to the conventional patch without DGS. The axial-ratio characteristics also show an improvement in CP bandwidth compared to the traditional patch. The obtained bandwidth with fractal DGS is 40 MHz, as in Fig. 6. The axial-ratio plot indicates that a fine-tuning below 3 dB is obtained at the 1.8 GHz frequency range.

The gain of the proposed CP antenna is reasonably stable across the axial-ratio bandwidth, i.e. (1.75–1.8 GHz), and its value is between 3.39 and 3.75 dBi, as shown in Fig. 7.

Smith chart showing a comparison between the impedance matching for conventional patch and the fractal DGS patch is illustrated in Fig. 7. The radiation pattern here in Fig. 8 depicts a gain of 3.75 dBi and a much better cross-polarization level of − 29.25 dB, which is − 16 dB in the case of the conventional patch. Using this fractal structure, the XP levels have significantly improved.

4   Conclusion

We can also use fractal DGS and generate enhanced bandwidth CP antenna with good gain than conventional shapes. Fractal DGS provides improved axial-ratio bandwidth
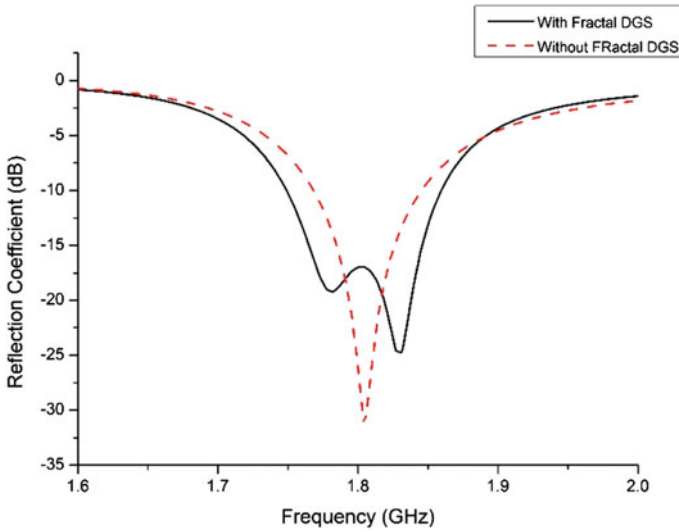
Fig. 5 Comparison between the return loss plots of conventional and with fractal DGS (third iteration) disk sector patches
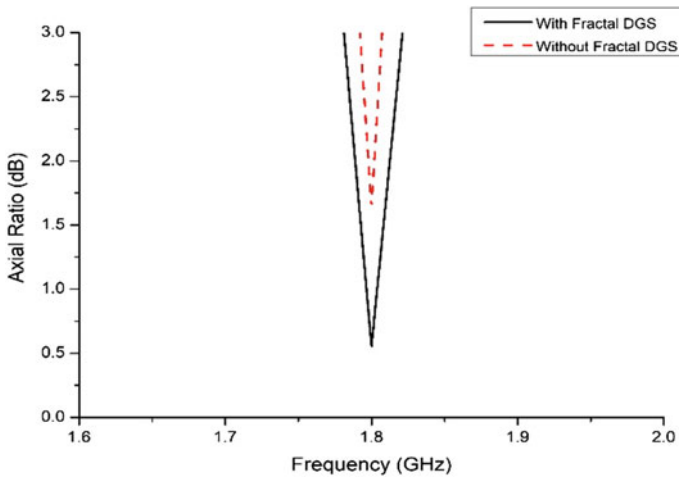
Fig. 6 Comparison between the axial-ratio plots of conventional and with fractal DGS (third iteration) disk sector patches

and gives better cross-polar levels. It is evident from the results that the use of this strategy reduced the size of the antenna from 75 × 75 mm to 60 × 60 mm with improved impedance bandwidth of 110 MHz and axial-ratio bandwidth of 40 MHz which was 70 and 10 MHz in the conventional patch antenna case.
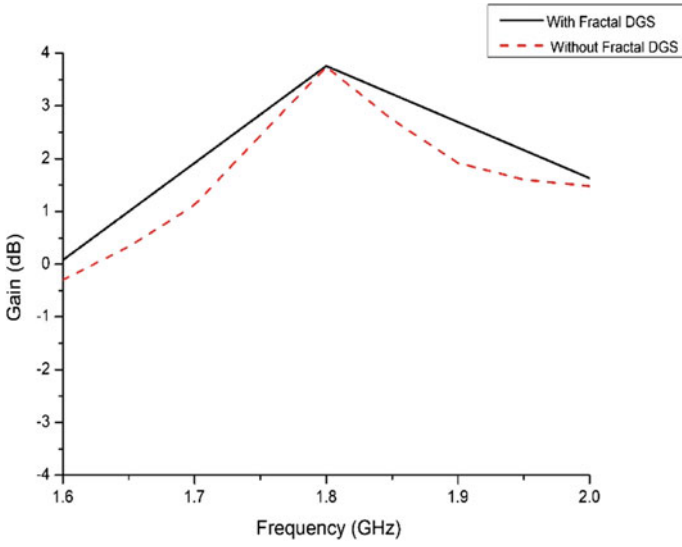
Fig. 7 Gain versus frequency for the third iteration of fractal DGS antenna
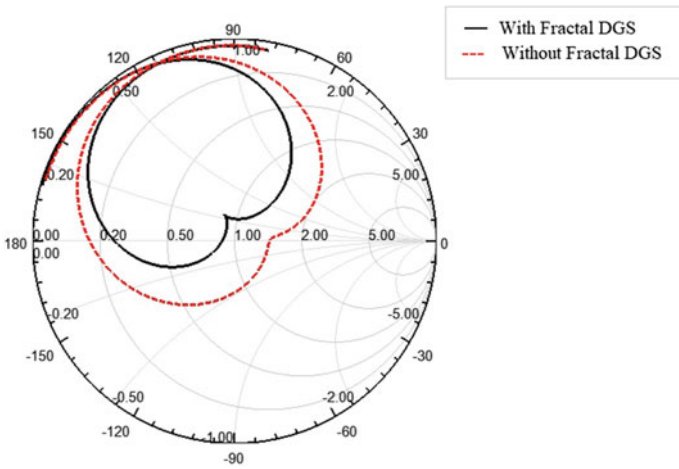
Fig. 8 Smith chart showing a comparison between the impedance matching for conventional patch and the fractal DGS patch
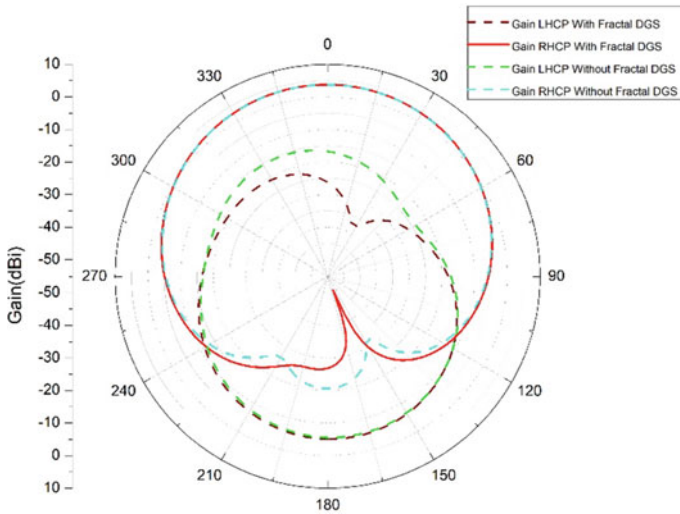
Fig. 9 Radiation pattern of conventional and with third iterative fractal DGS disk sector patch

References

1. Ray KP, Kumar G (2003) Broadband microstrip antennas. Artech house, Boston, London
2. Balanis CA (2015) Antenna theory: analysis and design, 3rd edn. Wiley, Hoboken
3. Hsu W-H, Wong K-L (1998) Circularly-polarised disk-sector microstrip antenna. Electron Lett 34:2188–2190
4. Wei K, Li JY, Wang L, Xu R, Xing ZJ (2017) A new technique to design circularly polarized microstrip antenna by fractal defected ground structure. IEEE Trans Antennas Propag 65(7):3721–3725
5. Mathew S, Anitha R, Vinesh PV, Vasudevan K (2014) Sector-shaped dual-polarized patch antenna for UMTS/WIMAX applications. In: 2014 IEEE International Microwave and RF Conference (IMaRC). IEEE, Bangalore
6. Prajapati PR, Murthy GGK, Patnaik A, Kartikeyan MV (2015) Design and testing of a compact circularly polarised microstrip antenna with fractal defected ground structure for L-band applications. IET Microwaves Antennas Propag 9(11)
7. Kim CS, Park JS, Ahn D, Lim JB (2000) A novel 1-D periodic defected ground structure for planar circuits. IEEE Microw Guided Wave Lett 10(4):131–133
8. Guha D, Biswas S, Antar YMM (2011) Defected Ground Structure for microstrip Antennas. Wiley, United Kingdom
9. Tanaka T, Takahashi M, Ito K (2006) Miniaturization of circularly polarized patch antenna using circular sector element. In: IEEE international workshop on antenna technology small antennas and novel metamaterials. IEEE, pp 209–212
10. Gupta S, Patil S, Dalela C, Kanaujia BK (2021) Analysis and design of inclined fractal defected ground-based circularly polarized antenna for CA-band applications. Int J Microwave Wireless Technol 13(4):397–406
11. Gupta S, Kanaujia BK, Dalela C, Patil S (2020) Design of circularly polarized antenna using inclined fractal defected ground structure for S-band applications, pp 1–15
12. Ambekar AG, Deshmukh AA, Chavali VAP (2021) Investigation into circular polarized response of square microstrip antenna using defected ground structure. In: International conference on communication information and computing technology (ICCICT)

Two-Element MIMO Antenna with Polarization Diversity for 5G Application

Nabeela, R. Ramya, and Shilpi Gupta

Abstract A two-element multiple-input multiple-output (MIMO) antenna of size 80 × 40 mm with circular polarization diversity for sub-6 GHz application is proposed in this paper. The single antenna operating at 3.5 GHz frequency consists of a sidewalk brick-shaped patch antenna. An offset feed is employed to get circular polarization. The step monopole ground of length λ/4 is used to get broad bandwidth. The axial ratio bandwidth improves further when an inverted L-shaped strip and an L-shaped strip are added to the resonating edge of the patch. The impedance bandwidth of 51.6% is obtained from 3.06 to 5.19 GHz, while the 3-dB axial ratio bandwidth of 16% is from 3.32 to 3.91 GHz. The antenna exhibits a tilted directional radiation pattern with 2.4 dB gain and 90% efficiency. Two-element MIMO antenna with a circular polarization diversity arrangement is designed with a distance of approximately λ/4. The isolation obtained between two antennas is more than 14 dB. Envelope correlation coefficient (ECC) is well below 0.005 with a diversity gain value close to 10. The antenna has application in a 5G sub 6 GHz band and wireless communication.

Keywords Circular polarization diversity · MIMO antenna · ECC · Diversity gain

1 Introduction

Circularly polarized antennas are employed in satellite communication links and radio frequency identification systems because of the advantages like receiver alignment insensitivity, multipath loss suppression, and equipment orientation insensitivity. The funnel-shaped radiating structure with monopole proposed in [1] gives wider bandwidth. Corrugated funnel-shaped radiating elements increase the

Nabeela · R. Ramya (✉) · S. Gupta
Sardar Vallabhbhai National Institute of Technology, Surat, Gujarat 395007, India
e-mail: d18ec001@eced.svnit.ac.in

S. Gupta
e-mail: sgupta@eced.svnit.ac.in

antenna's electrical length. A slotted common ground plane makes these monopoles feasible to resonate at a lower operating frequency of 2.96 GHz. A monopole tapered feed antenna with an inverted L-shaped strip (ILSS) and L-shaped strip (LSS) along the monopole's left/right radiating edge is discussed in [2]. Here, the protruding strips help to generate the degenerate mode. A compact printed monopole antenna with a hook-shaped branch shown in [3], is made up of a hook-shaped branch connected to a partial rectangular ground plane and a flipped unequal arm with an L-shaped microstrip feed, making it possible for the antenna to achieve wideband circular polarization. In [4], two orthogonal modes are generated by putting a G-shaped parasitic strip into a C-shaped monopole antenna structure. A monopole antenna with L-shaped resonator and the modified ground plane proposed in [5] produces a broader bandwidth. C-shaped monopole antenna with a triangular stub in the ground is reported in [6]. A wide impedance bandwidth and axial ratio bandwidth are achieved by cutting the corner on the modified C-shaped patch and adding triangular stubs on the ground plane. A circular printed antenna with staircase ground is proposed [7].

Essential requirements of 5G antennas are high gain, stable radiation pattern, and broader bandwidth. A single-element antenna cannot satisfy these requirements, so a multi-antenna system is required. MIMO antenna means more than one antenna in a system. Various diversity techniques can be implemented for MIMO antennas, namely space diversity, polarization diversity proposed in [8] and pattern diversity in [9], and a combination of both pattern and polarization diversity in [10]. A 4 × 4 MIMO antenna non-elliptical cuts in the ground plane, C-shaped microstrip line feed aids the circular polarization and is presented in [11]. A single-element MIMO antenna with pattern and polarization diversity is proposed [12]. A circularly polarized MIMO antenna with the truncated patch is discussed in [13] for WLAN application. Three-element MIMO antenna with two dipole antennas for linear polarization and chamfered edge patch antenna for circular polarization with pattern diversity is proposed [14]. The paper presented in [1] discusses a coplanar waveguide-fed CP MIMO antenna for off-body communications. Adding two strips at the right and left sides of the feed alters the surface currents to produce CP. This paper's two-element MIMO monopole antenna is proposed for a 5G sub-6 GHz application. The single antenna consists of a sidewalk brick-shaped patch with an inverted L-shaped strip (ILSS) and an L-shaped strip (LSS) provided at the radiating edge of the patch. The ground is a $\lambda/4$ monopole step ground. MIMO arrangement consists of two such antennas facing each other with polarization diversity between them.

The paper's organization is as follows: In the first section, the single antenna design, mathematical modeling, evolution stages, and performance analysis of a single antenna are covered. The second section consists of the MIMO antenna's performance analysis and conclusion.

2 Antenna Design and Geometry

The geometry of the proposed monopole antenna is shown in Fig. 1. The substrate used is FR4, with a height of 1.6 mm. The design consists of a rectangular patch chamfered at the edges with $L_s \times W_s$, length and width, respectively. The chamfer length of L_s makes an inclination of $45°$, giving it a sidewalk brick-like shape. The patch is fed offset to ease the generation of degenerate modes. Monopole step ground is designed with L_m and L_{m1} on the patch's left and right sides, respectively. Inverted L-shaped strip (ILSS) and L-shaped strip (LSS) are added with a gap of distance G at the radiating edge of the patch to get the circular polarization. Optimized values of the parameter are given in Table 1.

2.1 Mathematical Modeling of the Antenna

The dimensions of the proposed antenna in Fig. 1 are approximated using the following design equations.

1. Width of the patch:

$$W = \frac{c}{2f_o\sqrt{\frac{\epsilon_r + 1}{2}}} \tag{1}$$

2. Effective length:

Fig. 1 Geometry of the proposed antenna
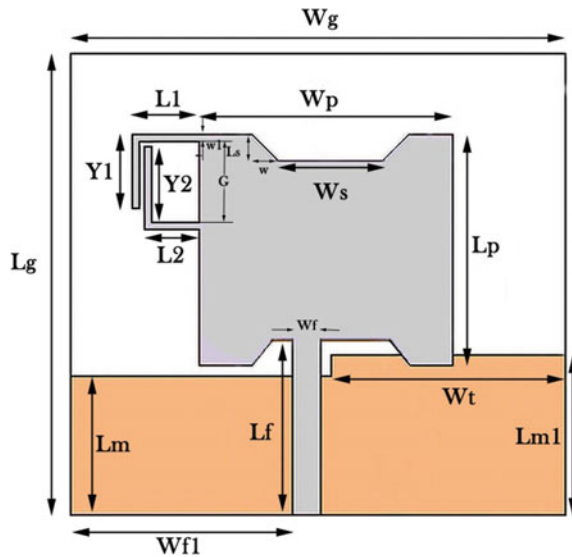
Table 1 Parameter values of
the proposed antenna

Parameters	Value (mm)	Parameters	Value (mm)
L_g	38	L_f	13.6
W_g	38	W_f	3.05
L_s	1.6	W_{f1}	15.95
W_s	0.6	L_m	11.2
W_{m1}	18.7	L_1	4
Y_1	8	Y_2	8.5
L_r	1.8	G	7.93
W_r	7.9	W_1	0.8
L_{m1}	18	W_p	18
L_p	22	S	0.6

$$L_{\text{eff}} = \frac{c}{2f_o\sqrt{\epsilon_{\text{eff}}}} \tag{2}$$

3. Length extension (ΔL):

$$\Delta L = 0.412h \frac{(\varepsilon_{\text{eff}} + 0.3)\left(\frac{W}{h} + 0.264\right)}{(\varepsilon_{\text{eff}} - 0.258)\left(\frac{W}{h} + 0.8\right)} \tag{3}$$

4. The actual length of the patch:

$$L = L_{\text{eff}} - 2\Delta L \tag{4}$$

2.2 Antenna Design Evolution Stages

Antenna 1 illustrated in Fig. 2 depicts a simple rectangular patch antenna whose reflection coefficient plots are shown in Figs. 3 and 4, respectively. Modifications in the patch are done to make the antenna resonate at 3.5 GHz and excite circular polarization. Antenna II is the patch antenna with sides chamfered, and the feed is placed off-center to generate CP. Antenna II has an axial ratio below 3-dB at 3.5 GHz. The patch antenna gives very low bandwidth, so partial ground is cut, leaving ground length almost equal to λ/4, making it a monopole antenna (Antenna III). Monopole antenna increased the impedance bandwidth drastically compared to regular patch antenna, as shown in Fig. 3.

Further modifications in the ground plane and the patch are done to get broad impedance and axial ratio bandwidth. Firstly, the length of the ground cuts to make it a step-ground Antenna IV to give additional current path length. This step ground helps increase the axial ratio bandwidth at the 3.6 GHz frequency, as shown in Fig. 4. Thereby, an inverted L-shaped strip (ILSS) is added to the patch's radiating edge
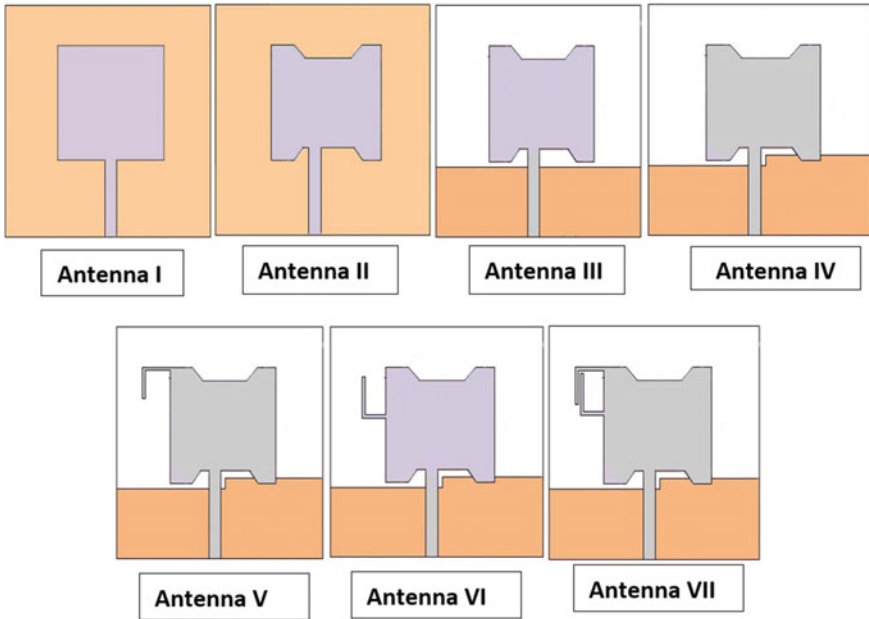
Fig. 2 Geometry of evolution of the antenna design from Antenna I to Antenna VII
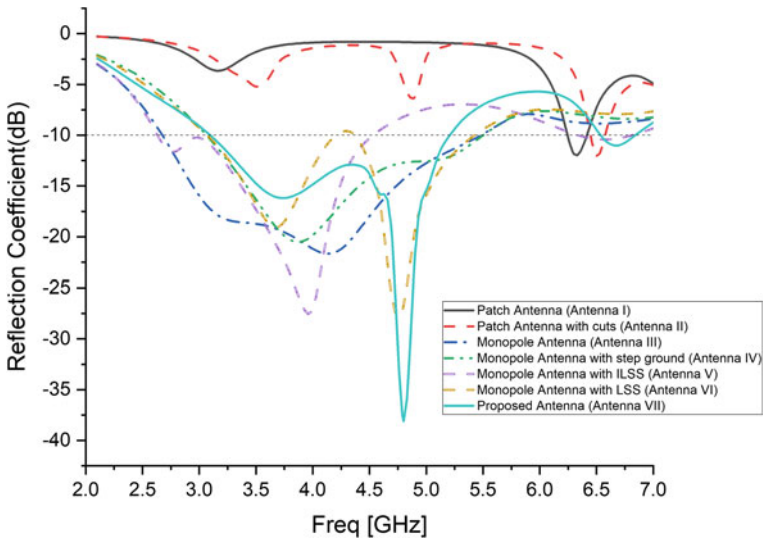
Fig. 3 Simulated reflection coefficient
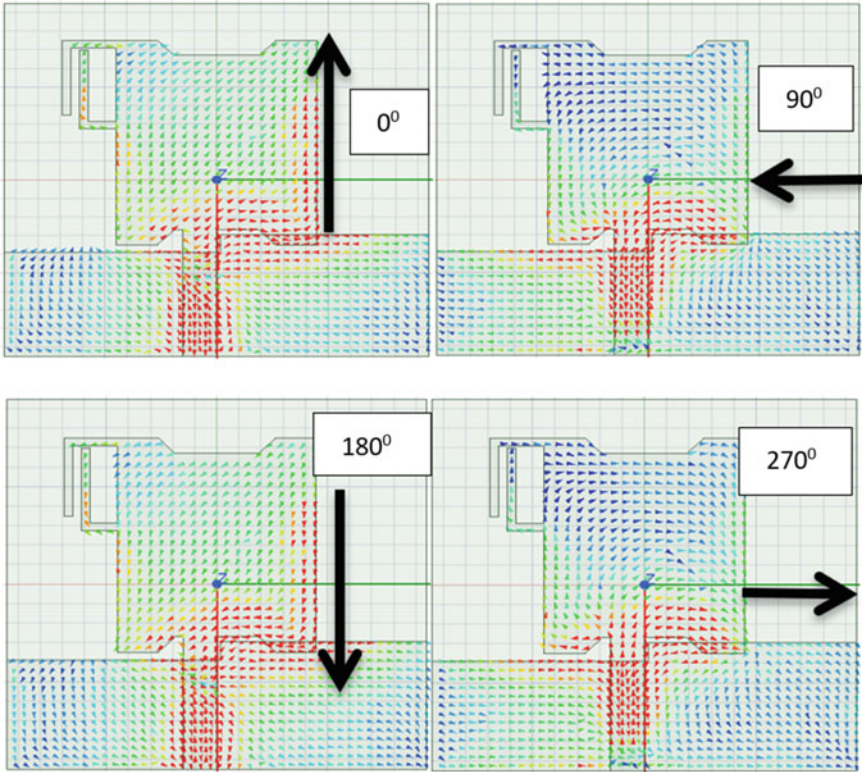
Fig. 4 Surface current distribution of the proposed antenna at 3.5 GHz

patch in Antenna V to make it resonate at a lower frequency, as depicted in Fig. 3. Antenna VI has an L-shaped strip (LSS) added to the patch to analyze its outcome. This LSS resonates the antenna at a higher frequency, as shown in Fig. 3 reflection coefficient plot. Finally, ILSS and LSS are combined to get broad bandwidth, as in Fig. 3: Antenna VII. The axial ratio bandwidth of the proposed antenna increases with wide impedance bandwidth compared to the traditional patch antenna. The surface current distribution of the proposed antenna at 0, 90, 180, 270° is shown in Fig. 4. The current distribution illustrates the field's rotating anticlockwise direction and is right-hand circularly polarized (RHCP).

3 Performance Analysis of Single-Antenna Unit

Figure 5 shows the S parameter plot and the axial ratio plot of the proposed antenna. Impedance bandwidth from the plot is 51.6% from 3.06 to 5.19 GHz, while the 3-dB

axial ratio bandwidth is 16% from 3.32 to 3.91 GHz. The axial ratio bandwidth is 31% that of impedance bandwidth.

Figure 6 shows the radiation pattern of the proposed antenna in XZ and YZ planes at 3.5 GHz. The antenna has a tilted unidirectional radiation pattern. The antenna's gain obtained is 2.4 dB with a cross-polarization value of less than − 30 dB. The efficiency plot shown in Fig. 7 displays that the efficiency is greater than 90% for the whole operating frequency range of the antenna.
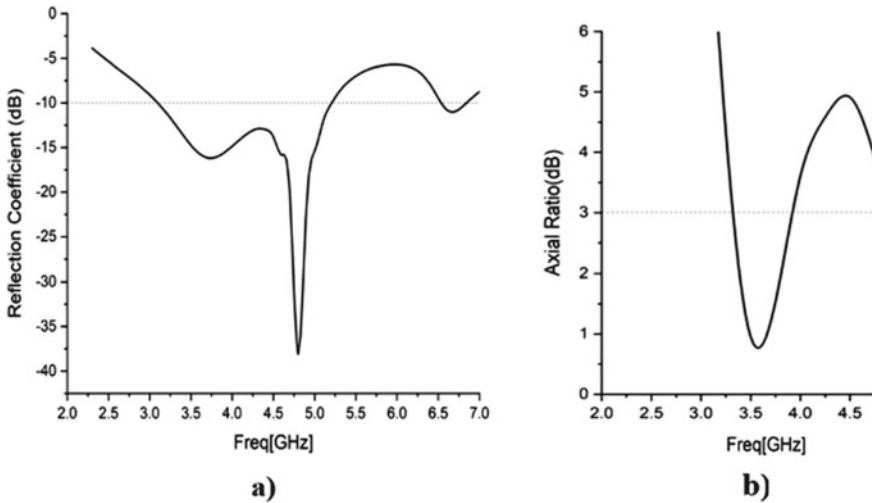
Fig. 5 Simulated **a** reflection coefficient **b** axial ratio of the proposed antenna
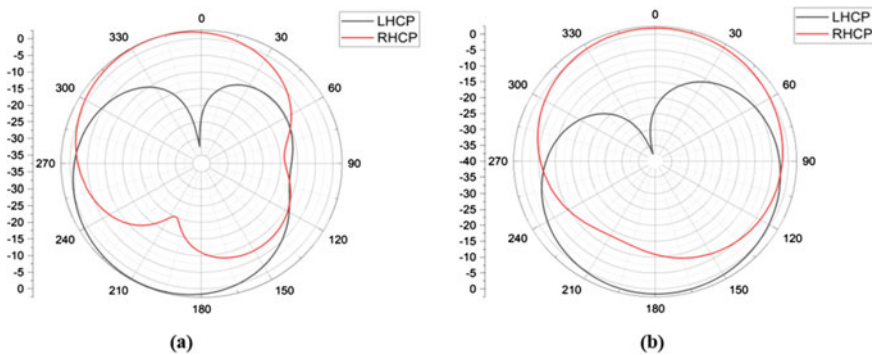
Fig. 6 Simulated radiation pattern of the proposed antenna **a** XZ plane **b** YZ plane at 3.5 GHz
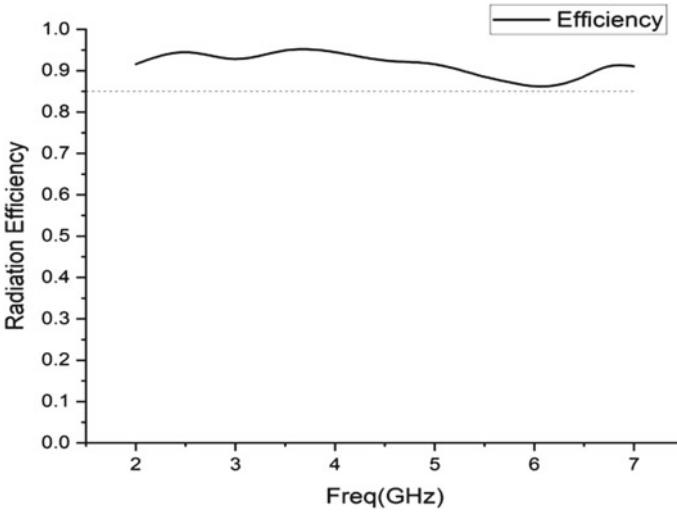
Fig. 7 Efficiency of the proposed antenna

4 Polarization Diversity MIMO Antenna Design

A two-element MIMO antenna with a dimension of $L_g1 \times W_g1$ having polarization diversity is designed to achieve maximum diversity and compact size. As shown in Fig. 8, the two antennas radiate in RHCP and LHCP, respectively. When two antennas have different polarization, they do not interfere, giving high isolation. The distance between the antennas is approximately λ/4 by placed facing one another, as shown in Fig. 8. By arranging the antennas in this manner, maximum isolation can be obtained compared to other side-by-side arrangements. Placing the antenna side by side, the polarization purity is affected. Optimized values are given in Table 2.

4.1 MIMO Antenna Performance Analysis

Figure 9 shows the reflection coefficients, S_{11} has a bandwidth of 54.6% from 3.26 to 5.71 GHz, and S_{22} has 52.7% from 3.28 to 5.63 GHz. These two antennas are highly isolated, with around 24 dB isolation at 3.5 GHz and more than 14 dB isolation in the whole antenna operating range. The isolation achieved is due to polarization diversity between the two antennas without any isolation enhancement techniques reported in the literature. Figure 10 shows the axial ratio of the two antennas. Antenna 1 gives a 3-dB axial ratio bandwidth of 27.7% from 3.42 to 4.52 GHz, while Antenna 2 gives a 3-dB axial ratio bandwidth of 26% from 3.39 to 4.42 GHz. The axial ratio bandwidth is about 50% of that of impedance bandwidth. The AR bandwidth compared to
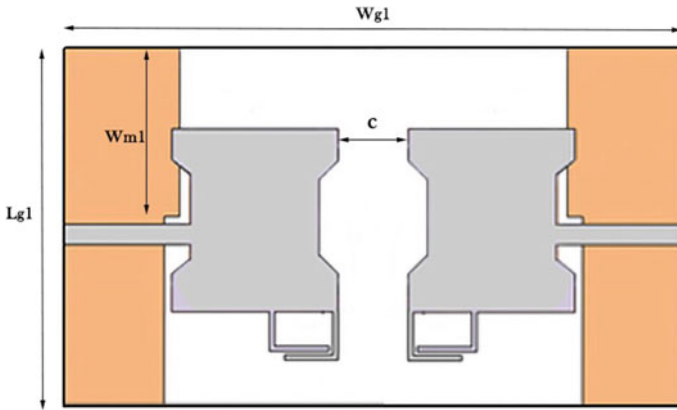
Fig. 8 Geometry of the proposed MIMO antenna

Table 2 Parameter values of the proposed MIMO antenna

Parameters	L_g1	W_g1	W_m1	c
Value (mm)	40	80	19.7	12

impedance bandwidth in MIMO is increased from 31% in single antennas to 50% in MIMO antennas.
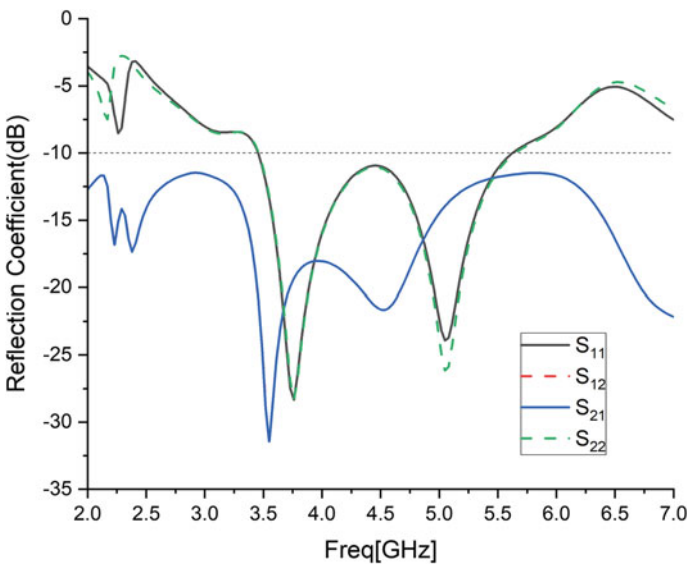
Fig. 9 Simulated reflection coefficient of MIMO antenna
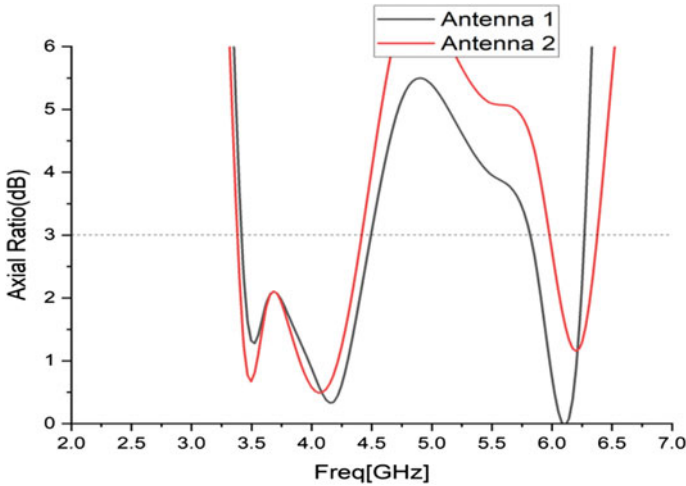
Fig. 10 Axial ratio of the MIMO antenna

The radiation pattern of both antennas in the XZ plane and YZ plane is shown in Fig. 11. The radiation pattern illustrates that Antenna 1 is RHCP and Antenna 2 is LHCP. The cross-polarization level value for both antennas is less than −20-dB. The radiation can be seen from the YZ plane with a gain of 3-dB. Radiation efficiency is more than 90% for the whole operating range of operation shown in Fig. 12. This value indicates that the antenna radiates 90% of its accepted power.

Figure 13 shows the envelope correlation coefficient (ECC) versus frequency plot. The value of ECC obtained is less than 0.005, which is significantly lower than the ideal value of < 0.5; both antennas' radiation pattern is independent of each other. The formula used to calculate ECC is given below by Eq. 5.

$$\text{ECC} = \frac{\left| S_{11}^* \, S_{12} + S_{21}^* \, S_{22} \right|^2}{\left(1 - |S_{11}|^2 - |S_{21}|^2\right) \left(1 - |S_{22}|^2 - |S_{12}|^2\right)} \tag{5}$$

Figure 14 shows the MIMO antenna's diversity gain (DG) plot. Here, DG value is almost 10 in the operating band. This value of DG assures that after introducing a diversity scheme, transmission power reduces considerably, which is an added advantage. The formula for DG is given by Eq. 6.

$$\text{DG} = 10 \times \sqrt{\left(1 - |\rho|^2\right)} \tag{6}$$
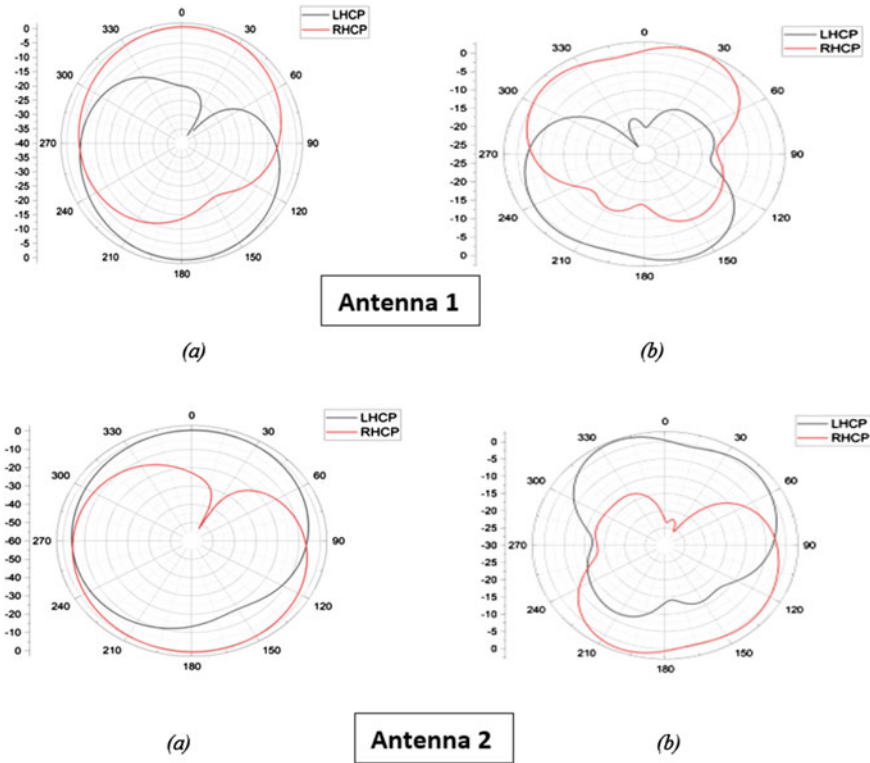
Fig. 11 Simulated radiation pattern of the proposed MIMO antenna **a** XZ plane **b** YZ plane for Antenna 1 (RHCP) and Antenna 2 (LHCP) at 3.5 GHz

5 Conclusion

A two-element MIMO antenna with polarization diversity has been presented in this paper. The performance of the single patch antenna is enhanced in terms of bandwidth when monopole design with step ground and ILSS and LSS strips addition is introduced. ILSS and LSS helped to change the current length of the antenna because of which axial ratio bandwidth increased. The impedance bandwidth of 51.6% is obtained from 3.06 to 5.19 GHz, while the 3-dB axial ratio bandwidth of 16% is from 3.32 to 3.91 GHz. The antenna exhibits a radiation pattern with 2.4-dB gain and 90% efficiency. The two-element MIMO antenna with circular polarization diversity arrangement gave high isolation of more than 14 dB between two antennas and increased the AR bandwidth to 27%. ECC is well below 0.005 with a diversity gain value close to 10. This value indicates a good MIMO antenna performance.
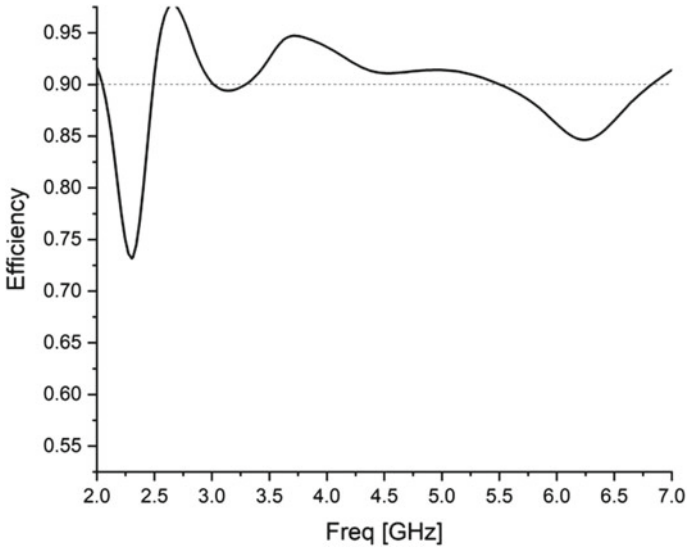
Fig. 12 Efficiency of the MIMO antenna
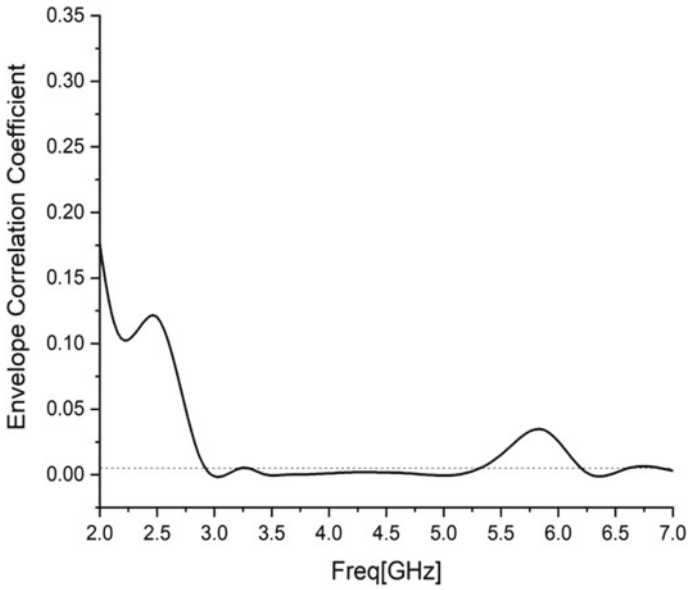
Fig. 13 Envelope correlation coefficient of the MIMO antenna

Fig. 14 Diversity gain of
the MIMO antenna
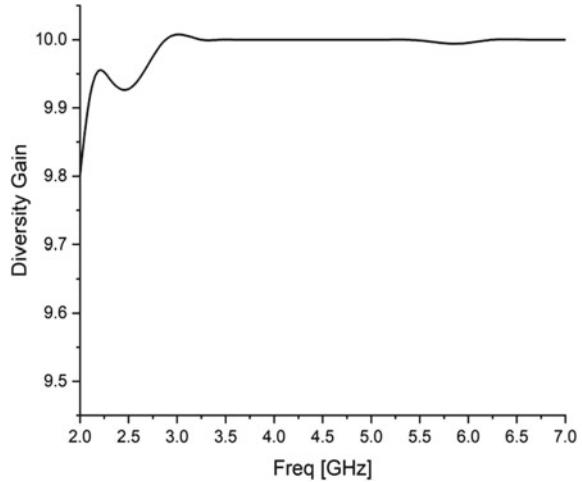
References

1. Nikhare NP, Shinde PN, Shinde JP (2016) Circularly polarized MIMO monopole antenna with defected ground structure for S-band application. In: 2016 international conference on computing communication control and automation (ICCUBEA). IEEE, Pune, India
2. Chandu DS, Karthikeyan SS (2018) Broadband circularly polarized printed monopole antenna with protruded L-shaped and inverted L-shaped strips. Microwave Opt Technol Lett 60(1):242–248
3. Samsuzzaman M, Islam MT, Singh MJ (2018) A compact printed monopole antenna with wideband circular polarization. IEEE Access 6:54713–54725
4. Midya M, Bhattacharjee S, Mitra M (2019) Broadband circularly polarized planar monopole antenna with G-shaped parasitic strip. IEEE Antennas Wirel Propag Lett 18(4):581–585
5. Alsariera H, Zakaria Z, Azmi (2020) New broadband L-shaped CPW-fed circularly polarized monopole antenna with asymmetric modified ground plane and a couple series-aligning inverted L-shaped strip. AEU Int J Electron Commun 118
6. Li ZY, Zhu XS, Yin C-Y, Huang Y (2018) A broadband circularly polarized monopole antenna. RF Microwave Comput Aided Eng 29(6)
7. Behera BR, Meher PR, Mishra SK (2019) Compact and efficient printed monopole antenna with broadband circular polarization. In: 2019 6th international conference on signal processing and integrated networks (SPIN)
8. Malviya L, Malik J, Panigrahi RK, Kartikeyan MV (2015) Design of a compact MIMO antenna with polarization diversity technique for wireless communication. In: International conference on microwave, optical and communication engineering
9. Xu Z, Deng C (2020) High-isolated MIMO antenna design based on pattern diversity for 5G mobile terminals. IEEE Antennas Wirel Propag Lett 19(3):467–471
10. Saurav K, Mallat NK, Antar YMM (2018) A three-port polarization and pattern diversity ring antenna. IEEE Antennas Wirel Propag Lett 17(7):1324–1328
11. Chakraborty S, Rahman MA, Hossain MA et al. (2020) A 4-element MIMO antenna with orthogonal circular polarization for sub-6 GHz 5G cellular applications. SN Appl Sci 2
12. Malik J, Patnaik A, Kartikeyan MV (2014) Novel printed MIMO antenna with pattern and polarization diversity. IEEE Antennas Wirel Propag Lett 14:739–742
13. Malviya L, Panigrahi RK, Kartikeyan MV (2016) Circularly polarized 2 × 2 MIMO antenna for WLAN applications. Prog Electromagnet Res C 66:97–107

14. Sharma Y, Sarkar D, Saurav K, Srivastava KV (2017) Three element MIMO antenna system with pattern and polarization diversity for WLAN applications. IEEE Antennas Wirel Propag Lett 16:1163–1166

Networking

Machine Learning-Based Investigation of Employee Attrition Prediction and Analysis

Kalgi Sheth, Jaynil Patel, and Jaiprakash Verma

Abstract Employees are a company's most valuable assets. However, if they left their jobs suddenly, it might cost a company a lot of money. Consequently, companies nowadays are actively seeking tools and technologies that can help in accurate and early employee attrition prediction. The main focus here shall be on the visualization of the available employee data in order to gain intuitive insights on the correlation among attributes and top causes behind the attrition. In this paper, we present the comparison of four algorithms used to predict whether an employee will leave or not, based on various attributes like age, salary, experience, etc., along with intuitive visualizations and its importance. The models used for prediction are random forest, logistic regression, K-nearest neighbor, and Naïve Bayes classifier. Thus, the visual analysis of employee attrition problem and accurate prediction can allow HR managers to take precautionary actions to retain the employee within the company.

Keywords KNN · Logistic regression · Random forest · Naïve Bayes classifier · Data visualization · Data mining · Employee attrition prediction

1 Introduction

We can define employee attrition as the event of an employee leaving the company. In case of involuntary attrition, the employees are fired by their employer due to reasons like poor level of performance, or current business needs for churning. In voluntary attrition, the good employees who have been performing well and have

K. Sheth (✉) · J. Patel
Technicolor, Bangalore, India
e-mail: kalgi.sheth@technicolor.com

J. Patel
e-mail: patel.jaynil@technicolor.com

J. Verma
Institute of Technology, Nirma University, Ahmedabad, India
e-mail: jaiprakash.verma@nirmauni.ac.in

been a good asset to the company leave by their own will. They may leave in search for better opportunities, or due to unsatisfactory job conditions. Even the companies which take good care of their employees and invest in their wellbeing and training, in an attempt to retain them for longer period of time, are prone to losing talented employees [1, 2]. The issues following employee attrition include an investment of time and resources in interviewing and training new employees.

Thus, predicting whether an employee will leave or not will help the company's management and HR act faster by enhancing their internal policies and strategies [3]. The talented employees who are at high risk of leaving can be offered several propositions, such as a salary increase or proper training, to reduce their chances of leaving. With the help of several machine learning models, the companies can predict the employee attrition to a certain rate beforehand [4]. The rich company data provided by the HR departments with data attributes like employee salary, distance form workplace, years since last promotion, etc., can be used to build and train a machine learning model that can predict the employees who are leaving the company [5]. Employee attrition prediction models can also analyze the correlation among such attributes for both current and terminated employees.

The following section describes the motivation for the work conducted in this study, as well as the contribution of other researchers in this field in the past. Section 3 will describe various machine learning algorithms used for prediction. The dataset description and characteristic is provided in Sect. 4 along with useful insights from data visualization. Section 5 is proposed work and experimentation followed by results in Sect. 6 and conclusion in Sect. 7.

2   Literature Survey

Sisodia et al. in [6] have used five different classification models to predict the employee attrition. They conclude that among linear SVM, random forest, decision tree, KNN, and Naïve Bayes, and random forest performs with best accuracy. They have also presented various intuitive visualizations for inferring insights form the available employee data and correlation between different attributes and their roles in employee's attrition.

Alduayj and Rajpoot in [7] have focused on the class imbalance issue encountered during employee attrition prediction. They have compared the results for three experiments. In first one, they train classification models on imbalanced dataset, in the second one, they use ADASYN to address the class imbalance in the dataset, and in the last experiment, they train the models on dataset obtained after manual undersampling. The best results were obtained for KNN ($k = 3$) classifier using ADASYN technique.

Ray and Sanyal in [8] have used the method of probabilistic estimation to predict whether and employee will stay or leave based on various factors. They have implement two methods. First prediction of employee attrition against single attributes like age, field of education, education level, and etc., using a simple Naïve Bayes

classifier. In second method, they have implemented an adaptive probabilistic estimation technique using a combination of these attributes against class label, where the combination of attributes is decided by the HR manager. Here, again a Bayesian classifier is used. Adaptive probabilistic estimation model performs better with vastly reduced rate of error for employee attrition prediction.

Bhartiya et al. in [9] have proposed a systematic flow for attrition prediction. They have elaborated on the process of data acquisition (collection), data conditioning (cleaning), data visualization and classification using linear SVM, random forest, decision tree, KNN, and Naïve Bayes. They also used evaluation metrics like AUC_ROC score and accuracy measure to compare the performance of all these classification algorithms.

Table 1 summarizes the related research work conducted in the domain of employee attrition analysis.

3　Classification Algorithms

Employee attrition problem lies in the domain of big data. Since this is an exploratory analysis and we are looking forward to extend the work in direction of big data mining, the application of deep learning algorithms to big data problems will prove to be costly in terms of time and computational power. Hence, for this study, we have worked with the following machine learning algorithms.

3.1　*Random Forest*

Random forest (RF) is a robust supervised machine learning algorithm, which is used for classification and regression problems. It makes use of multiple decision trees for training. Each tree gives a vote for a particular classification label. Thus, using these vote counts, the random forest model decides the resultant class label that has the highest number of votes. Since we are talking about large amount of data, random forest can help reduce overfitting of the model. It handles missing values. It is suited to both categorical and continuous data. Random forest algorithm holds the potential to scale and adapt to big data settings and environment.

3.2　*Logistic Regression*

It is a statistical technique for evaluating a dataset with one or more independent variables that influence the outcome. For example, as the number of hours worked increases, the likelihood of employee leaving the company rises. Logistic regression is very efficient to train and can be implemented easily for classification problems.

Table 1 Summary of past research work

Reference	Objective	Approach	Methodology	Findings	Limitations
Sisodia et al. [6]	Building a model to predict the rate of employee attrition	Understanding the relation among data attributes by using correlation methods and heat map	Used five different algorithms for prediction: linear SVM, decision tree classifier, random forest classifier, KNN classifier, and Naïve Bayes classifier	Random forest shows better performance than other classifiers in terms of evaluation parameters, according to the experimental findings	Their methodology can be optimized further to reduce the prediction error rate
Alduayj and Rajpoot [7]	Predict the employee attrition efficiently by addressing the class imbalance issue	Analyzing the difference between results obtained from training models over imbalanced and balanced dataset along with feature selection to optimize speed and performance of training and prediction	Training SVM, random forest, and KNN model on imbalanced dataset, use ADASYN to address the imbalance and train the models on new dataset Manual undersampling and training the same models	Out of the three experiments conducted, ADASYN with K-nearest neighbor classifier achieved and F1-score of 0.93	Dataset characteristics are not explained using visuals like charts and graphs
Ray and Sanyal [8]	Predict attrition using probabilistic estimation with less complexity	Adaptively refine the initial models to enhance prediction capabilities	Predict attrition against single attribute like age or education level using simple Bayesian classifier Predict attrition against a combination of these attributes using adaptive probabilistic estimation model	Adaptive probabilistic estimation model performs better with vastly reduced error rate for employee attrition prediction	Further, prediction efficiency can be increased using better performing models like SVM or decision tree

Table 1 (continued)

Reference	Objective	Approach	Methodology	Findings	Limitations
Yadav et al. [10]	To identify which factors have higher impact on employee attrition	Emphasis on the finding out the factors which lead to churning of experienced employees	Using various models for classification like logistic regression, SVM, random forest classifier, AdaBoost, and decision tree classifier Comparing results before and after feature selection as well as on the experienced employee dataset generated separately Used evaluation metrics like F1, recall, and accuracy to compare the models	Concluded that salary or promotions are not the sole reason for employee churning. Factors like experience, time spend in one company, etc., also effect the attrition behavior of an employee	Ignores the class imbalance issue
Yedida et al. [13]	Predicting employee attrition	Using K-nearest neighbor classification due to better performance on noisy data	Comparing KNN model for against other models like ANN, Gaussian Naïve Bayes, and logistic regression	With KNN model for employee attrition prediction, the accuracy achieved is 94.32%	Not addressing the dataset characteristics using visual in order to make inferences

3.3 K-Nearest Neighbors

K-nearest neighbor classification algorithm considers the minimum distance from a particular instance to the training dataset to fetch k-nearest neighbors. After fetching the k-nearest neighbors, the class to which the majority of k neighbors belong is considered as the final resultant class. We have used this algorithm because it naturally handles missing values in the data by imputation. It is a lazy learner algorithm. At expense of costly prediction phase, this algorithm provides the advantage of zero training time. It is well suited for classification on small datasets.

3.4 Naïve Bayes Classifier

Naïve Bayes classifier assumes that the all the attributes are independent of each other. Thus, it got the name naïve, since this is not always true in real world. It is a probabilistic classifier that can handle both discreet and continuous data. It is simple to implement and gives good results even with less amount of training data. Naïve Bayes classification algorithm is highly scalable. It has been observed to achieve higher accuracy as the size of the data increases.

4 Research Methodology

We have selected the HR Analytics Dataset available on Kaggle website, which is a sample dataset provided by IBM. It consists of 35 attributes as columns including the "Attrition" column which is the target class. The dataset consists of 1470 rows. Our primary objective is to understand and bring out hidden characteristics of the data before training our models for prediction. First, we enumerate the data based on different categories. We have tried to observe the presence of a pattern within the data as well as the correlation among certain attributes. Finally, we have tried to bring out the presence of any kind of bias within the data based on gender of an employee by plotting various attribute values for males and females side by side. Figure 1 shows the correlation among the data attributes in the given dataset.

We can clearly see that job level of an employee as well as his monthly income shows a strong positive correlation with total working years. Similar such observations can tell us which attributes are interdependent and share a strong correlation.

Figure 2 shows the number of people who left the company (Attrition = Yes), number of employees according to their travel frequency, department, and education field.

One of the most prominent observation and inference made from this plot below is that the majority class is Attrition = "NO". But for any company, much importance
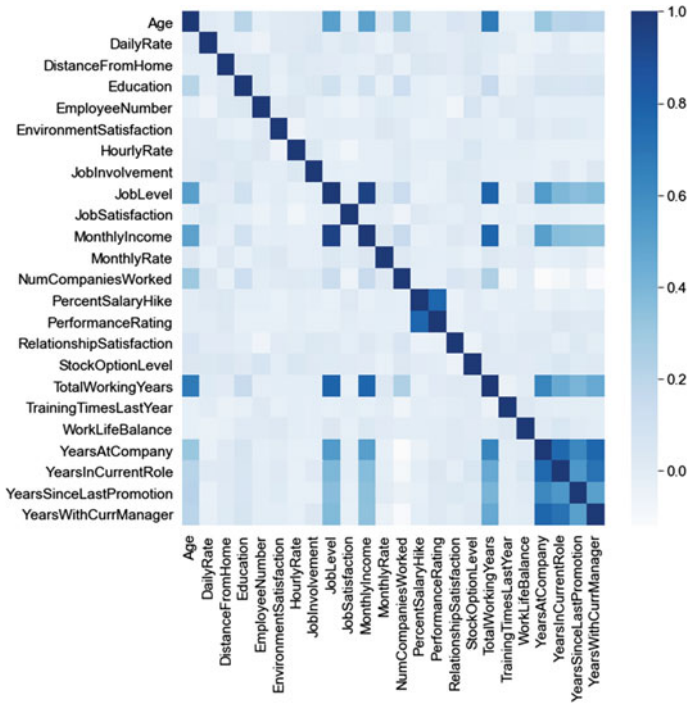
Fig. 1 Employee data correlation matrix
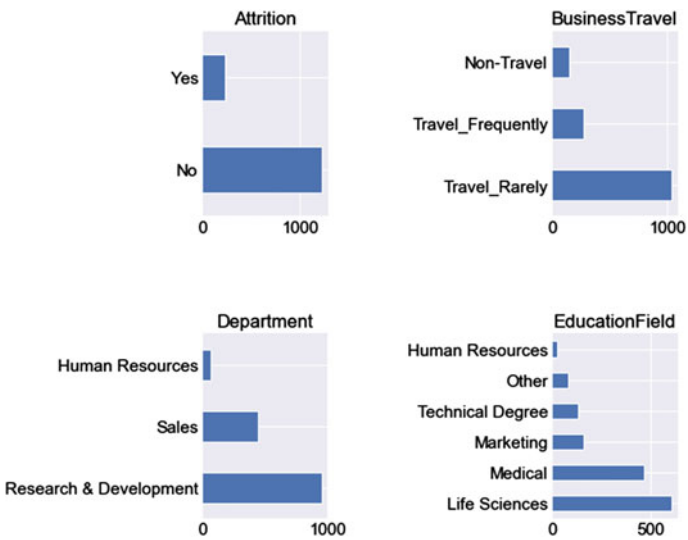
Fig. 2 Employee count by attrition class, travel, department, and education field
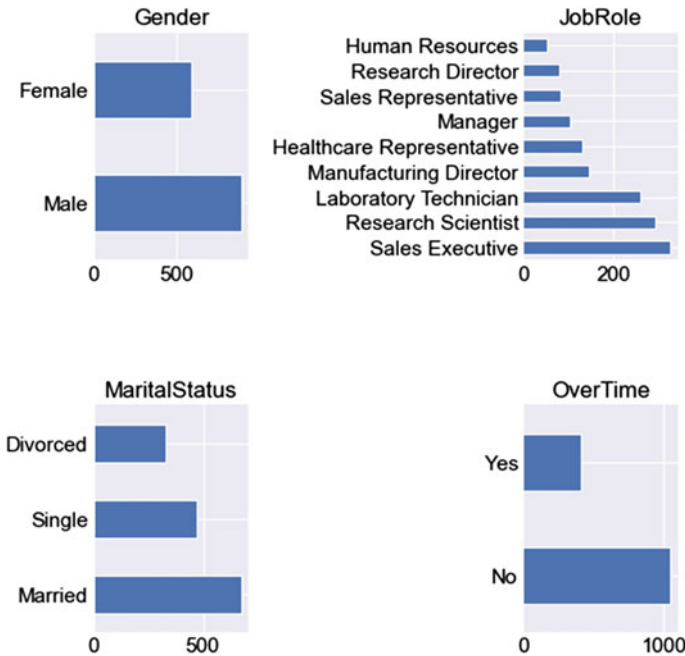
Fig. 3 Employee count by gender, job role, marital status, and overtime

should be given to those employees who are leaving that is the minority class in this dataset, Attrition = "YES". Thus, there is a prominently visible class imbalance in the dataset. This issue has to be addressed while preparing predictive models.

Figure 3 shows the gender distribution for employees of the company, number of employees according to their job roles, marital status, as well as those who do overtime versus those who do not.

We can see that there are less than 600 females in the company, whereas more than 800 males. Less than 500 employees do overtime. There are over 200 employees working as sales executives or research scientists, or lab technicians. The human resources department has less than 100 employees. Majority of the employees are married. Though, more than 250 employees are divorced.

Figure 4 shows the number of male and female employees against their monthly income for each role. This plot is trying to identify the presence of any gender bias in income distribution of employees based on their roles.

Across all job positions, the real disparity between men and women is found in the position of research director, where there is very little overlap in pay between men and women, implying a subtle gender bias. It is visible from the plot above that for the position of research director, the number of females with monthly salary above 15,000 is very less as compared to the number of males. Apart from that no other post shows considerable variation in monthly salary of males and females. Manufacturing director and sales representative are two positions which show maximum overlapping
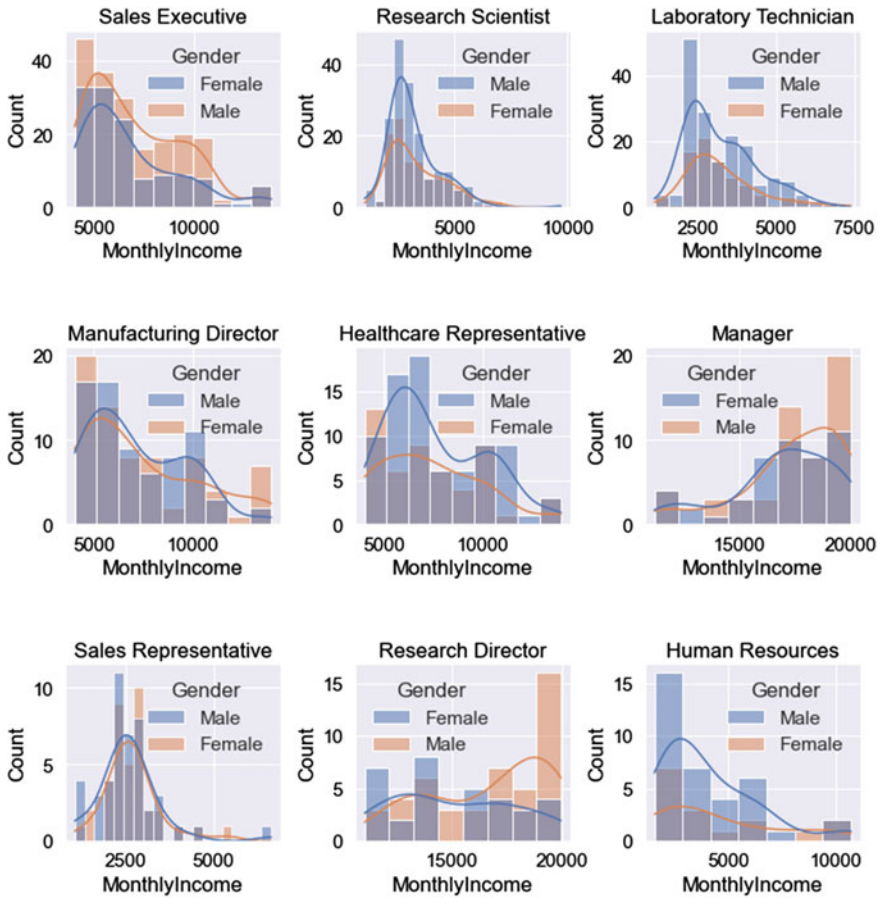
Fig. 4 Employee salary distribution by gender and department

in the monthly income, thereby indicating that there are similar number of males and females under same salary bracket.

Figure 5 shows the same plot for role of research director only, in order to get a clear understanding of the underlying bias.

As the salary amount is increasing, moving toward the right, we see that the number of males is increasing, while the number of females remains low. It means that there are very few females who are appointed as research directors with higher salaries. Moving toward the left we see that more numbers of females are appointed as research directors than males with less salaries. Thus, a clear bias exists saying females appointed as research directors are generally paid less compared to males.

Figure 6 shows the count of employees labeled as "YES" or "NO" for attrition attribute based on the number of companies they have worked in. We can see that the employees who have just worked for 1 company are more prone to leave.
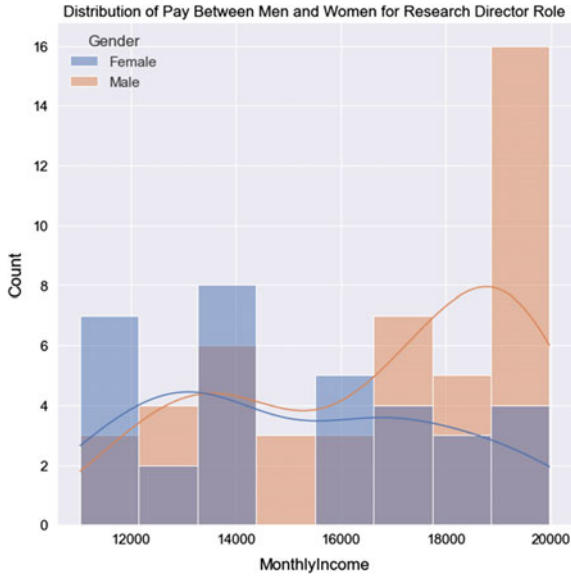
Fig. 5 Salary distribution by gender for research director role
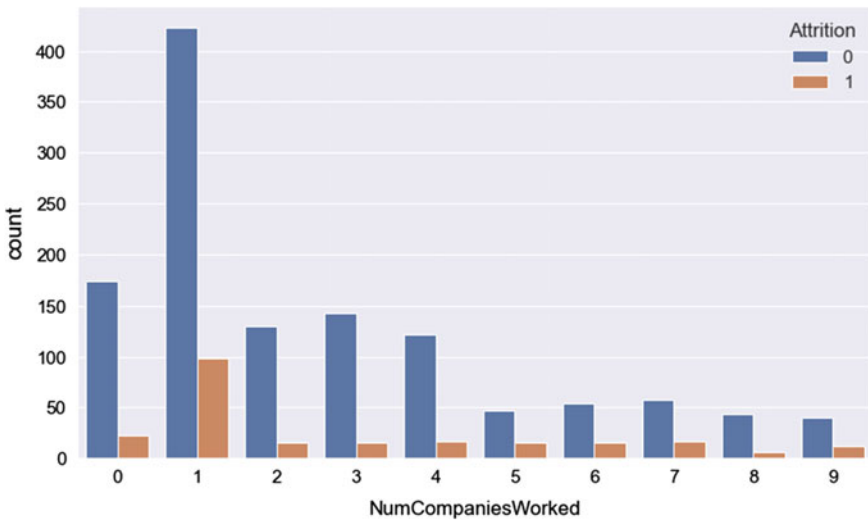
Fig. 6 Effect of number of companies worked for, on attrition
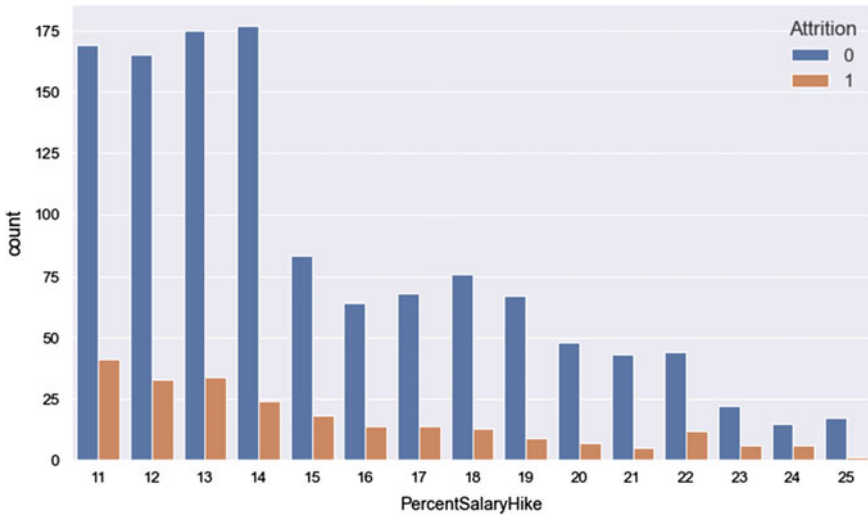
Fig. 7 Effect of salary hike on attrition

Figure 7 shows the effect of salary hike on attrition behavior of the employees. Employees with less salary hike are more prone to attrition.

5 Proposed Work

The employee attrition prediction problem is affected by a number of factors. But the major factor which affects the prediction in our case is the class imbalance present in the data. The class distribution in our dataset is as shown in Table 2.

It becomes crucial for the company to predict with more accuracy, the possibility of an employee leaving. Which means, the employees which have higher probability of leaving the company, should not be predicted and labeled incorrectly as "NO" because that can cause the company a huge loss. Although, if a person who is not probably leaving the company, but is wrongly predicted and labeled as "YES", then the company does not suffer great loss. To say, we cannot afford misclassification of such employees who are having high probability of attrition.

In this study, we have implemented the four different prediction algorithms. Table 3 shows each algorithm along with its characteristics.

Table 2 Class distribution in dataset

Attrition versus number of instances	
Yes (leaving)	237
No (not leaving)	1233

Table 3 Algorithms and characteristics

Algorithm	Sensitive to imbalance?	Can have weighted classes?
Logistic regression	Yes	Yes
Random forest	Yes	Yes
Naïve Bayes	Yes	No
K-nearest neighbors	Yes	No

Our approach to handle the class imbalance in the dataset is consisting of two methods—*weighted classes* and *SMOTE*.

5.1 Weighted Class

It is a statistical technique for evaluating a dataset with one or more independent variables that influence the outcome.

For example, as the number of hours worked increases, the likelihood of employee leaving the company rises. First, we identify the class distribution ratio. In our case, the class distribution ratio is calculated as below

$$\text{Ratio} \Rightarrow (\text{Attrition} = \text{YES})/(\text{Attrition} = \text{NO}) \tag{1}$$

Here, our minority class "YES" has 237 instances and majority class "NO" has 1233 instances. The calculated ratio is almost equal to 1:5. Thus, we shall assign the weights to the classes in inverse proportion of this ratio. Which means, while predicting, the weight assigned to the classes for (Attrition = YES): (Attrition = NO) is in proportion of the ratio 5:1 implying that any misclassification of the minority class shall be penalized heavily as compared to that of majority class.

5.2 Synthetic Minority Oversampling Technique

SMOTE is another method to handle the class imbalance in data. In SMOTE, we oversample the examples in the minority class. This can be accomplished by simply duplicating minority class examples in the training dataset before fitting a model. This can help to stabilize the class distribution, but it does not give the model any additional information. This technique was proposed by Chawla, et al. in [15].

To be more specific, a random example from the minority class is chosen first. Then, for that example, k of the closest neighbors are found (typically $k = 5$). A neighbor is chosen at random, and a synthetic example is generated. We wish to

CONFUSION MATRIX STRUCTURE		Actual Class Values	
		POSITIVE	NEGATIVE
Predicted Class Values	POSITIVE	True Positive (TP)	False Positive (FP)
	NEGATIVE	False Negative (FN)	True Negative (TN)

- True Positive (TP) = Number of *Positive Classes* Predicted *Correctly* as Positive
- False Positive (TP) = Number of *Negative Classes* Predicted *Incorrectly* as Positive
- False Negative (TP) = Number of *Positive Classes* Predicted *Incorrectly* as Negative
- True Negative(TP) = Number of *Negative Classes* Predicted *Correctly* as Negative

Fig. 8 Confusion matrix and related terms

identify which classifier best predicts employee attrition by addressing the class imbalance problem.

To compare the algorithms, we are using the following evaluation metrics.

Confusion Matrix It is a table that is often used to describe the performance of a classification model on a supervised learning problem. Figure 8 shows the structure of confusion matrix and the important terms related to it.

Recall It helps us realize what proportion of actual positives is correctly classified by our model.

$$\text{Recall} = (\text{TP})/(\text{TP} + \text{FN}) \tag{2}$$

In our case, we cannot take accuracy as a measure to evaluate and compare the algorithms because accuracy is a good measure only when the dataset is balanced. Our goal is to maximize the recall score, by increasing the number of True Positives in the prediction.

For example, if an employee X is has high probability of attrition in reality, but our model predicts and labels him as "NO", which means our model predicts that the employee not going to leave. In this case, the company shall be losing a valuable employee due to misclassification by the model. And losing an employee may cost company much more than what it spends on retaining the employee. Such kind of misclassification is not allowed at all, thus there is the need to increase the recall score.

Take another case, where the employee Y is not leaving the company in reality. But the model predicts and labels him as "YES". Now, the company will pay more attention to him, making efforts to retain him. The company does not lose an employee after all. Such kind of misclassification is still bearable as it is not critical.

6 Results and Discussions

For each algorithm, we have conducted evaluation before and after using methods to handle class imbalance. We have obtained the results based on four different cases:

- Case 1: Without handling class imbalance
- Case 2: Handling class imbalance using weighted classes
- Case 3: Handling class imbalance using SMOTE
- Case 4: Handling class imbalance using both methods.

Above mentioned Case 3 and 4 does not apply to KNN and Naïve Bayes as they cannot have classes with weights assigned to them. Our test data contained 441 instances. Out of which, 71 belonged to minority class "YES" and 370 belonged to majority class "NO".

Table 4 shows the collective results for performance of each algorithm without handling the imbalance in data.

Table 5 shows the collective results for performance of each algorithm after handling the class imbalance using weighted class technique.

Table 4 Algorithms and characteristics

Without handling class imbalance			
Algorithm	Recall	TP Minority class = 71	TN Majority class = 370
Random forest	0.1549	11	365
Logistic regression	0.0140	1	369
KNN	0.0422	3	368
Naïve Bayes	0.6760	48	295

Table 5 Algorithms and characteristics

Without handling class imbalance			
Algorithm	Recall	TP Minority class = 71	TN Majority class = 370
Random forest	0.1126	8	366
Logistic regression	0.6619	47	251
KNN	–	–	–
Naïve Bayes	–	–	–

Table 6 Algorithms and characteristics

Without handling class imbalance			
Algorithm	Recall	TP Minority class = 71	TN Majority class = 370
Random forest	0.3380	24	340
Logistic regression	0.5774	41	280
KNN	0.4366	31	265
Naïve Bayes	0.6478	46	272

Table 7 Algorithms and characteristics

Without handling class imbalance			
Algorithm	Recall	TP Minority class = 71	TN Majority class = 370
Random forest	0.2535	18	353
Logistic regression	0.9014	64	57
KNN	–	–	–
Naïve Bayes	–	–	–

Table 6 shows the collective results for performance of each algorithm after handling the class imbalance using SMOTE technique.

Table 7 shows the collective results for performance of each algorithm after handling the class imbalance using weighted class and SMOTE techniques combined.

7 Observations and Conclusion

From the results obtained, we can also conclude that without handling the class imbalance in the data, most of the models will not perform well. From Table 4, we can see that random forest, logistic regression, and KNN can correctly predict the majority class instances with high accuracy, but they fail to predict the minority class instances correctly.

Comparing all four algorithms, we observe that Naïve Bayes, does not show much difference before or after handling class imbalance. Random forest and KNN show considerable improvement in performance when used with SMOTE, while logistic regression shows great enhancement in performance when weighted class

technique is used. Logistic regression when implemented along with weighted class and SMOTE techniques combined, give the highest recall score of 0.9014 and is able to predict 64 out of 71 minority class instances correctly. And thus, for this study, we obtained the best performance from logistic regression model using class weights and SMOTE.

Although the recall score increases at the cost of accuracy. For applications like employee attrition prediction, such a model is very useful which has high recall, but for critical applications where even a single misclassification of either of the class is expensive and dangerous, then models with higher accuracy and high recall should be developed using better techniques.

There are many more methods to handle data imbalance like ADASYN SMOTE, Borderline SMOTE, undersampling, etc. In the future, we shall be attempting to obtained performance results using advanced data imbalance handling techniques on various machine learning algorithms for better predictions of employee attrition as well as other critical real world data.

References

1. Varian H (2018) Artificial intelligence, economics, and industrial organization. National Bureau of Economic Research, Cambridge, MA, USA
2. Vardarlier P, Zafer C (2020) Use of artificial intelligence as business strategy in recruitment process and social perspective. https://doi.org/10.1007/978-3-030-29739-8_17
3. Griffeth R, Hom P, Gaertner S (2000) A meta-analysis of antecedents and correlates of employee turnover: update, moderator tests, and research implications for the next millennium. J Manag 26:463–488. https://doi.org/10.1016/S0149-2063(00)00043-X
4. Jarrahi MH (2018) Artificial intelligence and the future of work: human-AI symbiosis in organizational decision making. Bus Horiz 61(4):577–586. ISSN: 0007-6813
5. Duan Y, Edwards JS, Dwivedi YK (2019) Artificial intelligence for decision making in the era of big data–evolution, challenges and research agenda. Int J Inf Manage 48:63–71. ISSN: 0268-4012
6. Sisodia DS, Vishwakarma S, Pujahari A (2017) Evaluation of machine learning models for employee churn prediction. In: 2017 International conference on inventive computing and informatics (ICICI). IEEE, Coimbatore, India, pp 1016–1020. https://doi.org/10.1109/ICICI.2017.8365293
7. Alduayj SS, Rajpoot K (2018) Predicting employee attrition using machine learning. In: 2018 International conference on innovations in information technology (IIT). IEEE, Al Ain, United Arab Emirates, pp 93–98. https://doi.org/10.1109/INNOVATIONS.2018.8605976
8. Ray AN, Sanyal J (2019) Machine learning based attrition prediction. In: 2019 Global conference for advancement in technology (GCAT). IEEE, Bangalore, India, pp 1–4. https://doi.org/10.1109/GCAT47503.2019.8978285
9. Bhartiya N, Jannu S, Shukla P, Chapaneri R (2019) Employee attrition prediction using classification models. In: 2019 IEEE 5th International conference for convergence in technology (I2CT). IEEE, Bombay, India, pp 1–6. https://doi.org/10.1109/I2CT45611.2019.9033784
10. Yadav S, Jain A, Singh D (2018). Early prediction of employee attrition using data mining techniques. In: 2018 IEEE 8th International advance computing conference (IACC). IEEE, Greater Noida, India, pp 349–354. https://doi.org/10.1109/IADCC.2018.8692137
11. Shankar RS, Rajanikanth J, Sivaramaraju VV, Murthy KVSSR (2018) Prediction of employee attrition using datamining. In: 2018 IEEE International conference on system, computation,

automation and networking (ICSCAN). IEEE, Pondicherry, India, pp 1–8. https://doi.org/10.1109/ICSCAN.2018.8541242

12. Hebbar AR, Patil SH, Rajeshwari SB, Saqquaf SSM (2018) Comparison of machine learning techniques to predict the attrition rate of the employees. In: 2018 3rd IEEE International conference on recent trends in electronics, information and communication technology (RTEICT). IEEE, Bangalore, India, pp 934–938. https://doi.org/10.1109/RTEICT42901.2018.9012243

13. Yedida R, Reddy R, Vahi R, Jana R, Abhilash GV, Kulkarni D (2018) Employee attrition prediction

14. Ozdemir F, Coskun M, Gezer C, Gungor VC (2020) Assessing employee attrition using classifications algorithms. In: Proceedings of the 2020 the 4th international conference on information system and data mining (ICISDM 2020). Association for computing machinery, NY, USA, pp 118–122. https://doi.org/10.1145/3404663.3404681

15. Ameer M, Rahul SP, Manne S (2020) Human resource analytics using power bi visualization tool. In: 2020 4th International conference on intelligent computing and control systems (ICICCS). IEEE, Madurai, India, pp 1184–1189. https://doi.org/10.1109/ICICCS48265.2020.9120897

16. Khadilkar N, Joshi D (2017) Predictive model on employability of applicants and job hopping using machine learning. Int J Comput Appl 171:37–41. https://doi.org/10.5120/ijca2017914966

17. Saradhi VV, Palshikar GK (2011) Employee churn prediction. Expert Syst Appl 38(3):1999–2006. ISSN: 0957-4174

18. Alamsyah A, Salma N (2018) A comparative study of employee churn prediction model. In: 2018 4th International conference on science and technology (ICST). IEEE, pp 1–4. https://doi.org/10.1109/ICSTC.2018.8528586

19. Nair P, Krishna J, Srivastava D (2019) Visual analytics toward prediction of employee erosion through data science tools. https://doi.org/10.1007/978-981-13-7166-0_71

20. Chawla N, Bowyer K, Hall L, Kegelmeyer W (2002) SMOTE: synthetic minority over-sampling technique. J Artif Intell Res (JAIR) 16:321–357. https://doi.org/10.1613/jair.953

21. Tallo TE, Musdholifah A (2018) The implementation of genetic algorithm in smote (synthetic minority oversampling technique) for handling imbalanced dataset problem. In: 2018 4th international conference on science and technology (ICST). IEEE, pp 1–4. https://doi.org/10.1109/ICSTC.2018.8528591

22. Tarusov T, Mitrofanova O (2019) Risk assessment in human resource management using predictive staff turnover analysis. In: 2019 1st international conference on control systems, mathematical modelling, automation and energy efficiency (SUMMA). IEEE, pp 194–198. https://doi.org/10.1109/SUMMA48161.2019.8947527

23. Bi T, Liu Y, Li P, Li S (2014) Telecom customer churn prediction method based on cluster stratified sampling logistic regression, pp 282–287. https://doi.org/10.1049/cp.2014.1576

24. Okfalisa, Gazalba I, Mustakim, Reza NGI (2017) Comparative analysis of k-nearest neighbor and modified k-nearest neighbor algorithm for data classification. In: 2017 2nd international conferences on information technology, information systems and electrical engineering (ICITISEE). IEEE, pp 294–298. https://doi.org/10.1109/ICITISEE.2017.8285514

25. Ranggadara I, Wang G, Kaburuan ER (2019) Applying customer loyalty classification with RFM and Naïve Bayes for better decision making. In: 2019 international seminar on application for technology of information and communication (iSemantic). IEEE, pp 564–568. https://doi.org/10.1109/ISEMANTIC.2019.8884262

26. Ullah I, Raza B, Malik AK, Imran M, Islam SU, Kim SW (2019) A churn prediction model using random forest: analysis of machine learning techniques for churn prediction and factor identification in telecom sector. IEEE Access 7:60134–60149. https://doi.org/10.1109/ACCESS.2019.2914999

27. Paschek D, Luminosu CT, Draghici A (2017) Automated business process management–in times of digital transformation using machine learning or artificial intelligence. In: MATEC web of conferences, vol 121, p 04007. https://doi.org/10.1051/matecconf/201712104007

28. Varian H (2018) Artificial intelligence, economics, and industrial organization. In: The economics of artificial intelligence: an agenda. University of Chicago Press, pp 399–419

29. Gordini N, Veglio V (2017) Customers churn prediction and marketing retention strategies. An application of support vector machines based on the AUC parameter-selection technique in B2B e-commerce industry. Ind Mark Manage 62. https://doi.org/10.1016/j.indmarman.2016.08.003.
30. Gupta P, Fernandes S, Jain M (2018) Automation in recruitment: a new frontier. J Inf Technol Teach Cases 8. https://doi.org/10.1057/s41266-018-0042-x
31. Jain N (2018) Big data and predictive analytics: a facilitator for talent management. In: Data science landscape: towards research standards and protocols. Springer, Singapore

CNN-Based Leaf Wilting Classification Using Modified ResNet152

Amita Mohta, Ishan Gupta, Ruchi Gajjar, and Manish I. Patel

Abstract Plants are prone to climatic changes which is considered to be one of the crucial challenges in agriculture. As a major part of the agricultural industry depends on rainwater for irrigation, climatic changes such as lack of rainfall may lead to shortage in water supply which may cause leaf wilting. If the extent of leaf wilting is not identified in the early stages, it may adversely affect the total yield. Leaf wilting is widely used as a parameter to compute drought tolerance in plants. The breeders manually collect the data for the extent of leaf wilting which consumes a lot time and efforts. This paper proposes a model with ResNet152 as the base architecture using transfer learning approach. The developed model uses leaf images as the input data and predicts the extent of leaf wilting into five different classes, namely 0, 1, 2, 3, and 4; 0 being the least amount of wilting and 4 being the highest amount of wilting. The proposed model achieves an accuracy of 87.00% which is better than other existing models. Further, the model was tested against some unlabelled images taken from the Internet and from the field for classification.

Keywords Convolutional neural network · Leaf wilting · ResNet152 · Transfer learning

A. Mohta (✉) · I. Gupta · R. Gajjar · M. I. Patel
Department of Electronics and Communication Engineering, Institute of Technology, Nirma University, Ahmedabad, India
e-mail: amita.mohta@gmail.com

R. Gajjar
e-mail: ruchi.gajjar@nirmauni.ac.in

M. I. Patel
e-mail: manish.i.patel@nirmauni.ac.in

1   Introduction

Agriculture represents about 70% of total freshwater consumption globally. Rainfall and moisture available in soil show substantial variations, both spatially and temporally. They are prime factors that influence the diversity and habitat in the environment and may lead to hinder the primary productivity in forestry and agricultural sectors [1]. It is difficult to forecast water availability which leads to increase in risk of drought in crops. Measuring the severity of droughts and their effect on the crops remain a challenge [2]. One of the major problems that arises in crops due to lack of water is leaf wilting. Wilting is a common symptom in plants that results from water loss in leaves and stems. The affected parts loose their turgidity and droop [3]. Early wilting detection plays an important role in crop precision management. The extent of leaf wilting serves as one of the low cost methods to determine the drought tolerance in the crops [4]. The breeders manually collect the data for the extent of leaf wilting. This is time-consuming and needs lot of human efforts. This process is prone to error and bias, hence the need for an automatic detection of these diseases using artificial intelligence techniques. In the recent years, the use of computer vision techniques for image processing and machine learning has significantly increased to reduce the human efforts in collecting the data for leaf wilting [5].

The convolution neural network (CNN) has been widely used in the field of image processing because it is efficient in image classification and recognition and has improved the accuracy of many machine learning tasks [6]. The CNN follows a hierarchical model which works on building a network and provides a fully connected layer in which all the neurons are connected to each other and the output is processed, making it useful in image classification and recognition because of its high accuracy [7].

This paper discusses about a model which uses the image dataset of leaves and classifies them into five different classes depending upon the extent of leaf wilting using CNN. Optimum base model, batch size and learning rate are defined experimentally. After training and validation of the model, images from Google as well as field are used to test the model. This automation of classifying the leaves will save time, effort and money along with the improved accuracy.

This paper is organized in the following sections. Section 2 of this paper discusses the other research works done to automate plant disease detection using machine learning apporaches. Section 3 of the paper describes the model proposed for leaf wilting classification. It discusses the advantage of using neural network approach, different CNN architectures and the model performance for different architectures. Section 4 contains the results and analysis which includes the dataset description, its division for training and validation, the final modified model architecture and the evaluation of model performance for various batch sizes along with the confusion matrix and evaluation parameters. It also deals with the field testing of the model. Section 5 concludes the paper.

2   Literature Survey

Numerous research works across the globe have been carried out, exploring different machine learning and deep learning approaches to automate plant disease detection and classification. A CNN model trained with the help of Plant Village Dataset proposed by Jay et al. [8] classifies plant diseases in leaves with an accuracy of 95.81%. CNN is also used in the paper written by Lu et al. [9] for the detection of diseases in the rice plants. The dataset was collected from rice experimental field. Almost all of these papers have tried to solve the problem using a similar approach. Another research implemented the model on an embedded hardware for real-time in-field plant disease detection [10]. Not much work has been reported on leaf wilting classification. The following are some of those works that focus on leaf wilting in plants. A research carried out by Ramos-Giraldo et al. [11] on the drought stress detection using machine learning techinques classified the stress levels into 5 categories using a transfer learning technique and a pre-trained model based on DenseNet-121. As a result, they achieved an accuracy of more than 80.00%. Another such research by Gandhi et al. [12] used the transfer learning approach with ResNet50 base architecture. They achieved an accuracy of 78.00% and further applied the ensemble method to increase the accuracy to 82.00%. They included the weather data for the ensemble method. Khamparia et al. [13] proposed a deep convolutional network for identification of seasonal crops disease. They considered 900 leaf images of the 3 different crops and classifed them into six different categories. They achieved the test accuracy of 86.00%. The research was further carried out for improved accuracy results.

   All of these research works used CNN as the basic approach and achieved the highest accuracy of 86.00%. The model proposed in this paper achieves an accuracy of 87.00%, resulting in a better and more accurate model for leaf wilting detection.

3   Model Description for Leaf Wilting Classification

The problem discussed in this paper is a multi-class classification of leaf wilting. The simplest method to classify the data using machine learning is support vector machines (SVM). SVM aims to find an optimal boundary between the possible outcomes. In its most simple type, SVM does not support multi-class classification. Instead, neural networks can be used for multi-class classification [12]. Neural networks are a series of algorithms that mimic the operation of human brain. CNN is a class of deep neural networks often used for analyzing visual images. Hence, as a solution, we propose the use of neural networks for this multi-class classification problem of leaf wilting. Furthermore, the classification capability gained from training on the ImageNet dataset by the base model can be improved using transfer learning. Transfer learning can be described as a method where a model is developed for a task and reused as the starting point for the model on a second task.

Table 1 Model performance for various architecture

Model architecture	Validation loss	Validation accuracy (%)
VGG16	1.6085	42.71
InceptionResNetV2	13.893	21.88
ResNet50	0.9156	63.54
ResNet152	1.2083	64.54

3.1 Model Selection

Firstly, a model architecture needs to be selected for the classification. There are several architectures available such as ResNet, VGG, InceptionResNet, etc. ResNet50 is a ResNet model having 50 layers. 48 layers of those are convolution layers along with one average pool and one maxpool layer. It has about 25 million training parameters. ResNet152 is another variant of ResNet architecture having 152 layers. ResNet152 has about 60 million training parameters [14]. VGG16 is a 16 layer deep CNN architecture. VGG16 has convolutional layers of 3 * 3 filters, 2 fully connected layers followed by a softmax output layer. It has about 138 million training parameters. InceptionResNetV2 is 164 layered deep CNN architecture that is trained on images from the ImageNet database. It has about 6.4 million training parameters [?].

A comparative analysis for base model among ResNet50, VGG16, InceptionRes-NetV2 and ResNet152 was performed. Each one of them was selected separately as the base model. Their output layer was replaced by a softmax output layer of 5 units. The model was executed for 10 epochs with a batch size of 14 and Adam optimizer. The validation accuracy and loss of each model was observed.

According to the observations in Table 1, ResNet152 offers the maximum validation accuracy among the other considered architectures.

4 Results and Analysis

4.1 Dataset Description

The image dataset contains the images of leaves which are preprocessed and fed as the input to the model for classification. The images are to be classified into 5 categories (0–4). Class 0 indicates the minimum or no leaf wilting and class 4 represents the maximum leaf wilting. Figure 1 shows the classes of the dataset. A CNN model pre-trained on the popular ImageNet dataset is used for this classification. The hyper-parameters are modified to increase the accuracy of the model which are described in the later sections. The dataset is imported from Github [15]. It consists of 896 images of resolution 640 × 480. A csv file containing the names of images with their respective classes was also imported along with the images. The dataset

Fig. 1 Sample dataset with classes of leaf wilting

Table 2 Dataset distribution

Class	0	1	2	3	4
Training images	417	134	93	96	56
Validation images	20	20	20	20	20
Total images	437	154	113	116	76

is highly imbalanced with class 0 having maximum data images. To counter this imbalance, we calculate the class weights of the 5 classes. Class weights modify the current training algorithm to take into account the skewed distribution of the classes. Class weights provide weights to the loss suffered differently based on the class in other to compensate the inequality in the training samples. Considering class weights makes sure that the model is equally good at identifying all classes. The minority class has higher class weight and majority class has lower class weight.

20 images from each class are separated for validation and the rest of the images are kept for training the model. This splits the data into 90–10 fashion. The exact count of images in each class for training and validation data is specified in Table 2.

4.2   Model Training

Transfer learning is a methodology where we use pre-trained deep learning models to fine-tune them to fit the data. As per the observations from Table 1, ResNet152 is used as the base model architecture for deep residual learning. ResNet learns the residual of the hypothesis function and input, i.e., it minimizes the residual error thus learning the mapping effectively. The architecture has a feed forward network which is used to calculate the residual of the function. The last layer in ResNet base is a Global Pooling 2D layer whose output is 2048 dimensional vector.

All the layers of ResNet152 are frozen and the output layer is removed. The layers are kept frozen because it gave the maximum validation accuracy as compared to some or all layers kept trainable. Along with the base model, there are 4 additional layers to improve the model accuracy. The final structure of the model is:

ResNet152 base—128 (FC layer 1, ReLU)—64 (FC layer 2, ReLU)—32 (FC layer 3, ReLU)—5 (Softmax output layer).

Figure 2 shows the modified model architecture with ResNet base model and 4 additional layers.

Various batch sizes were taken into account and their respective accuracies were observed for 10 epochs using Adam optimizer. Table 3 gives the accuracy results of taking different batch sizes.
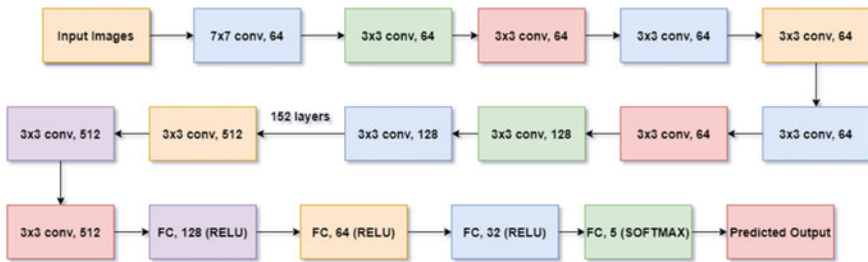
Fig. 2   Proposed model architecture

Table 3   Model performance for various batch sizes

Batch size	Accuracy (%)
14	**83.67**
16	83.33
32	80.20
64	78.12

Table 4 Hyper-parameter values

Hyper-parameters	Values
Number of epochs	50
Batch size	14
Learning rate	0.001
Optimizer	Adam
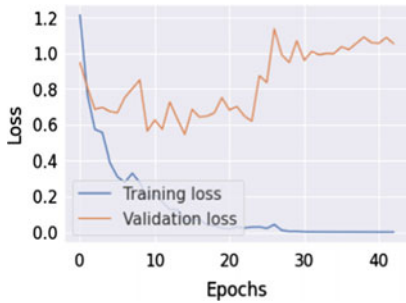
(a) Epoch versus Loss plot

(b) Epoch versus Accuracy plot

Fig. 3 Training and validation plots

4.3 Evaluation

From all the results observed above, the final architecture of the model is: ResNet152 base—128 (FC layer 1, ReLU)—64 (FC layer 2, ReLU)—32 (FC layer 3, ReLU)—5 (Softmax output layer). The final set of hyper-parameters are given in Table 4.

The maximum validation accuracy acheived by the described model for the given dataset classification is 87.00%.

Figure 3a shows the epoch versus loss plot for training and validation and Fig. 3b shows the shows epoch vs. accuracy plot for training and validation. It can be seen that both the curves flatten out at higher values of epochs.

From the confusion matrix given in Table 5, it can be observed that the dataset of class 4 has been classified without any error. The majority of the misplaced images lie in the class just next to the correct class. It can be observed from Fig. 1 that the classes 0, 1 and 2 have negligible difference which causes misclassification. As it can be seen in Table 5, 9 out of the 13 misclassified images lie in classes 0, 1 and 2.

Table 6 gives the classification report that contains the details of precision, recall, $F1$-score for each class, along with the overall accuracy of the model.

The comparision of accuracy of various model architectures previously designed for the similar applications is given in Table 7. It can be observed that the proposed model results in the highest accuracy among the compared models.

Table 5 Confusion matrix for predicted labels

Wilting levels	0	1	2	3	4
0	**17**	3	0	0	0
1	3	**16**	1	0	0
2	1	1	**15**	3	0
3	0	0	1	**19**	0
4	0	0	0	0	**20**

Table 6 Evaluation parameters

Wilting class	Precision	Recall	$F1$-score
0	0.81	0.85	0.83
1	0.80	0.80	0.80
2	0.88	0.75	0.81
3	0.86	0.95	0.90
4	1.00	1.00	1.00
Macro avg.	0.87	0.87	0.87
Weighted avg.	0.87	0.87	0.87
Accuracy	87.00%		

Table 7 Accuracy comparison for various model architecture

Model architecture	Validation accuracy (%)
ResNet152	64.54
Model proposed by Gandhi et al. [12]	82.00
Model proposed in this paper	**87.00**

4.4 Field Testing

To test the proposed model, 10 unlabelled images of plants were taken from the Internet and field and given to the model as input. The sample images of the test set are shown in Fig. 4. All the test images were resized to 640×480. The model classified the images in the expected classes. Figure 4c was classified into class 4 which can be justified by observation as the leaves are dry and highly wilted. Similarly, Fig. 4b was classified into class 1 and Fig. 4d was classified into class 0 because the former shows minor wilting and the latter shows healthy leaves with no wilting. Hence, the model gives accurate results with an accuracy of about 90%.

Table 8 gives the classification of the 10 images in the respective classes. The field image of dead leaves was classified in category 4 with highest wilting level as per the expectations. The image of a healthy plant taken from the Internet was classified into category 0, with least amount of wilting.
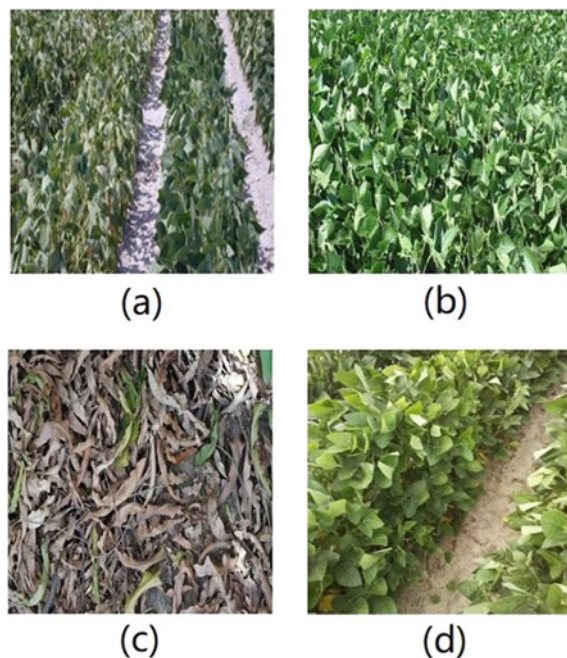
Fig. 4 Real field images

Table 8 Classification result of test images

Wilting level	0	1	2	3	4
Number of images	5	2	0	0	3

5 Conclusion

Using the CNN model proposed in this paper, the problem of leaf wilting is addressed. The automation of the classification process reduces the human intervention eventually reducing the chances of errors and bias. The model proposed is more accurate than the base model used and provided the validation accuracy of 87.00%. This can also be verified through the confusion matrix. The accuracy curve of both training and validation flatten out for higher epoch values, indicating that after a number of epochs, the accuracy does not increase with the increase in epoch values. The model predicted the classes of unlabelled data taken from the field and the Internet as per the expectations. This approach to evaluate leaf wilting can save the crops from temporary wilting and help to take preventive measures against wilting.

References

1. Engelbrecht B, Tyree M, Kursar T (2007) Visual assessment of wilting as a measure of leaf water potential and seedling drought survival. J Trop Ecol 23:497–500. https://doi.org/10.1017/S026646740700421X
2. Ramos-Giraldo P, Reberg-Horton C, Locke AM, Mirsky S, Lobaton E (2020) Drought stress detection using low-cost computer vision systems and machine learning techniques. IT Prof 22(3):27–29. https://doi.org/10.1109/MITP.2020.2986103
3. Britannica, The Editors of Encyclopaedia (2021) Wilt. Encyclopedia Britannica, 21 Sep 2017. https://www.britannica.com/science/wilt. Accessed 26 Apr 2021
4. Cai X, Sun Y, Zhao Y, Damerow L, Schulze Lammers P, Sun W, Lin J, Zheng L, Tang Y. Smart detection of leaf wilting by 3D image processing and 2D Fourier transform. Comput Electron Agric
5. Oladejo B, Ademola O (2020) Automated classification of banana leaf diseases using an optimized capsule network model, pp 119–130. https://doi.org/10.5121/csit.2020.100910
6. Xin M, Wang Y (2019) Research on image classification model based on deep convolution neural network. J Image Video Proc 40. https://doi.org/10.1186/s13640-019-0417-8
7. Bedi P, Gole P (2021) Plant disease detection using hybrid model based on convolutional autoencoder and convolutional neural network, Artificial Intelligence in Agriculture, vol 5. ISSN 2589-7217. https://doi.org/10.1016/j.aiia.2021.05.002
8. Trivedi J, Shamnani Y, Gajjar R (2020) Plant leaf disease detection using machine learning. In: Gupta S, Sarvaiya J (eds) Emerging technology trends in electronics, communication and networking. ET2ECN 2020. Communications in computer and information science, vol 1214. Springer, Singapore. https://doi.org/10.1007/978-981-15-7219-7_23
9. Lu Y et al (2017) Identification of rice diseases using deep convolutional neural networks. Neurocomputing 267:378–384
10. Gajjar R, Gajjar N, Thakor VJ et al (2021) Real-time detection and identification of plant leaf diseases using convolutional neural networks on an embedded platform. Vis Comput (2021). https://doi.org/10.1007/s00371-021-02164-9
11. Ramos-Giraldo P, Reberg-Horton C, Locke AM, Mirsky S, Lobaton E (2020) Drought stress detection using low-cost computer vision systems and machine learning techniques. IT Prof 22(3):27–29. https://doi.org/10.1109/MITP.2020.2986103
12. github.com (2020) Leaf-wilting-detection-transfer-learning [online]. Available at https://github.com/cagandhi/Leaf-Wilting-Detection-Transfer-Learning.git
13. Khamparia A, Saini G, Gupta D et al (2020) Seasonal crops disease prediction and classification using deep convolutional encoder network. Circuits Syst Signal Process 39:818–836. https://doi.org/10.1007/s00034-019-01041-0
14. Team K (n.d.) Keras documentation: ResNet and ResNetV2. Keras. https://keras.io/api/applications/resnet/
15. Team K (n.d.) Keras documentation: VGG16 and VGG19. Keras. https://keras.io/api/applications/vgg/
16. github.com (2019) Soybean-leaf-wilting-CNN [online]. Available at https://github.com/parvez2083/Soybean-Leaf-Wilting-CNN.git

Deep Learning-Based COVID-19 Detection Using Transfer Learning Through ResNet-50

Mansi Patel, Jeel Padiya, and Manish I. Patel

Abstract Catering to the widespread COVID-19 pandemic, the authors aim to develop a system based on machine learning combined with the knowledge of medical science. Considering the prevailing situation, it becomes necessary to diagnose the COVID-19 at initial stages. The idea behind the described designed model is to identify the spread of infection in patients as fast as possible. The paper sketches two different approaches: K-fold cross-validation and deep network designer which are based on deep learning technology for the prediction of COVID-19 in the initial stages by using the chest X-rays. The performance evaluation of the cross-fold validation process is compared with the designed application in the deep network designer to find an effective and efficient methodology for classification which attained better accuracy.

Keywords Coronavirus · COVID-19 · Chest X-rays · Deep learning · ResNet · Transfer learning · Cross-validation

1 Introduction

A rise in number of pneumonia patients was recorded in December 2019, which was believed to be caused due to severe acute respiratory syndrome coronavirus 2 (SARS-CoV-2). This disease was found pathogenic and highly mutable due to which it turned into a worldwide pandemic by March 2020 as announced by World Health Organization (WHO). The lack of resources like the unavailability of vaccines contributed to the widespread growth of the virus [1].

In recent years, deep learning has emerged as a boon to the various sectors contributing to an exceptional advancement in the field of medical science. It is

M. Patel (✉) · J. Padiya · M. I. Patel
Department of Electronics and Communication Engineering, Institute of Technology, Nirma University, Ahmedabad, India
e-mail: mansipatel0415@gmail.com

M. I. Patel
e-mail: manish.i.patel@nirmauni.ac.in

a core technology utilized in artificial intelligence as a tool for the early diagnosis of lung diseases. Using X-rays for the detection of COVID-19 in the initial stages has been found effective.

The objective behind the research work is to contribute to society by developing a system that utilizes the chest X-rays to train the deep learning model for identifying the presence of COVID-19 in the patients. The paper describes the detection done in two ways—the first method is by utilizing the pre-trained ResNet-50 model by Keras and the second approach is carried out through training the model in the Deep Network Designer app using the deep learning toolbox. Thus, the procedure to achieve maximum possible efficiency in the stipulated time is portrayed here. The concept of cross-validation is used to enhance the accuracy of the generated output.

Rest of the paper is arranged as follows. Section 2 covers recent work in this area. Some of techniques we used are described in Sect. 3. Section 4 proposes our approach. Section 5 elaborates the results followed by the conclusion in Sect. 6.

2 Related Work

Ismael et al. [2] have presented the analysis of COVID-19 using the techniques like deep learning, pre-trained convolutional neural network (CNN), feature extraction with end-to-end training. Various CNN models available and discussed in this paper include ResNet-18, ResNet101, ResNet-50, VGG-19, etc., and for classification, support vector machine (SVM) is used. The paper used a chest X-ray dataset comprising 180 COVID-19 and 200 normal patient's images. Here, results were obtained by using SVM and ResNet-50 providing 94.7% accuracy, while in the case of training the accuracy of about 92.6% was obtained.

Chowdhury et al. [3] used the chest X-ray for creation of framework of PDCON-VIDNet. The network is based on parallel-dilated convolutional neural networks. The authors used the method of dilated convolution for the parallel stacking in the suggested technique to capture as well as stretch the essential features. The developed model has accuracy of 96.58%. Hussain et al. [4] have worked on three models which are represented with the same technique of CNN having COVID and normal as two class, pneumonia COVID and normal as three class and at last having classification of four class as COVID, normal, non-COVID pneumonia, and non-COVID bacterial pneumonia where for this algorithm 22 layers of CNN were used. The accuracy obtained for the model is 99.1, 94.2, and 91.2% for two classes, three classes, and four class classification, respectively.

Jain et al. [5] have considered the dataset having three classes, which are COVID-19 chest X-ray, SARS-Cov2 CT scan, and chest X-ray images of pneumonia patients. Detection has been done in less than two seconds. Further, the relation is developed between pneumonia and COVID patients for which they have used Grad-CAM-based color visualization. Attia [6] presented work on the enhancement of chest X-ray images of the dataset that are affected by dark, noisy and low in contrast problems. They have identified that due to lack of quality there are chances for low-efficiency
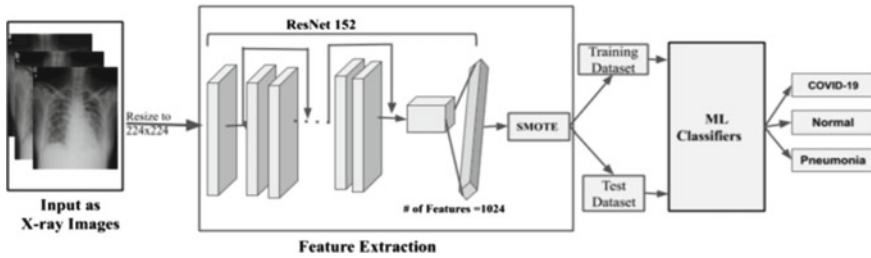
Fig. 1 Convolutional neural network

output from the deep learning architecture. Hence, some enhancement techniques like histogram equalization and contrast limited adaptive histogram equalization are applied.

3 Design Tools and Technologies

3.1 Convolutional Neural Network (CNN)

A convolutional neural network is an algorithm used in deep learning which uses datasets to recognize images. From the pixels of an image, we can generate completely connected network weights and CNN produces sufficient weights to scan small parts in a stipulated time.

CNN has input, output, and hidden layers as shown in Fig. 1. These hidden layers are made up of convolutional layers, pooling layers, ReLU, and fully connected layers. Here, the convolutional layer applies a signaling process like convolution to the input and this data is transferred to the next layer. Combining the output clusters into a single neuron is done using pooling. Here, the fully connected layers connect in such a way that each neuron in one layer is connected to neuron in the next 21 layers [7].

3.2 Deep Neural Network

Deep learning is the subset of machine learning, it teaches the computer to mimic like humans. It is used for classification and its architecture works by providing a suitable number of neural networks and a large set of data. The word "deep" refers to the various hidden layers present in the network to give desired output [8].

Deep convolutional neural network has led through a series of achievements for the classification of an image. Deep learning normally incorporates low, medium, or

Fig. 2 Single residual network
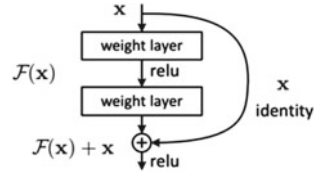
elevated level highlights and classifiers in a start to finish multilayer style, and the levels of highlights can be improved by the number of stacked layers.

3.3 Residual Network

A deep residual learning framework is a solution for the degradation problem in a system. In the deep residual learning framework by hoping of all the stacked layers, they form a residual mapping in the model as shown in Fig. 2. To say, the underlying mapping is $H(x)$ which is stacked with nonlinear layers to form another mapping $F(x) = H(x) - x$. Hence, the original one is recast into $F(x) + x$. The creation of $F(x) + x$ can be done through feed-forward neural networks [8].

Residual network or ResNet is a neural network that is used as a foundation for the creation of any model or a system to perform the tasks of computer vision.

3.4 ResNet-50 Architecture

The ResNet-50 [8] consists of five stages. All these five stages comprise a convolution block along with the identity block as shown in Fig. 3. Herein, each block consists of three convolution layers. Similarly, the identity blocks present in each stage also comprise three layers of convolution. On an overall basis, the trainable parameters in the ResNet-50 model range up to 23 million. This implementation of skip connection to add the output of previous as input of next helps to alleviate the problem of vanishing gradient in deep learning approaches.

The training error in the network decreases as the layers are increased from 18 to 34 and the 34-layer network is better by almost 2.8% than ResNet-18. In ResNet-50, the deeper bottleneck architecture is implemented. The residual building blocks of Resnet-18 and ResNet-34 have two layers at each stage. While in case of 23 bottleneck architecture each of the residual function F are stacked with three layers as depicted in Fig. 4.

These three layers of convolution are as follows: 1×1, 3×3, and 1×1. The first 1×1 layer helps in initially reducing dimensions, and the last 1×1 layer restores the dimensions which leave the middle layer with a bottleneck having smaller dimensions of input/output [8].
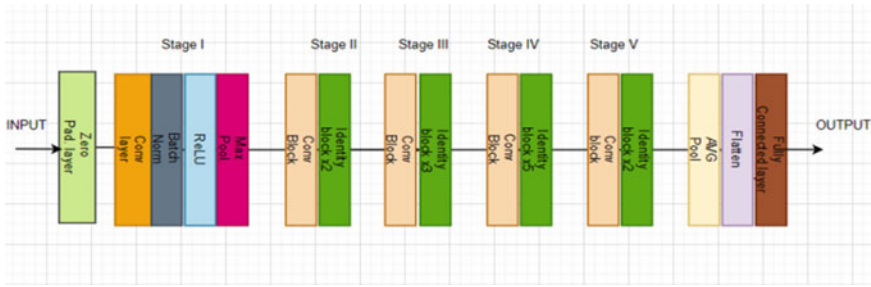
Fig. 3 ResNet architecture
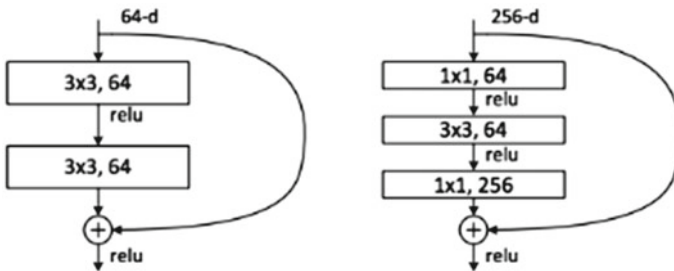
Fig. 4 Deep residual network. Left: building block of ResNet

3.5 Transfer Learning

Transfer learning is a methodology used in machine learning for reusing the pre-trained network. This reuse is done to increase the efficiency of the network by improving general features. So here, the system tries to exploit what was learned in one task and further, it tries to make it general. So basically, transferring weights is carried out. It is advisable to use a model that has learned from more labeled training data that needs to be transferred for transfer learning. Also, it is more used in natural language processing (NLP) and computer vision where high computational power is required. So, the network tries to detect features like edges, shapes, and other specifications in different layers and thus, in the next training, these layers need not be trained and further layers can be trained upon them. So, transfer learning is used to save training time, have good performance and also does not require a lot of data. Some approaches to transfer learning include training a model to release it, using a pre-trained model and feature extraction in the model [8].

4   Methodology

4.1   Dataset and Data Processing

The model uses the dataset collected from the repository of GitHub and Kaggle [9]. The training of the model is done on 2121 images which are divided into three subfolders of classes namely COVID, pneumonia, and normal.

During acquiring the images, there are chances of degradation of images due to some internal or external issues and there are chances of random noise and quantum noise to be present in the X-rays being captured. So, to overcome this type of degradation in images which may affect the system model we need to perform some kind of image enhancement or pre-processing techniques on images in the database [10]. For suppressing the distortion or to enhance the image properties, the pre-processing techniques are used.

The pre-processing techniques included in the algorithm are:

Image Resizing. All the images present in the dataset are resized to 224×224 before feeding to the model. This ensures the proper processing of the data while passing through various layers of the ResNet architecture.

Image Enhancement. The image quality is improved by implementing the contrast limited adaptive histogram equalization (CLAHE) [11]. CLAHE increases the image visibility level of foggy images. The distribution parameters play an important role in CLAHE to enhance the homogenous and heterogeneous noise.

4.2   System Flow

The COVID-19 detection in the paper is addressed through two different approaches.

K-fold Cross-Validation. The first approach followed in the process includes the algorithm using the concept of the K-fold cross-validation for the achievement of accuracy [12]. Here, the dataset is divided into fivefold, each of these fivefold are used as the testing sets in the model to make the classification process more accurate.

Initially, the data path of the image set is provided to the model, later the datastore is created which performs various processes on the collected images. The subfolders present in the dataset are read and the images present in all three classes of the subfolders are visualized. Now, the cross-fold validation is carried out wherein each fold is feed into the ResNet architecture. The pre-trained ResNet-50 architecture is imported into the system which comprises fully connected layers. The architecture passes the images through these layers for carrying out the convolution, feature activation, and classification process.

Hyperparameters provided to the model include optimizer = Adam, epoch = 8, batch size = 10, validation frequency = 50, initial learn rate = 1e-4, shuffle = every
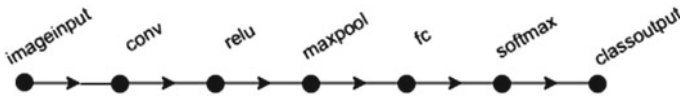
Fig. 5 Flow of layers in the constructed deep network designer model

epoch, and verbose = false. The image augmentation parameters like image rotation, reflection, and shear have been specified in the algorithm to scale all the images to the specific unique value.

Deep Network Designer. The app provides the option of importing available architecture of neural network along with the facility to develop and design an architecture of the network model by a combination of various layers. According to the structure of our algorithm, we require the ResNet architecture model for the training and classification of the fed images.

The created model in the app imports various layers. All these layers are connected sequentially to perform the functions of image acquisition, convolution, feature activation, and classification, respectively, as shown in Fig. 5.

After designing the model, dataset is imported to feed the training set as well as the validation images, respectively. Further, the training options are provided through specifying hyperparameters like optimizer = Adam, epoch = 8, batch size = 10, validation frequency = 50, initial learn rate = 1e-4, and shuffle = every epoch.

5　Results and Discussion

The described techniques were used to create the system for creating a COVID-19 detection model based on the concepts of deep neural networks by using the ResNet architecture. The generated results were studied to understand the performance of the system. The results obtained were in the form of various plots and graphs.

5.1　Cross-Validation

In the k-fold cross-validation process, the dataset is divided into the k equal parts wherein, k-1 folds act as training as data while the left fold works as the test set. Based on the done background, it is good to start with three folds process. Here, to get better performance, we have implemented fivefold cross-validation which divides data into five non-overlapping equal parts. The graph of percentage accuracy versus iterations and that of percentage loss versus iterations is plotted for fold 5 as shown in Fig. 6. If the number of folds is increased, then the accuracy of the system increases. So, to portray the results fold 5 is plotted. The plot describes the rate of change in

the accuracy of the model concerning the number of iterations taking place in the system. The number of iterations was decided based on the values of the maximum epoch and the batch size provided at the time of training. The batch size here means the parameter that decides the number of samples to work on, before the updating of the ongoing internal parameters of the model. At the time of completion of a single batch, the predicted output is compared with expected output variables. Finally, the calculation of error is done. While epoch decides the times the algorithm that is dumped on the system will work through the complete training dataset. The final fold graph provides accurate results. The time required in each fold to perform the iterations is shown in Table 1.

Figure 7 shows the confusion matrix obtained from the model. It is used to describe the performance of the classification model that is developed or to say it depicts the classifier performance. The matrix shows the performance of the dataset whose true values are available or calculated. The precision, sensitivity, and specificity calculated from the confusion matrix are provided in Table 2. These parameters are calculated through Eqs. 1, 2, and 3. The abbreviations TP, TN, FP, and FN stand for True Positive, True Negative, False Positive, and False Negative, respectively.
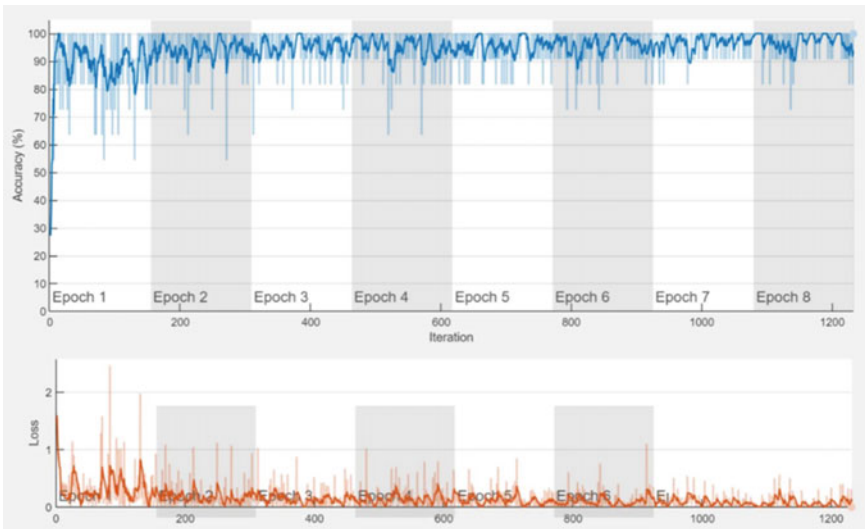
Fig. 6 Performance graph of fold 5 of cross-validation process

Table 1 Parameters of K-fold cross-validation

Number of folds	1	2	3	4	5
Iterations	1232	1232	1232	1232	1232
Time (min)	195.35	122.38	123.75	174.23	142
Accuracy (%)	94.01	94.27	94.32	95.43	96.11

$$\text{Precision} = \frac{\text{TP}}{\text{TP} + \text{TN}} \tag{1}$$

$$\text{Sensitivity} = \frac{\text{TP}}{\text{TP} + \text{FP}} \tag{2}$$

$$\text{Specificity} = \frac{\text{TN}}{\text{TN} + \text{FP}} \tag{3}$$

The receiver operating characteristic (ROC) generated is the graph of True Positive Rate versus False Positive Rate. It depicts the performance of the model calculated at each threshold value. The area under curve (AUC) obtained through the ROC curve is 0.999 which determines the overall performance of the model. Finally, a random image was classified, the image class was predicted. The ROC curve and classified image are shown in Fig. 8.

Fig. 7 Confusion matrix
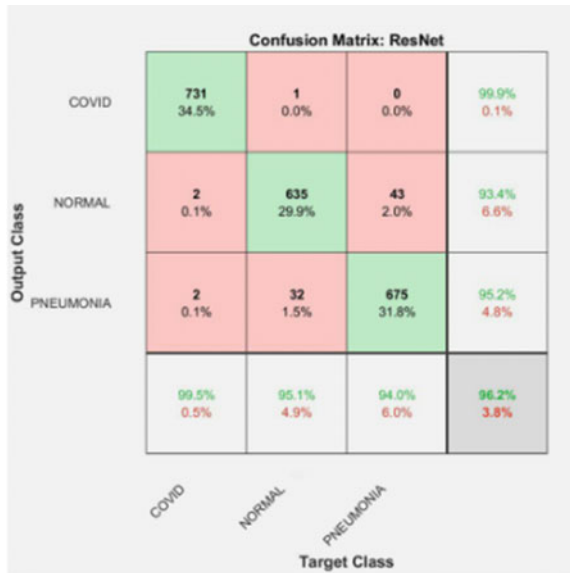
Table 2 Performance parameters calculated through confusion matrix

Class	Precision (%)	Sensitivity (%)	Specificity (%)
COVID	99.9	99.45	99.9
Normal	93.4	95.05	96.9
Pneumonia	95.3	94.01	97.6
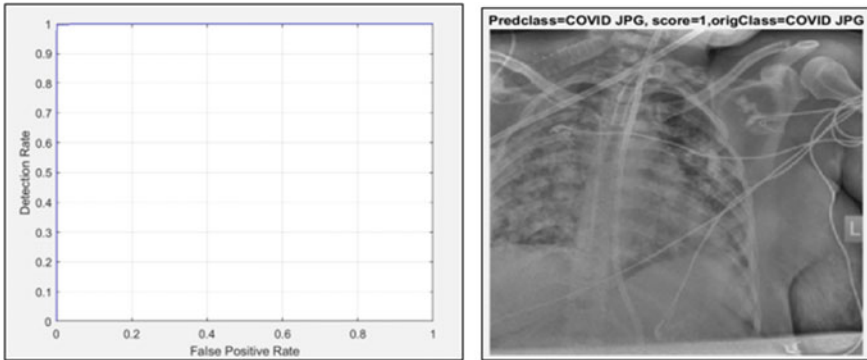
Fig. 8 Left: ROC curve, Right: Classification output

5.2 Performance of Deep Network Designer

In the designed application network, the output is generated in the form of the curve of the percentage of accuracy versus number of iterations and percentage loss versus several iterations as given in Fig. 9. The generated output is due to the last layer attached to the module which is the classification layer with some provided parameters. The deep network designer exports the trained network along with the training variable to carry out the prediction part in the module. Finally, the detection of a random image was done which predicted the output as shown in Fig. 10. Table 3 gives the information about the parameters based on which the network performance was calculated.

In Table 4, a comparison of the presented work with the existing methods has been done. It is observed not only images present in the dataset affect the system model
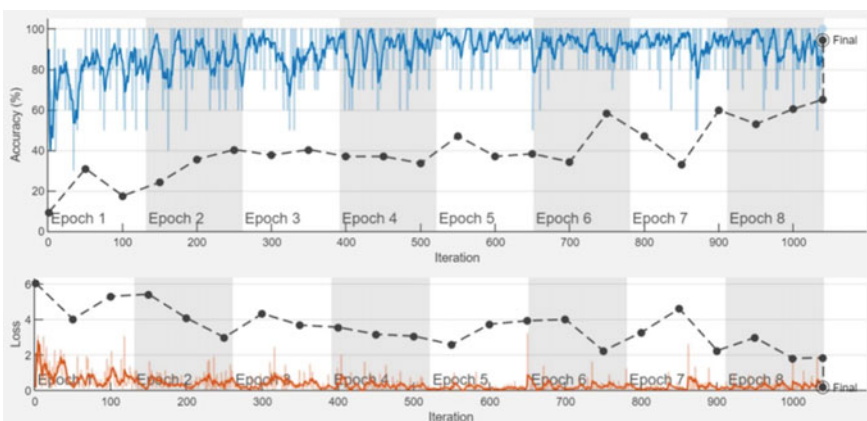
Fig. 9 Performance graph generated through deep network designer app

COVID JPG, 97.7%

Fig. 10 Classifier output with class and accuracy

Table 3 Classification report

Parameters	Value
Iterations	1040
Time (min)	327.35
Accuracy	94.63%
Validation frequency	50 iterations

but even the parameters like pre-processing techniques, feature extraction, filtering methods, and the used algorithm determine the amount of precision achieved by the model.

Table 4 Comparison with existing methods

References	Dataset	Methods	Accuracy (%)
Ismael et al. [2]	380 chest X-ray images (COVID-19 = 180, normal = 200)	ResNet-50 + SVM	94.7
Chowdhury et al. [3]	2905 images of chest X-ray (COVID-19 = 219, pneumonia = 1345, and normal = 1341)	Parallel-dilated CNN	96.58
Hussain et al. [4]	7390 images of X-ray (COVID-19 = 2843, pneumonia = 1439, and normal = 3108)	CNN (22 layers)	94.2
Presented Work	2121 X-ray (COVID-19 = 732, pneumonia = 709, and normal = 680)	Transfer Learning through ResNet-50	96.8

6 Conclusion

It is evitable that the prediction of the COVID-19 pandemic through the images of chest X-ray plays a vital role for the doctors as well as the patients by reducing the time of diagnosis along with the financial costs at the initial stages. The paper shows the implementation of the model using two different approaches which comprised of the varied detection method. The classification done through the concept of cross-validation proves to be more accurate with the model attaining an overall accuracy of 96.8%. In the case of the application constructed in the deep network, the designer achieves a performance accuracy of 94.63%. Although, the cross-validation technique portrays higher accuracy it compromises the time factor. It requires a longer time duration in the completion of the entire process as the number of folds increases. Comparatively, deep network designer provides easy simulation within less time duration. Further, the performance of the model can be improved by implementing various image enhancement techniques. Also, ease of access can be provided by the development of an android-based application for the early detection of the disease.

References

1. Mishra M, Parashar V, Shimpi R (2020) Development and evaluation of an AI System for early detection of Covid-19 pneumonia using X-ray (Student Consortium). In: 2020 IEEE Sixth international conference on multimedia big data (BigMM). IEEE, pp 292–296. https://doi.org/10.1109/BigMM50055.2020.00051
2. Ismael AM, Şengür A (2021) Deep learning approaches for COVID-19 detection based on chest X-ray images. Expert Syst Appl 164
3. Chowdhury NK, Rahman MM, Kabir MA (2020) Pdcovidnet: a parallel-dilated convolutional neural network architecture for detecting COVID-19 from chest x-ray images. Health Inf Sci Syst 8(1):1–14
4. Hussain E, Hasan M, Rahman MA, Lee I, Tamanna T, Parvez MZ (2021) CoroDet: a deep learning based classification for COVID-19 detection using chest X-ray images. Chaos, Solitons Fractals 142:110495. ISSN: 0960-0779
5. Jain G, Mittal D, Thakur D, Mittal MK (2020) A deep learning approach to detect Covid-19 coronavirus with X-ray images. Biocybernetics Biomed Eng 40(4):1391–1405. ISSN: 0208-5216
6. Attia SJ (2016) Enhancement of chest X-ray images for diagnosis purposes. J Nat Sci Res 6(2). ISSN: 2224-3186
7. Albawi S, Mohammed TA, Al-Zawi S (2017) Understanding of a convolutional neural network. In: 2017 International conference on engineering and technology (ICET). IEEE, pp 1–6. https://doi.org/10.1109/ICEngTechnol.2017.8308186
8. He K, Zhang X, Ren S, Sun J (2016) Deep residual learning for image recognition. In: 2016 IEEE conference on computer vision and pattern recognition (CVPR). IEEE, pp 770–778. https://doi.org/10.1109/CVPR.2016.90
9. Kumar R, Arora R, Bansal V, Sahayasheela VJ, Buckchash H, Imran J et al (2020) Accurate prediction of COVID-19 using chest X-ray images through deep feature learning model with SMOTE and machine learning classifiers. medRxiv
10. Narayanan BN, Davuluru VSP, Hardie RC (2020) Two-stage deep learning architecture for pneumonia detection and its diagnosis in chest radiographs. In: Medical imaging 2020: imaging informatics for healthcare, research, and applications. Int Soc Opt Photonics 11318:130–139

11. Ikhsan IAM, Hussain A, Zulkifley MA, Tahir NM, Mustapha A (2014) An analysis of x-ray image enhancement methods for vertebral bone segmentation. In: 2014 IEEE 10th International colloquium on signal processing and its applications. IEEE, pp 208–211. https://doi.org/10.1109/CSPA.2014.6805749
12. Fushiki T (2011) Estimation of prediction error by using K-fold cross-validation. Stat Comput 21(2):137–146

OCR for Devanagari Script Using a Deep Hybrid CNN-RNN Network

Rhea Sansowa , **Vincent Abraham** , **Manish I. Patel** ,
and **Ruchi Gajjar**

Abstract Optical character recognition (OCR) involves the electronic transcription of handwritten, printed text from either scanned documents or any sort of images. This multiclass classification problem comprising of recognizing the various characters in a language and correctly classifying them has found its way in plenty of computer vision applications. Although much work has been done for the English language, there have been only a few explorations pertaining to OCR for the Devanagari script. This paper proposes a hybrid CNN-RNN model to classify characters using the Devanagari handwritten character dataset. The main objective is to design a model with higher accuracy than the CNN model reported in literature for the same purpose. The models are trained and evaluated using the same procedures. On evaluating the models, the hybrid CNN-RNN model has a testing accuracy of 98.71%, which is higher than the CNN model, having 97.71% testing accuracy. It also fares better than the standard neural network architectures-VGG16 and AlexNet which when taken without the pre-trained weights result in 97.62 and 98.20% testing accuracy respectively. Hence, this successfully demonstrates the attributes of RNN in improved feature extraction when used along with convolutional layers.

Keywords Convolutional neural network · Devanagari script · Hybrid CNN-RNN · Long short-term memory · Optical character recognition · Recurrent neural network

R. Sansowa (✉) · V. Abraham · M. I. Patel · R. Gajjar
Department of Electronics and Communication Engineering Institute of Technology,
Nirma University, Ahmedabad, India
e-mail: rhea.s.sansowa@gmail.com

V. Abraham
e-mail: vincent.ahm@gmail.com

M. I. Patel
e-mail: manish.i.patel@nirmauni.ac.in

R. Gajjar
e-mail: ruchi.gajjar@nirmauni.ac.in

1 Introduction

Optical character recognition (OCR) is a technology that can be used to convert any scanned image with natural language into a searchable document, which can be edited and modified, reducing the searching time from hours to mere minutes. It also has applications in other fields such as license plate reading, digitizing historical documents, and books. The scanned text can also be used for text mining.

The preliminary idea of OCR surfaced well before the age of computers around 1950. Tausheek, in the year 1929, obtained a patent on the technology of template masking and matching, which was made using photodetectors and mechanical masks [1]. The research work done by Anderson R.H. in 1967 paved the way for more work in pattern extraction from images and its conversion into markup form [2]. With the increase in computational power of systems, the availability of GPU, and advents in deep learning, there has been a boost in OCR technology, and new neural network-models are now available for it. Deep learning models are ideal for OCR because feature selection is a key task [3] and in deep learning models, the features are built by the model itself, thus reducing efforts and improving classification [4]. Convolutional neural network (CNN) is one such neural network class. It is easier and less time consuming to train as number of parameters are relatively low compared to classes having fully connected layers [5]. CNN is most commonly used in such computer vision applications, while much use of RNN is not seen. Performance of this CNN model can be boosted by passing the extracted features by CNN into the RNN model for further classification [6]. CNN is used for feature extraction because it has robust feature extraction ability [7]. Substantial work has been done for OCR in English language, but there's still enormous scope for research related to Devanagari script. The main reason behind this is that there is no separation between characters in the script, and a lot of the characters look alike with only a slight distinction between them [8]. This paper focuses on improving the CNN model found in the existing literature [8] by adding RNN layers for further feature extractions and implementing to carry out OCR for Devanagari script with increased accuracy. These values are then compared with the existing architectures– AlexNet and VGG16 to gauge the performance of the proposed model.

1.1 *The Devanagari Handwritten Character Dataset*

Devanagari belongs to the Brahmic script family, and it makes up languages such as Hindi, Nepali, Marathi, and among other East and South Asian languages [9]. There are 36 consonants in this script, and a total of 12 vowels and 10 numbers. The vowels can also attach themselves to the consonants, resulting in derived consonants. There are some other special characters too found in this script.

The dataset chosen for this paper is called 'Devanagari Handwritten Character Dataset' (DHCD), and it has all the 36 consonants and the 10 numerical digits as a

part of the dataset [8]. It does not contain vowels, modified characters or special characters. In Tables 1 and 2, the characters and numerical digits in the Devanagari script contained by the dataset are displayed.

There are 92,000 images—78,200 for training and 13,800 for testing. The size of each PNG image is 32×32. The dataset is made of handwritten characters that were manually cropped, and characters were placed in the center of the image and were of size 28×28. A 2×2 padding of zeros was added on all sides of the characters. Sample images from the dataset are shown in Fig. 1.

Section 2 contains details about some of the research work done till date relevant to this topic, Sect. 3 contains basic theory about CNN and RNN after which in Sect. 4, the hybrid CNN-RNN model is proposed by making modifications to the CNN model reported in literature. The implementation details are covered at the beginning of Sect. 5 and results for all the models have been stated and interpreted. The paper is concluded in Sect. 6.

2 Literature Review

A fair amount of work has been done on image classification for various applications in fields such as OCR, healthcare, obstacle recognition, etc. using methodologies which are novel, or are optimizations on existing ones. Some of these literary works relevant to this paper's purpose would now be discussed in this section.

Table 1 Devanagari consonants

क	ख	ग	घ	ङ	च	छ	ज	झ	ञ
ट	ठ	ड	ढ	ण	त	थ	द	ध	न
प	फ	ब	भ	म	य	र	ल	व	श
		ष	स	ह	क्ष	त्र	ज्ञ		

Table 2 Devanagari numerical digits

०	१	२	३	४	५	६	७	८	९

Fig. 1 Sample images from the Devanagari handwritten character dataset

A dataset was introduced by [8] for the purpose of OCR for Devanagari script. Two CNN models were also proposed in the paper. The first model consisted of three convolutional layers and a fully connected layer. Based on the LeNet family, the second model consisted of two convolutional layers followed by two fully connected layers. To optimize the training process, methodologies like dropouts, batch normalizations and dataset increment were applied to the models, which led to the models achieving a testing accuracy of 98.47 and 98.26%. Hence, a dataset for the models to be trained on and a base CNN model was provided [8]. One of the more recent papers to use this dataset used a deep CNN model through which an accuracy of 97% was observed [10]. A hybrid CNN-RNN model for implementing Urdu OCR from printed documents was presented, annotated page by page [11]. It involved sequence to sequence transcription of the Urdu text, which was later divided at line levels and prepared into a dataset. The proposed model was a 7-layer deep convolutional network. The convolutional layers were used to extract the robust features from the input which were later mapped and fed into two BLSTM layers for the final transcription. Different variations in this model were also proposed in which the highest testing accuracy was achieved as 98.80%.

To carry out the task of image to markup generation, WYGIWYS model was built which used an attention-based mechanism instead of taking the standard mathematical approach to OCR [12]. After feature extraction was done using CNN, the grid was fed into an RNN encoder after which on decoding, using the attention-based mechanism, result is mapped to the vocabulary. The 'Image to Latex 100 K' dataset was used for this purpose. Its implementation yielded 74.00% accuracy. This was improved upon by building a complex attention model with CNN-LSTM for the particular purpose of recognition of various mathematical equations [13]. The proposed model had worked sequentially to read data which aided in keeping track of the data processed, which ultimately resulted in better performance with a higher accuracy of 76.00%. A parallel CNN-RNN model was proposed for the classification of breast biopsy images non-invasively into four classes to find type of cancer cells present in which both CNN and RNN were used for feature extraction, and an assumption was made about RNN having the same feature extraction ability as CNN in [7]. For weighing the features, a perceptron attention mechanism was used so that the model can be improved. Instead of conventional dropout, selective dropout, which uses pruning to discard the neurons, was used. The highest test accuracy was observed to be 97.50%.

The papers reviewed in this section show a clear benefit of adding RNN layers to a CNN model for image classification applications, resulting in a model with more accuracy. Furthermore, the models described in [7] and [11] acted as strong motivation and justifications in using RNN along with CNN for further feature extractions from input.

3   Background Theory

This section would talk about the various methodologies used for the purpose of this paper, and also the implementation details for achieving the desired objective.

3.1   *Convolutional Neural Networks (CNN)*

A convolutional neural network plays a vital role in robust feature extractions of the fed in input and hence is a convenient choice for OCR. Its foundation was laid when Fukushima (1980) came up with the neocognitron model for visual pattern recognition [14]. Through its training process, which usually consists of back-propagation through gradient descent, a CNN can extract local features of the input adaptively, without any need for explicitly stating the features to be learnt. A CNN generally consists of convolutional layers, max-pooling (sub-sampling) layers, and fully connected (dense) layers. The convolutional and max-pooling layers are responsible for feature extraction. In contrast, the dense layer maps the extracted features to a given number of nodes for the terminal classification.

3.2   *Recurrent Neural Networks (RNN) and Long Short-Term Memory (LSTM)*

In recurrent neural networks, the current output depends upon the current and previous inputs fed into the network. This attribute of past dependency has allowed RNNs to be used for various applications involving time-series predictions and exploring the temporal dynamics between the information [15]. RNNs achieve this dependency by having the output at each timestep be the weighted sum of the current inputs, added with the activation output of the previous node. The training process here takes place through backpropagation through time. RNNs face the issue of not maintaining the long-term dependencies between the data due to vanishing or exploding gradients. To overcome this, LSTM is used wherein a gated cell is present that stores or forgets the previous input information based on its weights. Hence, this additional gradient of the gated cell allows the network to have long-term dependencies between the inputs. In this paper, LSTM layers would be used along with CNN layers to perform further feature extractions and train a model with higher accuracy.

4 The Proposed Hybrid CNN-RNN Model Architecture

This section discusses the architecture of the proposed CNN-RNN model which is designed by extending the CNN model referred from literature [8]. The architecture of the proposed model is shown in Fig. 2.

The convolutional layers in the model consist of kernels of size (5 × 5), and the max-pooling layers consist of kernels of size (2 × 2) and strides of 2. The features extracted from the three convolutional layers are flattened, time-mapped and later fed into the LSTM layers, which perform the final feature extraction before feeding them into the fully connected layers.

The activation function used for the convolutional layers is the Rectified Linear Unit (ReLu) function which responds nonlinearly to negative inputs and linearly to the positive inputs. Hence, it overcomes the issues faced by other activation functions such as vanishing gradients wherein, the gradients move closer and closer to zero the further they move from the output nodes during backpropagation. Each of the LSTM layers use the sigmoid activation function for the input, output and forget gates, allowing the gates to store or lose the information (0 or 1). The output nodes in the layers use the hyperbolic tangent (tan h) activation function, which provides the range (–1, 1), acting as an optimum activation function for back-propagation. The activation function used for both the dense layers is the softmax function, which takes the input vector and maps it to its corresponding probabilities, which for the output layer provides the information on what character the input is more likely to be. The character with the highest probability is then taken as the predicted output.

Furthermore, some essential methodologies used here for efficient training and to avoid overfitting in the model are batch normalizations and dropouts. Batch normalization refers to standardizing the inputs corresponding to each mini-batch for the subsequent layers, allowing the networks to train faster. Dropouts refer to dropping out some randomly selected neurons (based on the dropout rate) by assigning their weight values zero. Dropouts reduce overfitting and allow the trained models to be more robust [16].
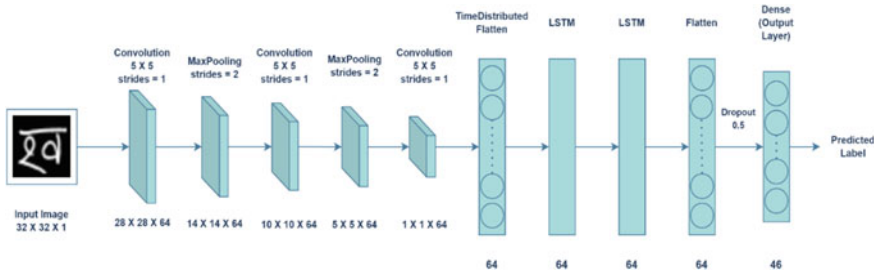
Fig. 2 The proposed hybrid CNN-RNN model

By increasing the number of filters in the convolutional layers, change in the dropout rate, using the softmax activation function for both of the dense layers, and addition of the LSTM layers, performance of the referred CNN model was improved.

5 Results and Discussion

This section discusses the procedure followed for implementation of the models as well as the results observed on deploying the dataset on the defined models.

5.1 *Implementation Details*

Firstly, the data is loaded into the Python environment, where basic pre-processing operations are performed on the images. The images are turned into gray-scale to reduce the number of channels so that the training process can be sped up, and reshaping is done on the image where its size goes from (32, 32) to (32, 32, 1) to show the number of channels. Then assignment of labels is carried out which are then converted into one hot encoded form.

The next step involves defining the model architectures. The CNN-RNN model is defined following the architecture described in the previous section, along with the rest of the models. For validation, 30% of the training set is used wherein at the end of each epoch, the validation accuracy is monitored and the necessary decisions are made using callbacks. The callbacks used include stopping the training process on detecting no significant change in validation loss as well as reducing the learning rate on detecting a plateau. After completion of the training process, training and testing accuracy is obtained. The accuracy versus epochs graph and metrics such as precision, recall and F1 score are then obtained for the models. The models are then tested against a set of custom input images. For its pre-processing, images are resized, inverted, and rescaled to be given as the input. The predicted output for these images is then observed.

5.2 *Accuracy Versus Epochs*

The models were trained by applying early stopping and using a function to reduce learning rate when the model stops improving. This gave the models ample amount of time for fine-tuning, resulting in high accuracies.

The plotted results for AlexNet, VGG16, CNN [8] and proposed CNN-RNN model are as shown in Figs. 3, 4, 5, and 6 respectively. From these figures, it can be observed that all of the models achieve considerably high values of training and testing accuracies, the CNN-RNN model achieving the highest.

Fig. 3 Accuracy versus epochs for AlexNet model
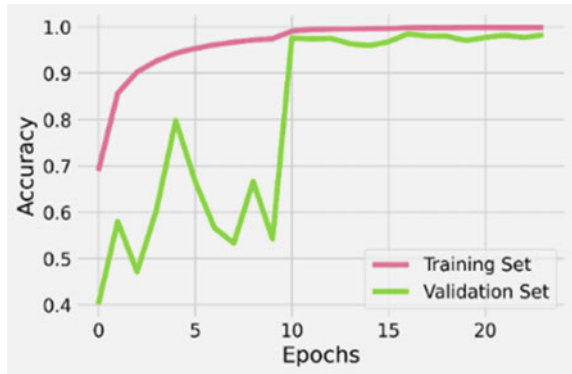
Fig. 4 Accuracy versus epochs for VGG16 model
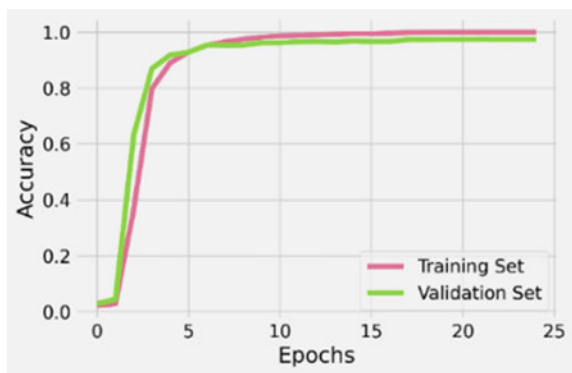
Fig. 5 Accuracy versus epochs for CNN [8] model
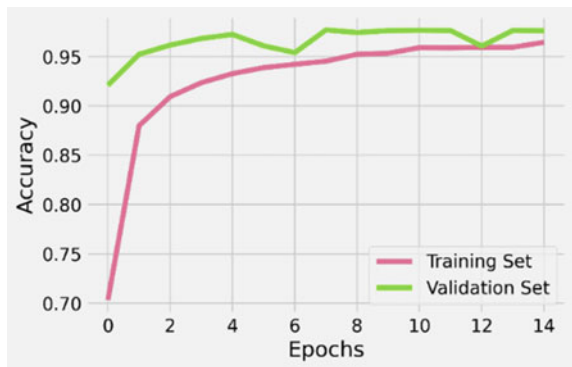
Fig. 6 Accuracy versus epochs for the hybrid CNN-RNN model
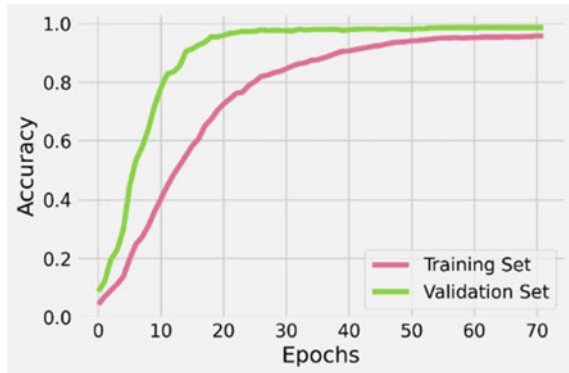
5.3 Quantitative Results

Accuracy of the proposed CNN-RNN model has been compared with the existing CNN model in addition to two of the standard CNN models-AlexNet and VGG16. Alexnet was one of the first deep neural networks to achieve classification accuracy comparable to traditional methods for ImageNet dataset using CNN [17]. VGG16 on the other hand boosts the performance of AlexNet by converting large filters into multiple smaller ones, which increases the depth of the network and ultimately, improves the performance [18]. Training and testing for these two models are carried out without using the pre-trained weights and just the model architecture is utilized.

From the obtained values in Table 3, it can be said that the proposed CNN-RNN model outperforms the CNN, VGG16, and AlexNet models in terms of both training and testing accuracy. It is also to be noted that the CNN-RNN model has about 50 times lesser training parameters in relation to the standard models taken yet it outmatches their performance. The CNN-RNN model also outperforms the CNN model proposed in [10] which had an accuracy of 97%.

For the evaluation of models, the standard metrics-precision, recall, and F1 score are used. Precision is the fraction of the true positive cases predicted from all positive cases. The fraction of real positive cases which were correctly forecast as

Table 3 Accuracy obtained for the models

Model Name	Accuracy		Trainable parameters
	Training (%)	Testing (%)	
AlexNet	99.48	98.20	23,628,846
VGG16	99.25	97.62	14,738,286
CNN [8]	98.93	97.71	85,262
CNN [21]	97		Not mentioned
Hybrid CNN-RNN	99.63	98.71	280,174

Table 4 Macro precision, recall and F1 score for the models

Model name	Precision	Recall	F1 score
AlexNet	0.98245	0.98245	0.98225
VGG16	0.97548	0.97536	0.97537
CNN [8]	0.97731	0.97703	0.97706
Hybrid CNN-RNN	0.98712	0.98703	0.98704

such is called the recall value [19]. The F1 score is the harmonic mean of precision and recall [20]. As this is a multi-class problem, we use macro values for all the above-mentioned measures which results into the average value of the metric per class [19]. The macro precision, recall, and F1 score values obtained are shown in Table 4.

5.4 Dealing with Custom Inputs

Output was obtained for some images which were not present in the training and the testing dataset to see if the constructed models work on real-life data. Figure 7 shows the steps involved to deploy the model on custom images.

6 Conclusion

The accuracy for OCR for Devanagari script can be enhanced by adding recurrent neural network layers to the CNN model. By making a hybrid model, the classification capability increases, and the misclassification rate drops down. The precision and recall values obtained are also higher than the CNN model reported in literature. The CNN-RNN model performed better than CNN, VGG16, and AlexNet, with the training and testing accuracy of 99.63 and 98.71%, respectively. The number of trainable parameters for this model was about 50 times lesser than AlexNet and VGG16 and yet superior performance was obtained. For future work, a more inclusive data set containing vowels and special characters can be adopted for a more practically applicable transcription.
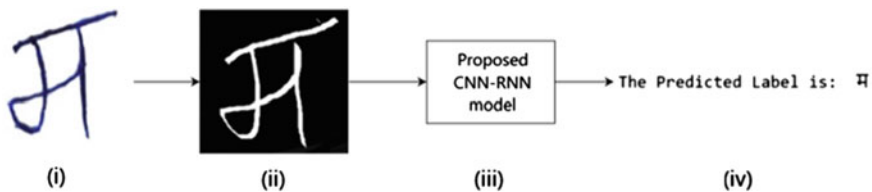
Fig. 7 Classification result of custom input i image of scanned character, ii pre-processed image, iii passing image through the proposed CNN-RNN model, iv predicted output label

References

1. Mori S, Suen C, Yamamoto K (1992) Historical review of OCR research and development. Proc IEEE 80:1029–1058. https://doi.org/10.1109/5.156468
2. Bahdanau D, Cho K, Bengio Y (2014) Neural machine translation by jointly learning to align and translate. ICLR arXiv:1409.0473
3. Ruck D, Rogers S, Kabrisky M, Mills J (1990) Multisensor fusion classification with a multilayer perceptron. In: 1990 IJCNN international joint conference on neural networks. IEEE, pp 863–868. https://doi.org/10.1109/ijcnn.1990.137802
4. Lee H, Grosse R, Ranganath R, Ng AY (2009) Convolutional deep belief networks for scalable unsupervised learning of hierarchical representations. In: Proceedings of the 26th annual international conference on machine learning-ICML'09. ICML, pp 609–616. https://doi.org/10.1145/1553374.1553453
5. Lecun Y, Bottou L, Bengio Y, Haffner P (1998) Gradient-based learning applied to document recognition. Proc IEEE 86:2278–2324. https://doi.org/10.1109/5.726791
6. Guo Y, Liu Y, Bakker EM et al (2017) CNN-RNN: a large-scale hierarchical image classification framework. Multimedia Tools Appl 77:10251–10271. https://doi.org/10.1007/s11042-017-5443-x
7. Yao H, Zhang X, Zhou X, Liu S (2019) Parallel structure deep neural network using CNN and RNN with an attention mechanism for breast cancer histology image classification. Cancers 11:1901. https://doi.org/10.3390/cancers11121901
8. Acharya S, Pant AK, Gyawali PK (2015) Deep learning based large scale handwritten Devanagari character recognition. In: 2015 9th International conference on software, knowledge, information management and applications (SKIMA). IEEE, pp 1–6. https://doi.org/10.1109/skima.2015.7400041
9. Fischer SR (2004) History of writing. Reaktion Books, London, pp 32–37
10. Kavya A, Vivek N, Harika M, Nidumolu V (2020) Handwritten Devanagari character classification using CNN. Lect Notes Networks Syst 145:309–317. https://doi.org/10.1007/978-981-15-7345-3_25
11. Jain M, Mathew M, Jawahar C (2017) Unconstrained OCR for Urdu using deep CNN-RNN hybrid networks. In: 2017 4th IAPR Asian conference on pattern recognition (ACPR). IEEE, pp 747–752. https://doi.org/10.1109/acpr.2017.5
12. Deng Y, Kanervisto A, Rush A (2016) What you get is what you see: a visual markup decompiler. In: Association for the advancement of artificial intelligence. arXiv, abs/1609.04938, pp 32–37
13. Mishra V, Kaur D (2018) Sequence-to-sequence learning using deep learning for optical character recognition (OCR). In: 2018 International conference on computational science and computational intelligence (CSCI). IEEE, pp 324–329. https://doi.org/10.1109/csci46756.2018.00069
14. Fukushima K (1980) Neocognitron: a self-organising neural network model for a mechanism of pattern recognition unaffected by shift in position. Biol Cybern 36:193–202. https://doi.org/10.1007/bf00344251
15. Sherstinsky A (2020) Fundamentals of recurrent neural network (RNN) and long short-term memory (LSTM) network. In: Special Issue on machine learning and dynamical systems. J Physica D 404:132306. Elsevier. https://doi.org/10.1016/j.physd.2019.132306
16. Park S, Kwak N (2017) Analysis on the dropout effect in convolutional neural networks. In: Computer vision-ACCV 2016. Springer, Cham, pp 189–204. https://doi.org/10.1007/978-3-319-54184-6_12
17. Krizhevsky A, Sutskever I, Hinton G (2017) Imagenet classification with deep convolutional neural networks. Commun ACM 60:84–90. https://doi.org/10.1145/3065386
18. Simonyan K, Zisserman A (2014) Very deep convolutional networks for large-scale image recognition. ICLR arXiv:1409.1556

19. Paredes-Valverde M, Colomo-Palacios R, Salas-Zárate M, Valencia-García R (2017) Sentiment analysis in spanish for improvement of products and services: a deep learning approach. Sci Program 2017:1–6. https://doi.org/10.1155/2017/1329281
20. Salas-Zárate, MDP, Valencia-García R, Ruiz-Martínez A, Colomo-Palacios R (2016) Feature-based opinion mining in financial news: an ontology-driven approach. J Inf Sci43:458–479. https://doi.org/10.1177/0165551516645528
21. Prechelt L (1998) Automatic early stopping using cross validation: quantifying the criteria. Neural Netw 11:761–767. https://doi.org/10.1016/s0893-6080(98)00010-0

A Dataset Preparation Framework for Education Data Mining

Mala H. Mehta , **N. C. Chauhan** , **and Anu Gokhale**

Abstract Education data mining (EDM) is an important application domain of data mining. It focuses on generating interesting, novel, and useful patterns in benefit of academia. Institute Graduation Rate prediction, student dropout prediction, student group formation, students' performance prediction, and student failure analysis are some of the challenging problems to address in field of education data mining. For education domain, useful research is conducted with either online available datasets or local dataset available with the organization. Dataset preparation for generalized analytical use is a challenge for field of EDM. Much of the time of the researchers is invested in identification and preparation of proper dataset that can be used for development of novel techniques and algorithms. In this paper, a novel framework of EDM dataset preparation is presented. Illustratively, this framework is successfully applied and tested for Institute Graduation Rate prediction problem. It is vital for researchers to have data at hand first to carry out further research. This paper illustrates a framework by which, education domain researchers could prepare datasets from huge data repositories as per their application need.

Keywords Data preparation framework · Institute graduation rate prediction · Education data mining

M. H. Mehta (✉)
Gujarat Technological University, Gujarat, India
e-mail: malamehta.it@svitvasad.ac.in

N. C. Chauhan
A D Patel Institute of Technology, Gujarat, India
e-mail: it.ncchauhan@adit.ad.in

A. Gokhale
Illinois State University, Normal, USA
e-mail: aagokhale@ilstu.edu

1 Introduction

Digitized educational data is the main resource for education data mining to generate useful knowledge. Data mining's main aim is to find novel, interesting, and actionable patterns out of large amount of data. Student performance prediction, student dropout prediction, students' enrollment prediction, institution graduation rate, and students' placement prediction are some of important prediction tasks in education data mining. Student classifications based on their learning levels, grouping elective courses are some examples of classification and grouping of students. Subgroup discovery techniques focus on finding rules based on some property of interest. It is a kind of semi-supervised learning techniques which can be applied on education domain problems to find out useful rules. Different kinds of learning that are addressed by education data mining include cognitive learning, individual learning, group learning, etc. Learning analytics is essentially a branch of EDM, where analysis of learning patterns of students is performed. In education domain, every institute wants to give best output in terms of placements, academic or non-academic results, and graduation rates. Role of online learning has greatly enhanced in academia. In such scenario, need of investigating data mining techniques in education domain has a paramount importance. In order to perform any novel and useful data mining research in academia, suitable data is essential. Computer-generated data in education field is not available easily. Those which are available are either very small or not openly available. Many researchers have done experiments with datasets they have created with specific problem domain. To find related data or create problem-specific data is a crucial challenge in the field. In this paper, a dataset preparation framework is proposed using which education domain researchers can prepare their problem specific dataset. For this work, an open-source repository is used, from which targeted data is extracted step by step for suggested problem definition. The framework suggested here could be well expanded or applied to other big repositories for preparation of dataset. Proposed framework could be considered as an illustration for preparation of education datasets. Remaining paper is organized in following way. Section 2 describes detailed survey of education data mining and dataset used in the study. Section 3 presents description of a big data repository which is used for data preparation framework. Section 4 presents dataset preparation framework. Section 5 presents a case study of Institute Graduation Rate prediction problem using proposed framework. Finally, the conclusion is presented at the end.

2 Literature Survey

2.1 Education Data Mining

Useful, actionable, and novel knowledge can be generated out of electronic data gathered by various educational and government institutes. Student dropout rates,

student deteriorating performance, students' placement, and teaching learning challenges exist in education data mining. Traditional systems or online systems could offer data to analyze for wide range of problems, but in many cases data is hard to create. Education domain problems can be categorized into three areas. First, classification or prediction problems, examples are student performance prediction, student dropout rate prediction, or Institute Graduation Rate prediction. Second, clustering or grouping problems, examples are efficient student grouping for group learning, ideal student grouping for assigning projects, etc. Third, subgroup discovery problems are semi-supervised techniques which prepare groups with respect to property of interest. Education data mining has a wide range of application areas which consists of a large survey.

Romero and Ventura [1] present an updated survey of published paper of year 2013. Authors are well-known contributors in field of EDM. Paper provides current state of the art by reviewing publications, key milestones, educational environments, specific tools, and free available datasets for education. Authors have also discussed newly coined terms: academic analytics, teaching analytics, data-driven education, data-driven decision-making in education, big data education, and education data science. Hanan et al. [2] present a detailed survey and study emphasizing that certain EDM and LA techniques could be successfully used in higher education. EDM and LA techniques could be used by academia to prepare student-focused strategies. EDM and LA could be used to provide required tools to institutions for continuous improvement of students. Said et al. [3] present an objective of examining the role of data mining in education in past. It also focuses the recent trends in education field with data mining techniques. Paper also reviews the likelihood of employing machine learning techniques in education domain. Advantages of data mining to be used in education field are narrated by Alisa [4]. Paper gives a detailed survey about methods, process, and benefits with applications of education data mining.

Important analytics related to experimentation on data gathered from over 2000 college students is depicted by Renzhe et al. [5]. Study focuses on examination of utility of institutional data, learning management system (LMS) data, and survey data for fairly and accurately predicting long-term and short-term student success. Analysis shows that institutional and LMS data is having good predictive power in comparison with survey data. Paper further focuses on need of more robust techniques to find out so that any biases occurred in observation could be eliminated. Paper employed three classification algorithms for calculating accuracy, SVM, logistic regression and random forest. Amirah et al. [6] present analysis for prediction of student performance in context of Malaysia. Main objective of the study is to provide an overview on data mining techniques used to predict student performance. Paper also focuses on how prediction algorithms could be used to find out important attributes in student data. Paper concludes with analysis that neural network and decision tree are two methods highly used by researchers for predicting student performance. An experimental study of three well-known data mining techniques (decision tree, random forest, and naïve Bayes) on two open-source datasets is studied by Ferda [7]. Results show that data mining methods are effective for student performance prediction task. Tismy et al. [8] proposes a web-based system which uses

naïve Bayes mining technique to extract useful information. Experiment includes 700 students with 19 features. Results prove that naïve Bayes method gives more accuracy over other mining methods. Future academic performance of applicant of master of data science program is assessed by Yijun et al. [9]. For this, study has used historical data of students like admission data, grade data, and school ranking. Study uses different mining algorithms to distinguish between students who will perform well and others who will perform poor. Analysis of the study could be well used in the future admission procedures. Amjad [10] explores multiple factors theoretically assumed to affect students' performance in higher education. Study finds a qualitative model which best classifies and predicts the students' performance based on related social and personal factors. Authors have used Weka tool for experimentation purpose and considered decision tree and naïve Bayes mining methods for getting results. A classification model to predict student performance using deep learning is developed by Guo et al. [11]. Proposed model is trained on large real-world students' dataset. Experimental results show that proposed model is effective and can be used into academic pre-warning mechanism.

Hang et al. [12] present a framework of assessing risks of students drop out from online courses. Study considers both offline and online factors around k-12 students. It addresses challenges of multiple modalities, length variability, time sensitivity, and data imbalance. Results show that proposed student dropout framework gives efficient results. Building models to find the characteristics and features involved in context-agnostic engagement is focused by Sahan et al. [13]. Learner engagement is considered important in the study. The idea of building a predictive model for population-based engagement in education is investigated in the paper. To achieve the task, authors have introduced a large and novel video lectures dataset. Testing of different strategies for quantifying learners' engagement is also studied. Results show that proposed model gives promising results and can be incorporated in open educational resources as recommendation system as well. Weijie and Zachary [14] provides most comprehensive evaluation of data sources, models, and their performance on downstream prediction tasks. Authors have investigated different data sources like enrollment histories and grades, course catalog descriptions, and course syllabi from LMS. Authors have considered different representation models like bag-of-words, multifactor course2vec, LSTM-learned representations, and attributed multiplex heterogeneous network embeddings. Course similarity, enrollment prediction, grade prediction, prerequisite prediction, and average enrollment prediction tasks are addressed in the paper. Useful results are discussed and concluded. Palwinder and Kamaljit [15] present data collection, data cleaning, data mining, and prediction of students' performance tasks. Paper provides a detailed survey of EDM including EDM tools also.

Sultan et al. [16] present an innovative data mining technique to understand and summarize the information of Oman's education data generated from the ministry of education Oman "Education portal". Authors use k-means clustering technique to determine students' profiles. Findings of study show the applicability of k-means technique for profiling of students allowing for better understanding of students' behavior and their academic performance. An approach which first performs cluster

analysis by organizing collections of patterns into groups based on students' behavior similarity using course material is proposed in [17] by Snjezana. Decision tree technique is used to generate representation for decision-making. Decision tree provides deeper understanding of how students learn. Doipayan et al. [18] investigate the use of clustering techniques to identify learner types in Massive Open Online Courses (MOOCs). K-means clustering technique is used to identify learner type in MOOC. Authors present a method to apply k-means algorithm for learner type identification in highly technical and advanced MOOC. Investigation of groups of learners thus achieved by clustering technique is done, and distinctness is observed. Four groups of learners are identified as fully engaged learners, consistent viewers, sporadic learners, and one-week engaged learners. Survey of different clustering techniques as applied in EDM is narrated in [19]. A review and classification of different contributions in the area of EDM are studied and presented. Clustering techniques and how they are applied in educational context are investigated. Clustering [20] portrays how the clustering techniques classify students in well-defined clusters. Research paper focuses on application of clustering in EDM done by researchers. It endows academicians to estimate their students' capabilities and follow up by forming a new system entry.

Siqian et al. [21] present knowledge modeling challenge in EDM. Paper presents student knowledge model that can capture knowledge growth as a result of learning from a diverse set of learning materials. Proposed multi-view knowledge model is evaluated by authors and is concluded that it can give efficient results. An unsupervised approach to build precedence graph of similar MOOCs, where nodes are clusters of lectures with similar content and edges depict alternative precedence relationships, is proposed in [22]. Results show that proposed approach of PCK-means combined with pairwise constraints outperforms k-means clustering algorithm on different parameters. The methods for automatically identifying recommended textbook materials those are most suitable and appropriate to student are explored in [23]. Experiments include incorporating students' current knowledge state on domain concepts associated with activity to recommend personalized remedial section. Results show that incorporating knowledge states can significantly improve quality of recommendations as compared to traditional content-based recommendations. Problem of modeling of early prediction for at-risk students is discussed in [24]. Paper proposes a solution using only students' interactions on virtual learning environment of Brazilian distance learning technical high school. To maximize results, an elitist genetic algorithm is developed. Results prove that suggested model is efficient in early prediction of students at risk of drop out. Paper also concludes that application of genetic algorithm to the tuning of hyperparameters classifiers can improve their performance in comparison with other techniques. Song et al. [25] propose a novel reinforcement learning-based long-short-term rewards framework for critical decision identification. Tutoring system datasets show that proposed framework indeed identifies critical decisions. Furthermore, academicians can take full advantage of proposed framework by implementing critical decisions. A method of discovering and redacting private information in education context is presented in [26]. Proposed method utilizes set operations to restrict the list of words that might be private which are then confirmed as private or non-private via manual annotations of machine

learning techniques. Proposed method is tested on two online course datasets with ensemble machine learning model giving good results.

Problem of university enrollment management strategies planning is focused in [27]. In the study, data of large public university is used to increase student enrollment. In proposed work, at first, machine learning classifier is used to predict enrollment of admitted first-year first-time students. Secondly, results of first step are then used with genetic algorithm to optimize scholarship disbursement. Proposed model is proved successful in real-world as well as on practical results also. EDM on educational big data mining algorithms' study is presented in [28]. It analyzes relevant elements of EDM and introduces big data technology on requirements of education applications. It introduces common educational big data mining algorithms and their applications and finally discussed development trend of educational big data mining algorithms. Christian et al. [29] Review describes affordances and applications of micro-level, meso-level, and macro-level big data. It also analyzes challenges of accessing, analyzing, and using big data. The challenges include balancing data privacy-protection with data sharing and research, training researchers in educational data science methods, and navigating tension between explanation and prediction. To get potential benefits of education data mining, these challenges are worth addressable.

2.2 Integrated Postsecondary Education Data System (IPEDS)

Integrated Postsecondary Education Data System (IPEDS) [30] is a system of US Department established for reviewing and funding education institutes of various states of USA. The National Center for Education Statistics (NCES) [31] is the primary federal entity for collecting, analyzing, and reporting data related to education in the USA and other nations. IPEDS is a useful system of NCES. The Integrated Postsecondary Education Data System surveys approximately 7500 postsecondary institutions, including universities and colleges, as well as institutions offering technical and vocational education beyond the high school level. IPEDS, which began in 1986, replaced the Higher Education General Information Survey (HEGIS). IPEDS consists of nine integrated components that obtain information on who provides postsecondary education (institutions), who participates in it and completes it (students), what programs are offered, and what programs are completed. It gives data of both the human and financial resources involved in the provision of institutionally based postsecondary education.

Research is carried out on IPEDS data which is mainly focused on statistical and descriptive aspect of contents of IPEDS. Objective of developing models for IPEDS data that calculates predicted graduation rates is presented in [32]. CART data mining technique is used to predict graduation rates for different college models developed. Results show the difference between actual and predicted graduation rate values and

provide useful analysis. [33] determines if IPEDS data variables were appropriate proxies for the USNWR factors in regard to predicting peer assessment score and rank. Paper adopts methodology of descriptive statistics with correlation and regression analysis. Major findings show that IPEDS variables proxies are correlated with USNWR variables as well. How transferred students are defined and reported, both to IPEDS and other resources, and how IPEDS could modify its current collection to learn more about transfer students are discussed in [34]. Authors have conducted interviews to gather input data. Descriptive analysis is carried out which shows output in terms of major and minor cases of importance of targeted data. Factors for students who initially take admissions, studied for one year and then transfer out to other institutes, are investigated in [35]. To carry out study, principle component analysis followed by various data mining techniques artificial neural network, decision tree, linear regression (LR), support vector machine (SVM), and random forest is used to find ROC and AUC. According to ROC and AUC, both SVM and LR have highest accuracy, while decision tree was having least. Above literature survey shows useful work in area of education data mining having focus on IPEDS. Traditional data mining techniques are used for research.

3 IPEDS Dataset

IPEDS dataset [30] is an open repository containing many years' data related to educational institutions. IPEDS is a large and complex system of data. IPEDS is a comprehensive federal database with vast amounts of data about all higher educational institutions. Data source is IPEDS website which is available for freely downloading the data. Data could be seen for various years, e.g., 2004–2005, 2005–2006. Each dataset has three files within it: (1) Access database file containing values about various fields/features of institutions, (2) Excel file which contains Metadata, and (3) Word file for information related to final release version of the year. Access file contains *n* number of tables. Tables are related to different survey components which can be understood by referencing Metadata Excel file. Metadata of IPEDS contains (1) Introduction, (2) Tables' information, (3) Variable information, and (4) Value set information and Metadata definitions. Metadata information is vital to understand for any researcher before using IPEDS data for analysis of their problem. Tables of IPEDS dataset are connected with one another involving important connection of data. Every variable/feature of each table may have many values indicating each useful educational parameter. IPEDS data is summary data at institutional level, and it does not contain per student record information. Careful analysis of tables and Metadata files reveals that some files may have one record per institution, whereas other files could have multiple records per institute.

Algorithmic Framework for Dataset preparation, a research and analytical problem P

    INPUT:

- A set of educational data having X entities.
- Type of prediction task at hand.

  PROCEDURE:

1. Data collection: Collecting x targeted entity (depends on P) data.
2. Feature Analysis: Studying and determining features of data.
   2.1 Meta data Analysis

3. Feature Extraction: Extracting features related to problem P from multiple modules m of x.
   3.1 Perform feature extraction operations.

4. Data Integration: Integrating subparts received as output of step no. 3.
   4.1 Data Transformation
   4.2 Vertical-Horizontal Integration

  OUTPUT:

- Dataset for a problem P

Fig. 1 Algorithmic dataset preparation framework

4 Dataset Preparation Framework

An algorithmic framework for extraction and preparation of suitable dataset for a given problem from a huge data repository is depicted in Fig. 1. Input for dataset preparation framework includes a large data resource X including x entities and a well-defined educational problem P at hand. Data collection regarding defined problem (e.g., for how many years' student cohort researcher wants to pursue research) should be first step to carry out. Each defined problem requires its own feature set of its domain. It is important for a researcher to first determine what input variables are vital for the study undertaken. Next step is feature analysis in which Metadata understanding is necessary. After Metadata analysis only, features could be determined. Feature extraction could be regarded as the most important step. Feature extraction asks for a careful series of operations to perform. If Metadata is well understood, relations of modules and variables could be pulled out in right context of P. Output of above step leads to final step of integration of all extracted variables/features leading to a final dataset related to P. Integration involves any needed data transformation along with horizontal and vertical integration where column by column data is matched and horizontally put together creating a single large data frame.

5 A Case Study: Institute Graduation Rate Prediction Problem

Proposed framework is applied on Institute Graduation Rate (IGR) prediction problem to realize the effectiveness and applicability of the framework. Informally, IGR prediction problem [36] could be defined as:

Given training samples $(X_i, z_i) \ldots (X_n, z_n)$ where X_i is the feature vector for institute a, and A is the set of n institutes where $A = \{a_1, a_2, a_3, \ldots, a_n\}$. The $X_i \in R$ where R is feature set containing total number of features and z_i is academic performance status. To predict the performance of an institute, the following prediction function is proposed:

$$z_i = F(X) \tag{1}$$

Learning Task: Its aim is to learn a predictive function F or alternatively to predict academic performance. It is written as:

$$Z = F(X)'' \tag{2}$$

Proposed framework is applied step by step to achieve desired output from a large dataset containing data related to IGR prediction problem. The flowchart shown in Fig. 2 illustrates the framework for data preparation for IGR prediction problem from IPEDS dataset. Graduation rate prediction task is vital for any institute. Correctly predicted graduation rates can determine institute's future direction of further academic activities. Low graduation rates prediction may indicate improper academic planning. Good graduation rates determine which institutional factors are important and influence students to get graduation. Analysis of Institute Graduation Rate may give institutions a feasible direction to pursue improvement in certain academic components or modules.

5.1 Data Collection

For presented research, IPEDS dataset is downloaded from NCES–IPEDS website [30, 31]. Different years' cohort data is available on IPEDS. For considered case study, a total of 8 years sub-cohorts is considered, from year 2004–2011. Target student cohort for research is 4-year graduation rate of the sub-cohorts of full-time, first-time students seeking a bachelor's or equivalent degree for 4-year institutions.
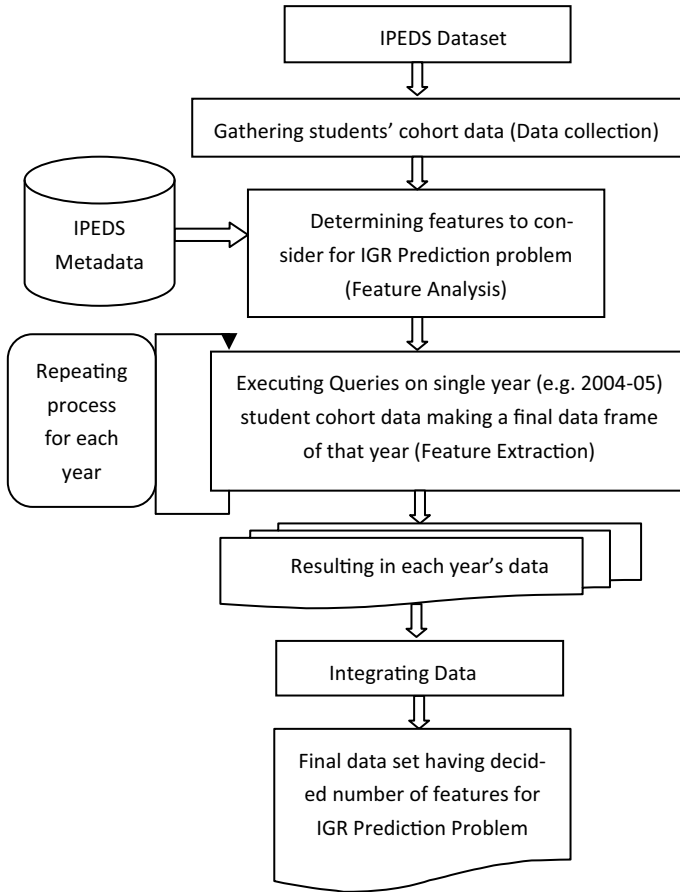
Fig. 2 Illustration of dataset preparation framework for IGR prediction problem

5.2 Feature Analysis and Metadata Analysis

To perform feature analysis, it is important to understand for the analyst or researcher that which features are vital for proposed problem. For IGR prediction problem, potential features were first listed down and then it was matched with dataset for availability. For this purpose, to study, Metadata file was necessary. Metadata files of IPEDS system consists of all tables, its variables/features, and value sets of variables. At first place, all Metadata were studied carefully. Tables were analyzed, and features were studied. After careful investigation, 143 features were selected manually from dataset. Table 1 presents some selected features for IGR prediction problem.

Table 1 Features selected for IGR prediction

Feature selected	Feature description	Survey component of feature selected
Chg1ay3	Published in-district tuition and fees	Institute characteristics
Chg5ay3	On campus, room, and board	
Chg9ay3	Off campus (with family) and other expenses	
SLO3	Distance learning opportunities	
SLO7	Weekend/evening college	
LIBAC	Library facilities at institution	
BOARDAMT	Typical board charge for academic year	
SGRNT_N	Number receiving state/local grant aid	Number receiving state/local grant aid
FTPT	Full-and part-time status (Employees)	Human resource
FSTAT	Faculty status	
OPRFSTF	Other professional FTE staff	
BENTYPE	Fringe benefits	

5.3 Feature Extraction Operations

IPEDS dataset has many tables where each institute is identified by a unique primary key. Every survey component which contains n number of tables has m number of attributes/features and corresponding instances. The overall IPEDS dataset thus possesses thousands of features and millions of instances. To extract decided features with data, several query operations were fired on different tables by JOIN operation. JOIN operation is used to join multiple tables and fetching details those exist in concerned multiple tables. Such 68 JOIN queries were fired, and features data were extracted. For each year, a final data frame was created by firing queries in sequence. Following queries are few examples of 2004 student cohort.

Query 1:
SELECT GR2010.UNITID, GR2010.GRTOTLT, GR2010.GRTOTLM, GR2010.GRTOTLW, DRVGR2010.GBA4RTT, DRVGR2010.GBATRRT INTO Query1 FROM DRVGR2010, GR2010 WHERE (((DRVGR2010.UNITID) = [GR2010].[UNITID]) AND ((GR2010.GRTYPE) = 13));

Query 2:
SELECT IC2004_PY.UNITID, IC2004_PY.CHG1PY3, IC2004_PY.CHG4PY3, IC2004_PY.CHG5PY3, IC2004_PY.CHG6PY3, IC2004_PY.CHG7PY3, IC2004_PY.CHG8PY3, IC2004_PY.CHG9PY3, IC2004_PY.CMP1PY3 INTO QUERY2.

FROM IC2004_PY;

Query 3:
SELECT   Query2.*,   IC2004.ENRLM,   IC2004.ENRLW,   IC2004.ENRLT,
IC2004.APPLCN, IC2004.ADMSSN, IC2004.CNTLAFFI, IC2004.PUBPRIME,
IC2004.PUBSECON,   IC2004.RELAFFIL,   IC2004.LEVEL5,
IC2004.OPENADMP,   IC2004.ENRLFTM,   IC2004.ENRLFTW,
IC2004.ENRLPTM, IC2004.ENRLPTW, IC2004.SATPCT, IC2004.ACTPCT,
IC2004.SLO3, IC2004.SLO5, IC2004.SLO51, IC2004.SLO52, IC2004.SLO53,
IC2004.SLO6,   IC2004.SLO7,   IC2004.STUSRV1,   IC2004.STUSRV2,
IC2004.STUSRV3,   IC2004.STUSRV4,   IC2004.STUSRV8,   IC2004.LIBFAC,
IC2004.ATHASSOC,   IC2004.ASSOC1,   IC2004.ASSOC2,   IC2004.ASSOC3,
IC2004.ASSOC4,   IC2004.ASSOC5,   IC2004.SPORT1,   IC2004.CONFNO1,
IC2004.SPORT2,   IC2004.CONFNO2,   IC2004.SPORT3,   IC2004.CONFNO3,
IC2004.SPORT4,   IC2004.CONFNO4,   IC2004.CALSYS,   IC2004.APFEE,
IC2004.TUITVARY,   IC2004.ROOM,   IC2004.ROOMCAP,   IC2004.BOARD,
IC2004.MEALSWK,   IC2004.ROOMAMT,   IC2004.BOARDAMT,
IC2004.RMBRDAMT,   IC2004.ENRLFT,   IC2004.ENRLPT,   IC2004.PT_FP,
IC2004.ALLONCAM   INTO   Query3   FROM   IC2004,   Query2   WHERE
((((IC2004.UNITID) = [Query2].[UNITID]));

Above queries extract features as needed for further analysis from dataset tables by executing JOIN operations. Apart from JOIN queries, importing tables are required from one database to another. Researcher may find that few features available in one data base may be absent in another data base tables creating nulls in final data frame.

5.4   Data Integration

5.4.1   Data Transformation

Data transformation is needed in terms of file type conversion if any. Data base files are needed to convert into other file formats for further data mining techniques' applications. Researchers could convert database files into any other format which is of their research interest.

5.4.2   Vertical and Horizontal Integration

Section 5.3 creates multiple data frames for each year student cohort. Each year data frame consisted of around 1000 instances and around 100 features. To make a single large data frame, one by one, each data frame was merged into second data frame. In this operation, columns were matched resulting in vertical integration. Data frame data was put horizontally beneath another data frame resulting in horizontal integration. Output of final step was a large data frame having 11290 rows and

Table 2 Prepared dataset statistics and comparison with existing datasets

Dataset name	Dataset Source	Method of data retrieval	Instances and features	Associated task	Reference No
IGR prediction dataset	IPEDS	Following dataset preparation framework	11290 × 142	Regression	Dataset prepared in this work
Students' performance evaluation dataset by optimal group formation	MCA students' results studying at college	On campus	56 × 2	Optimal group formation	Devasenathipathi and Modi [37]
Student performance prediction dataset	LON-CAPA [38]	From LON-CAPA datasets	227 × 6	Classification	Minaei-Bidgoli and William [39]
Students' failure association analysis dataset	Istanbul, Egypt, IMKB Vocational Commerce High School	On campus	28 × 74	Association rule mining	Buldu and Ucgun [40]
Students degree completion dataset	Different universities of Pakistan	On campus	776 × 33	Classification	Daud et al. [41]
Student university performance prediction dataset	Under UNWE project, Dataset of Bulgarian university is used	CRISP-DM	10330 × 20	Classification	Kabakchieva [42]

143 columns. Table 2 presents prepared dataset statistics. A comparison with other existing datasets is also described. It can be analyzed by the given statistics that by following presented dataset preparation framework step by step, a large dataset could be created for a specific definition task. Prepared dataset can be also used for classification task by converting response variable into categorical one.

6 Conclusion

Objective of this study was to present and demonstrate a framework of dataset preparation for education data mining. Education domain generates large amount of digital data every year due to online teaching and learning practices. Many institutions carry

out activities which are digital. Apart from this, students' personal and academic data is also stored. But the challenge lies in getting associated dataset for any education researcher's problem. In this paper, a dataset preparation framework is proposed. A case study for the proposed framework is also given to show the effectiveness and practical applicability of framework. Researchers in education domain can be benefitted by this study, and they can create their own problem-specific dataset for a suitable research purpose.

References

1. Romero C, Ventura S (2020) Educational data mining and learning analytics: an updated survey. WIREs Data Min Knowl Discov 10(e1355):1–21
2. Hanan A, Hosam A, Wan MF (2019) Education data mining and learning analytics for 21st century higher education: a review and synthesis. Telematics Inform 37:13–49
3. Said A, Muhammad A, Ashraf E, Khaled S (2020) Mining in educational data: review and future directions. Springer Nature Switzerland AG, pp 92–102
4. Alisa B (2020) Benefits of educational data mining. J Int Bus Res Mark 6(1)
5. Renzhe Y et al (2020) Towards accurate and fair prediction of college success: evaluating different sources of student data. In: Proceedings of the 13th international conference on educational data mining. ERIC, pp 292–301
6. Amirah MS, Wahidah H, Abdul NR (2015) A review on predicting student's performance using data mining techniques. Procedia Comput Sci 72:414–422
7. Ferda U (2020) Data mining-methods, applications and systems. IntechOpen
8. Tismy D, Vinushree TP, Vinayak H (2016) Prediction of students performance using educational data mining. In: Proceedings of international conference on data mining and advanced computing. IEEE, Ernakulam, India, pp 1–5
9. Yijun Z et al (2020) Predicting student performance in a master of data science program using admission data. In: Proceedings of the 13th international conference on educational data mining. ERIC, pp 325–333
10. Amjad AS (2015) Educational data mining & students' performance prediction. Int J Adv Comput Sci Appl 7(5):212–220
11. Guo B et al (2015) Predicting students performance in educational data mining. In: Proceedings of international symposium on educational technology. IEEE, Wuhan, China, pp 125–128
12. Hang Li, Wenbiao D, Zitao L (2020) Identifying at-risk K-12 students in multimodal online environments: a machine learning approach. In: Proceedings of the 13th international conference on educational data mining. ERIC, pp 137–147
13. Sahan B et al (2020) Predicting engagement in video lectures. In: Proceedings of the 13th international conference on educational data mining. ERIC, pp 50–60
14. Weijie J, Zachary A (2020) Evaluating sources of course information and models of representation on a variety of institutional prediction tasks. In: Proceedings of the 13th international conference on educational data mining. ERIC, pp 115–125
15. Palwinder KM, Kamaljit SS (2020) Educational data mining tools and framework for predicting students academic performance. Int J Adv Sci Technol 29(10S):2525–2533
16. Sultan JSA, Izwan NMS, Jastini MJ (2017) Profiling oman education data using data mining approach. In: Proceedings of AIP conference proceedings. AIP, pp 1–6
17. Snjezana K (2020) Educational data mining using cluster analysis and decision tree technique: a case study. Int J Eng Bus Manage 12:1–9
18. Doipayan R et al (2017) Synthesis of clustering techniques in educational data mining. In: American society for engineering education, pp 1–20

19. Ashish D, Saeed A, Maizatul AI, Hamidreza M (2015) Clustering algorithms applied in educational data mining. Int J Inf Electron Eng 5(2):112–116
20. Anuradha C, Velmurugan T, Anandavally R (2015) Clustering algorithms in educational data mining: a review. Int J Power Control Comput 7(1):47–52
21. Siqian Z, Chunpai W, Shaghayegh S (2020) Modelling knowledge acquisition from multiple learning resource types. In: Proceedings of the 13th international conference on educational data mining. ERIC, pp 313–324
22. Fareedah A, Abdussalam A (2020) Unsupervised approach for modelling content structures in MOOCs. In: Proceedings of the 13th international conference on educational data mining. ERIC, pp 18–28
23. Khushboo T, Lei Z, Daqing H, Peter B (2020) Recommending remedial readings using student knowledge state. In: Proceedings of the 13th international conference on educational data mining. ERIC, pp 233–244
24. Emanuel MQ et al (2020) A learning analytics approach to identify students at risk of dropout: a case study with a technical distance education course. Appl Sci 10(3998):1–20
25. Song J, Guojing Z, Tiffany B, Min C (2020) Pick the moment: identifying critical pedagogical decisions using long-short term rewards. In: Proceedings of the 13th international conference on educational data mining. ERIC, pp 126–136
26. Nigel B, Wes CR, Luc P, Najmuddin S (2020) Hello, [REDACTED]: protecting student privacy in analyses of online discussion forums. In: Proceedings of the 13th international conference on educational data mining. ERIC, pp 39–49
27. Lovenoor A, Dev N, Jevin W (2020) Increasing enrolment by optimizing scholarship allocation using machine learning and genetic algorithms. In: Proceedings of the 13th international conference on educational data mining. ERIC, pp 29–38
28. Ji L, Xiao Z, Lei Z (2020) Research on the algorithm of education data mining based on big data. In: Proceedings of the IEEE 2nd international conference on computer science and educational informatization. IEEE Xplore, Xinxiang, China, pp 344–350
29. Christian F et al (2020) Big data in education. SAGE
30. IPEDS. Retrieved from https://nces.ed.gov/ipeds/. Accessed on 21 Jun 2021
31. NCES. Retrieved from https://nces.ed.gov/. Accessed on 16 May 2021
32. Bailey BL (2006) Let the data talk: developing models to explain IPEDS graduation rates' data. Wiley Inter Science—special issue: data mining in action case studies of enrollment management 131:101–115
33. Angela EH, William FP (2017) Predicting U.S. news and world report ranking of regional universities in the south using public data. School of Education, Colorado State University, Ph. D. diss.
34. Miller A, Clery S, Topper A (2018) Assessing the capacity of IPEDS to collect transfer student data. Project report, NPEC, Coffey Consulting
35. Whitlock JL (2018) Using data science and predictive analytics to understand 4-year university student churn. Ph. D. diss., Department of East Educational Leadership and Policy Analysis, East Tennessee, State University
36. Mehta MH, Chauhan NC, Gokhale A (2021) Predicting institute graduation rate with genetic algorithm assisted regression for education data mining. ICTACT J Soft Comput 11(2):2266–2278
37. Devasenathipathi N, Modi N (2011) Applying GA to improve students' academic performance by group formation. Int J Data Warehouse Min 1(2):142–146
38. LON-CAPA. Retrieved from http://lon-capa.org. Accessed on 17 Sep 2021
39. Minaei-Bidgoli B, William F (2003) Using genetic algorithms for data mining optimization in an educational web-based system. In: Proceedings of international conference on genetic and evolutionary computational. Springer-Verlag Berlin Heidelberg, Chicago, IL, USA, pp 2252–2263
40. Buldu A, Ucgun K (2010) Data mining application on students' data. Procedia Soc Behav Sci 2(2):5251–5259

41. Daud A et al (2017) Predicting student performance using advanced learning analytics. In: Proceedings of the international conference on world wide web companion. ACM, Perth, Australia, pp 415–421
42. Kabakchieva D (2013) Predicting student performance by using data mining methods for classification. Cybern Inf Technol 13(1):61–72

Generative Adversarial Network-Based Improved Progressive Approach for Image Super-Resolution: ImProSRGAN

Vishal Chudasama, Heena Patel, Kalpesh Prajapati, Anjali Sarvaiya, and Kishor Upla

Abstract Recently, convolutional neural networks (CNNs) have been explored to achieve exceptional performance on super-resolution (SR) in terms of distortion metrics. In these methods, pixel-based loss functions have been employed to optimize their networks leading to overly smooth blurry solutions. In contrast, a generative adversarial network (GAN) has the proficiency to bring out perceptually better SR solutions. In the case of larger upscaling factors, some degradations are still discovered in the SR observations that can be reduced by increasing the number of convolution layers. However, such approach tends to increase the number of trainable parameters and additionally provides a lot of burden on resources which leads it to be unavailable for many real-world tasks. Here, we propose an improved progressive approach for SISR using GAN (i.e. ImProSRGAN). The potency of the proposed model has been seen by conducting different experiments where we observe that the introduced ImProSRGAN model performs better than existing GAN-based SISR approaches even though picking up fewer training parameters.

Keywords Perceptual quality · Super-resolution · Convolution layers · Adversarial learning

1 Introduction

The methodology of estimating a high-resolution (HR) image from corresponding single low-resolution (LR) analogue is presented as single image super-resolution (SISR). This is a conventional problem in the community of computer vision that has enjoyed much attention and progress in the last few decades on many potential

V. Chudasama (✉)
Sony Research India (SRI), Bangalore, India
e-mail: vishalchudasama2188@gmail.com

H. Patel · K. Prajapati · A. Sarvaiya · K. Upla
Sardar Vallabhbhai National Institute of Technology (SVNIT), Surat, India
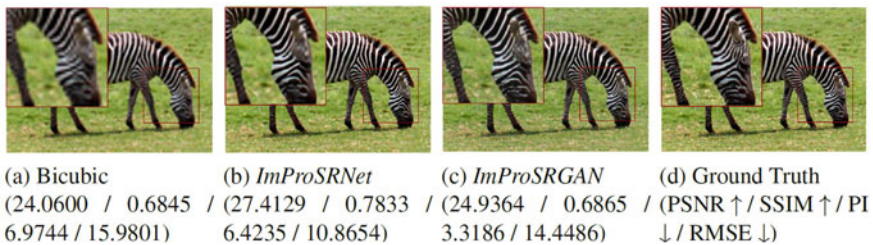e-mail: kpu@eced.svnit.ac.in

applications (i.e. such as remote sensing, object detection/recognition, face detection/recognition, medical analysis, and satellite imaging) [33, 34].

Recently, many learning-based approaches aim to reconstruct HR image via convolutional neural networks (CNNs) by minimizing a pixel-wise loss between the current estimation and the ground-truth images [13, 22]. Since downsampling operation removes the high-frequency details from the input image, the task of SISR approach is to reconstruct all those details with pixel-wise accuracy. Therefore, all the state-of-the-art models learn to obtain the mean of all possible textures in order to minimize the pixel-wise loss [2, 11, 13, 22, 37], and as a result, it increases the peak signal-to-noise ratio (PSNR) which is frequently used quality assessment measure to compare the SISR algorithms. Unfortunately, the SR result having a high PSNR value does not result in a better SR image in terms of perceptual quality [20, 31, 32]. It looks blurry and also lacks of high-frequency textures in the SR images. This can be understand from Fig. 1, where the SR result of the introduced model achieved on the Set14 data set is displayed for upscaling factor 4. The associated distortion errors (i.e. PSNR and SSIM) and perception measure (i.e. pair of root MSE (RMSE) and perceptual index (PI) are also listed at the bottom of every SR solution. Here, we employ the pair of RMSE and PI to assess the SR image's perceived quality as recommended by Blau et al. [5]. Lower PI with less RMSE values indicates SR image having better perceptual quality. In Fig. 1b, we show the SR result produced from the introduced *ImProSRNet* model (i.e. generator networks of proposed *ImProSRGAN*) where the introduced model is trained using pixel-wise (i.e. Charbonnier) loss function to get better distortion measures. As one can notice from Fig. 1b that the *ImProSRNet* method obtains higher PSNR and SSIM values with lower value of RMSE metric. However, they obtain high PI values which results the lower perceptual quality of this SR observation. This can also be validated by the visual inspection of those SR results displayed in Fig. 1b. As a result, the superior distortion metrics (RMSE, PSNR, and SSIM) do not accurately represent perceptually convincing solutions [5, 20].

Goodfellow et al. [14] initially enacted a generative adversarial network (GAN), in which the generator network seeks to deceive the discriminator network by creating realistic samples, while the discriminator network is established to discern between fake and genuine samples. However, the generator produces perceptually reason-

(a) Bicubic
(24.0600 / 0.6845 /
6.9744 / 15.9801)

(b) *ImProSRNet*
(27.4129 / 0.7833 /
6.4235 / 10.8654)

(c) *ImProSRGAN*
(24.9364 / 0.6865 /
3.3186 / 14.4486)

(d) Ground Truth
(PSNR ↑ / SSIM ↑ / PI
↓ / RMSE ↓)

Fig. 1 SR result comparison for upscaling factor × 4

able answers as a result of the combined training of both networks. [20, 24, 26, 31, 32]. In this publication, we provide a new GAN-based solution noted hereafter as *ImProSRGAN* in order to synthesize the SR results with better perception quality. The SR image produced using the introduced GAN-based model, i.e. *ImProSRGAN* is also depicted in Fig. 1c. In terms of perceptual quality, it is clear that the SR image formed using the introduced *ImProSRGAN* approach is highly comparable to the ground-truth image even it is lacking in terms of fidelity-based measure such as PSNR, SSIM, and RMSE. In this manuscript, to validate the perception quality, we utilized the perceptual index (PI) which should be low for better quality. An experimental result demonstrates that the proposed *ImProSRGAN* generates SR images with better perceptual plausible solution.

The above experiment is further extended and discussed for other data sets in the experimental Sect. 4 where the SR outcomes achieved from the introduced *ImProSRGAN* model are compared with recent GAN-based SISR solutions such as SRGAN [20], EnhanceNet-PAT [26], EUSR-PCL [6], 4PP-EUSR [7], and NatSR [27]. The results of the experiments suggest that our method shows superior performance with higher perceptual quality than SRGAN [20], EnhanceNet-PAT [26], EUSR-PCL [6], 4PP-EUSR [7] and NatSR [27] methods. The proposed approach surpassed the NatSR [27] EUSR-PCL [6] and 4PP-EUSR [7] models by having a substantially reduced number of trainable parameters.

The following are the manuscript's main contributions:

- We present *ImProSRGAN*, a progressive technique based on a computationally efficient CNN network that can provide SR results with superior high-frequency detail retention by utilizing adversarial learning.
- We present a novel residual network, i.e. ResBlock in *ImProSRNet*, i.e. the generator network of the proposed *ImProSRGAN*, which aids in learning a detailed feature from the LR observation with fewer training parameters.
- Despite having a much reduced number of training parameters, the presented ImProSRGAN approach yields state-of-the-art results in terms of perceptual vision of SR results.

The remaining of the manuscript is designed as follows. For the SISR problem, Sect. 2 offers an brief survey of different types of CNN as well as GAN-based models. The network design of the introduced model is briefly discussed in Sec. 3. Experiments for a more thorough examination of our proposed model are carried out, and the results are discussed in Sect. 4. Finally, we come to a conclusion work in Sect. 5.

2 Related Work

Numerous SISR methods have been presented in the literature to enhance the performance quality of SR images [33, 34]. Deep learning (primarily CNN)-based SISR approaches produced better SR images than conventional SISR techniques because to the availability of costly parallel technologies, such as graphics processing units

(GPUs) and the enormous volume of data. In this section, we go through the SISR approaches in detail, including CNN and GAN-based categorization.

CNN-based SISR methods: Based on the upscaling mechanism utilized in the network, CNN-based SISR algorithms can be classified as direct or progressive. Pre-upscaling and post-upscaling-based SR methods are the two types of direct methods. The LR image is first upsampled using an appropriate interpolation methodology in pre-upscaling SR algorithms, and then CNN is utilized to restore the lost high-frequency information [11, 16, 17]. All of those approaches, however, operate in SR manifold, which raises the complexity and so necessitates a considerable amount of memory. To address these problems, post-upscaling-based SR approaches have been developed, in which features are retrieved directly from LR observations and upscaled at the network's end using either transposed [12] or sub-pixel [20] convolutions. As a result, when compared to pre-upsampling-based SR approaches, the computational cost and memory requirements are lower. Many strategies in [2, 13, 19, 21, 22, 37] have been described in this area to improve the SR approach's speed and memory needs. However, in order to retrieve final SR images, these algorithms cascade the upsampling layers, resulting in checkerboard artefacts for higher upscaling values [18, 32]. Progressive upsampling-based SISR methods [18, 32], from the other hand, reconstruct the SR image in intermediate phases by executing factor 2 upscaling on the input image at a time. Since the quality of SR solutions was enhanced by utilizing a progressive upscaling technique [18, 32], the goal of this study is to use the same strategy to acquire SR data.

GAN-based SISR methods: The SR results produced by the above CNN-based SR techniques produce blurry solutions with a loss of high-frequency information [4, 35]. GAN was recently implemented in the SISR job [6, 7, 20, 24, 26, 27, 29–32] to address this constraint. The discriminator aids the generator in generating the SR solutions with more high-frequency features. Ledig et al. [20] introduced SISR with GAN (SRGAN) and established state-of-the-art performance in terms of SR outcomes with better perceptual quality. Among all of these GAN-based methods, the ProGanSR [32], ESRGAN [31], EPSR [29], and PESR [30] methods all require over 15M training parameters to quantify their SR performance, making them inappropriate for real-world scenarios. Hence, in this research work, we compare the SR outcomes with that of only those SISR methods [6, 7, 20, 26, 27] which have fewer than 7M training parameters in their network.

3   Proposed Method

Two networks are utilized in the proposed *ImProSRGAN* model: a generator and a discriminator. By delivering believable observations, the generator network attempts to deceive the discriminator network, while the discriminator network distinguishes between fake and real samples. The generator network produces perceptually plausible solutions as a result of the combined training of both networks.
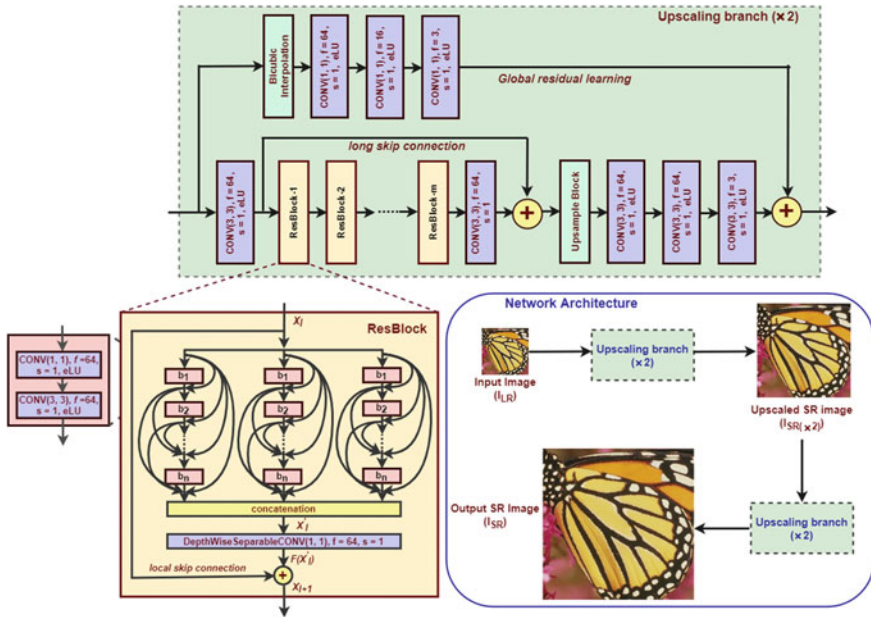
Fig. 2 Design of the introduced generator network *ImProSRNet*

Generator network: The generator network of proposed *ImProSRGAN* (i.e. *ImProS-RNet*) is shown in Fig. 2 for upscaling factor 4. Initially, the LR image would be applied to the upscaling branch, which culminates in the SR image getting upscaled by a factor of two ($I_{SR(\times 2)}$). The upscaled image $I_{SR(\times 2)}$ would then be rebuilt using the same upscaling branch as before, this time for the upscaled factor 4.

At first, the input LR image is processed through convolution operation to retrieve the features layouts from the LR image in the upscaling branch (see Fig. 2). After that, the feature layouts are processed through a succession of *m* ResBlocks. In this article, we develop a unique ResBlock that aids the proposed network in extracting more complicated features from LR data. The ResBlock's network architecture can also be visualized in Fig. 2. It comprised of $n = 6$ densely correlated convolution blocks piled in three parallel planes. It is made up $n = 6$ number of densely connected convolution blocks connected in three parallel stacks. By reusing feature outcomes that have already been learnt, the present layer is forced to learn additional detail. Each convolution block is made up of two convolutional layers, each with an exponential linear unit (eLU) [9] activation function. Finally, three distinct feature maps are combined and fed into a depthwise separable convolution [8]. In the proposed ResBlock, the local residual learning is also incorporated as a skip connection, which enhances the information flow while also assisting in the reduction of the vanishing gradient problem. We also utilize a long skip link after $m = 10$ ResBlock (see Fig. 2), bypassing the higher layer gradients and going straight to the initial convolution layer.

The upsampling block receives the output feature maps. As [23] recommended, we utilize resize convolution in this case. In the proposed method, after the resize convolution layer, we add two convolution layers to further eliminate checkerboard anomalies exhibited in SR results. In addition, a modified global residual learning (GRL) is presented, in which a bicubic interpolation layer is processed on the input LR image, followed by three 1×1 convolution layers. The network learns the identity function with the help of this type of GRL. The modified GRL also assists in training process stability and minimizes discolouration in the final image. Ultimately, the upscaling branch network delivers the SR image with a factor of 2 upscaling ($I_{\text{SR}(\times 2)}$). This upsampled SR image is processed through the same upscaling branch network once more to acquire the SR image with upscaling factor 4 (i.e. I_{SR}).

Discriminator network: The SR as well as the associated ground-truth HR image are fed into the discriminator network, which discriminate the reproduced SR image and the real ground-truth image. In Table 1, the discriminator network's network design is displayed. It seems to have eight convolution layers with a factor of two rising kernel filter spanning from 32 to 256 followed by three fully connected layers, and one sigmoid activation layer. We used the network guidelines recommended by Radford et al. [25] in the design of the discriminator network. Strided convolutions are now used to preserve the size of the feature outcomes of each convolutional layer when the number of features in the specified discriminator network is doubled. HR and SR images are sent across the discriminator network, which isolates them by assigning a probability value between 0 and 1, with a greater probability value (i.e. tends to 1) indicating the actual HR image and a lower probability value suggesting a false image produced by the generator network.

Table 1 Discriminator network of the proposed *ImProSRGAN* method

Layer	Output size	Kernel filters	Stride measure
Input (SR or HR image)	$128 \times 128 \times 3$	–	–
3×3 Conv, LeakyReLU	$128 \times 128 \times 32$	32	1
3×3 Conv, BN, LeakyReLU	$64 \times 64 \times 32$	32	2
3×3 Conv, BN, LeakyReLU	$64 \times 64 \times 64$	64	1
3×3 Conv, BN, LeakyReLU	$32 \times 32 \times 64$	64	2
3×3 Conv, BN, LeakyReLU	$32 \times 32 \times 128$	128	1
3×3 Conv, BN, LeakyReLU	$16 \times 16 \times 128$	128	2
3×3 Conv, BN, LeakyReLU	$16 \times 16 \times 256$	256	1
3×3 Conv, BN, LeakyReLU	$8 \times 8 \times 256$	256	2
Flatten	16384	–	–
Fully connected-1, LeakyReLU	$512 \times 1 \times 1$	512	–
Fully connected-2, LeakyReLU	$64 \times 1 \times 1$	64	–
Fully connected-3, Sigm	$1 \times 1 \times 1$	1	–

Here, BN and Sigm denote batch normalization and sigmoid activation functions, respectively

4   Experimental Analysis

In this section, we cover the implementation as well as the empirical studies of the proposed approach for SISR on upscaling factor $\times 4$. To examine the performance of various SISR algorithms, we deployed the benchmarking data sets called Set5, Set14, BSD100, and Urban100. The SR outcomes obtained with the presented generator network (i.e. *ImProSRNet*) are compared with the outcomes obtained with conventional CNN-based recent approaches in terms of SSIM and PSNR. However, the developed GAN-based approach, *ImProSRGAN*, is compared to recent GAN-based algorithms such as SRGAN [20], EnhanceNet-PAT [26], EUSR-PCL [6], 4PP-EUSR [7], and NatSR [27]. As recommended by Blau et al. [5], we employ the perceptual index (PI)-RMSE technique to accomplish perceptual comparison. We have also used the learned perceptual image patch similarity (LPIPS) score [36] to corroborate the SR outcomes gained from GAN-based SR methodologies. The lower the LPIPS number, the greater the perceived quality of the SR image.

In order to train our postulated networks (i.e. *ImProSRNet* and *ImProSRGAN*), we leverage the two-stage training approach given by Kim et al. [12], which helps to minimize undesirable local minima. The well-known RAISE [10] and DIV2K [1] data sets after the pre-processed through the data augmentation techniques have been used in order to train the proposed networks. At first, the *ImProSRNet* is trained using a Charbonnier loss function [3] on RAISE data set for 5×10^5 number of training iterations. Later on, the same network, *ImProSRNet*, is further trained with DIV2K training data set for a total of 1.5×10^5 iterations. After that, to train the introduced GAN model, *ImProSRGAN*, we utilize a loss function L_{SR} made up of a well-balanced combo of Charbonnier loss ($i.e. L_C$) [3], perceptual loss ($i.e. L_{\text{VGG19-C}}$) [15], and standard GAN adversarial loss (i.e. $L_{\text{adversarial}}$) [14] functions,

$$L_{\text{SR}} = 10^{-5} L_C + L_{\text{VGG19-C}} + 10^{-3} L_{\text{adversarial}}. \tag{1}$$

and it is further trained up to 4×10^5 training iterations at a learning rate value of 10^{-4}. The models are optimized using an Adam optimizer with $\beta_1 = 0.9$.

4.1   Ablation Study

Table 2 presents an analysis of presented network with numerous settings in terms of SSIM and PSNR scores on the Urban100 data set for the upscaling factor 4. Here, all of the networks are trained with same training strategy as stated previously. Table 2 also includes the appropriate trainable parameters for easier analysis.

- **Modified Global residual learning approach**: We use a conventional GRL methodology to train our suggested *ImProSRNet* model in order to see how efficient the modified GRL technique is in the proposed method. The PSNR and SSIM scores of *ImProSRNet* with modified GRL are considerably superior than those of the proposed technique with conventional GRL approach, as given in Table 2.

Table 2 Suggested *ImProSRNet* technique is compared to several situations on the Urban100 data set

Models	Number of training parameters	PSNR ↑/SSIM ↑
Conventional GRL	3547k	26.1077/0.7862
With post-upscaling	3045k	25.9598/0.7821
PReLU activation function	3561k	26.0344/0.7836
ReLU activation function	3349k	25.2435/0.7545
L_1 loss function	3548k	26.0953/0.7855
L_2 loss function	3548k	26.1188/0.7850
Proposed	3548k	**26.1312/0.7867**

The highest values are stated in bold type text here

- **Post-Upscaling approach**: To further understand the usefulness of progressive upscaling, we explicitly train our introduced *ImProSRNet* network using a post-upscaling approach. The quantitative measurement of the proposed network using a progressive upscaling technique outperforms the identical network using a post-upscaling strategy that can be accessed from the Table 2. This demonstrates the success of proposed models' progressive upsampling method.
- **Importance of eLU activation function**: To demonstrate the efficacy of the eLU activation function [9], *ImProSRNet* network further trained using PReLU and ReLU activation functions. The proposed model's SSIM and PSNR measures are superior than those of algorithms trained with ReLU and PReLU activation. (see Table 2).

4.2 Comparative Analysis

The introduced and available CNN and GAN-based SR techniques are compared quantitatively and qualitatively in this subsection. Table 3 gives the quantitative analysis of the *ImProSRNet* (i.e. generator network of proposed *ImProSRGAN*) model with other existing CNN-based SR approaches (i.e. only those that required fewer than 7M trainable parameters) in terms of fidelity errors (i.e. SSIM and PSNR). In addition to that, for a more obvious comparison, the required trainable parameters of these CNN-based SR algorithms are also listed in this table. The superior values in Table 3 are enlighted in emphasized in bold, while the second superior values are enlighted in emphasized in italic. Table 3 gives that the proposed *ImProSRNet* technique achieves greater PSNR and SSIM scores than the other models, with the exception of the current FRSR [27] model, which has comparable SR performance. However, it is worth noting that the introduced method, *ImProSRNet*, acquires this performance with significantly fewer trainable parameters than contemporary MSRN [21], SeaNet$_{Base}$ [13], and FRSR [27] methods.

Table 3 Quantitative analysis in terms of SSIM and PSNR

CNN models	Training parameters	PSNR ↑/SSIM ↑			
		Set5	Set14	BSD100	Urban100
SRCNN [11]	57k	30.48/0.7503	27.49/0.7503	26.90/0.7101	24.52/0.7221
VDSR [16]	665k	31.35/0.8838	28.02/0.7678	27.29/0.7252	25.18/0.7525
DRCN [17]	1775k	31.53/0.8854	28.03/0.7673	27.24/0.7233	25.14/0.7511
LapSRN [18]	812k	31.54/0.8866	28.09/0.7694	27.32/0.7264	25.21/0.7563
SRDenseNet [28]	2015k	32.02/0.8934	28.50/0.7782	27.53/0.7337	26.05/0.7819
SRResNet [20]	1500k	32.05/0.8910	28.53/0.7804	27.57/0.7354	26.07/0.7839
CARN [2]	1592k	32.13/0.8937	28.60/0.7806	27.58/0.7349	26.07/0.7837
MADNet [19]	1002k	32.01/0.8925	28.45/0.7781	27.47/0.7327	25.77/0.7751
proSR$_s$ [32]	3100k	32.13/0.8941	*28.62*/0.7815	27.58/0.7354	26.01/0.7830
MSRN [21]	6330k	32.07/0.8903	28.60/0.7751	27.52/0.7273	26.04/*0.7896*
SeaNet$_{Base}$ [13]	4224k	32.18/*0.8948*	28.61/0.7822	27.57/*0.7359*	26.05/*0.7896*
FRSR [27]	4800k	*32.22*/*0.8948*	**28.63**/*0.7827*	*27.60*/**0.7369**	**26.21/0.7904**
ImProSRNet	3548k	**32.26/0.8956**	**28.63**/*0.7824*	**27.61**/**0.7369**	*26.13*/0.7865
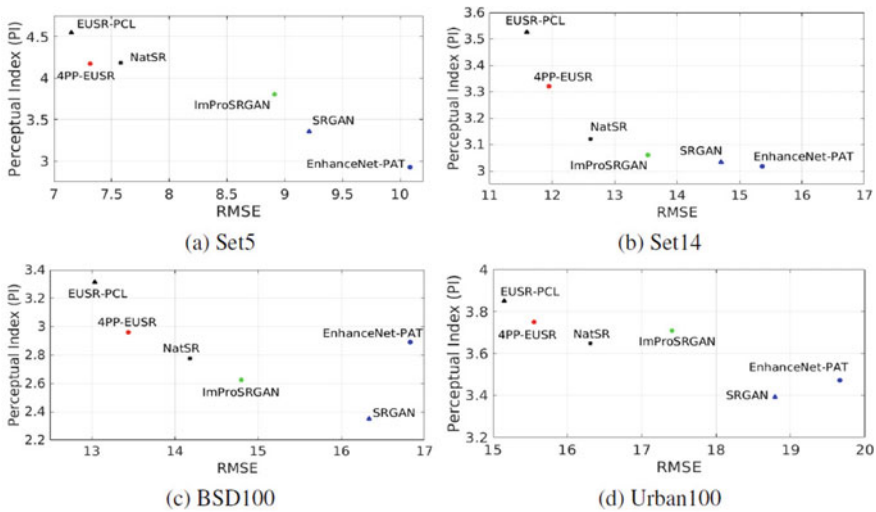
Fig. 3 Comparison of various GAN-based methods in terms of PI and RMSE for the scaling factor × 4

To evaluate the GAN-based SISR methods, we show the comparison on the pair of PI and RMSE measurements in Fig. 3 to test the perception quality of the SR images. Better perceptual quality is indicated by a lower PI and RMSE value. The graph of PI versus RMSE for different GAN-based approaches for the Set5, Set14, BSD100, and Urban100 benchmark data sets is shown in Fig. 3a–d. In comparison with the other approaches, EnhanceNet-PAT [26] has a lower PI value but a higher

RMSE value, as displayed in Fig. 3a, b. On the BSD100 and Urban100 data sets, SRGAN has a lower PI when the RMSE is high (see Fig. 3c, d. The SR images created using EnhanceNet-PAT [26] and SRGAN [20] approaches have more degradations and noise as compare to than the other models (see Figs. 5, 6, 7, and 8), indicating that lower values of both PI and RMSE are necessary to achieve higher perceptual quality. According to Fig. 3a–d, one can note that the proposed approach ImProSRGAN outperforms NatSR [27], EUSR-PCL [6], and 4PP-EUSR [7] methods with slightly lower PI values and slightly lower RMSE values; nevertheless, it outperforms SRGAN [20] and EnhanceNet-PAT [26] methods with a better PI-RMSE pair measure. In comparison with other GAN-based SISR techniques, this analysis shows that the proposed *ImProSRGAN* model produces balanced PI-RMSE values.

Zhang et al. [36] recently introduced LPIPS, a new perceptual metric that has been shown to be successful in measuring visual perception quality. A lower LPIPS score suggests a higher visual perception quality. This metric is utilized to verify the perceived quality of super-resolved images that have been synthesized by GAN-based models. For upscaling factor $\times 4$, a graph of LPIPS values obtained for various data set (i.e. Set5, Set14, BSD100, and Urban100) of several GAN models with regard to the corresponding number of trainable parameters is shown in Fig. 4. From Fig. 4a–c (i.e. Set5, Set14, and BSD100), one can see that the proposed *ImProSRGAN* model outperforms all other GAN-based solutions. For Urban100 data set, the presented *ImProSRGAN* model performs better than all other GAN methods except NatSR [27]
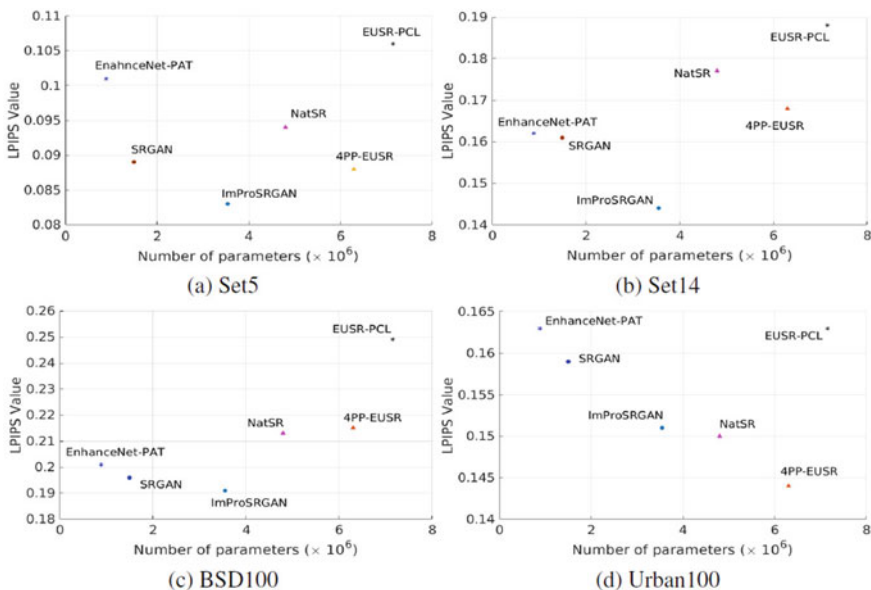
Fig. 4 Effect of perceptual metric LPIPS values of the GAN-based SR methods w.r.t. training parameters for upscaling factor 4

and 4PP-EUSR [7] models, which have slightly lower LPIPS measures; however, the introduced *ImProSRGAN* model achieves this performance with significantly fewer trainable parameters than other methods such as NatSR [27], EUSR-PCL [6], and 4PP-EUSR [7] models.

To demonstrate the qualitative improvement, we demonstrate the SR solutions for a single image of benchmark testing data sets using the presented and other existing GAN-based approaches [6, 7, 20, 26, 27], as well as the state-of-the-art RCAN [37] model based on CNN in Figs. 5, 6, 7, and 8. The corresponding LPIPS value is also stated at the bottom of each SR result for easier comparison. When compared to the RCAN [37], SRGAN [20], EnhanceNet-PAT [26], EUSR-PCL [6], 4PP-EUSR [7], and NatSR [27] appraoches, the performance of the proposed *ImProSRGAN* approach dem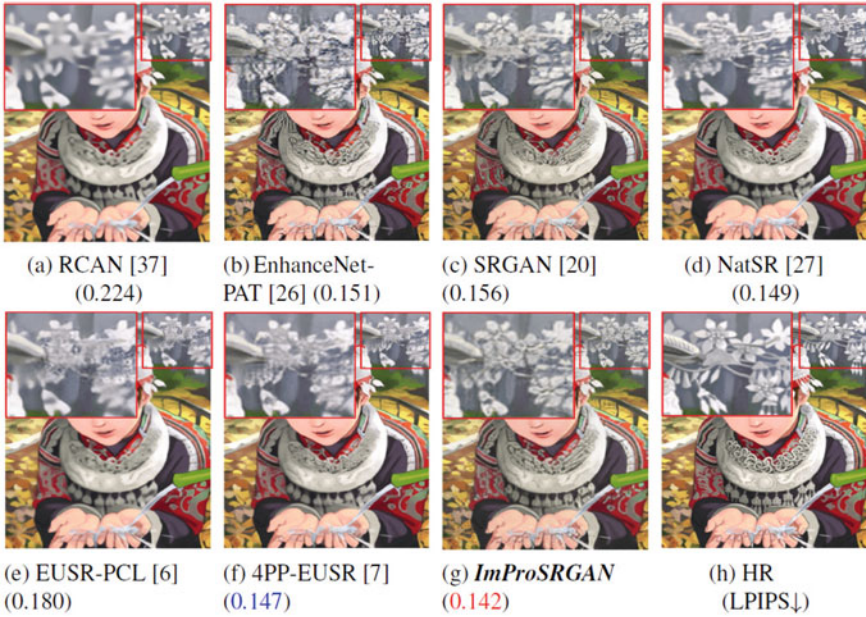onstrates better texture details (Fig. 5a–g). When compared to the same with those methodologies, its quantitative performance is likewise better in terms of LPIPS measure. Figure 6 shows the SR solutions obtained using the RCAN method and several GAN-based algorithms on a single image of the Set14 testing data set. The leaves of zoomed-in areas in the SR solution created with the *ImProSRGAN* model are closer to the ground-truth image than the leaves of other SR results. Furthermore, the proposed *ImProSRGAN* achieves better LPIPS measure than other existing SR algorithms. In addition, Fig. 7 shows the SR outcomes achieved on the BSD100 data set using several SR approaches. Similar to previous studies, the proposed *ImProSRGAN* algorithm performs superior than the other techniques in terms

(a) RCAN [37] (0.122)

(b) EnhanceNet-PAT [26] (0.086)

(c) SRGAN [20] (0.093)

(d) NatSR [27] (0.081)

(e) EUSR-PCL [6] (0.099)

(f) 4PP-EUSR [7] (0.084)

(g) *ImProSRGAN* (0.065)

(h) HR (LPIPS↓)
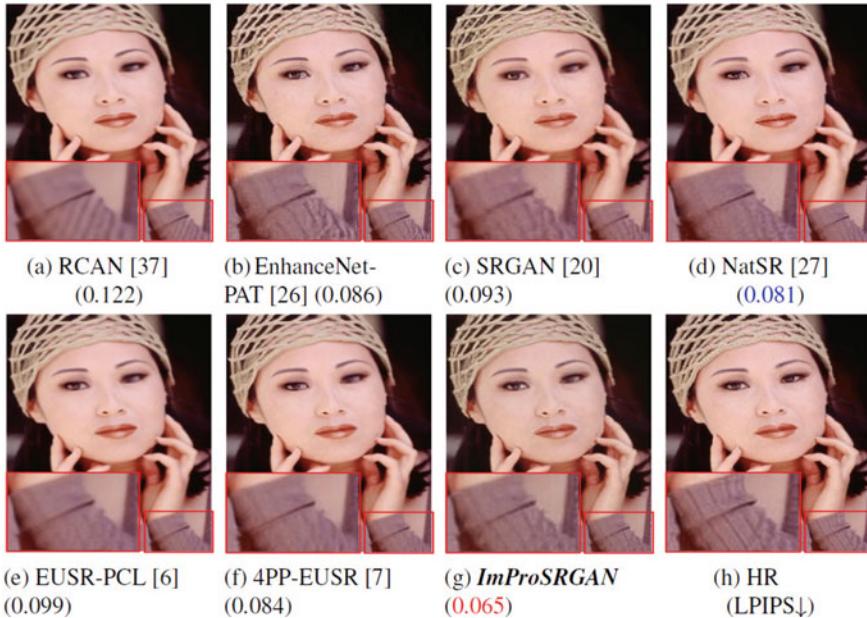
Fig. 5 Visual inspection of the SR outcomes on a representative image from the Set5 testing data set for upscaling factor 4

(a) RCAN [37] (0.224) (b) EnhanceNet-PAT [26] (0.151) (c) SRGAN [20] (0.156) (d) NatSR [27] (0.149)

(e) EUSR-PCL [6] (0.180) (f) 4PP-EUSR [7] (0.147) (g) *ImProSRGAN* (0.142) (h) HR (LPIPS↓)

Fig. 6 Visual inspection of the SR outcomes on a representative image from the Set14 testing data set for upscaling factor 4

(a) RCAN [37] (0.234) (b) EnhanceNet-PAT [26] (0.166) (c) SRGAN [20] (0.160) (d) NatSR [27] (0.158)

(e) EUSR-PCL [6] (0.165) (f) 4PP-EUSR [7] (0.148) (g) *ImProSRGAN* (0.138) (h) HR (LPIPS↓)
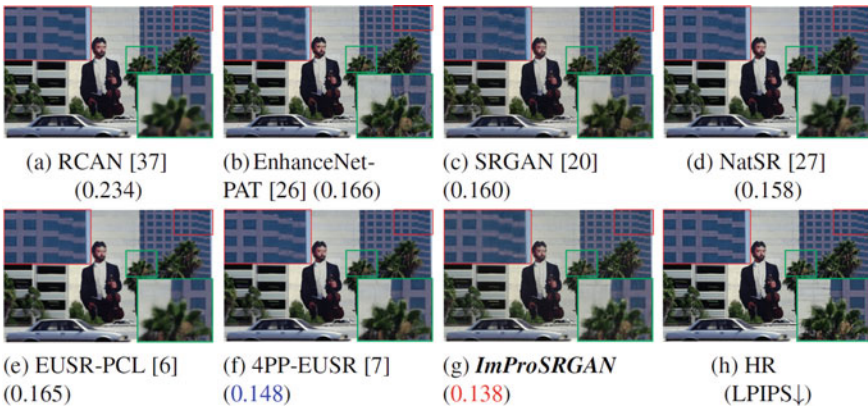
Fig. 7 Visual inspection of the SR outcomes on a representative image from the BSD100 testing data set for upscaling factor 4

Fig. 8 Visual inspection of the SR outcomes on a representative image from the Urban100 testing data set for upscaling factor 4

of quantitative performance. The SR picture created using the proposed *ImProS-RGAN* approach acquires better high-frequency information than the CNN-based RCAN model and other existing GAN-based models, according to visual observation (see tree portions and strip-lines of building regions in the zoomed-in part of Fig. 7). In the SR results of the Urban100 data set (shown at Fig. 8), the proposed *ImProSRGAN* approach demonstrates more high-frequency details with a slightly lower LPIPS measure than NatSR [27] and 4PP-EUSR [7]. However, the proposed *ImProSRGAN* model achieves this performance with around 30–75% lesser trainable parameters as compared to 4PP-EUSR [7], EUSR-PCL [6], and NatSR [27], and approximately 85% fewer training parameters than the RCAN [37] model.

5 Conclusion

In this manuscript, we introduce *ImProSRGAN* on upscaling factor $\times 4$ as a new improved progressive network for SISR using GAN. The proposed *ImProSRNet* model outperforms existing CNN-based SISR methods via achieving better SSIM and PSNR values. Even though the SR images have higher PSNR and SSIM, they have a blurry appearance. As a result, a new GAN-based approach called *ImProS-RGAN* is proposed to acquire better high-frequency information. The introduced *ImProSRGAN* is analysed by comparing it with available GAN-based approaches in terms of perception metrics (i.e. a pair of PI-RMSE measures and LPIPS) as well as visual evaluation. With superior perceptual quality and quantitative measurements, the proposed model *ImProSRGAN* surpasses existing techniques. Furthermore, compared to the other existing techniques, the proposed model sets this SR performance with significantly fewer training parameters.

References

1. Agustsson E, Timofte R (2017) Ntire 2017 challenge on single image super-resolution: dataset and study. In: IEEE conference on CVPR workshops, vol 3, p 2
2. Ahn N, Kang B, Sohn KA (2018) Fast, accurate, and lightweight super-resolution with cascading residual network. In: ECCV, pp 252–268
3. Barron JT (2017) A more general robust loss function. arXiv:1701.03077
4. Blau Y, Mechrez R, Timofte R, Michaeli T, Zelnik-Manor L (2018) The 2018 PIRM challenge on perceptual image super-resolution. ECCV 11133:334–355
5. Blau Y, Michaeli T (2018) The perception-distortion tradeoff. In: IEEE conference on CVPR, pp 6228–6237
6. Cheon M, Kim JH, Choi JH, Lee JS (2018) Generative adversarial network-based image super-resolution using perceptual content losses. In: ECCV
7. Choi JH, Kim JH, Cheon M, Lee JS (2019) Deep learning-based image super-resolution considering quantitative and perceptual quality. Neurocomputing
8. Chollet F (2017) Xception: Deep learning with depthwise separable convolutions. In: IEEE conference on CVPR, pp 1251–1258
9. Clevert DA, Unterthiner T, Hochreiter S (2015) Fast and accurate deep network learning by exponential linear units (ELUS). arXiv:1511.07289
10. Dang-Nguyen DT, Pasquini C, Conotter V, Boato G (2015) Raise: a raw images dataset for digital image forensics. In: ACM multimedia systems conference, pp 219–224
11. Dong C, Loy CC, He K, Tang X (2016) Image super-resolution using deep convolutional networks. IEEE Trans PAMI 38(2):295–307
12. Dong C, Loy CC, Tang X (2016) Accelerating the super-resolution convolutional neural network. In: ECCV, pp 391–407
13. Fang F, Li J, Zeng T (2020) Soft-edge assisted network for single image super-resolution. IEEE Trans Image Process 29:4656–4668
14. Goodfellow I, Pouget-Abadie J et al (2014) Generative adversarial nets. In: Advances in neural information processing systems, pp 2672–2680
15. Johnson J, Alahi A, Fei-Fei L (2016) Perceptual losses for real-time style transfer and super-resolution. In: ECCV. Springer, pp 694–711
16. Kim J, Lee JK, Lee KM (2016) Accurate image super-resolution using very deep convolutional networks. In: IEEE conference on CVPR, pp 1646–1654
17. Kim J, Lee JK, Lee KM (2016) Deeply-recursive convolutional network for image super-resolution. IEEE conference on CVPR, pp 1637–1645
18. Lai WS, Huang JB, Ahuja N, Yang MH (2017) Deep Laplacian pyramid networks for fast and accurate super-resolution. In: IEEE conference on CVPR
19. Lan R, Sun L, Liu Z, Lu H, Pang C, Luo X (2020) MADNet: a fast and lightweight network for single-image super resolution. IEEE Trans Cybern:1–11
20. Ledig C, Theis L et al (2017) Photo-realistic single image super-resolution using a generative adversarial network. In: IEEE conference on CVPR, pp 4681–4690
21. Li J, Fang F, Mei K, Zhang G (2018) Multi-scale residual network for image super-resolution. In: ECCV, pp 517–532
22. Lim B, Son S, Kim H, Nah S, Lee KM (2017) Enhanced deep residual networks for single image super-resolution. In: IEEE conference on CVPR workshops, pp 1132–1140
23. Odena A, Dumoulin V, Olah C (2016) Deconvolution and checkerboard artifacts. Distill 1(10):e3
24. Park SJ, Son H, Cho S, Hong KS, Lee S (2018) SRFeat: single image super-resolution with feature discrimination. In: ECCV, pp 439–455
25. Radford A, Metz L, Chintala S (2015) Unsupervised representation learning with deep convolutional generative adversarial networks. arXiv:1511.06434
26. Sajjadi MS, Schölkopf B, Hirsch M (2017) Enhancenet: single image super-resolution through automated texture synthesis. In: IEEE conference on ICCV. IEEE, pp 4501–4510

27. Soh JW, Park GY et al (2019) Natural and realistic single image super-resolution with explicit natural manifold discrimination. In: IEEE conference on CVPR, pp 8122–8131
28. Tong T, Li G, Liu X, Gao Q (2017) Image super-resolution using dense skip connections. In: IEEE conference on ICCV. IEEE, pp 4809–4817
29. Vasu S, Thekke Madam N, Rajagopalan A (2018) Analyzing perception-distortion tradeoff using enhanced perceptual super-resolution network. In: ECCV
30. Vu T, Luu TM, Yoo CD (2018) Perception-enhanced image super-resolution via relativistic generative adversarial networks. In: ECCV
31. Wang X, Yu K et al (2018) ESRGAN: enhanced super-resolution generative adversarial networks. ECCV 11133:63–79
32. Wang Y, Perazzi F et al (2018) A fully progressive approach to single-image super-resolution. In: IEEE conference on CVPR workshops
33. Wang Z, Chen J, Hoi SC (2019) Deep learning for image super-resolution: a survey. arXiv:1902.06068
34. Yang W, Zhang X, Tian Y, Wang W, Xue JH, Liao Q (2019) Deep learning for single image super-resolution: a brief review. IEEE Trans Multimedia
35. Zhang K, Gu S, Timofte R et al (2020) Ntire 2020 challenge on perceptual extreme super-resolution: methods and results. In: IEEE conference on CVPRW, pp 2045–2057
36. Zhang R, Isola P, Efros AA, Shechtman E, Wang O (2018) The unreasonable effectiveness of deep features as a perceptual metric. In: IEEE conference on CVPR, pp 586–595
37. Zhang Y, Li K, Li K, Wang L, Zhong B, Fu Y (2018) Image super-resolution using very deep residual channel attention networks. In: ECCV, pp 286–301

Community Detection Using Label Propagation Algorithm with Random Walk Approach

Hemi Patel and Jai Prakash Verma

Abstract Community detection is widely used research topic. Community detection refers to detect same type of community structure in given graph or network. Nowadays, community detection is used for many applications like fraud detection, recommendation system, segmentation, etc. In this paper, our objective is to find the label for the unlabelled node using random walk and then label propagation algorithm. In this method, labelled and unlabelled data is provided as input and then, we take random walk until we find the unlabelled node, after that label for unlabelled node is provided based on labelled node using label propagation algorithm. The output of this method will be label for unlabelled node by using this we can divide the network into community. Comparison of different algorithm for community detection is discussed in this paper.

Keywords Community detection · Community structure · Label propagation algorithm · Random walk · Semi-supervised machine learning

1 Introduction

Community detection is widely used topic nowadays because by using community detection in complex network we can able to link module and also it helps us to find the similar type of nodes in network [1]. For example, consider recommendation system of Facebook or Instagram, so in this type application, we get friend suggestion based on mutual friends. This is the one of the common applications of the community detection, we can also take the example of global post of the Instagram, and it also suggests the post according to our interest. To understand the working behind these systems first of all we have to understand the basic concept, like community structure,
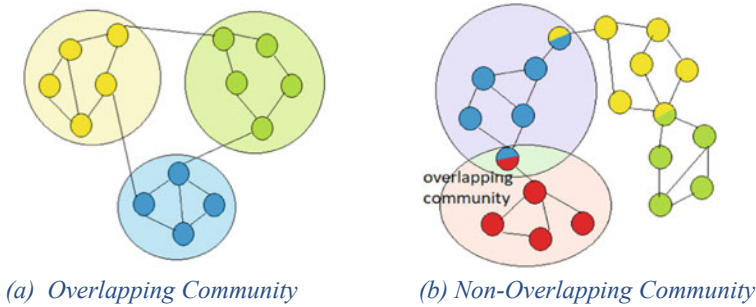
H. Patel (✉)
Cypress Semiconductor Technology India Pvt Ltd, Bangalore, India
e-mail: Hemi.Patel@infineon.com

J. P. Verma
Institute of Technology, Nirma University, Ahmedabad, India
e-mail: jaiprakash.verma@nirmauni.ac.in

(a) Overlapping Community   (b) Non-Overlapping Community

Fig. 1 Types of community detection

community detection, methods of community detection: agglomerative and divisive [2].

Community structure is most widely used term for the network. If we can group the nodes in to similar types of the nodes than this complex network is known as the community structure. In the other words, we can say that if we are able to divide the network in the group of similar types (community), then these is also known as community structure [3]. Now, the process of dividing these networks (community structure) into groups is known as the community detection [4].

In agglomerative method, we will start with the graph without edges and after similarity constraint and using different methods we will find the weight of the edge and add edge according to that, so in this method, we will add edges one by one and at last we get the graph with strongly and weakly connected edges [5]. In divisive method, we will find the weight of the edge and then based on weight we will decide if remove that edge or not. So, in this method, we will start with the whole graph and one by one remove the edge based on weight [6].

There are two types of the community structure: overlapping and non-overlapping. Overlapping means one node belongs to more than one community. In the real-world network, we have this type of the community. Non-overlapping means one node can belongs to only one community (Fig. 1).

1.1 Need Analysis

In this paper, the label propagation algorithm using random walk is introduced for community detection. In this algorithm, first random walk is taken from the one unlabelled node, until we reach to the labelled node which will act as the absorb state and the unlabelled node will labelled as label of labelled node. After random walk, the label propagation algorithm is applied, and at the end, we get matrix with the probability, based on highest probability the label is decided. The detailed discussion on this algorithm is done in the later sections. This method is known as

Table 1 Applications of community detection

Application area sub-area	Application area sub-area
Link prediction	Link prediction
Social network analysis (Instagram, Facebook, amazon)	Community detection
Recommendation system	Customer segmentation
Network summarization	Member grouping
Smart advertising	Customer segmentation
Politics (elections)	Politics (elections) evolution of influence
Health (medical)	Cancer/tumour detection Tissue/organ detection
Criminology	Criminal identification Bot detection Fraud detection

semi-supervised technique because in this method we provide the labelled as well as unlabelled data (Table 1).

This paper starts with the introduction to the community detection, Sect. 2 contains the information of literature survey, Sects. 3 and 4 contain flow chart, algorithm and related concepts, Sects. 5 and 6 contain implementation related information and last section is about future work and conclusion.

2 Related Work

This concept of community structure detection first mention by the Girvan and Newman in 2002 [1]. In this paper, they remove the edge sequentially. After this, in 2006 pones and Latapy introduced the algorithm in this they merge the two community, then comes modularity approach in this they check the quality of graph clustering and gives the rank between – 1 to 1. In community detection, basically there are five approaches which are discuss as under.

2.1 Community Detection Approaches

First approach is optimization, in which we talk about modularity which is used to describe the quality of community detection done on the community structure [7]. In this type of method, there is a predefined function which help to decide whether the partition is good or not [8]. Algorithms which used optimization approaches are discuss as under: Spin glass, fast greedy, and Leiden. Second approach used

is probabilistic-based approach, in which we decide whether node belongs to the given community based on the probability. The famous probabilistic approach is a randomized algorithm [9, 10], in which one function is define for finding the probability. Third approach is clustering methods. In these, the clustering is done on similarity measure [11]. There are predefined functions that will find the similarity, these methods are used for clustering like Markov clustering [12], rapidly Newman, Dbscan (density-based clustering algorithm) [13], etc. For the graph similarity, there are many methods like multi-scale graph convolution network (MGCN), graph convolution network (GCN), attraction force, and DD. Graph colouring is also used this approach. In this, partition is made based on similarity of two vertices and the colouring is applied [14]. Another method used for similarity is attraction force similarity which is calculated from below steps: directed and in-directed attraction force, structural similarities, attribute similarity, and attraction-force similarity. After calculating all these, we apply AFcluster algorithm for finding community [15]. Forth method is dynamic approach which include random walk that means we start random walk from any node and we stop at the labelled node which act as the absorb state and the walk will stop at that node, after that the label is decided based on probability. Another approach is, first sort nodes according to repeatability, then consider one node and find the neighbour of that with highest repeatability, after that find coefficient and trust value. Based on random walk algorithm, it will be decided that in which layer it belongs to intra or inter [16]. Last approach is heuristic approach which consists of agglomerative methods, one of the agglomerative methods is Louvain method, in this method, there are two approaches, we can find local maxima of modularity and move each node to the neighbour's community and another method is that we can aggregate all nodes and build new graph. Another example of the Louvain method is randomized Louvain method. In this method, first local maxima of modularity (quality) is calculated by moving each node to neighbour's community after that it aggregate all nodes and build new community [17, 18].

Community detection algorithm for big social network the following method is used. Monte Carlo maximum likelihood (MCML) is used for hybrid structure. There are three steps: (1) preprocessing, (2) remove weak edge, and (3) multilevel coarsening. Another algorithm is shared MCML algorithm. Steps are as under: (1) parallel preprocessing and (2) parallel multilevel coarsening. This hybrid algorithm can also be used, which contains the following steps: (1) network partitioning, (2) apply MCML, (3) renumber vertices and merge partitioning, and (4) again apply MCML algorithm [8].

2.2 Different Label Propagation Algorithm

For the community detection, label propagation is widely used method and also excellent approach. Here, we discuss about all label propagation algorithm used for community detection using different approaches which are as under. First, we

start with the basic label propagation algorithm which work in iterative form. Label propagation means labelling all the node in the graph [4]. There are three classifiers for the label prediction. Local classifier relational classifier and collective classifier which will be discussed later. There are basically five steps for this method. Starting with initialization, then take variable *t* which will store the track of the iteration then after every iteration update the value assign to the node and repeat this process until it become near equally same as neighbour and then assign the label to that node. There are various approaches for the label propagation methods which are as under: weighted label propagation—in these the algorithm is used for overlapping and non-overlapping both the community structure, the weights (using predefined function) are assign to node and based on that label is decided. Dominant label propagation: in this confidence is used to decide the label of the node. Node gravitation-based label propagation: label is decided based on node weight and node similarity. Link-based propagation algorithm: community detected based on edges. Last is graph layout-based label propagation algorithm: this algorithm divided in to two parts first is layout part and detection part. In layout part, it finds the position initialization, force generation, energy minimization, node movement, and termination condition. In second phase it will start with label initialization, then node choice label lunch, label acceptance, detection termination, and at last post-processing [19].

3 Proposed Research Work

In this paper, label propagation algorithm using random walk is proposed. By using this algorithm, label of the node is decided the objective of these algorithm is to find the label of the unlabelled node by taking random walk from unlabelled node to the labelled node. So first, it will take random walk and at last, it will apply the label propagation algorithm for label prediction.

As we can see in the block diagram (Fig. 2) first details about graph such as vertex, edges, and labels are provided as input. By using these data adjacency matrix is created, then degree matrix is calculated using adjacency matrix and then inverse of degree matrix is created and then based on these matrices transition matrix is created. This matrix is used by label propagation algorithm, and the label is decided based on output of this algorithm. Which is discussed in details in below sections.

4 Methodology and Concepts

As we discuss in above section, first we apply random walk and then we apply label propagation algorithm. So, this process completed in two parts.
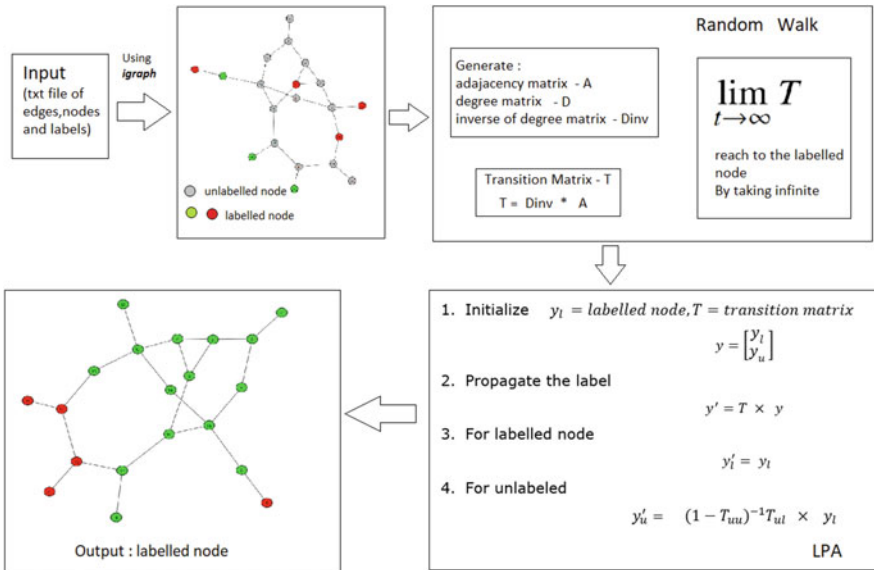
Fig. 2 Block diagram

4.1 Random Walk

First, we will discuss about random walk. In random walk, there are three steps:

- Start random walk from unlabelled node
- Keep random walk until we reach to labelled node
- Adopt the label which hit

We will start with unlabelled node and take random walk until get any labelled node which node act as the absorb state means we cannot go further. Here, the main idea is to take random walk from the node and find any labelled node, after that based on that labelled node, we have to predict the label for unlabelled node. Labelled node will act like absorb state which means we cannot go further from that node. From the below graph first, we will find the adjacency matrix and the degree matrix which are as under:

Adjacency Matrix:

$$A = \begin{bmatrix} 1 & 0 & 0 & 0 & 0 & 0 & 0 & 0 \\ 0 & 1 & 0 & 0 & 0 & 0 & 0 & 0 \\ 0 & 0 & 0 & 1 & 0 & 0 & 0 & 0 \\ 1 & 0 & 1 & 0 & 1 & 0 & 0 & 0 \\ 0 & 0 & 0 & 1 & 0 & 1 & 0 & 1 \\ 0 & 1 & 0 & 0 & 1 & 0 & 1 & 0 \\ 0 & 0 & 0 & 0 & 0 & 1 & 0 & 1 \\ 0 & 0 & 0 & 0 & 1 & 0 & 1 & 0 \end{bmatrix}$$

Degree Matrix:

$$D = \begin{bmatrix} 1 & 0 & 0 & 0 & 0 & 0 & 0 & 0 \\ 0 & 1 & 0 & 0 & 0 & 0 & 0 & 0 \\ 0 & 0 & 1 & 0 & 0 & 0 & 0 & 0 \\ 0 & 0 & 0 & 3 & 0 & 0 & 0 & 0 \\ 0 & 0 & 0 & 0 & 3 & 0 & 0 & 0 \\ 0 & 0 & 0 & 0 & 0 & 3 & 0 & 0 \\ 0 & 0 & 0 & 0 & 0 & 0 & 2 & 0 \\ 0 & 0 & 0 & 0 & 0 & 0 & 0 & 2 \end{bmatrix}$$

After obtaining A and D, we have to find inverse of D (degree matrix), now for obtaining transition matrix below equation is used
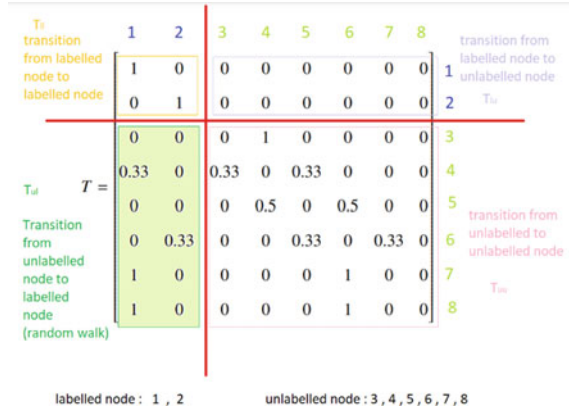
$$T = D^{-1} \times A$$

- T_{ll} Probability to get from labelled nodes to labelled nodes $= I$
- T_{lu} Probability to get from labelled nodes to unlabelled nodes $= 0$
- T_{ul} Probability to get from unlabelled nodes to labelled nodes
- T_{uu} Probability to get from unlabelled nodes to unlabelled nodes

After multiplying adjacency matrix and inverse of degree matrix, we will get transition matrix as shown in Fig. 3. As we can see in the figure, this figure divided into four parts: First is T_{ll}, which is showing the probability for transition from labelled node to labelled node, which is not important part of the matrix because we already have label for these nodes and this reason also true for part 2 which is T_{lu} (already have label for node and also it is going to the unlabelled not which is not required). Now, for the T_{uu}, it is also not useful because from travelling unlabelled to unlabelled node is not worthy in this method. Last is T_{ul}, unlabelled to labelled node traversal, it is important part of the matrix because we have to find the label for unlabelled data and we start the traversal from this node and find the labelled node for predicting the label for the given node. As highlighted in Fig. 3, this portion will be taken consideration for further calculations.

Now, we will find

Fig. 3 Matrix

T_{ll} transition from labelled node to labelled node	1	2	3	4	5	6	7	8	transition from labelled node to unlabelled node
	1	0	0	0	0	0	0	0	1
	0	1	0	0	0	0	0	0	2 T_{lu}
	0	0	0	1	0	0	0	0	3
T_{ul}	0.33	0	0.33	0	0.33	0	0	0	4
	0	0	0	0.5	0	0.5	0	0	5
Transition from unlabelled node to labelled node (random walk)	0	0.33	0	0	0.33	0	0.33	0	6
	1	0	0	0	0	1	0	0	7
	1	0	0	0	0	1	0	0	8

$T =$

transition from unlabelled to unlabelled node T_{uu}

labelled node : 1 , 2   unlabelled node : 3 , 4 , 5 , 6 , 7 , 8

$$\lim_{t \to \infty} T$$

because in the random walk, we can go to any labelled node with the infinite nodes. It is indicating that when we start random walk from any unlabelled node, we can travelled through any number of nodes. So in general, we assume that we visit infinite nodes to find the labelled node.

$$\lim_{t \to \infty} T = \begin{bmatrix} I & 0 \\ T_{ul} & T_{uu} \end{bmatrix} \times \begin{bmatrix} I & 0 \\ T_{ul} & T_{uu} \end{bmatrix} \times \begin{bmatrix} I & 0 \\ T_{ul} & T_{uu} \end{bmatrix} \times \cdots$$

after multiplying all the matrixes, we will get

$$\lim_{t \to \infty} T = \begin{bmatrix} I & 0 \\ (1 - T_{uu})^{-1} T_{ul} & 0 \end{bmatrix}$$

The above equation is transition matrix after visiting ∞ nodes in the given graph. Based on this matrix, we will apply the label propagation algorithm, which is second part of this proposed method and is discussed in Sect. 4.2.

4.2 Label Propagation Algorithm

Now put value of T for ∞ steps in the below equation

$$\begin{bmatrix} y_l' \\ y_u' \end{bmatrix} = \lim_{t \to \infty} T \times \begin{bmatrix} y_l \\ 0 \end{bmatrix}$$

So, we get

$$\begin{bmatrix} y'_l \\ y'_u \end{bmatrix} = \begin{bmatrix} I & 0 \\ (1 - T_{uu})^{-1} T_{ul} & 0 \end{bmatrix} \times \begin{bmatrix} y_l \\ 0 \end{bmatrix}$$

So, from the above equation, we can say that

$$y'_l = y_l$$

$$y'_u = (1 - T_{uu})^{-1} T_{ul} \times y_l$$

Here, we will discuss the steps for the LPA algorithm.

1. Initialize, y_l = Labelled node and T = Transition matrix

$$y = \begin{bmatrix} y_l \\ y_u \end{bmatrix}$$
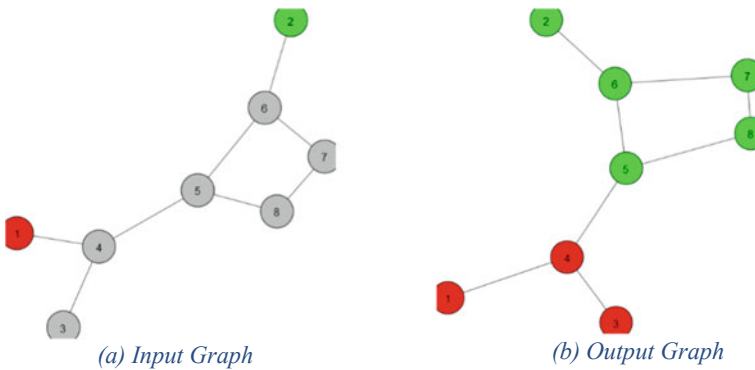
2. Propagate the label

$$y' = T \times y$$

3. For the labelled node

$$y'_l = y_l$$

4. For the unlabelled node

$$y'_u = (1 - T_{uu})^{-1} T_{ul} \times y_l$$

5. Now take maximum value for unlabelled node from the calculated matrix

(a) Input Graph   *(b) Output Graph*

Fig. 4 Label propagation algorithm

So, after following the above steps, we will get the following result (Fig. 4).

So, from the matrix, we can decide the label for the given node, so for node-1, it is showing red label with the probability of 1. For node-2, it is showing green label. Node-3 has red label with the probability of 0.7333 and green label with the probability of 0.266, so we will consider maximum value from the given data and with maximum value 0.7333 the label of the node-3 is red. The same process will be followed for the all the nodes.

$$A = \begin{bmatrix} 1 & 0 \\ 0 & 1 \\ 0.733 & 0.266 \\ 0.733 & 0.266 \\ 0.4666 & 0.5333 \\ 0.266 & 0.733 \\ 0.333 & 0.666 \\ 0.399 & 0.599 \end{bmatrix}$$

5   Execution and Implementation

This algorithm is implemented in Python using Jupyter notebook. The modules used for implementations are igraph, Pycairo, NumPy, and cairocffi. igraph is used to visualization of the graph and networks. This module used widely in academic and research area. From the text file of edges first, we extract the data and then help of the igraph we plot the graph and also provide the labels. Pycairo and cairocffi basically contain graphics libraries. NumPy is used for matrix operations.

5.1   Dataset Selection and Preprocessing

In this paper, email dataset is used which contain 20 nodes and these nodes are connected through edges which is provided as the text file. After fetching data from text file, we assign one ID and label to nodes and create graph using igraph. After that we added edges one by one and then assign labels to the nodes. Now, the graph is ready for further calculation.

Table 2 Comparison of LPA time

Number of nodes	Wall time (ms)
8	7.6
20 (Figs. 5 and 6)	56.7
50	107.4

5.2 Evaluation Measures

For the different number of nodes, the time taken will also be different. In this implementation, the wall time is measure for the label propagation algorithm with different number of nodes. Time taken is as under (Table 2).

This is only time taken for the label propagation algorithm, random walk time is not taken in to the consideration. Here, we have not took more than 50 nodes because of the system limitation and another reason is that the matrix generated from these nodes will be $n \times n$ for the n numbers of nodes.

6 Results and Discussion

As we can see in the Table 3, we compare various algorithms and the CPU time taken for each algorithm. From the table, we can say that label propagation algorithm gives best result in minimum time label propagation which is 314 μs. Divisive method of Girvan-Newman also gives good performance. Whereas spin-glass algorithm which uses optimization algorithm is taking maximum time for the given dataset of email. Here, various optimization, clustering algorithms is discussed.

Louvain method which is taking 5.93 ms CPU time. It is taking more time because it moves nodes to the nearer community and then check for the modularity (quality). In this method, clustering is time consuming part. Infomap is also using the concept of clustering, it is taking less time compare to Louvain method but it is still more

Table 3 Comparison of different algorithm

| Algorithm	Time required (CPU time)
Louvain method (Hierarchical clustering algorithm)	5.93 mS
Walk trap (Random walk)	2.3 mS
Label propagation algorithm	314 μs
Girvan-Newman algorithm (Edge betweenness centrality-divisive method)	901 μs
Infomap algorithm (Clustering algorithm)	2.18 ms
Spin glass (Optimization algorithm)	327 ms
Fast greedy (Optimization algorithm)	3.86 ms
Leiden (Optimization algorithm)	2.12 ms

Fig. 5 Input
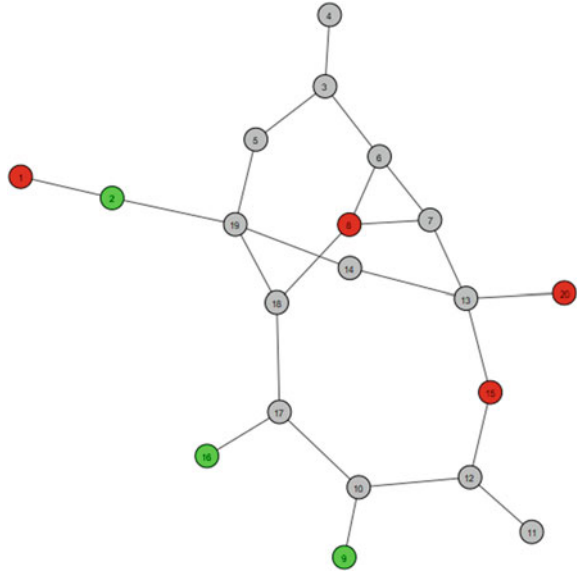
Fig. 6 Output
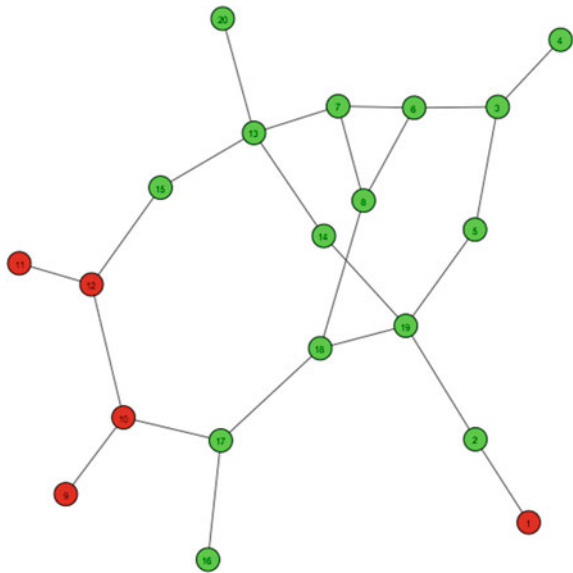
than LPA [18]. Optimization algorithms are also taking more time compare to other algorithms. In optimization algorithm, Leiden is taking least time but it much more than label propagation algorithm. As shown in the table, for label prediction, LPA is taking less time. So we add random walk [4] in this concept for the traversal, and after traversal it will apply LPA which will help to predict the label. Reason for selecting

LPA is that it is taking less time for label prediction among all and we merge the concept of random walk because it is simple and also powerful mathematical tool for extracting the information like similarity from the graph.

7   Conclusion and Future Work

In this paper, community detection model is implemented by random walk and label propagation algorithm. First of all, the random walk is start from the unlabelled node and it walks until it reaches to the labelled node. Labelled node works as absorbing state means it cannot go further, after this the label propagation algorithm is applied and label is decided for the unlabelled node. The problem occurs when the number of nodes increase. When nodes increase, then matrix size is also increase. So, this is one limitation is observed for the proposed approach. To overcome this limitation, we can apply dimensionality reduction. So, this is the future work of our topic. Community detection is used for recommendation system, market segmentation, fraud detection, medical application like cancer detection based on symptoms, criminology, etc.

References

1. Su Y, Zhou K, Zhang X, Cheng R, Zheng C (2021) A parallel multi-objective evolutionary algorithm for community detection in large-scale complex networks. Inf Sci
2. Ma H, Liu Z, Zhang X, Zhang L, Jiang H (2021) Balancing topology structure and node attribute in evolutionary multi-objective community detection for attributed networks. Knowl Based Sys
3. Wang X, Li J, Yang L, Mi H (2021) Unsupervised learning for community detection in attributed networks based on graph convolutional network. Neurocomput 456:147–155. ISSN:0925-2312
4. Kirianovskii I, Granichin O, Proskurnikov A (2016) A new randomized algorithm for community detection in large networks. IFAC
5. Moscato V, Sperlì G (2021) A survey about community detection over on-line social and heterogeneous information networks. Knowl -Based Sys 224:107112. ISSN:0950-7051
6. Verma P, Goyal R (2021) Influence propagation based community detection in complex networks. Mach Learn Appl 3:100019. ISSN:2666-8270
7. Sarma D, Alam W, Saha I, Alam MN, Alam MJ, Hossain S (2020). Bank fraud detection using community detection algorithm. In: ICIRCA
8. Sharma R, Oliveira S (2017) Community detection algorithm for big social networks using hybrid architecture. Big Data Res
9. Ding SX, Li L, Krüger M (2019) Application of randomized algorithms to assessment and design of observer-based fault detection systems. Autom, China
10. Hijab M, Damodaram A Weighted randomized algorithms for efficient load balancing in distributed computing environments. Mater Today
11. Zhang F, Wu B, Wang B, Tong J, Gao F (2013) Community detection in directed graphs via node similarity computation. In: ICWMMN
12. Matsui T, Rene AON (2020) A pervasive community detection method through modular decomposition of Markov chain for social media analysis. In: International conference on soft computing and intelligent systems

13. Gupta S, Mittal S, Gupta T, Singhal I, Khatri B, Gupta AK, Kumar N (2017) Parallel quantum-inspired evolutionary algorithms for community detection in social networks. Appl Soft Comput
14. Liao W, Deng K, Wang S (2019) Community detection based on graph coloring. In: SSCI
15. Zhou H, Xi B, Zhang Y, Li J, Zhang F (2018) A graph clustering algorithm using attraction-force similarity for community detection. IEEEAccess
16. Okuda M, Satoh SI, Sato Y, Kidawara Y (2021) Community detection using restrained random-walk similarity. IEEE Trans Pattern Anal Mach Intell
17. Girvan M, Newman MEJ (2002) Community structure in social and biological networks. In: Proceedings of the national academy of sciences
18. Zhang Y, Liu Y, Jin R, Tao J, Chen L, Wu X (2020) Gllpa: a graph layout based label propagation algorithm for community detection. Knowl Based Syst
19. Long H, Wu T, Yin H (2020) A skeleton-based community detection algorithm for directed networks. In: ICISCAE

Comparative Analysis of Generative Adversarial Network-Based Single-Image Super-Resolution Approaches

Kalpesh Prajapati, Vishal Chudasama, Heena Patel, Anjali Sarvaiya, and Kishor Upla

Abstract In the past decade, a convolutional neural network that can work on image became most popular since there were many powerful GPUs and datasets available to work. Convolutional neural network advanced the performance in various image processing tasks. In single-image-based super-resolution, convolutional neural network predicated methods have obtained remarkable performance in terms of error quantification (i.e., PSNR and SSIM) than earlier traditional machine learning predicated methods. Even though achieving better error measurements, the super-resolution results look blurry in appearance because of the classical L_1 or L_2 loss functions that have been used in the training process. Recently, generative adversarial network has been used to obtain a super-resolve image with better perceptual quality as compared to a convolutional neural network. In this manuscript, the technique and performance of those generative adversarial networks for single-image super-resolution approaches are compared for upscaling factor $\times 4$.

Keywords Single-image super-resolution · Convolutional neural network · Generative adversarial network

1 Introduction

Super-resolution (SR) problem refers to reproduce a high-resolution (HR) image from its corresponding low-resolution (LR) counterparts. There are mainly two approaches to handle the problem. First is single-image super-resolution (SISR), in which only single image is used as input. Another approach called multi-images super-resolution (MISR) which uses multiple images to gather information from different sources to produce the single-SR image. However, the MISR approach is less
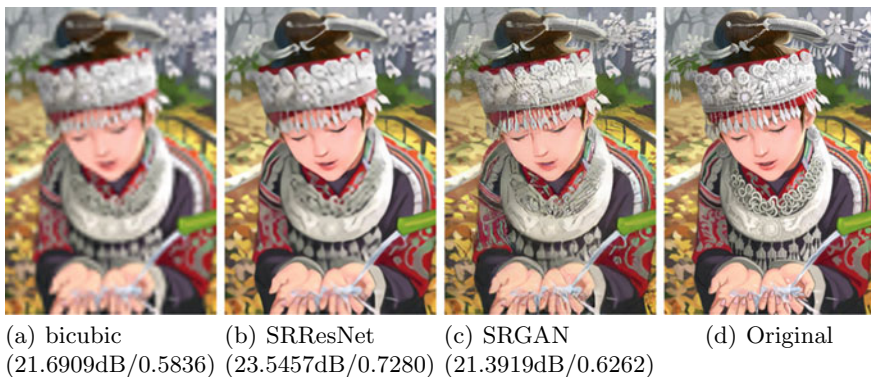
K. Prajapati (✉)
HCL Technologies Ltd., Noida, India
e-mail: kalpesh.jp89@gmail.com

V. Chudasama · H. Patel · A. Sarvaiya · K. Upla
Sardar Vallabhbhai National Institute of Technology (SVNIT), 395007 Surat, India

effective than SISR in SR task [1, 10, 19] because it needs image registration and fusion to perform super-resolution. Recently, a convolutional neural network (CNN) has been applied [12, 17] for the SISR task and achieves breakthrough performance because of its learning capacity in multi-dimensional space. Dong et al. have been introduced the first CNN for SR task called as SRCNN [2] which was implemented using just three convolutional layers. Following that, numerous CNN-based models have been introduced to improve quantitative performance related to peak-signal-to-noise-ratio (PSNR) and structural similarity index (SSIM). These techniques employ pixel-based $L1$ or $L2$ loss functions to achieve better score of these measures. However, even though achieving high PSNR and SSIM values from those methods, the high-frequency texture details cannot be obtained and such methods generate blurry images. Here, the SR results of the recently proposed CNN-based method (i.e., SRResNet [7]) are shown in Fig. 1. One can observe here that despite attaining better fidelity value (i.e., PSNR and SSIM), the quality of SR results appears to be blurry.

Recently, a generative adversarial network (GAN) can extract perceptual features at a high frequency [7, 11, 17]. In GAN, the generator network generates the images in natural manifold, while the remaining network that is discriminator network identifies the difference of the generated images from the HR images. Due to such adversarial training of GAN, the SR observations with more perceptual texture details have been produced. Ledig et al. [7] have proposed GAN for the SISR task and suggest the SRGAN model to super-resolved the LR samples for upscaling factor $\times 4$. The SR result of the SRGAN model is demonstrated in Fig. 1. Here, one can easily visualize the SR result of SRGAN has more detailed information and texture details than the CNN-based network called SRResNet (i.e., the generator network of SRGAN model) even though obtaining less PSNR and SSIM measures. After SRGAN model, many models have been introduced to further improve the SR outcomes with more perception details. In this manuscript, we have compared and analyzed these popular and enhanced GAN-based SISR methods.

(a) bicubic   (b) SRResNet   (c) SRGAN   (d) Original
(21.6909dB/0.5836) (23.5457dB/0.7280) (21.3919dB/0.6262)

Fig. 1 Example of SR images where less PSNR results also shows better visual quality than the method with high PSNR value. The PSNR and SSIM measures are written at each SR result for comparison

In Sect. 2, we give a brief review of GAN-based SISR methods. The comparative analysis of these methods has been carried out in Sect. 3. Finally, in Sect. 4, we conclude the comparison.

2 General Analysis

In this section, we highlight some review of SISR techniques which are based of GAN framework as discussed earlier.

2.1 Super-Resolution Using Generative Adversarial Network (SRGAN)

SRGAN was the first framework which is introduced by Ledig et al. [7] to super-resolved the LR observation using GAN for upscaling factor $\times 4$. SRGAN is made of SR network which acts as generator and its counterpart discriminator networks. The SR network estimates the SR image which is fed into a discriminator that tries to differentiate it from the real one image. The structure of the generator network is depicted in Fig. 2.
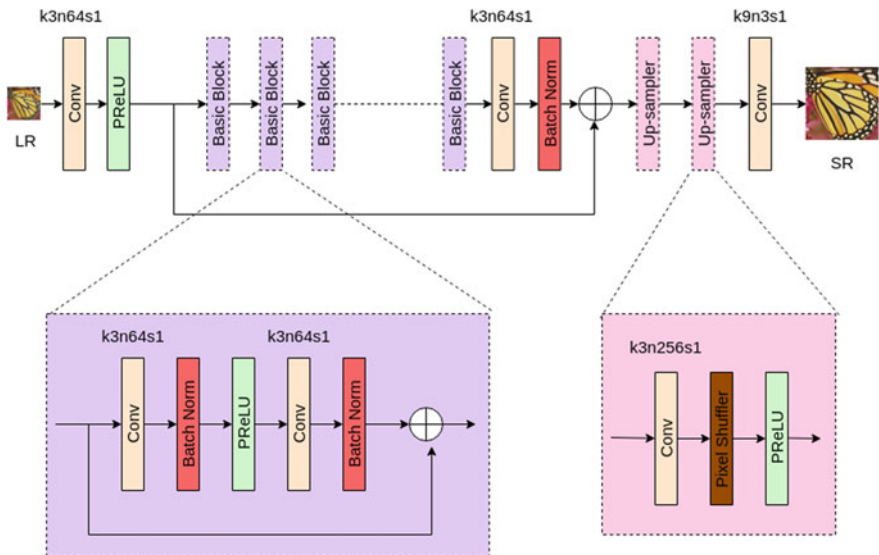
Fig. 2 Architecture design of the generator network of SRGAN [7]. Here, k, n and s indicate the kernel size, number of channels and value of stride
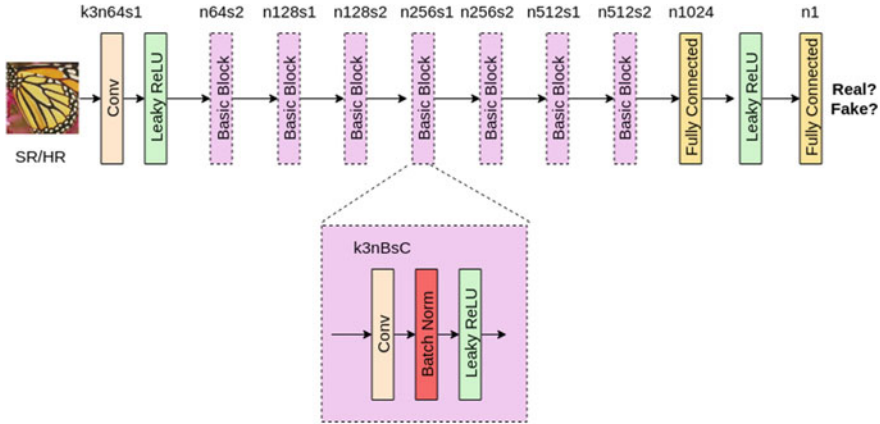
Fig. 3 Architecture design of the discriminator network of SRGAN [7] for upscaling factor $\times 4$

Here, the generator architecture is made of three stages. In the first stage, the LR observation is first fed to one convolution layer which generates the low-level features from the LR image. These feature maps are further fed to several basic blocks in the second stage which are used to extract detailed high-frequency texture details. The design of the basic block is also depicted in Fig. 2 which is inspired by residual network proposed in [3]. In the last stage, two upsamplers are used to get feature maps with the desired resolution. Here, the sub-pixel upsampling network [14] is used to upsample the feature maps. Finally, these upsampled features are fed to single convolution layer which gives the SR image.

The discriminator network takes the SR image and discriminates it from the real HR image. The design of the discriminator is shown in Fig. 3 which is made of eight convolution blocks followed by couple of fully connected (FC) layers. Here, the network architecture design follows the design suggestions given by Radford et al. [13]. All convolutional layers have 3×3 sized filters, and the corresponding feature maps are increased from 64 to 512. To reduce the image resolution, authors use the strided convolutions whenever the number of features of layers doubles. Finally, the 512 feature maps are passed to couple of FC layers and followed by one sigmoid layer which gives the corresponding probability value for image discrimination.

2.1.1 Loss Function

The loss functions such as L_1 and L_2 loss functions struggle to recover lost high-frequency details. However, minimizing these loss functions tends to generate overly-smooth observations [4, 5]. Instead of pixel-wise error measurement, Johnson et al. [5] introduce a better measure which measures the error based on the extracted feature maps obtained from the pre-trained VGG network. In SRGAN, Ledig et al. suggest to use this loss function as the combination of a VGG loss (l_X^{SR}) and an GAN loss component as,

$$l^{\text{SR}} = \underbrace{l_X^{\text{SR}}}_{\text{content loss}} + \underbrace{10^{-3} l_{\text{Gen}}^{\text{SR}}}_{\text{adversarial loss}} . \tag{1}$$

The VGG loss is defined as the square difference of the extracted feature maps of generated image $G(I^{\text{LR}})$ with the corresponding HR image I^{HR}.

$$l_{\text{VGG}/i,j}^{\text{SR}} = \frac{1}{W_{i,j} H_{i,j}} \sum_{x=1}^{W_{i,j}} \sum_{y=1}^{H_{i,j}} (\phi_{i,j}(I^{\text{HR}})_{x,y} - \phi_{i,j}(G(I^{\text{LR}}))_{x,y})^2, \tag{2}$$

where $\phi_{i,j}$ indicates the extracted features from the jth convolution before ith max-pooling layer from the pre-trained VGG19 model. $W_{i,j}$ and $H_{i,j}$ denote the width and height of the extracted feature maps.

Along with the content loss, the adversarial loss function is also added which encourages the SRGAN network to produce more perceptual details. The adversarial loss l_{Gen} is defined over all training samples (i.e., m) as,

$$l_{\text{Gen}}^{\text{SR}} = \sum_{n=1}^{m} -\log D(G(I^{\text{LR}})), \tag{3}$$

where $D(G(I^{\text{LR}}))$ denotes the discriminator output value of the generated image $G(I^{\text{LR}})$.

2.2 Single-Image Super-Resolution with Feature Discrimination (SRFeat)

In order to produce perceptually plausible images, the authors proposed a adversarial learning-based super-resolution method called SRFeat [11]. In SRFeat model, two discriminators (i.e., one discriminator that works on image and another discriminator which works on features) are used to boost the SR quality. The image discriminator works similar to the discriminator of SRGAN, while the feature discriminator acts after obtaining the feature maps from the VGG network.

The SR model of SRFeat is shown in Fig. 4. Here, the model gets I^{LR} as input that is passed through a convolution layer in order to get the low-level information from an LR image. These feature maps are then applied to multiple residual blocks which capture the higher-level complex features. The residual block is also depicted in Fig. 4 which consists of short-range skip connections that helps the network to avoid gradient vanishing problem. The long-range skip path is also incorporated to fuse the features from different basic blocks. The output of each basic blocks is connected via one 1×1 convolution layer. The pixel-shuffler layer [14] is added which up-samples the feature to the desired resolution. Finally, the upsampled maps are converted in to SR image having 3 channels by using a convolution layer.
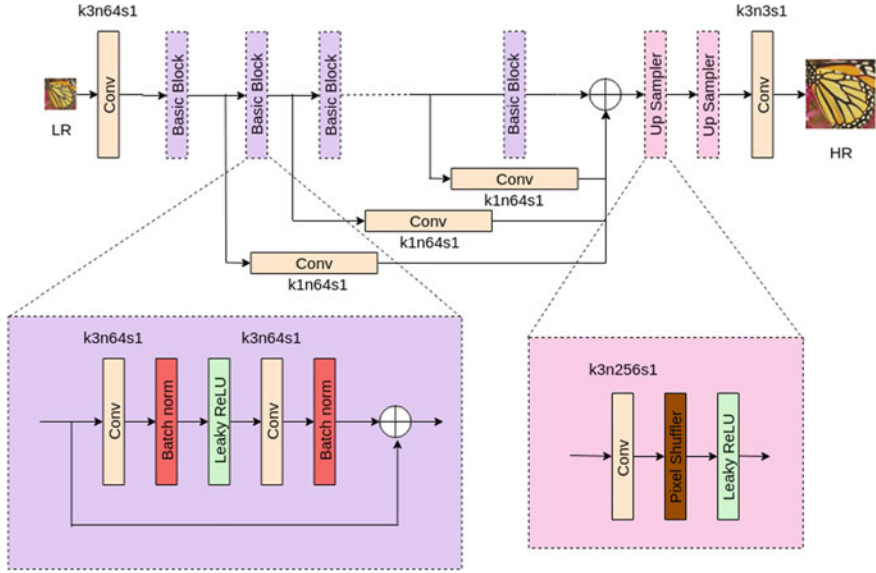
Fig. 4 Generator network design of SRFeat model

SRFeat uses two discriminators named as image-based discriminator D_i and feature-based discriminator D_f. The aim of the image-based discriminator is to identify the fake SR images and the HR images considering the pixel values, while the feature discriminator discriminates fake images and HR images by considering their extracted feature maps of the VGG network. Here, the D_i and D_f have the same network architecture as the discriminator of the SRGAN model (which is illustrated in Fig. 3). The working flow of these two discriminators is illustrated in Fig. 5. Both the discriminator networks gave the probability value that defines how much input images are real or fake.

2.2.1 Objective Function

To train the SRFeat model, a weighted loss function is used which is defined as,

$$l_{\text{Gen}} = l_p + \lambda l_{\text{ig}} + l_{\text{fg}}. \tag{4}$$

The weighting factor for GAN loss is denoted as λ above. The l_p is a perceptual loss term which is used to enforce the model to generate SR images in natural manifold. The perceptual loss function l_p is defined same as equation (2). The l_{ig} denotes an image generator loss which is used to produce high-frequency texture details and it is defined as

$$l_{\text{ig}} = -\log D_i(I^{\text{SR}}). \tag{5}$$
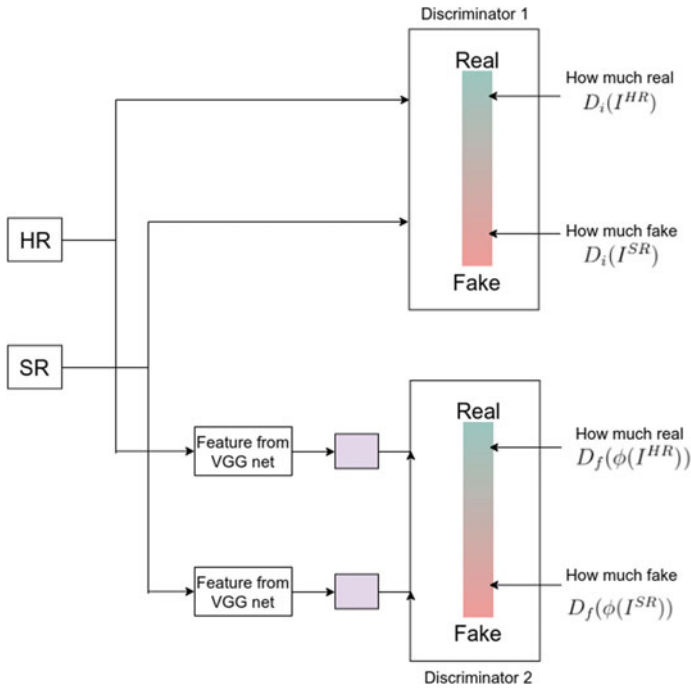
Fig. 5 Working flow of discriminator networks of SRFeat model

However, the image discriminator loss function l_{id} is defined as,

$$l_{id} = -\log D_i(I^{HR}) - \log(1 - D_i(I^{SR})), \qquad (6)$$

where $D_i(I)$ indicates the output of the image discriminator D_i. The feature generator loss l_{fg} and the feature discriminator loss l_{fd} terms are defined as,

$$l_{fg} = -\log D_f(\phi(I^{SR})), \qquad (7)$$

$$l_{fd} = -\log D_f(\phi(I^{HR})) - \log(1 - D_f(\phi(I^{SR}))), \qquad (8)$$

where $D_f(\phi)$ denotes the output of feature discriminator. Both the perceptual and the feature generator as well as discriminator losses are based on feature maps extracted from VGG network. However, the perceptual loss promotes the perceptual consistency between I^{SR} and I^{HR}, while the feature generator and discriminator losses enable the generation of perception image details.
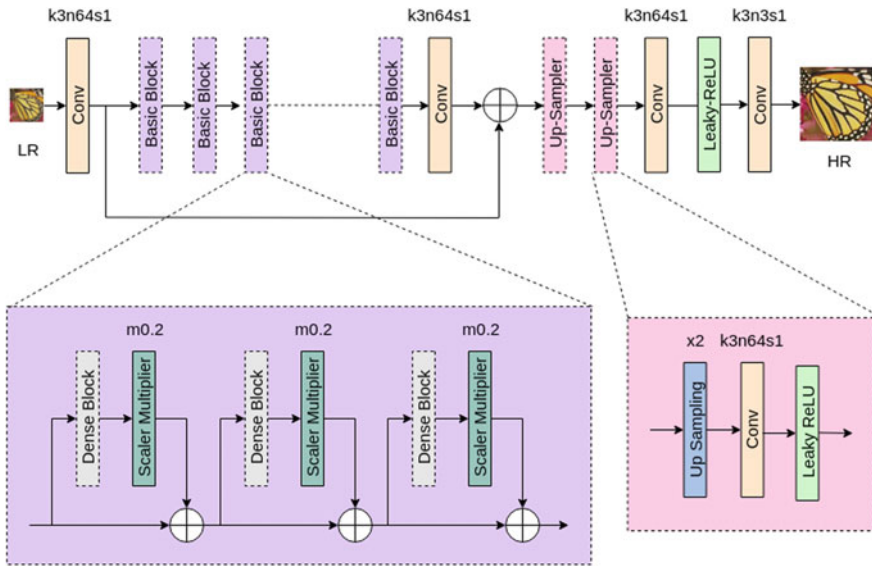
Fig. 6 Generator network design of ESRGAN

## 2.3 Enhanced Super-Resolution Using Generative Adversarial Network (ESRGAN)

To further improve the SR result of SRGAN [7], Wang et al. [17] introduced ESRGAN by making few changes to the generator network of SRGAN. The architecture of the generator of ESRGAN is displayed in Fig. 6. The main modifications in generator network are as follows:

1. All batch normalization (BN) layers have been removed and
2. Propose a novel residual block called residual-in-residual dense block (i.e., RRDB) that consists of multiple residual networks and their dense connections which is illustrated in Figs. 6 and 7.

As per the literature [8], removing BN layers increases the SR performance and reduces computational complexity. The authors experiment to observe the effect of the BN layer and found that the artifacts are observed due to the BN layer. Also, removing BN layers improves the generalization ability and reduces the computational complexity [17].

Wang et al. [17] have introduced a novel block called RRDB which is illustrated in Fig. 7. The RRDB consists of a more complex structure as compared to the residual block of SRGAN which boosts the overall performance. In addition to this, the following are the several tricks introduced by Wang et al. [17] which helps to train a deeper network.
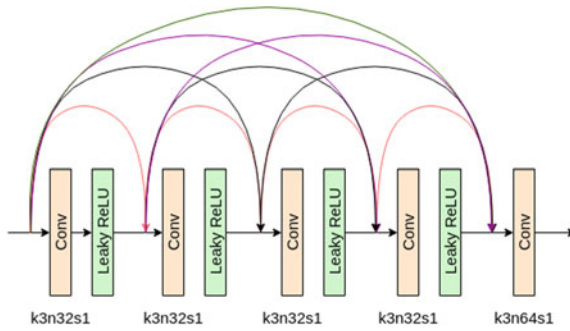
Fig. 7 Dense block architecture design of RRDB module
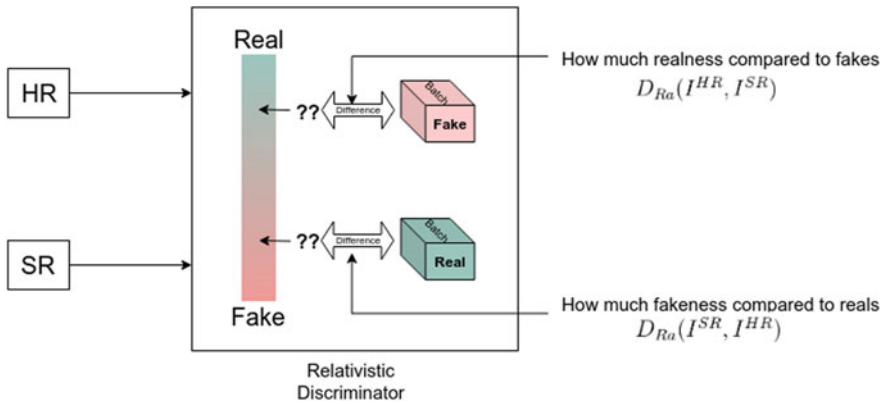
Fig. 8 Working flow of discriminator networks of ESRGAN model

- **Residual scaling** [8, 15]: The residuals are scaled-down by multiplying a constant to avoid instability issue of training.
- **Smaller initialization**: From the experiments, authors from [17] found that the smaller initial parameter variance makes the training procedure easy.

The discriminator network of the ESRGAN model has the same architectural design as the discriminator of the SRGAN model except one difference that the first fully connected layer has 100 neurons instead of 1024 neurons in the SRGAN model. The working flow of the discriminator network of the ESRGAN model is depicted in Fig. 8. Here, instead of the standard discriminator, ESRGAN employs the relativistic discriminator [6].

2.3.1 Objective Function

The objective/loss function used for the generator network is as,

$$l_{\text{Gen}} = l_p + \lambda l_{\text{Ra}}^G + \eta L_1, \tag{9}$$

where l_p, l_{Ra}^G and L_1 are the perceptual, adversarial and content loss functions, respectively. The λ, and η are the weighting factors of adversarial and content loss, respectively.

ESRGAN suggests to use perceptual loss l_p by extracting feature maps prior to the activation layer compared to suggested in SRGAN. Authors from [17] found that the activated features are very sparse which provides weak supervision, and hence, it tends to inferior the performance. Also, they observe that features after activation layer have incoherent brightness in generated samples as comparison to the HR image.

The content loss is depicted as $L_1 = \mathbb{E}_{I^{\text{LR}}} ||G(I^{\text{LR}}) - I^{\text{HR}}||_1$ that calculates the 1-norm difference between SR image ($G(I^{\text{LR}})$) and the HR image (I^{HR}).

l_{Ra}^G is loss calculated from the relativistic discriminator. In ESRGAN, instead of using simple discriminator, they use a novel approach of relativistic discriminator [6]. As compared to the discriminator in SRGAN, a relativistic average discriminator, denoted as D_{Ra}, predicts that how much the HR image I^{HR} has relatively more realistic compared to SR image I^{SR}. The RaD is formulated as $D_{\text{Ra}}(I^{\text{HR}}, I^{\text{SR}}) = \sigma(C(I^{\text{HR}}) - \mathbb{E}_{I^{\text{SR}}}[C(I^{\text{SR}})])$, where $\mathbb{E}_{I^{\text{SR}}}[\cdot]$ represents the averaging process for all super-resolved images in the batch and $C(x)$ is the output value obtained from the discriminator network. The adversarial loss for SR network is defined as,

$$l_{\text{Ra}}^G = -\mathbb{E}_{I^{\text{HR}}}[\log(1 - D_{\text{Ra}}(I^{\text{HR}}, I^{\text{SR}}))] - \mathbb{E}_{I^{\text{SR}}}[\log(D_{\text{Ra}}(I^{\text{SR}}, I^{\text{HR}}))], \tag{10}$$

This loss function contains both SR image as well as the HR image. Due to this, the generator network takes advantage of the gradients from both the images in adversarial learning, while in SRGAN, adversarial loss contains only SR image.

The discriminator loss is then defined in a similar way as:

$$l_{\text{Ra}}^D = -\mathbb{E}_{I^{\text{HR}}}[\log(D_{\text{Ra}}(I^{\text{HR}}, I^{\text{SR}}))] - \mathbb{E}_{I^{\text{SR}}}[\log(1 - D_{\text{Ra}}(I^{\text{SR}}, I^{\text{HR}}))]. \tag{11}$$

3 Result Analysis

Here, we show the hyper-parameter settings and training brief of the GAN-based models which are discussed in Sect. 2. The corresponding SR performance of these methods is also compared and analyzed in detail. We perform all the experiments with an upscaling factor of $\times 4$. The LR samples are generated by downscaling HR samples using bicubic down-sampling. The batch size is fixed to 16 for all

three models. We use the size of the randomly cropped HR image is 128×128 for ESRGAN only and 192×192 for SRGAN and SRFeat network.

For training, the DIV2K dataset [16] is used which have 800 high-quality images. For data diversity, we firstly generate sub-images of 480×480 from the original DIV2K dataset with half (240) overlapping. By doing this way, we generate approximately 32,000 images that guarantee diversity in random cropping in the training phase. The augmentation with random flipping and rotation is used on training dataset. Here, all GAN-based models have been trained in two phases. In the first phase, the PSNR-oriented models (named as SRGAN-P1 and SRFeat-P1, i.e., generator network of SRGAN and SRFeat models) are trained using L_2 loss function for SRGAN and SRFeat, while the ESRGAN-P1 (generator network of ESRGAN) is optimized based on the L_1 loss. The learning rate of 2×10^{-4} is used for SRFeat and ESRGAN, while in SRGAN, it is initialized by 1×10^{-4} and reduced by a half at every 2×10^5 of iterations. We use half the learning rate in SRGAN to make the identical setting as per SRGAN [7]. The pre-trained PSNR-oriented models are employed as an initialization for the generator. Such idea helps those models to generate more perceptually plausible samples. Here, the learning rate is set to 1×10^{-4} which is halved after every 50k number of iterations.

To train these networks, we use Adam optimization with $\beta1 = 0.9$ and $\beta2 = 0.999$ setting up to iteration of 1×10^6 for phase 1 and 5×10^5 for phase 2. We tested all three models on benchmark testing datasets: Set5, Set14, BSD100 and Urban100. For all three models, we keep 64 number of filters for each convolution layer. Also, we keep length (number) of basic block equal to 23 in ESRGAN and SRGAN while it is 16 in SRFeat. All these models have been implemented with the PyTorch framework.

3.1 Quantitative Results

To compare the performance of the PSNR-oriented networks (i.e., SRGAN-P1, SRFeat-P1 and ESRGAN-P1), we calculate PSNR and SSIM [18] on the Y channel as suggested in [2]. We calculate those measures after removing the four pixels from the boundary of SR images. Table 1 gives quantitative comparison for all approaches trained in phase 1 (PSNR) on benchmark datasets. Here, we also compare the reproduced results with the results published in their original papers. The corresponding changes of different methods than that from the original paper are also listed in Table 1. It is noteworthy to mentioned that reproduced quantitative measurements are similar to the measurements that we found from their original papers. Also, one can notice that the measurements of ESRGAN-P1 are far better than that of SRGAN-P1 and SRFeat-P1 models.

Existing quantitative metrics are not feasible to evaluate the perception measure of images. Hence, to provide a appropriate measurement which have major correlation with the perception ability of human, Mittal et al. [9] proposed a perception-based metric called natural image quality evaluator (i.e., NIQE) by collecting a 'quality-

Table 1 Quantitative comparison of fidelity-based network in terms of PSNR and SSIM measures for upscaling factor ×4

		SRGAN-P1		SRFeat-P1		ESRGAN-P1	
		Published	Our	Published	Our	Published	Our
	HR	96	192	296	192	128	128
	Depth	16	23	16	16	23	23
	Dataset	ImageNet	DIV2K	ImageNet	DIV2K	DIV2K	DIV2K
	Platform	Theano	PyTorch	Tensorlayer	PyTorch	PyTorch	PyTorch
	PSNR	32.05	32.05	32.14	32.07	32.60	32.60
Set5	SSIM	0.9019	0.8931	0.8918	0.8935	0.9002	0.8999
	PSNR	28.49	28.92	28.61	28.93	28.88	29.23
Set14	SSIM	0.8184	0.7953	0.7816	0.7947	0.7896	0.8025
	PSNR	27.58	27.55	27.59	27.56	27.76	27.72
BSD100	SSIM	0.7620	0.7349	0.7557	0.7351	0.7432	0.7425

Changes in hyper-parameters compared to original published work are also mentioned here

Table 2 Comparison of the SR results of PSNR-oriented networks and GAN-based models in terms of the NIQE score

	Set5	Set14	Urban100	BSD100
Nearest	13.8277	9.9865	8.0572	10.6913
Bicubic	6.4626	5.9530	5.4512	5.7889
SRGAN-P1	6.3304	5.3379	4.6678	5.3987
SRGAN	4.0869	3.2607	3.1981	3.0450
SRFeat-P1	6.2912	5.3074	4.6618	5.4166
SRFeat	4.7884	3.6454	3.5468	3.3551
ESRGAN-P1	6.0675	5.6071	4.7959	5.3442
ESRGAN	4.1357	3.5447	3.4323	3.2155
Original	4.8498	5.0076	3.7024	3.1359

Here, the lower NIQE value indicates the better perception quality

aware' statistical features. Such features have been collected from the natural and undistorted images. Here, the lower NIQE measure suggests better perception quality. Table 2 displays NIQE scores for PSNR-oriented networks and GAN-based methods for upscaling factor ×4. Along with these, the NIQE score of SR results obtained from the nearest neighbor and bicubic interpolation techniques is also written in this table. Here, one can find that the GAN-based models have obtained lower NIQE values than that of corresponding PSNR-oriented networks. This indicates that SR results of GAN-based models have better perceptual quality. Also, it can be found from this Table 2 that the ESRGAN model has obtained better NIQE values than that of SRGAN and SRFeat models in all testing benchmark datasets.
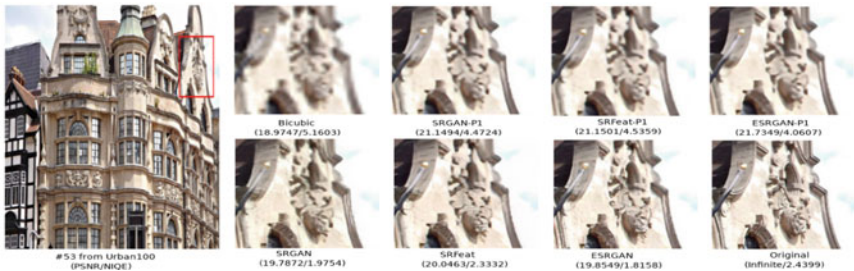
(a) Representative image from Set5
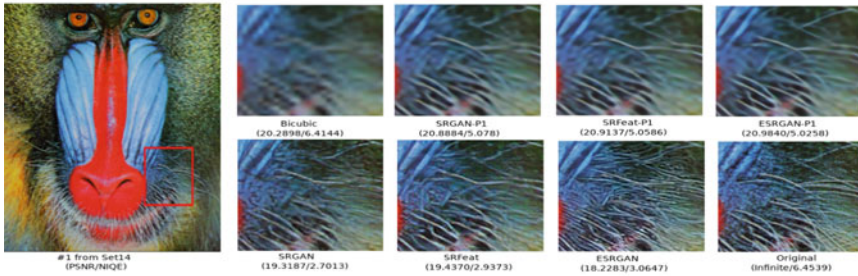
(b) Representative image from Set14

(c) Representative image from BSD100

(d) Representative image from Urban100

Fig. 9 Qualitative comparison of SR images from PSNR-oriented networks and GAN-based models for upscaling factor ×4

3.2 Qualitative Results

In addition to quantitative comparison, we also compare these GAN-based methods qualitatively. Figure 9 depicted the visual performance of Bicubic, SRGAN, SRFeat and ESRGAN models for one of the representative image in each benchmark datasets. For better comparison, the corresponding PSNR and SSIM measures are mentioned at each cropped images. It is easily noticed from Fig. 9 that the SR results of the PSRN-oriented networks, i.e., SRGAN-P1, SRFeat-P1 and ESRGAN-P1 look blurry in appearance, while the SR results of GAN-based models have more texture details. Also, the SR observation of the ESRGAN model has better perceptual quality than other networks.

4 Conclusion

In this manuscript, we discuss the popular GAN-based SISR models SRGAN, SRFeat and ESRGAN model. In order to obtain the high PSNR and SSIM measures, the PSNR-oriented networks such as SRGAN-P1, SRFeat-P1 and ESRGAN-P1 (which are the generator networks of SRGAN, SRFeat and ESRGAN models, respectively) are trained using pixel-wise loss functions. The SR results of these networks are compared with that of the corresponding GAN-based models and found that the SR results of PSNR-oriented networks look blurry in appearance, while the SR results of GAN-based models have more high-frequency texture details. By observing the performance of the SRFeat, we can conclude that additional discriminator which works on edges of SR and HR images improves the perceptual quality of SR image. However, the performance of ESRGAN outperforms than any other methods using relativistic average GAN loss. Moreover, we seen that the traditional quantitative measures such as PSNR and SSIM are not correlating the quality with human perception and it is still an challenging research problem to explore.

References

1. Anwar S, Khan S, Barnes N (2019) A deep journey into super-resolution: a survey. arXiv:1904.07523
2. Dong C, Loy CC, He K, Tang X (2014) Learning a deep convolutional network for image super-resolution. In: European conference on computer vision. Springer, pp 184–199
3. He K, Zhang X, Ren S, Sun J (2016) Deep residual learning for image recognition. In: Proceedings of the IEEE conference on computer vision and pattern recognition, pp 770–778

4. Huang J, Mumford D (1999) Statistics of natural images and models. In: Proceedings 1999 IEEE computer society conference on computer vision and pattern recognition (cat. no PR00149), vol 1. IEEE, pp 541–547
5. Johnson J, Alahi A, Fei-Fei L (2016) Perceptual losses for real-time style transfer and super-resolution. In: European conference on computer vision. Springer, pp 694–711
6. Jolicoeur-Martineau A (2018) The relativistic discriminator: a key element missing from standard GAN. arXiv:1807.00734
7. Ledig C, Theis L, Huszár F, Caballero J, Cunningham A, Acosta A, Aitken A, Tejani A, Totz J, Wang Z et al (2017) Photo-realistic single image super-resolution using a generative adversarial network. In: Proceedings of the IEEE conference on computer vision and pattern recognition, pp 4681–4690
8. Lim B, Son S, Kim H, Nah S, Mu Lee K (2017) Enhanced deep residual networks for single image super-resolution. In: Proceedings of the IEEE conference on computer vision and pattern recognition workshops, pp 136–144
9. Mittal A, Soundararajan R, Bovik AC (2013) Making a "completely blind" image quality analyzer. IEEE Signal Process Lett 20(3):209–212
10. Nasrollahi K, Moeslund TB (2014) Super-resolution: a comprehensive survey. Mach Vis Appl 25(6):1423–1468
11. Park SJ, Son H, Cho S, Hong KS, Lee S (2018) SRFeat: single image super-resolution with feature discrimination. In: Proceedings of the European conference on computer vision (ECCV), pp 439–455
12. Prajapati K, Chudasama V, Upla K (2020) A light weight convolutional neural network for single image super-resolution. Proc Comput Sci 171:139–147
13. Radford A, Metz L, Chintala S (2015) Unsupervised representation learning with deep convolutional generative adversarial networks. arXiv:1511.06434
14. Shi W, Caballero J, Huszár F, Totz J, Aitken AP, Bishop R, Rueckert D, Wang Z (2016) Real-time single image and video super-resolution using an efficient sub-pixel convolutional neural network. In: Proceedings of the IEEE conference on computer vision and pattern recognition, pp 1874–1883
15. Szegedy C, Ioffe S, Vanhoucke V, Alemi AA (2017) Inception-v4, inception-resnet and the impact of residual connections on learning. In: Thirty-first AAAI conference on artificial intelligence
16. Timofte R, Agustsson E, Van Gool L, Yang MH, Zhang L (2017) Ntire 2017 challenge on single image super-resolution: methods and results. In: Proceedings of the IEEE conference on computer vision and pattern recognition workshops, pp 114–125
17. Wang X, Yu K, Wu S, Gu J, Liu Y, Dong C, Qiao Y, Change Loy C (2018) ESRGAN: enhanced super-resolution generative adversarial networks. In: Proceedings of the European conference on computer vision (ECCV)
18. Wang Z, Bovik AC, Sheikh HR, Simoncelli EP et al (2004) Image quality assessment: from error visibility to structural similarity. IEEE Trans Image Process 13(4):600–612
19. Yang CY, Ma C, Yang MH (2014) Single-image super-resolution: a benchmark. In: European conference on computer vision. Springer, pp 372–386